

NATURAL-GRADIENT TRACER TESTS IN A  
HIGHLY FRACTURED SOIL

Richard T. DeCesar  
B.S., Shippensburg State College, 1978  
M.S., Oregon Graduate Center, 1984

A dissertation submitted to the faculty  
of the Oregon Graduate Center  
in partial fulfillment of the  
requirements for the degree of  
Doctor of Philosophy  
in  
Environmental Science

July 1987

The dissertation "Natural-Gradient Tracer Tests in a Highly Fractured Soil" by Richard T. DeCesar, has been examined and approved by the following Examination Committee:

---

James F. Pankow, Thesis Advisor  
Professor and Department Head

---

Richard L. Johnson  
Assistant Professor

---

Joseph F. Keely  
Assistant Professor

---

Carl D. Palmer  
Assistant Professor

---

Richard A. Elliott  
Professor

## DEDICATION

This dissertation is dedicated to Sarah Devlin DeCesar whose love, support and perspective helped me to reach this goal.

## ACKNOWLEDGMENTS

I would like to acknowledge the many people who contributed to the work which led to this dissertation. I am especially grateful to my advisor, Dr. James F. Pankow, without whose ideas, suggestion, guidance and support this work would not have been completed. I am grateful to Dr. Richard L. Johnson whose assistance with numerous aspects of this study was crucial to its success. I am thankful to Philip Curtis for assisting in the field work and making the drives from Portland to Alkali Lake interesting. I would like to thank William Asher for his efforts in the HPLC-laser induced fluorescence analysis and Lorne Isabelle for helping me get out of the machine shop with the necessary equipment and all ten of my fingers. The sound advice of Dr. John Cherry and Dr. Leslie Smith at critical junctures were important to this work. I also appreciate the encouragement of Dr. John Cooper and Dr. James Huntzicker throughout the years that this work was conducted. I gratefully acknowledge the financial support provided by a Clark Fellowship, the Northwest Environmental Research Consortium, the U.S. Environmental Protection Agency (Grant #'s R80827201-02 and R812553010) and the U.S. Geological Survey (Agreement # 14-08-001-A0410).

## CONTENTS

Approval	ii
Dedication	iii
Acknowledgements	iv
List of Tables	viii
List of Figures	ix
Abstract	xix
I. INTRODUCTION	1
I.A. Background	1
I.A.1. Groundwater Contamination: A Rationale for Concern	1
I.A.2. Transport in Fractured Geological Materials	3
I.A.3. Previous Studies of Solute Transport in Fractured Media	5
I.B. Description of the Alkali Lake Chemical Disposal Site	13
II. IMPLEMENTATION OF THE NATURAL-GRADIENT TRACER TESTS	20
II.A. Justification for a Natural-gradient Tracer Test	21
II.B. Objectives of the Natural-gradient Tracer Tests	23
II.C. Tracer Test Experimental Design	24
II.C.1. The Tracer Test Study Site	24
II.C.2. Piezometer Design and Installation	26
II.C.3. Tracer Compounds	29
II.C.4. Monitoring Network	32
II.C.5. Injection Procedures	36

II.C.6. Sampling Procedure and Schedule	40
II.C.7. Analytical Procedure	42
II.C.7.a. HPLC Separation	44
II.C.7.b. Laser-induced Fluorescence Detector	46
II.C.7.c. Standard Operating Procedure	51
II.C.8. Tracer Dye Stability	54
II.D. Partition Coefficient Measurements	55
II.E. Characterization of the Groundwater Flow System	58
II.E.1. Water Table Measurements	58
II.E.2. Hydraulic Conductivity Measurements	68
II.E.2.a. Experimental	68
II.E.2.b. Results	71
III. TRACER PLUME MAPPING METHODOLOGY	78
III.A. Data Set Used for Contour Method Evaluation	80
III.B. Evaluation Procedure	80
III.C. Description of the Mapping Procedures	81
III.C.1. Inverse Distance Squared (IDS) Mapping Procedure	83
III.C.2. Kriging - Isotropic Linear Variogram (KILV) Mapping Procedure	84
III.C.3. Kriging - Anisotropic Linear Variogram (KALV) Mapping Procedure	85
III.C.4. Nonparametric Geostatistical Gridding (NGG) Mapping Procedure	87
III.C.5. Triangular Mesh Weights (TMW) Mapping Procedure	88
III.D. Results and Discussion	89

III.E. Conclusions	101
IV. DESCRIPTION OF TRACER MIGRATION PATTERNS	104
IV.A. Tracer Concentration Contour Maps	105
IV.B. Intergrated Transects of the Tracer Plumes	136
IV.C. Empirical Evidence for an Exponentially Decaying Source Function	148
IV.D. Moments of the Tracer Plumes	155
IV.E. Summary	168
V. MODELING THE OBSERVED TRANSPORT OF THE TRACER COMPOUNDS	170
V.A. Introduction	170
V.B. Application of the Idealized Fracture Network Model	171
V.B.1. Determining the Appropriate Fracture Network Model	171
V.B.2. Application of the Selected Fracture Idealization	178
V.C. Application of the EPM Model	186
V.C.1. One-dimensional Homogeneous EPM Simulations	186
V.C.2. Two-dimensional Homogeneous EPM Simulations	209
V.C.3. Heterogeneous EPM Simulations - Introduction	222
V.C.4. Heterogeneous EPM Simulations - Applications	225
V.D. Applying the Tracer Test Modeling Results to Understanding Contaminant Migration from the CDS	231
VI. CONCLUSIONS	234
References	240
Vita	246

## LIST OF TABLES

II.C.1	Fluorescein dyes injected for tracer test #1.	30
II.C.2	Piezometer installation schedule.	35
II.C.3	Compositions of the fluorescein dye mixtures injected for tracer test #1.	38
II.C.4	Sampling schedules for tracer tests #1 and #2.	43
II.C.5	HPLC gradient elution parameters.	45
II.C.6	Estimated coefficients of variation for fluorescein and 4'-chlorofluorescein.	53
II.C.7	Results of the fluorescein stability analysis.	56
II.E.1	Hydraulic conductivity ( $K_H$ ) measurements.	73
III.C.1	Inter-method comparison of the gridding methods with respect to honoring the measured values.	95
III.C.2	Inter-method comparison of the gridding methods with respect to predicting the removed values using the reduced data set.	97
III.C.3	Inter-method and inter-data set comparison of center of mass calculations. Values given are x,y coordinates in meters.	99
III.C.4	Inter-method and inter-data set comparison of mass balance calculations. Values given are percent of injected fluorescein mass.	100
IV.D.1	Spatial moments of the vertically averaged fluorescein plume from tracer test #1.	158
IV.D.2	Spatial moments of the vertically averaged 4'-chlorofluorescein plume from tracer test #2.	159
V.C.1	Longitudinal dispersivities calculated with Equation V.9.	227



## LIST OF FIGURES

I.B.1	Topographic map of Alkali Lake playa and surrounding area (Pankow et.al., 1984).	14
I.B.2	Topographic map of the CDS vicinity (Pankow et.al., 1984).	15
I.B.3	A typical core taken from a depth of 1.5 m illustrating the abundance of horizontal and vertical fractures found throughout the site area.	18
II.C.1	Map showing the location of the tracer test site relative to the CDS (after Johnson, 1984).	25
II.C.2	Schematic drawing of the multi-level piezometers used to sample the tracer plumes.	27
II.C.3	Chemical structures of several of the fluorescein dyes used as tracers.	31
II.C.4	HPLC chromatogram of the reactant and products of the 4'-chlorofluorescein synthesis.	33
II.C.5	Map showing the final sampling grid used for the tracer tests.	34
II.C.6	Schematic drawing of the injection apparatus used for tracer test #1.	39
II.C.7	Schematic drawing of the apparatus used to obtain groundwater samples from the multi-level piezometers.	41
II.C.8	Typical chromatogram for the fluorescein dye mixture used in tracer test #1 illustrating the peak shape and resolution provided by the HPLC separation.	47
II.C.9	Schematic drawing of the laser-induced fluorescence detection apparatus.	49
II.C.10	Diagram of the low-noise, high-gain circuit used to amplify signals from the photodiode.	50

II.C.11	HPLC laser-induced fluorescence calibration curves for several of the tracer dyes (injection volume = 10 l).	52
II.E.1	Map showing the locations of piezometers used for water table measurements during the tracer tests (*'s represent piezometer locations).	60
II.E.2	Water table map in centimeters for 6/14/84.	61
II.E.3	Water table map in centimeters for 11/10/84.	62
II.E.4	Water table map in centimeters for 4/8/85.	63
II.E.5	Water table map in centimeters for 7/15/85.	64
II.E.6	Water table map in centimeters for 10/3/85.	65
II.E.7	Water table in centimeters at piezometers S-3 and S-15 as a function of time during the period 1984-1985.	66
II.E.8	Hydraulic gradient in the tracer test site as a function of time during the period 1984-1985.	67
II.E.9	Map showing the locations within the tracer site where slug tests were performed to determine $K_H$ .	69
II.E.10	Schematic drawing of the slug test reservoir (after Johnson, 1984).	70
II.E.11	Typical regression curve used to estimate $K_H$ from slug test data.	72
II.E.12	Frequency histograms of $K_H$ based on $K_H$ measurements made within the tracer site.	74
II.E.13	Frequency histograms of $\ln(K_H)$ based on $K_H$ measurements made within the tracer site.	75
II.E.14	$K_H$ as a function of distance along the 14 m transect on which $K_H$ was measured within the tracer site.	77
III.C.1	Longitudinal and transverse linear variograms calculated on the basis of the complete data set.	86

III.C.2	Concentration contour maps produced by the IDS method for the A) complete data set, B) perturbed data set and C) reduced data set.	90
III.C.3	Concentration contour maps produced by the KILV method for the A) complete data set, B) perturbed data set and C) reduced data set.	91
III.C.4	Concentration contour maps produced by the KALV method for the A) complete data set, B) perturbed data set and C) reduced data set.	92
III.C.5	Concentration contour maps produced by the NPK method for the A) complete data set, B) perturbed data set and C) reduced data set.	93
III.C.6	Concentration contour maps produced by the TMW method for the A) complete data set, B) perturbed data set and C) reduced data set.	94
IV.A.1	Contour map of fluorescein concentration measured on day 50 of tracer test #1 at the 1.8 m sampling depth.	106
IV.A.2	Contour map of fluorescein concentration measured on day 50 of tracer test #1 at the 2.4 m sampling depth.	107
IV.A.3	Contour map of fluorescein concentration measured on day 50 of tracer test #1 at the 3.0 m sampling depth.	108
IV.A.4	Contour map of fluorescein concentration measured on day 93 of tracer test #1 at the 1.8 m sampling depth.	109
IV.A.5	Contour map of fluorescein concentration measured on day 93 of tracer test #1 at the 2.4 m sampling depth.	110
IV.A.6	Contour map of fluorescein concentration measured on day 93 of tracer test #1 at the 3.0 m sampling depth.	111
IV.A.7	Contour map of fluorescein concentration measured on day 123 of tracer test #1 at the 1.8 m sampling depth.	112

IV.A.8	Contour map of fluorescein concentration measured on day 123 of tracer test #1 at the 2.4 m sampling depth.	113
IV.A.9	Contour map of fluorescein concentration measured on day 123 of tracer test #1 at the 3.0 m sampling depth.	114
IV.A.10	Contour map of fluorescein concentration measured on day 232 of tracer test #1 at the 1.8 m sampling depth.	115
IV.A.11	Contour map of fluorescein concentration measured on day 232 of tracer test #1 at the 2.4 m sampling depth.	116
IV.A.12	Contour map of fluorescein concentration measured on day 232 of tracer test #1 at the 3.0 m sampling depth.	117
IV.A.13	Contour map of fluorescein concentration measured on day 342 of tracer test #1 at the 1.8 m sampling depth.	118
IV.A.14	Contour map of fluorescein concentration measured on day 342 of tracer test #1 at the 2.4 m sampling depth.	119
IV.A.15	Contour map of fluorescein concentration measured on day 342 of tracer test #1 at the 3.0 m sampling depth.	120
IV.A.16	Contour map of fluorescein concentration measured on day 419 of tracer test #1 at the 1.8 m sampling depth.	121
IV.A.17	Contour map of fluorescein concentration measured on day 419 of tracer test #1 at the 2.4 m sampling depth.	122
IV.A.18	Contour map of fluorescein concentration measured on day 419 of tracer test #1 at the 3.0 m sampling depth.	123
IV.A.19	Vertically averaged contour map of fluorescein concentration measured on day 50 of tracer test #1.	124

IV.A.20	Vertically averaged contour map of fluorescein concentration measured on day 93 of tracer test #1.	125
IV.A.21	Vertically averaged contour map of fluorescein concentration measured on day 123 of tracer test #1.	126
IV.A.22	Vertically averaged contour map of fluorescein concentration measured on day 232 of tracer test #1.	127
IV.A.23	Vertically averaged contour map of fluorescein concentration measured on day 342 of tracer test #1.	128
IV.A.24	Vertically averaged contour map of fluorescein concentration measured on day 419 of tracer test #1.	129
IV.A.25	Contour map of 4'-chlorofluorescein concentration measured on day 10 of tracer test #2 at the 1.8 m sampling depth.	130
IV.A.26	Contour map of 4'-chlorofluorescein concentration measured on day 20 of tracer test #2 at the 1.8 m sampling depth.	131
IV.A.27	Contour map of 4'-chlorofluorescein concentration measured on day 45 of tracer test #2 at the 1.8 m sampling depth.	132
IV.A.28	Contour map of 4'-chlorofluorescein concentration measured on day 101 of tracer test #2 at the 1.8 m sampling depth.	133
IV.A.29	Contour map of 4'-chlorofluorescein concentration measured on day 178 of tracer test #2 at the 1.8 m sampling depth.	134
IV.B.1	Integrated transects derived from the vertically averaged fluorescein concentrations for day 50 of tracer test #1.	137
IV.B.2	Integrated transects derived from the vertically averaged fluorescein concentrations for day 93 of tracer test #1.	138

IV.B.3	Integrated transects derived from the vertically averaged fluorescein concentrations for day 123 of tracer test #1.	139
IV.B.4	Integrated transects derived from the vertically averaged fluorescein concentrations for day 232 of tracer test #1.	140
IV.B.5	Integrated transects derived from the vertically averaged fluorescein concentrations for day 342 of tracer test #1.	141
IV.B.6	Integrated transects derived from the vertically averaged fluorescein concentrations for day 419 of tracer test #1.	142
IV.B.7	Integrated transects derived from the vertically averaged 4'-chlorofluorescein concentrations for day 10 of tracer test #2.	143
IV.B.8	Integrated transects derived from the vertically averaged 4'-chlorofluorescein concentrations for day 20 of tracer test #2.	144
IV.B.9	Integrated transects derived from the vertically averaged 4'-chlorofluorescein concentrations for day 45 of tracer test #2.	145
IV.B.10	Integrated transects derived from the vertically averaged 4'-chlorofluorescein concentrations for day 101 of tracer test #2.	146
IV.B.11	Integrated transects derived from the vertically averaged 4'-chlorofluorescein concentrations for day 178 of tracer test #2.	147
IV.C.1	Schematic drawing of a vertical cross-section of an idealized fractured porous system surrounding an injection well.	149
IV.C.2	$\ln[\text{fluorescein}]$ as a function of time after injection for tracer test #1 at sampler (1,1,8) which was located approximately 1 m from an injection well.	150
IV.C.3	$\ln[4'\text{-chlorofluorescein}]$ as a function of time after injection for tracer test #2 at sampler (10,-4,6) which was located approximately 4 m from an injection well.	151

IV.C.4	Maximum relative 2',7'-dichlorofluorescein concentration as a function of elapsed time between tracer injection and sampling initiation for a series of "push-pull" tests.	154
IV.C.5	ln[tracer mass in the source region] as a function of time after injection for tracer tests #1 and #2.	156
IV.D.1	Plume center of mass as a function of time after injection for tracer tests #1 and #2.	162
IV.D.2	Average plume velocity as a function of time after injection for tracer tests #1 and #2.	163
IV.D.3	Principal values of the longitudinal and horizontal transverse plume variances as a function of time after injection for tracer test #1.	165
IV.D.4	Principal values of the longitudinal and horizontal transverse plume variances as a function of time after injection for tracer test #2.	166
V.B.1	Schematic drawing of an idealized three-dimensional fracture network.	173
V.B.2	Schematic drawings of an idealized two-dimensional fracture networks: A) Plan view and B) Vertical cross-section.	175
V.B.3	Modeled concentrations provided by the two numerical integration algorithms as a function of distance along a fracture compared with the results of Sudicky and Frind (1982).	181

V.B.4	Schematic diagram of the procedure used to apply the principle of superposition to simulate a pulse type source with a constant source function. Curve A is the relative concentration for a continuous positive source starting at $t = 0$ ; Curve B is the relative concentration of a continuous negative source starting at $t = p$ where $p$ is the duration of the injection pulse; and Curve C is the sum of A and B and represents the relative concentration resulting from a pulse type source.	183
V.B.5	$f(x)$ as a function of $x$ where $f(x)$ is the integrand in Equation V.3 illustrating the highly oscillatory nature of the function.	185
V.C.1	Relative concentration produced by the analytical one-dimensional solution as a function of distance from the source for two test cases.	189
V.C.2	Relative concentration produced by RAND1D as a function of distance from the source for two tests cases.	194
V.C.3	Comparisons between the measured and modeled integrated fluoresein transects for days 50 and 232 of tracer test #1	196
V.C.4	Comparisons between the measured and modeled integrated fluoresein transects for days 93 and 342 of tracer test #1	197
V.C.5	Comparisons between the measured and modeled integrated fluoresein transects for days 123 and 419 of tracer test #1	198
V.C.6	Sensitivity of the one-dimensional EPM simulations to retardation factor for the day 342 snapshot of tracer test #1.	200
V.C.7	Sensitivity of the one-dimensional EPM simulations to longitudinal dispersivities of 3 and 6 m for the day 342 snapshot of tracer test #1.	201



V.C.8	Sensitivity of the one-dimensional EPM simulations to longitudinal dispersivities of 6 and 12 m for the day 342 snapshot of tracer test #1.	202
V.C.9	One-dimensional EPM simulations based on the day 342 snapshot of tracer test #1 illustrating the dispersion promoting aspect of an exponentially decaying source function.	204
V.C.10	One-dimensional EPM simulations based on the day 342 snapshot of tracer test #1 illustrating the dispersion inhibiting aspect of an exponentially decaying source function.	205
V.C.11	Center of mass velocity measured for tracer tests #1 and #2 and modeled for test #1 as a function of time after injection.	207
V.C.12	Concentration distribution produced by RAND2D compared with the analytical solution for a pulse type source.	210
V.C.13	Modeled two-dimensional fluorescein concentration distributions for day 50 of tracer test #1.	212
V.C.14	Modeled two-dimensional fluorescein concentration distributions for day 93 of tracer test #1.	213
V.C.15	Modeled two-dimensional fluorescein concentration distributions for day 123 of tracer test #1.	214
V.C.16	Modeled two-dimensional fluorescein concentration distributions for day 232 of tracer test #1.	215
V.C.17	Modeled two-dimensional fluorescein concentration distributions for day 342 of tracer test #1.	216
V.C.18	Modeled two-dimensional fluorescein concentration distributions for day 419 of tracer test #1.	217

V.C.19	Sensitivity of the two-dimensional EPM simulations to source width for the day 342 snapshot of tracer test #1.	218
V.C.20	Sensitivity of the two-dimensional EPM simulations to transverse dispersivity for the day 342 snapshot of tracer test #1.	219
V.C.21	Two-dimensional EPM simulations based on the day 342 snapshot of tracer test #1 illustrating the relative influence of longitudinal and transverse dispersion.	221

## ABSTRACT

### Natural-Gradient Tracer Tests in a Highly Fractured Soil

Richard T. DeCesar, Ph.D.  
Oregon Graduate Center, 1987

Supervising Professor: James F. Pankow

Solute transport in a fractured porous clay aquifer has been investigated in a study which included field, laboratory, and mathematical modeling components. The presence of a fracture network in 'low' permeability materials is important because it results in a reduction in their ability to retard groundwater flow and contaminant migration. Central to the investigation was the conduction of a large-scale natural-gradient tracer test. The test site was the Alkali Lake chemical disposal site located in southeastern Oregon on a 5 km diameter playa in the Alkali Lake basin. A 200 ppm fluorescein dye solution with an initial injection volume of 60 liters was used as the tracer. Injection took place between 1 and 2 meters below the water table at a location approximately 300 meters downgradient of the disposal site. Monitoring of the advancing tracer was accomplished through a network of multi-level piezometers which was installed over a 60 by 35 meter field and was sampled periodically for over one year.

An equivalent porous media model has been found to be effective for simulating the tracer plume as it migrated through the fractured porous aquifer. The high density of fractures at this site is responsible for the validity of the equivalent porous media approach. The results of the model simulations indicate the principal factors controlling tracer migration are matrix diffusion and the high variability in hydraulic conductivity. The strong influence of  $K_h$  variability and matrix diffusion on the tracer migration demonstrates that understanding transport through a fractured porous media requires characterization of the fracture specific and porous media properties of the system. The results of the investigation will be useful for understanding solute migration in other fractured systems.

## I. INTRODUCTION

The primary goal of the research reported here was to understand the processes controlling the transport (advection, dispersion, and diffusion) of non-sorbing, nonreactive solutes in the densely fractured porous soil surrounding the Alkali Lake chemical disposal site. The processes studied included: advection, hydrodynamic dispersion, matrix diffusion, and dispersion due to variability in the hydraulic conductivity. To determine the relative roles of the processes, a series of field, laboratory, and computer modeling experiments were conducted.

### I.A. Background

#### I.A.1. Groundwater Contamination: A Rationale For Concern

Groundwater is a source of drinking water for approximately one-half of the population of the United States. Much of this is used directly without pre-treatment. Extensive contamination of this natural resource, often caused by the presence of various synthetic organic pollutants, has been found in many areas of the country. The following examples illustrate some typical groundwater contamination scenarios: 1) 1978: four wells providing 80 percent of the drinking water to Bedford, Mass. were shut down due to trichloroethylene (TCE) and dioxane contamination; 2) 1980: California health officials closed

39 public wells supplying water to more than 400,000 people in the San Gabriel Valley because of TCE contamination; 3) 1979-1981: a total of 32 private wells were closed in Lake Carmel, N.Y. due to benzene contamination; and 4) 1980-1982: numerous wells in California's San Joaquin Valley were shut down due to dibromochloropropane contamination.

Some sources of this groundwater contamination are leaky underground storage tanks, accidental spills during transport of chemicals, and the estimated 200,000 improperly designed and operated landfill sites in this country (U.S. EPA, 1980). Due to our continuing need for disposal sites, landfills represent a great risk to groundwater quality far into the future. The severity of the problem is further compounded by the fact that many of the contaminants are mobile, persistent, toxic, and carcinogenic.

The above discussion indicates a need to develop a sound scientific basis to aid in designing strategies for ensuring the protection of groundwater quality. A fundamental understanding of the processes controlling contaminant transport in the subsurface will provide the means for making effective decisions regarding the clean-up of existing contamination problems and the construction of new landfill and chemical waste disposal sites. The enormous costs associated with either inadequate groundwater protection or effective remedial action and site construction underscore the value of developing the capability

to predict accurately the movement of hazardous compounds in contaminated and uncontaminated groundwater zones.

#### I.A.2. Transport in Fractured Geological Materials

The majority of efforts to increase our understanding of the migration of groundwater contaminants have been directed towards transport phenomena in porous media. This approach has involved viewing the geological system as an arrangement of grains with the movement of water and solutes occurring in the channels between the grains (e.g., see Bear, 1972; Fried, 1975; and Freeze and Cherry, 1979). This methodology has been applied extensively and with considerable success to aquifers composed of sand or gravel (e.g., MacFarlane et al., 1983, and Sudicky et al., 1983).

In many instances, contamination has occurred in materials which are normally perceived to possess a very low intrinsic permeability (e.g. clay and shale). These materials however often contain a secondary permeability continuum formed by a network of fractures. Fluid movement in such dual-permeability systems can be almost entirely through the open fracture network rather than between the individual grains. In addition to their dual-permeability nature, fractured media are dual-porosity systems. That is, there is porosity associated with the fractures as well as with the bulk soil or rock adjacent to the fractures. In materials such as fractured clay or

shale, most of the groundwater is essentially immobile due to the high ratio of bulk porosity to fracture porosity. The presence of fracture networks in "low" permeability materials is of interest because they are capable of significantly enhancing groundwater flow and contaminant migration. For example, Freeze and Cherry (1979, p. 152) report that field tests commonly exhibit a 1 to 4 order of magnitude increase in the bulk hydraulic conductivities of clays and glacial tills compared to intergranular hydraulic conductivities determined by laboratory tests on unfractured samples. These large increases in hydraulic conductivity can produce dramatic increases in groundwater flow and contaminant migration rates. Nevertheless, the fact that diffusion to the bulk matrix can immobilize a large fraction of the water provides the opportunity for retardation of contaminant migration. Indeed, this process provides for contaminant mass transfer between the mobile fracture water and the adjacent porous matrix.

The physical and chemical processes governing solute transport are the same in both fractured and unfractured porous media, i.e., advection, mechanical dispersion, molecular diffusion, biodegradation, and chemical reactions. However, the effects and relative influence of these processes can be quite different and complex in fractured porous media due to the dual nature of such systems. Compounding the complexity of this problem from the point of view of the modeler is the fact that previous investigations in this area have employed two



distinct conceptual frameworks. While interpretations of field investigations usually have treated the fracture networks as equivalent porous media (EPM), theoretical and laboratory studies have utilized highly idealized fracture systems. Prior to this study, neither approach had been evaluated in terms of its ability to describe contaminant migration at field scales.

The characterization of fractured porous systems requires determining fracture specific parameters such as fracture aperture, fracture spacing, and fracture density, as well as standard porous media parameters such as bulk porosity and hydraulic conductivity. Knowledge of these parameters can provide estimates of the relative importance of some of the transport mechanisms which may be operative in fractured porous deposits. For example, solute retardation due to matrix diffusion increases with increasing porosity of the soil or rock matrix located adjacent to the fractures. Also, dispersion of a contaminant plume due to mixing at fracture joints can strongly influence the concentration profile of a groundwater contaminant if the fracture network is highly interconnected.

### I.A.3. Previous Studies of Solute Transport in Fractured Media

For some fractured geological systems (e.g. fractured clays and glacial tills), virtually all of the bulk flow and solute advection occurs in the fractures. The dispersion of solutes in such systems

occurs as a result of complex velocity distributions in the fracture network, molecular diffusion in the fractures, and diffusion into and out of the matrix surrounding the fractures. As described above, modeling of the overall transport process in fractured systems has been carried out using two distinct approaches. The first has been to use idealized fracture networks to model the system on the scale of individual fractures. The application of such models requires detailed information on all geometrical aspects of the fracture network. The second approach has been to treat the fractured medium as an equivalent porous medium characterized by hydrogeological properties (porosity, hydraulic conductivity, etc.) averaged over some volume greater than the typical three-dimensional interfracture spacing. In this case, one assumes that the transport process is similar to that which occurs in a granular porous medium. One then proceeds to use the many models which exist for porous media. The rationales for using the EPM approach are 1) in the limit of increasing fracture density, a fractured system is identical to a porous granular system, 2) as the scale of interest increases relative to the average interfracture spacing, the apparent behavior of a fractured system more closely approximates that of a porous granular system, and 3) dead-end pore effects are assumed to be (or are) negligible.

### I.A.3.a The Idealized Fracture Network Approach

The primary impetus for the development of the idealized fracture network approach has been concern over the siting of nuclear waste repositories in deep granitic formations (Witherspoon et al., 1981). The interfracture spacings in such formations are often large enough to justify the simplifications required by the idealized fracture approach. The results of studies in this area have provided much insight into dispersion due to fracture aperture variability, mixing at fracture intersections, and matrix diffusion. For the purpose of discussion here it is useful to separate these studies into those which treat transport in an isolated fracture and those employing fracture networks.

Investigations of transport through a single fracture have emphasized the effects of 1) matrix diffusion, 2) aperture size and the corresponding water velocity, 3) dispersion within a fracture due to the velocity distribution within a constant aperture fracture, 4) the porosity of the surrounding matrix, 5) sorption on the fracture walls, 6) sorption within the surrounding matrix, and 7) dispersion due to a varying fracture aperture. Most theoretical studies in this area have modeled the fracture as an opening of aperture  $2b$  between two parallel plates with the following additional assumptions:

1. the fracture aperture is much smaller than the fracture width and length;

2. transport within a fracture is independent of neighboring fractures due to a sufficiently large interfracture spacing;
3. solute transport within the porous matrix is entirely by molecular diffusion due to the low permeability of the matrix; and
4. all advective transport takes place in the fracture.

Examples of this approach using analytical solutions are given by Tang et.al. (1981), Neretnieks (1980), and Hull (1985). Numerical models of transport in a single parallel plate fracture have been described by Grisak and Pickens (1980) and Noorishad and Mehran (1982). Treatment of a fracture as a cylindrical macropore has been carried out by van Genuchten (1984). As a whole, these studies have provided valuable insight into the parameters which influence matrix diffusion and its enormous potential for retarding contaminant migration. For example, Noorishad and Mehran (1982) demonstrated that the retardation capacity of matrix diffusion is strongly dependent on fracture flow velocity and matrix porosity, with the most retardation occurring at low velocity and high porosity. Another feature of the single fracture models is their ability to calculate the solute concentration profiles within the porous matrix. This ability is valuable when trying to understand the mass balance of a migrating solute.

Laboratory tracer tests with drill cores (Neretnieks et.al., 1982, and Moreno et.al., 1985) have verified the importance of matrix diffusion as a retardation process and validated the ability of single

fracture models to predict the retardation. (A tracer test conducted in an excavated cylindrical sample of glacial till (Grisak et.al., 1980) also showed significant retardation due to matrix diffusion.) In addition, these tests have also pointed to longitudinal dispersion due to intra-fracture velocity variations across the width of a single fracture as an important mass transport process. Further evidence on this process was found in breakthrough curves obtained in a recent field study (Novakowski, 1985) which involved a forced-advection tracer test in an isolated fracture located at a depth of approximately 100 m within fractured plutonic rock. A high flow rate was used to minimize the role of matrix diffusion.

Most investigations of solute transport through fracture networks have been designed to address one of the following processes:

1. the reduction in the retardation capacity from matrix diffusion due to interactions between neighboring fractures; or
2. the dispersion of a migrating solute due to mixing at fracture junctures.

Examples of modeling efforts to address process 1 are given by Sudicky and Frind (1982), Barker (1982), and Huyakorn et.al. (1983). These studies considered transport through highly regular fracture networks. In spite of the simplified nature of the networks, the results demonstrated a dramatic decrease in matrix diffusion effects with decreasing interfracture spacing due to the limited matrix volume available to each fracture for solute storage. Both physical (Hull,

1985) and mathematical (Schwartz et.al., 1983) modeling has been used to study process 2. The results indicate that significant solute spreading can be caused by both mixing at fracture intersections and a complex velocity field due to fracture aperture variability. In addition, the variance of a migrating plume (i.e. the second central moment of the concentration distribution) may increase nonlinearly with time. This nonlinearity is of particular concern if one attempts to model dispersion in a fracture network using the principles of hydrodynamic dispersion which assume the plume variance increases linearly with time. In summary, studies of transport in fracture networks have effectively demonstrated that fracture geometry is an important parameter in fractured media transport. The main limitations of applying fracture network models to field scale problems are the requirements of both a detailed characterization of the fracture geometry and the computational complexity.

#### I.A.2.b. EQUIVALENT POROUS MEDIA APPROACH

When dealing with field scale contamination problems in a fractured porous medium, it is common to treat the system as an equivalent porous medium (EPM). The EPM approach is a continuum technique utilizing aquifer properties averaged over some representative volume. The advantage of the EPM approach is that neither a complete specification of the fracture geometry nor a

simulation of flow and transport within each fracture is required. Therefore, the EPM approach is preferred when it can be shown to be appropriate.

The fundamental assumption required by the EPM concept (Johnson, 1984) is that at any given time nearly all of the solute should be in equilibrium between the immobile matrix water and the flowing fracture water. Under this condition, the EPM model states that the solute will effectively move as if the entire porous system (matrix and fractures) is available for advective transport. To meet the above assumption, the interfracture spacings must be small in comparison to the scale of the transport process under consideration, and the fractures must be continuous over long distances (Pankow et.al., 1986). With increasing travel time, the EPM approach becomes more and more appropriate. Johnson (1984) gives the minimum time necessary for transport in a system of regularly spaced fractures to approach EPM behavior as:

$$t = B^2 / D' \quad (I.1)$$

where  $D'$  = solute diffusion coefficient in the porous matrix  
and  $B$  = one-half the interfracture spacing.

In a fractured porous system fulfilling the basic EPM assumption, the retardation of a non-sorbing solute due to matrix diffusion can be described in a manner entirely analogous to sorption within an

unfractured granular medium. For transport of a non-sorbing solute in a system of evenly spaced parallel fractures, the retardation factor of the solute relative to the actual fracture fluid velocity is given as (Johnson et.al., 1985):

$$R = 1 + n_m B / n_f b \quad (I.2)$$

where  $n_m$  = matrix porosity;

$n_f$  = ratio of the open volume in the fractures to the total volume of the fractures; and

$b$  = one-half the fracture aperture.

Continuing the analogy to sorption in granular media, the effective EPM velocity of a non-sorbing solute ( $v_{EPM}$ ), in terms of the groundwater velocity in the fractures ( $v_f$ ), is given by (Pankow et.al., 1986):

$$v_{EPM} = v_f / R \quad (I.3)$$

When the EPM approach is valid, the principles of transport in porous media may be applied to fractured porous systems using  $v_{EPM}$  as the advection velocity.



## I.B. DESCRIPTION OF THE ALKALI LAKE CHEMICAL DISPOSAL SITE

The area surrounding the Alkali Lake Chemical Disposal Site (CDS, Figures I.B.1 and I.B.2) was the field site for this study. During the period 1969-1971, a total of 25,000 drums (206 L or 55 gallon capacity) of herbicide manufacturing wastes were stockpiled on pallets at the CDS. These wastes were generated from 1960-1970 as by-products in the manufacturing process used to produce large quantities of the herbicide 2,4-D (2,4-dichlorophenoxyacetic acid). The hauling of wastes to the CDS was discontinued in 1971. In November 1976 the drums were crushed and buried in 12 shallow (0.60-0.75 m deep), unlined trenches 130 m long and 20 m apart (U.S. EPA, 1976; and Oregon Department of Environmental Quality (ODEQ), 1977).

The site is located on the southeast edge of the 5 km diameter playa in the Alkali Lake basin (Lake County, Oregon, Figures I.B.1 and I.B.2). Natural surface and groundwater discharges have formed a shallow ephemeral lake on the playa. Occasionally, there is standing water within 100 m of the CDS. The water table at the site is usually 1-2 m from the ground surface. As is typical for closed basins, net evapotranspiration exceeds net precipitation in the playa. Groundwater flowing into the playa is fresh (total dissolved solids (TDS) = 200-500 mg/l, conductivity = 100-250  $\mu\text{mhos/cm}$ , and pH = ~8), but groundwater passing beneath the surface of the CDS is saline and strongly alkaline (TDS = 11,000 mg/l, conductivity = 4000-12,000  $\mu\text{mhos/cm}$ , and pH = 10) (Pankow et.al. 1984). Local groundwater flow in the site is driven by:

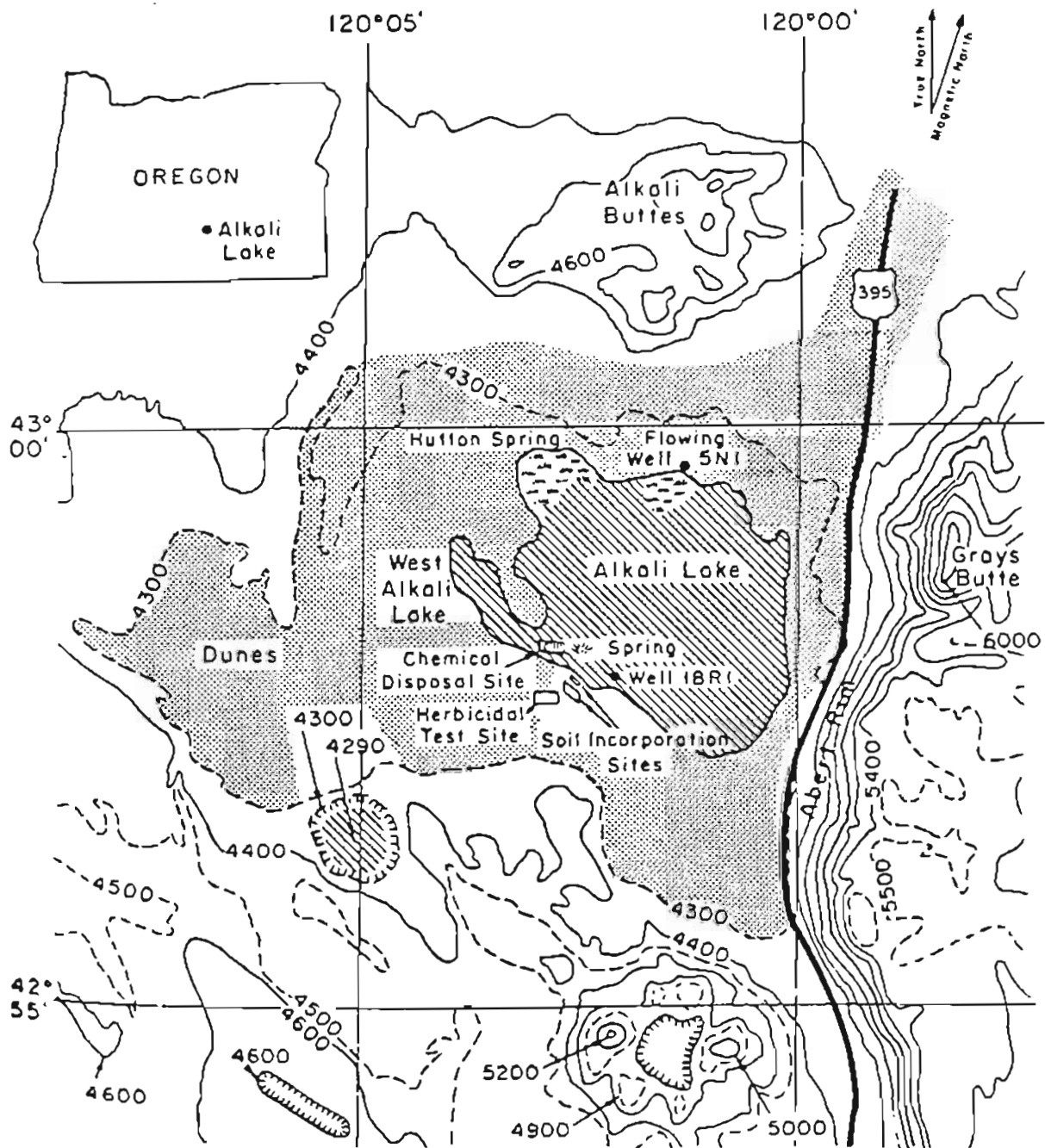


Figure I.B.1 Topographic map of Alkali Lake playa and surrounding area (Pankow et.al., 1984).

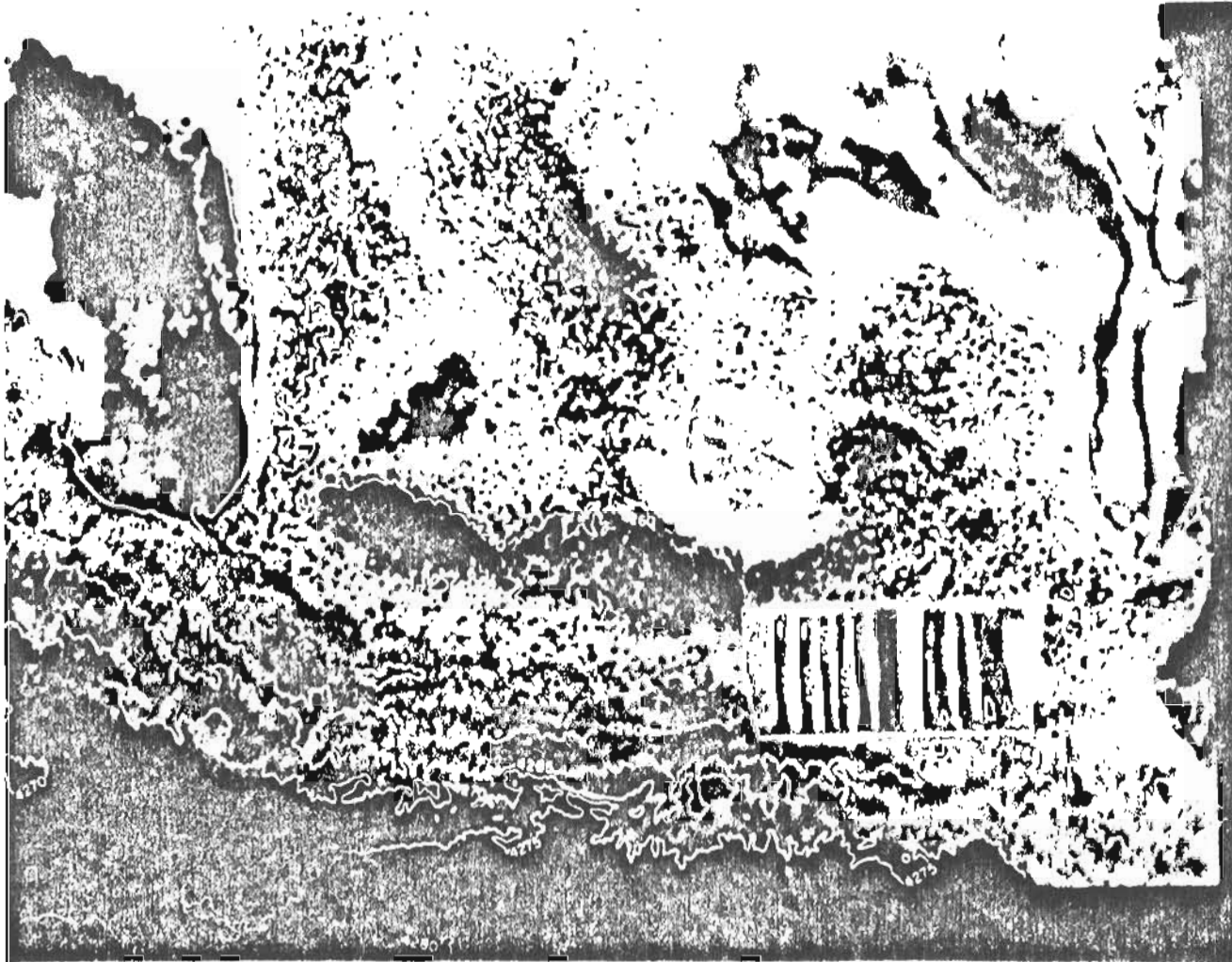


Figure I.B.2 Topographic map of the CDS vicinity (Pankow et.al., 1984).

1) springs which create a groundwater mound east of the site; and 2) the sump effect of the topographically low "West Alkali Lake" (Pankow et.al. 1984).

The site is located in a sparsely populated area characterized by a low level of economic development. Access to the site is provided by Highway 395 which runs along the east edge of the playa. The elevation of the site is 1300 m above sea level (U.S.EPA, 1983). The climate is typical of a high altitude western North American desert. During the period 1972-1981, annual precipitation averaged 17.5 cm (NOAA, 1983). The average annual temperature is 8.5°C (NOAA, 1983), with summer extremes commonly reaching 38°C and winter lows often less than -23°C. The soil commonly freezes to a depth of 7-15 cm (Pankow et.al., 1984). Vegetation at the site is sparse, representing 12% coverage in the vicinity of the CDS (Pankow et.al., 1984). The predominant plant is greasewood (Sarcobatus vermiculatus).

The area around the CDS is composed of fractured porous soil (Johnson, 1984). The principal components of the soil are alluvium, lake sediments, and eolian deposits (Newton and Baggs, 1971). Grain size determinations (Pankow et.al., 1984) indicate a predominance of silt-sized materials with some clay-sized particles in the site area. The surface beds are believed to extend to a depth of at least 30 m (Newton and Baggs, 1971).

Visual evidence of the fracture network has been obtained by the examination of outcrops, removal of soil cores, and excavation of a trench. Figure I.B.3 shows a typical core obtained taken from a depth of 1.5 m and illustrates the abundance of horizontal and vertical fractures found throughout the site area. The estimates of interfracture spacing provided by the cores are: 2-5 mm horizontal spacing, and 2-3 cm vertical spacing, with the horizontal fractures occurring in a much more regular pattern than the vertical fractures. The orientations of the vertical fractures appeared to be random.

Recent studies conducted at the Oregon Graduate Center (Pankow et.al., 1984; Johnson, 1984; and Johnson et.al., 1985) have provided a detailed mapping of the herbicide by-product contaminant plume and a wealth of information on the hydrogeological character of the site. The plume follows the principal direction of groundwater flow with the leading edge as of 1983 at least 460 m from the western edge of the CDS. Since the wastes have been migrating for a maximum of seven years (1983 - 1976), the groundwater velocity near the site has averaged 18 cm/day. Hydrogeological parameter estimates include bulk porosity = 0.65, hydraulic conductivity =  $5 \times 10^{-4}$  m/sec, and hydraulic gradient = 0.0002 - 0.001. Modeling results were used to estimate a number of fracture specific parameters (Johnson, 1984), including: aperture of horizontal fractures = 0.150 mm, horizontal interfracture spacing = 3 mm, groundwater velocity in the fractures = 0.7 m/day, and matrix

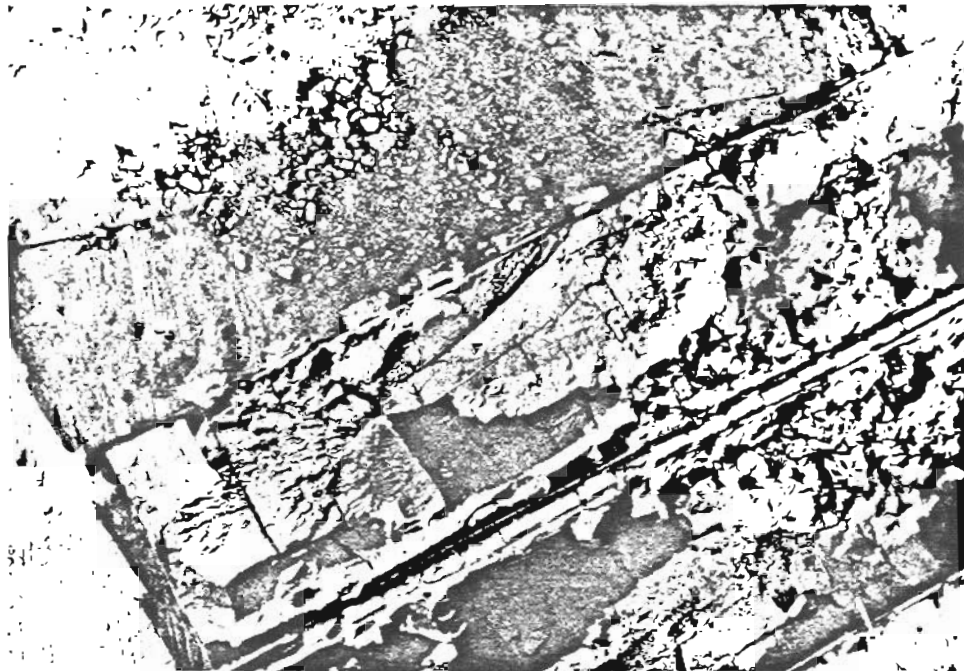


Figure I.B.3 A typical core taken from a depth of 1.5 m illustrating the abundance of horizontal and vertical fractures found throughout the site area.

diffusion coefficient for fluorescein =  $0.05 \text{ cm}^2/\text{day}$ . In addition, that study has resulted in the availability of a dense grid of piezometers for measuring the areal hydraulic head distribution. The investigation discussed in this thesis builds on the foundation provided by the work of Johnson (1984).

The Alkali Lake CDS is an attractive site for studies of flow and solute transport through fractured porous media since it provides the combination of a contaminant plume within a fractured porous deposit through which there is an appreciable groundwater velocity. The following features further enhance its suitability as a study site:

1. written permission was granted to perform the necessary field operations;
2. the wastes were buried in November 1976, providing a well-defined boundary condition on the period of contaminant input;
3. the contaminant plume, and therefore the region of interest, is confined vertically between 1 and 4 m below the surface (Johnson et.al. 1985) enabling the use of hand augering and other non-capital intensive field methods; and
4. the density of the fractures found at the site provides an excellent opportunity for evaluating the effectiveness of the EPM approach under conditions apparently meeting the EPM assumptions.

## II. IMPLEMENTATION OF THE NATURAL GRADIENT TRACER TESTS

Central to this research was the conduction of two large-scale natural gradient tracer tests in the saturated fractured soil at the Alkali Lake CDS. Each test was initiated by making a controlled injection below the water table of a known quantity of tracer solution. This was followed by periodic monitoring downgradient of the injection site to determine the temporal changes in the size and shape of the tracer plume as it evolved under the influence of the natural flow regime. The purpose of these tests was to observe field-scale solute transport in fractured porous media under semi-controlled conditions. This method of observing solute migration contrasted with previous field investigations of solute transport in fractured porous systems which studied either accidental plumes, or tracers migrating under an imposed gradient (i.e. long term pumping and/or injection). A natural-gradient rather than a forced-advection test was chosen for this study in order to more closely approximate the conditions under which migration occurs in contaminant plumes. The choice to study a plume originating from a controlled injection instead of one or more of the compounds associated with the chemical wastes buried at the CDS was made to provide a source which was well-defined in terms of time of release and initial size, shape, and concentration.



## II.A. Justification for a Natural Gradient Test

Over the last 5 to 10 years there has been an increase in the use of the natural gradient tracer test method as a tool for investigating transport processes. Most recent applications of the method have been conducted in sand or gravel aquifers, and the results have demonstrated the value of the procedure. A classic study in this field was conducted by Sudicky et.al. (1983) in a sandy aquifer near the abandoned Borden landfill in southern Ontario. The principal outcome of that study was the first definitive demonstration of a non-linear relationship between increasing plume variance and travel distance. That study was also the first field test which provided estimates of the dispersion coefficient in all three principal directions. A second injection test at the Borden site (Sutton and Barker 1985) was designed to identify differences in the migration patterns of organic tracers and a conservative tracer (chloride). The organic compounds, which included n-butyric acid, phenol, p-chlorophenol, and dimethyl phthalate, were found to migrate at the same velocity as  $\text{Cl}^-$ , but they were attenuated to different degrees. Since the migration rates were the same, it was concluded that sorption was unimportant for these compounds in this aquifer. Biodegradation was the postulated cause of the different attenuation rates.

In the tracer tests conducted by Sudicky et.al. (1983) and Sutton and Barker (1985), a somewhat surprising phenomenon occurred.

In both cases the initial plume split into two zones shortly after injection. This was explained as being due to local heterogeneity and illustrates that natural gradient tracer tests must be considered as only semi-controlled experiments. A third test at the Borden site (Patrick et.al. 1985) focused on biodegradation of several migrating organic compounds including benzene, toluene and xylene. In that experiment the tracer plume spread during the early part of its migration and then, as in the study by Barker and Sutton (1985), began to shrink due to biodegradation of the organic species.

A natural gradient tracer test (Naymik and Sievers, 1985) conducted in a sand and gravel aquifer in west central Illinois provided an estimate of the longitudinal dispersivity ( $\alpha \sim 0.7$  cm). As with some of the tracer tests discussed above, the results of Naymik and Sievers (1985) illustrated the unpredictability associated with natural gradient tests in that after only 50 ft. of migration the sampling network was only able to account for less than 1% of the injected mass. In contrast, 70 - 90% of the tracer mass is being accounted for in a large scale injection test which is currently underway in the sand and gravel aquifer on Cape Cod, Massachusetts (LeBlanc, 1987). The sampling array for this test consists of over 9500 discrete sampling points installed in a region measuring over 20 feet in depth, 50 feet in width and approximately 1000 feet in length. Although still in progress, preliminary results indicate that heterogeneities in the hydraulic conductivity are having a strong

impact on the shape of the plume.

The above discussion indicates that the natural gradient tracer test procedure is a valuable method for increasing the understanding of the processes controlling the transport and fate of contaminants in groundwater. The success of the tracer studies discussed above was a strong influence on the decision of our laboratory to implement a series of natural gradient tests at the Alkali Lake CDS.

During 1983 a 2-dimensional tracer test was conducted at the CDS (Johnson, 1984). After one year the areal shape of the plume was found to be smooth, and one-dimensional modeling of the plume permitted the advection velocity for a non-sorbing solute to be estimated as 0.05 m/day and the longitudinal dispersion coefficient as  $0.15 \text{ m}^2/\text{day}$ . The success of this tracer experiment indicated that a large-scale tracer test at the CDS would provide significant insights into the processes controlling transport in fractured porous media. The injection experiments conducted for this investigation are the first large-scale three-dimensional tracer tests conducted in fractured porous soil.

## II.B. Objectives of the Natural Gradient Tests

The three major objectives of the natural gradient tracer tests implemented for this investigation were to:

1. observe solute transport originating from a well-defined source

function in a fractured porous soil under the influence of the natural flow regime;

2. develop the data base required to evaluate the EPM and idealized fracture system models in terms of their abilities to explain solute transport on a field scale in a fractured porous medium; and
3. determine the processes controlling migration (advection and dispersion) in a highly fractured medium.

## II.C. Tracer Test Experimental Design

### II.C.1. The Tracer Test Study Site

The site selected for the subsurface injection of tracer dyes was approximately 300 m downgradient from the northwest corner of the CDS (Figure II.C.1). As illustrated in Figure II.C.1, the tracer test site for this study was in the same general area as the small-scale test conducted by Johnson (1984). Therefore, the results of Johnson (1984) were very useful in determining the intersampler spacing for this study. The injection region of the first tracer test bisects the eastern edge of a relatively level, almost vegetation-free area extending approximately 40 m in width and 70 m in length. The flatness and lack of vegetation facilitated the layout and installation of the array of samplers. The tracer site was within the plume of contaminants migrating from the CDS, but was in a region where the concentrations were fairly low. These features permitted the

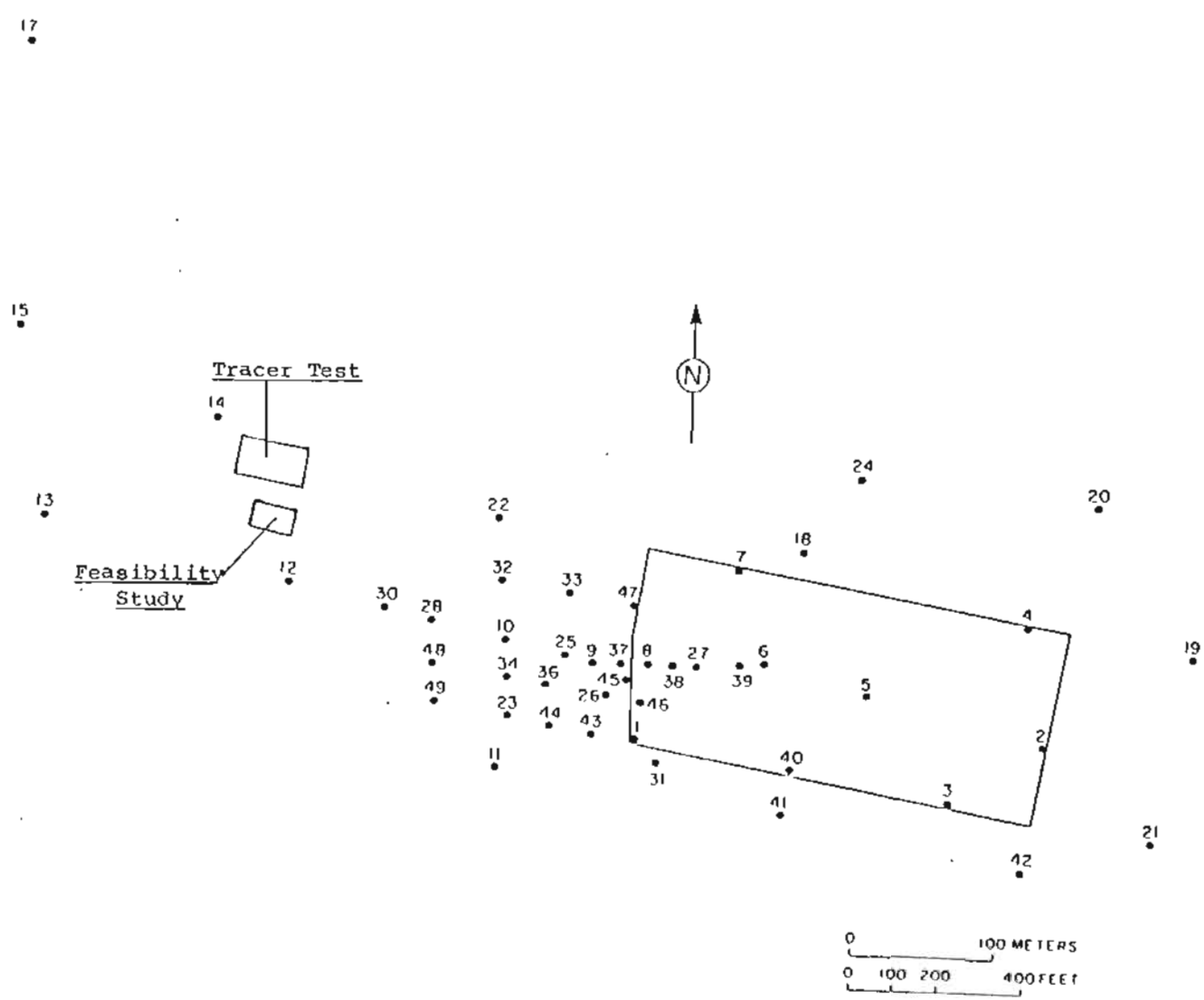


Figure II.C.1 Map showing the location of the tracer test site relative to the CDS (after Johnson, 1984).

concentration contour plots of the contaminant plume (Johnson et.al., 1985; and Johnson, 1984) to serve as pre-injection guidelines for predicting the direction of tracer migration, but minimized personal exposure to the existing contamination during field operations.

### II.C.2. Piezometer Design and Installation

The piezometers used for sampling and injection included one-, two-, and three-level versions of a single basic design. The multi-level piezometers allowed 3-dimensional characterization of the migrating tracer plume. Schematic representations of each version are shown in Figure II.C.2. The components were machined and assembled at the Oregon Graduate Center. The small diameter of the casing and screened interval provided several advantages. Firstly, removal of only a small volume was required to purge the standing groundwater prior to sampling. This minimized the induced movement of the tracer due to pumping and also limited the mass of tracer dye which was removed from the aquifer by pumping. Secondly, the small diameter minimized the effects on the aquifer caused by the installation and presence of the piezometers. In addition, the piezometers were economical, durable and readily constructed, installed, and sampled by one person.

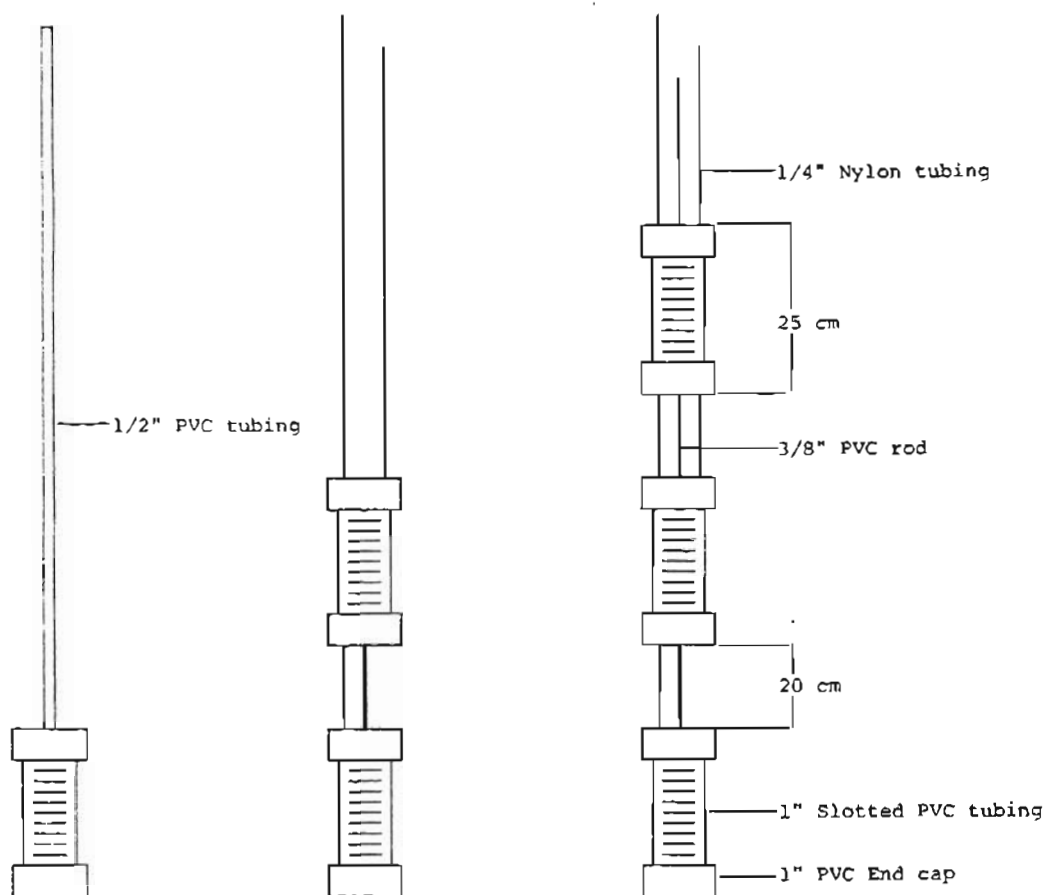


Figure II.C.2 Schematic drawing of the multi-level piezometers used to sample the tracer plumes.

Each discrete sampling level was hydraulically isolated from its neighbors by a 0.25 cm thick, 5 cm diameter, rubber gasket and a bentonite packer. The packers were formed by inserting five bentonite "cigars" between adjacent levels. The "cigars" were cylindrical in shape and approximately 15 cm long and 1.2 cm in diameter. To form the "cigars", a ten cylinder aluminum mold was filled with 0.5 l of powdered bentonite and pressed at 2000 psi with a Wabash hydraulic press.

The installation procedure for the multi-level samplers was as follows:

1. A hole was hand-augered to a depth of 3 m using a 3.8 cm diameter auger head (Art's Machine Shop, American Falls, Idaho).
2. A piezometer was pushed in the hole until the top of the lowest screened level was 8 cm below the ground surface.
3. Five bentonite "cigars" were inserted into the hole in the space between the bottom and middle levels.
4. Steps 2 and 3 were repeated for the middle level.
5. The piezometer was pushed to the bottom of the hole using a 2.4 m long, 2.5 cm diameter PVC pipe.
6. Approximately 1.5 l of granular bentonite were inserted into the hole above the upper screened interval.
7. The remainder of the hole was backfilled with soil.

The piezometers were left undisturbed for at least one day after installation to allow time for the bentonite to swell and seal off the adjacent levels. Next, the piezometers were developed by surging groundwater into and out of each screened level until a steady flow was



established. Generally, less than one minute of surging was required to develop each level.

### II.C.3. TRACER COMPOUNDS

An ideal conservative tracer for groundwater studies should be 1) soluble in water, 2) nonreactive with geological materials, 3) not significantly retained on the solid phase by adsorption or ion-exchange, 4) non-biodegradeable, 5) non-hazardous, 6) inexpensive, 7) detectable at low levels by a straightforward analytical procedure, and 8) present at low background concentrations. A tracer with these properties will correctly simulate the transport process experienced by a nonreactive, non-sorbing contaminant. On the other hand, tracers which partition between the solid and liquid phase are useful for simulating the transport of sorbing contaminants.

Fluorescein and a series of fluorescein derivatives were used as the tracer compounds. The tracers were chosen to meet the above criteria. The dyes are nonreactive, non-biodegradeable, and have been used as groundwater tracers by many investigators. They include species that will be both sorbing and non-sorbing under the conditions found at Alkali Lake. Table II.C.1 contains a list of the tracers which were used and their corresponding partition coefficients. The structures of several of the compounds are shown in Figure II.C.3. With the exception of 4'-chlorofluorescein, the compounds are readily

TABLE II.C.1 Fluorescein dyes injected for tracer test #1

Compound	M.W. (g/mole)	Partition Coefficient (ml/g)
fluorescein	332	0
2',7'-dichlorofluorescein	401	0
4',5'-dibromofluorescein	490	0
2',4',5',7'-tetrabromofluorescein	692	2
4',5'-dibromo-2',7'-dinitrofluorescein	624	18
2',4',5',7'-tetrabromo- 4,5,6,7-tetrachlorofluorescein	830	10

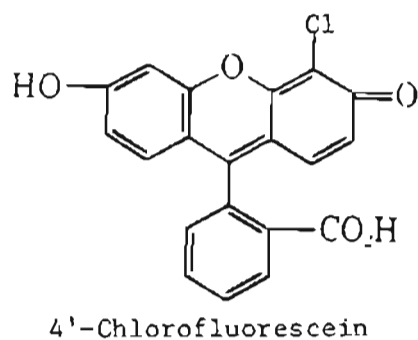
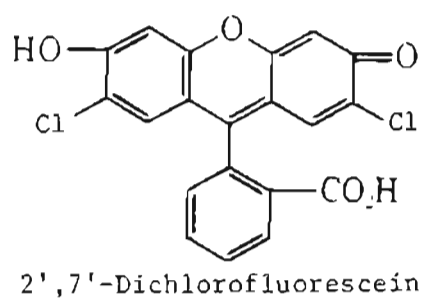
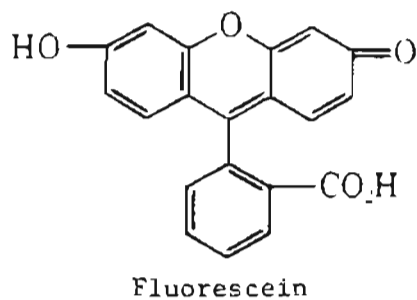


Figure II.C.3 Chemical structures of several of the fluorescein dyes used as tracers.

available. Since a source for monochlorofluorescein could not be found, it was synthesized in the lab.

The 4'-chlorofluorescein synthesis was carried out by a 1:1 stoichiometric reaction of hypochlorous acid (HOCL) and fluorescein (Hurst et.al., 1984). All reagents were prepared in 25 mM phosphate at pH 7.3. The reaction consisted of the the drop-wise addition of 600 mL of 0.14 mM HOCL to 3400 mL of 3 mM fluorescein with rapid stirring. The HPLC chromatogram (Figure II.C.4) of the reactant and products together with the relative retention times given in Hurst et.al. (1984) suggests approximately 60% yield with formation of a small fraction of 4',5'-dichlorofluorescein. Since a standard was unavailable, the nominal concentration of the synthesized 4'-chlorofluorescein was set arbitrarily at 2.5 mM (1000 ppm). The lack of an absolute standard did not effect the tracer test results because all calculations made for this study required only relative concentrations and were independent of absolute concentrations.

#### II.C.4. MONITORING NETWORK

The final sampling grid is illustrated in Figure II.C.5. This array included 77 three-level and 12 one-level piezometers, providing 243 discrete sampling points for characterizing the tracer plumes. Table II.C.2 contains the piezometer installation schedule. The samplers located close to the initial injection area were installed

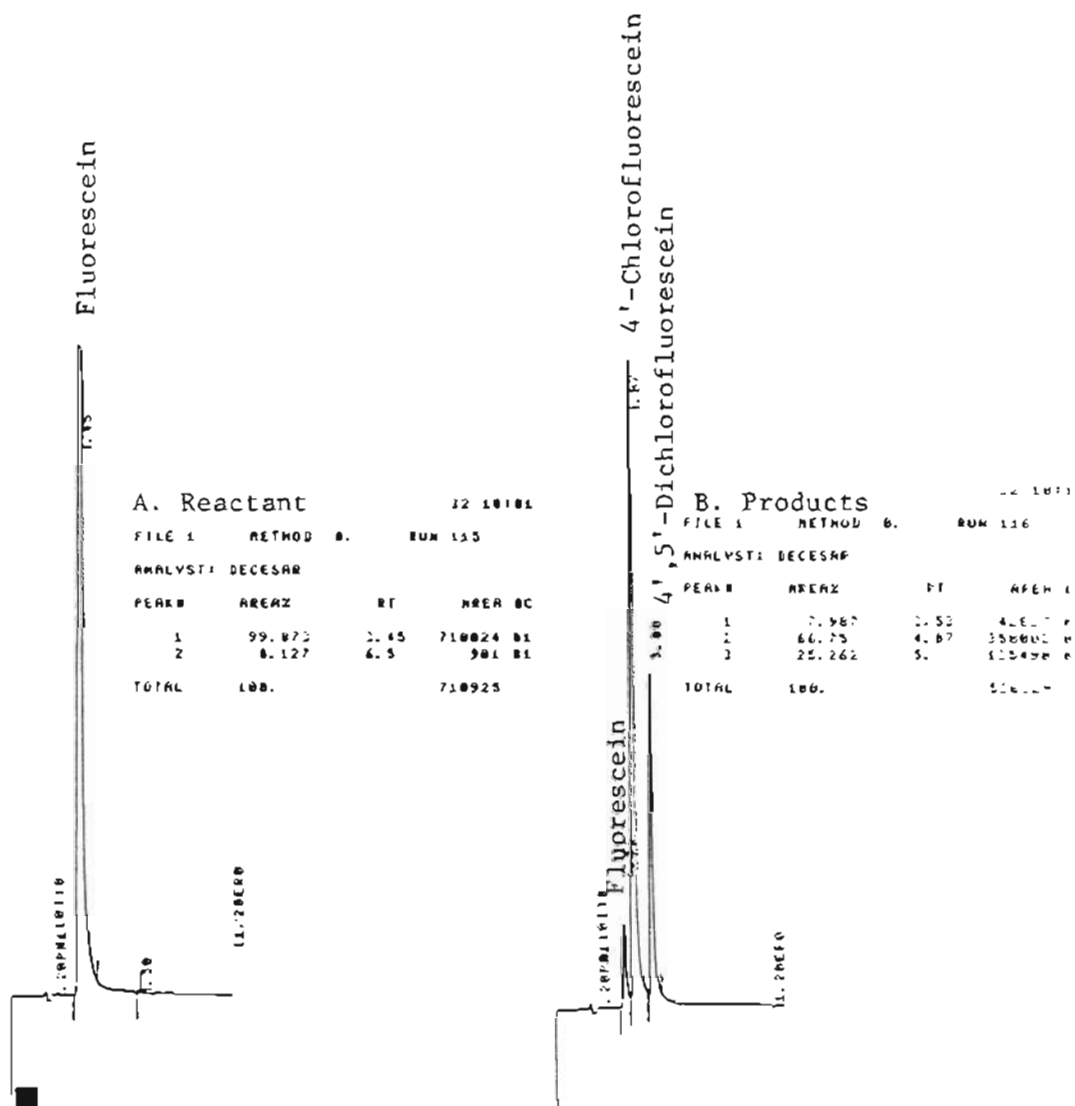


Figure II.C.4 HPLC chromatogram of the reactant and products of the 4'-chlorofluorescein synthesis.

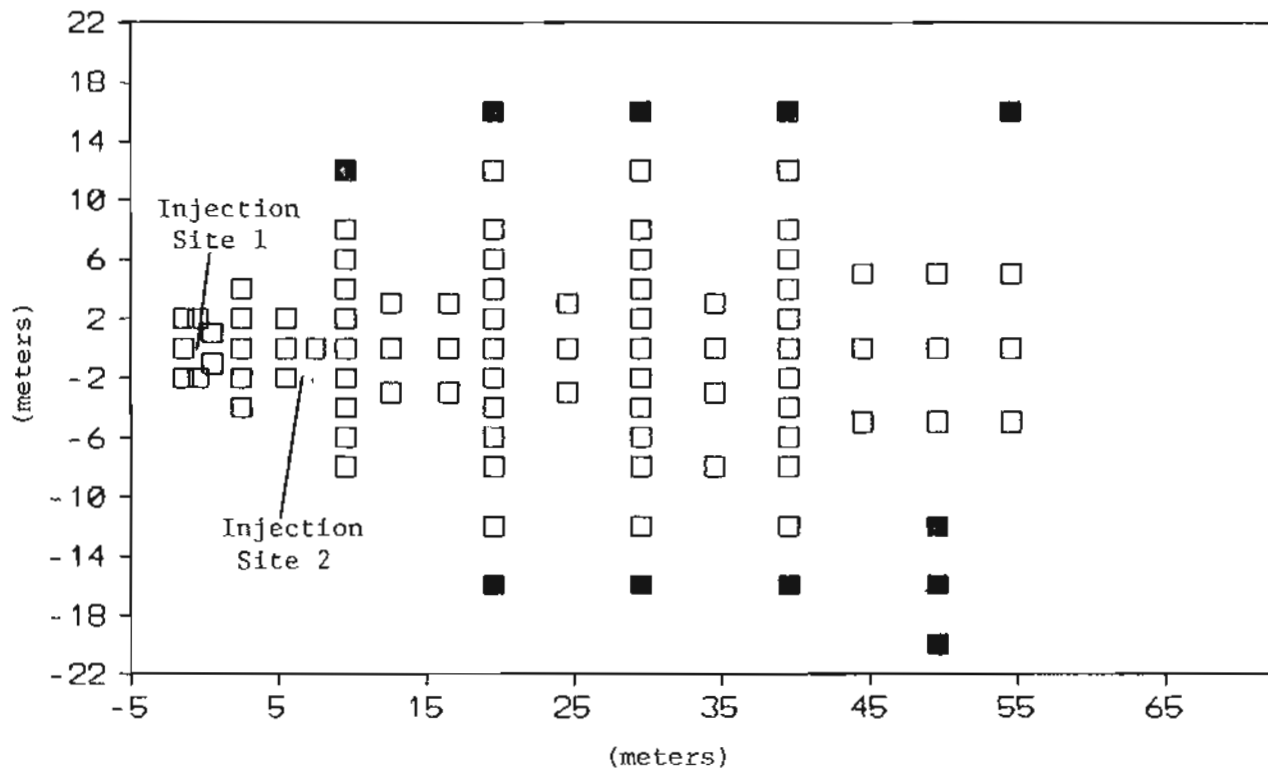


Figure II.C.5 Map showing the final sampling grid used for the tracer tests. Open squares represent three-level piezometers and closed squares represent one-level piezometers.

TABLE II.C.2 Piezometer installation schedule

Date	Number of Samplers Installed	Comments
8/10/84	46	Most were three-level; Network dimensions 22 m long by 24 m wide
9/29/84	16	All were three-level; Network extended to 37 m long by 24 m wide
11/11/84	20	All were three-level; Network extended to 57 m long by 24 m wide
3/30/85	6	All were one-level; Installed injection wells for tracer test #2; widened network to 28 m
4/18/85	2	Both were one-level; widened network to 32 m
4/28/85	5	All were one-level; widened network to 36 m

prior to injection. The large majority of the full network was completed within 3 months. The areal layout of the grid was based on the results of the small scale tracer study conducted by Johnson (1985). The ring of one-level samplers around the outer edge of the grid was installed seven months after the initial injection in response to the results of the early rounds of sampling.

#### II.C.5. Injection Procedures

The monitoring network described above was used for two tracer tests. The dates of injection were August 10, 1984 and April 8, 1985. The locations for the injections are labeled on Figure II.C.5 as Injection Site 1 and Injection Site 2, respectively. The first injection occurred through three two-level piezometers with their upper screened sections between 1.8 and 2.1 m below the ground surface and their lower screened sections between 2.4 and 2.7 m below the ground surface. The horizontal distance between the piezometers was 0.9 m.

Two dye mixtures and two injection levels were employed to facilitate the investigation of the vertical dependency of the transport processes. It was anticipated that this dependency would be significant due to the decrease in hydraulic conductivity with depth which is commonly associated with fractured systems. Although this study focused on non-sorbing compounds, both sorbing and non-sorbing



species were used. Table II.C.3 contains the compositions of the two fluorescein mixtures used. Solution A was injected through the upper level of the wells and Solution B through the lower levels. The injection apparatus is shown schematically in Figure II.C.6. Each screened section of each injection well received 10 l of either Solution A or B. The dye mixtures were gravity-fed from plastic reservoirs located approximately 0.5 m above ground level. The drainage rate was regulated manually with the reservoir outlet valves to ensure simultaneous injection through each of the six screened intervals. Complete injection of the six reservoirs occurred within 20 minutes.

The second tracer test was initiated to enable more complete characterization of the early stages of plume migration. The injection to start the second tracer test occurred through two single level wells located 0.6 meters apart with their screened sections between 1.7 and 2.0 m below the surface. Ten liters of a 200 ppm 4'-chlorofluorescein solution were used. The injection occurred over a period of 5 minutes. The injection apparatus and procedures were the same as the first test.

The initial dimensions of a tracer pulse may be estimated if it is assumed that negligible mixing occurred during the injection process. For the three wells used to initiate the first test, a tracer injected at only one level formed an approximately rectangular block 3 m long by 1.2 m wide by 1.2 m deep. A pulse of dye introduced at both levels occupied a volume 3 m long by 1.2 m wide by 2.1 m deep.

TABLE II.C.3 Compositions of the fluorescein dye mixtures injected for tracer test #1

Compound	Solution A (ppm)	Solution B (ppm)
fluorescein	100	100
2',7'-dichlorofluorescein	100	0
4',5'-dibromofluorescein	0	100
2',4',5',7'-tetrabromofluorescein	100	100
4',5'-dibromo-2',7'-dinitrofluorescein	100	0
2',4',5',7'-tetrabromo- 4,5,6,7-tetrachlorofluorescein	100	0

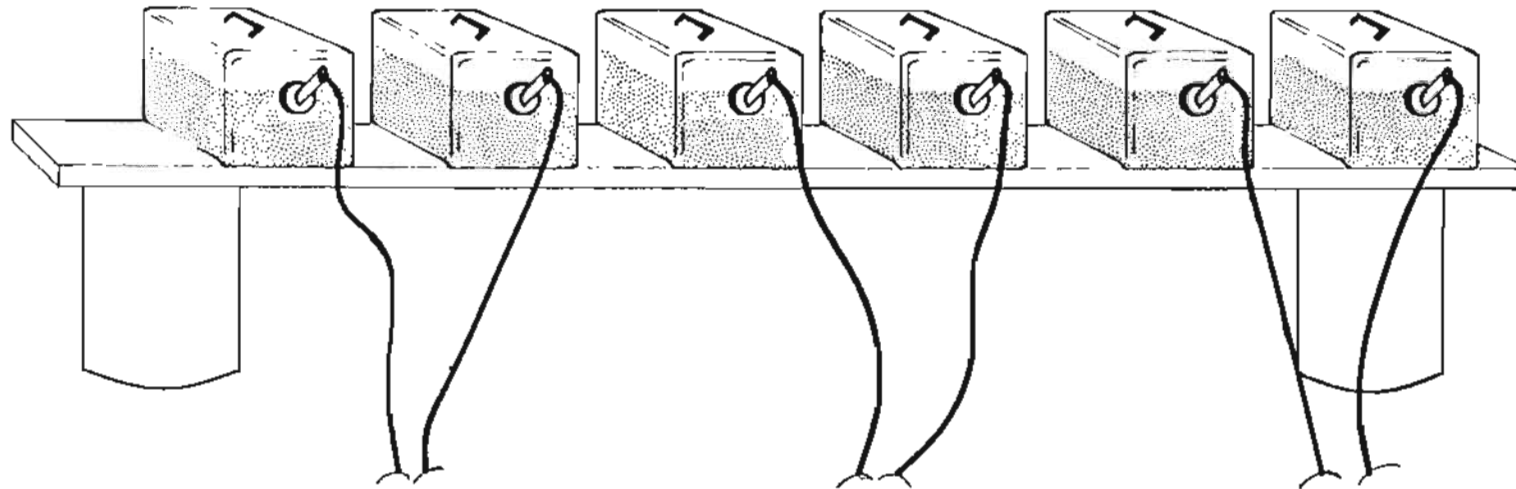


Figure II.C.6 Schematic drawing of the injection apparatus used for tracer test #1.

### II.C.6. Sampling Procedure and Schedule

The sampling procedures and apparatus for this study were designed to minimize 1) cross-contamination between sampling points, and 2) contact time between the groundwater and sampling equipment. In addition to the constraints required to maintain good quality control, the climate and location of the CDS together with a desire to commit only one person for the task of routine tracer network sampling, often imposed a number of additional requirements. These included:

1. Since access to the tracer site was often impossible with a motor vehicle, the equipment had to be transportable by one person.
2. One person operation of the sampler was required.
3. Operation of the sampler without electrical power was required.
4. The sampler had to be sturdy and easily repaired in the field; this excluded the use of complex and/or fragile components.
5. Since sampling occurred on several occasions in snow and rain, and with temperatures below  $-15^{\circ}\text{C}$ , the sampler had to be robust with respect to temperature and moisture extremes.

The sampling apparatus designed to meet the above criteria is shown in Figure II.C.7. The first step in sampling was connection of the inlet tube of the sampling apparatus to the outlet tube of one of the screened levels of a multi-level piezometer. The two-hole rubber stopper next to the sampler inlet tube (Figure II.C.7) was then inserted into a waste bottle and approximately 100 ml of groundwater was hand pumped out to remove the standing water in the screened

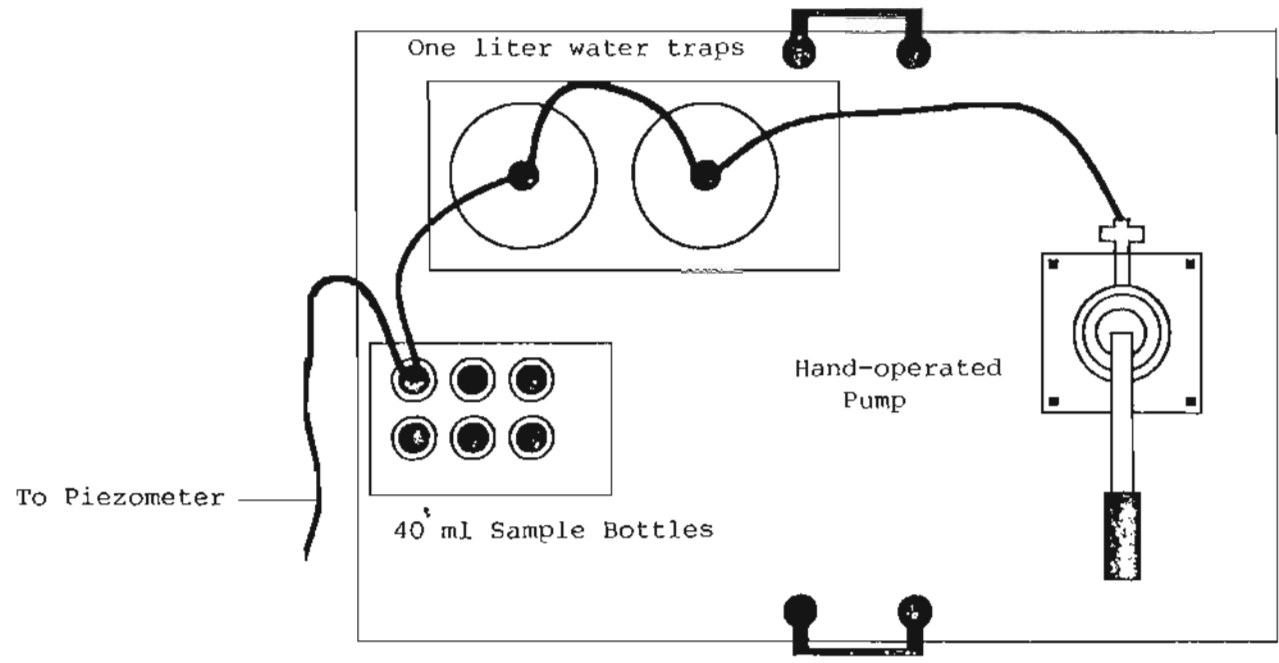


Figure II.C.7 Schematic drawing of the apparatus used to obtain groundwater samples from the multi-level piezometers.

section. The two-hole stopper was then moved to a clean, labeled sample bottle and a 20 ml groundwater sample was withdrawn. The containers used for sampling were 30 ml glass vials with foil-lined plastic caps. Each sample was placed in an opaque container immediately after collection to minimize photodegradation. Using this procedure, one person could sample the entire monitoring network in approximately six hours.

The first and second tracer tests included 7 and 6 rounds of sampling, respectively. The dates of sampling are presented in Table II.C.4. The first test was monitored for over a year while the second test was monitored for approximately 6 months. The gap in sampling the first test from mid-December to late March was due to the severe weather at the site during this period.

#### II.C.7. Analytical Procedures

The analytical needs of the project required the development of a procedure capable of rapid and accurate quantification of a series of fluorescein dyes in a large number of samples. From the results of the 2-D tracer test (Johnson, 1984), it was anticipated that the method would require very low detection limits (~ppb levels) and a wide dynamic range covering at least four orders of magnitude for each of the dyes. In addition, it was desired to keep pre-analysis handling

TABLE II.C.4 Sampling schedules for tracer tests #1 and #2

Sampling Date	Tracer Test #1	Tracer Test #2
8/10/84	X	
9/29/84	X	
11/11/84	X	
12/11/84	X	
3/30/84	X	
4/9/85		X
4/18/85		X
4/28/85		X
5/24/85		X
7/15/85	X	X
10/3/85	X	X

and work-up at a low level to minimize exposure to the hazardous organic contaminants which were in the groundwater due to migration from the CDS. Finally, due to the caustic nature of the groundwater (pH = 10), equipment capable of withstanding strongly alkaline solutions was needed to minimize equipment downtime.

A procedure employing HPLC separation coupled with detection and quantification by laser-induced fluorescence was developed to meet the above requirements. The technique provided a rapid (20 minutes per run for the suite of 7 dyes), sensitive (detection limit < 5 ppb for each of the dyes using the standard operating conditions), and precise (relative uncertainty <25% for concentrations greater than 1 ppb) analysis for all of the dyes with no sample preparation. The method is described below.

#### II.C.7.a. HPLC SEPARATION

A Spectra Physics (San Jose, CA) Model 8100 high pressure liquid chromatograph was used to separate the tracer dyes. The separation procedure employed a 5  $\mu$ m bead size, 25 cm long, C-18 analytical column (Supelco, Bellefonte, PA) preceded by a 3 cm C-18 guard column (Brownlee Laboratory, Santa Clara, CA). The outlet of the analytical column was connected to the fluorescence detector. Both 50 and 100  $\mu$ l injection volumes were employed. Table II.C.5 contains the two sets of operating parameters used. The first set was utilized when all seven



TABLE II.C.5 HPLC elution parameters

Time (min)	%A <sup>1</sup>	Set 1 (Gradient)		Flow (ml/min)
		%B <sup>2</sup>	%C <sup>3</sup>	
0.0 - 1.6	40	45	15	1.5
1.6 - 7.1	70	30	0	1.5
7.1 - 20	40	45	15	1.5
Set 2 (Isocratic)				
---	47	38	15	1.5

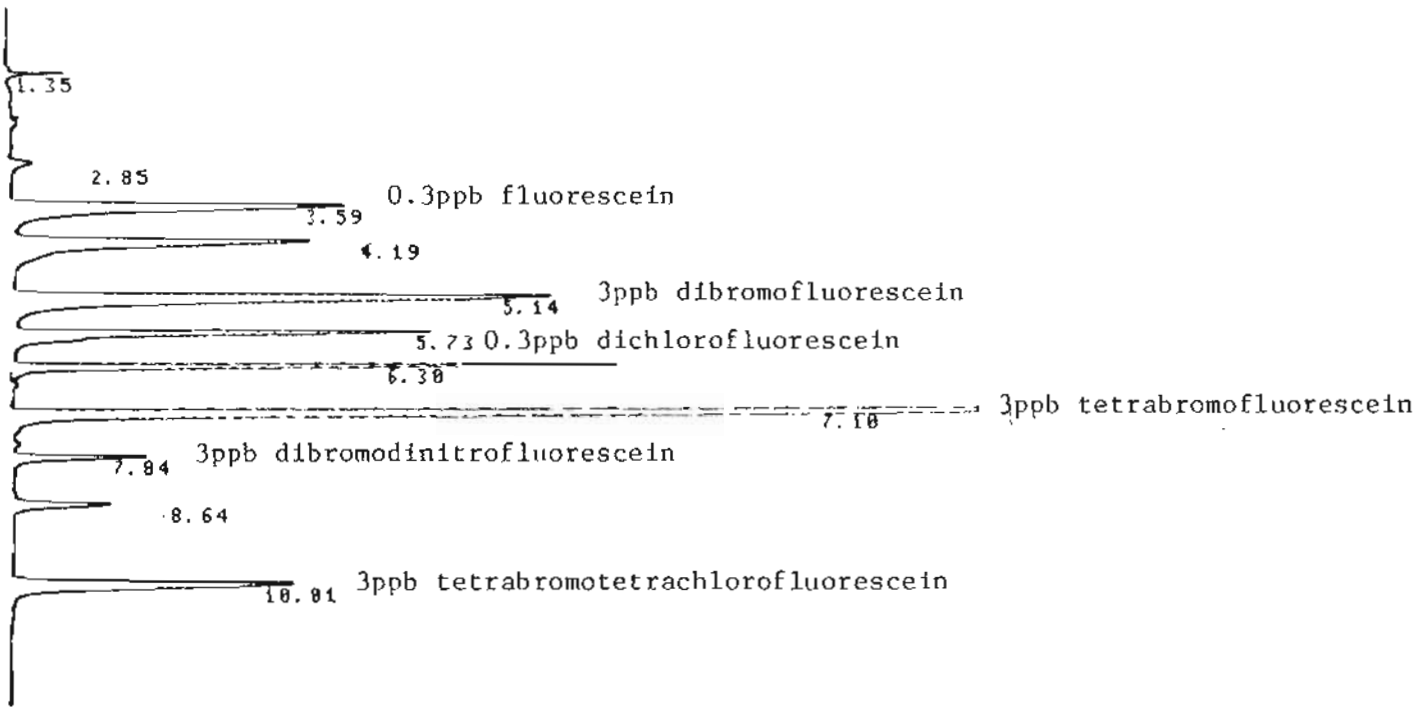
1. Solution A - 90% CH<sub>3</sub>OH : 10% H<sub>2</sub>O
2. Solution B - H<sub>2</sub>O
3. Solution C - 25 mM PO<sub>4</sub> buffer; pH=7.3

dyes were determined, and the second set when only fluorescein and 4'-chlorofluorescein were determined. The solvent gradient elution scheme in the first set required several cycles at the start of the day to condition the column. An example of the peak shape and resolution provided by the HPLC separation is shown in Figure II.C.8.

#### II.C.7.b. LASER-INDUCED FLUORESCENCE DETECTOR

The primary impetus for developing a laser-induced fluorescence detector was the sensitivity and wide dynamic range offered by such a system. There has been a rapid evolution in laser-induced fluorescence detectors in the last 10 years. Recent reports have cited detection limits of 20 femtogram of fluoranthene (Folestad, 1982) and a potential linear dynamic range exceeding 7 orders of magnitude (Klinger, 1983). The critical feature in such determinations is the design of a flow cell which interfaces the column eluent with the laser excitation source and emission detector. Most of the interface schemes that have been devised are very complex and rely on highly specialized equipment. Some examples include a capillary tube-optical fiber combination (Sepaniak and Yeung, 1980), a flowing suspended droplet (Diebold and Zare, 1977), a sheath flow based flow cell (Hershberger et.al., 1979), and a free falling capillary jet cell (Folestad et.al., 1982). Early in this study, the capillary jet cell was evaluated extensively and rejected due to high noise levels caused by pump-induced instability of

Figure II.C.8 Typical chromatogram for the fluorescein dye mixture used in tracer test #1 illustrating the peak shape and resolution provided by the HPLC separation.



the jet. A slightly modified micro-flow cell (Precision Cells, Inc., Hicksville, NY) was then tested and found to work well.

The apparatus used for fluorometric detection is shown in Figure II.C.9. Radiation from an argon ion continuous wavelength (CW) laser (Coherent Radiation, Palo Alto, CA) was focused with a 50 cm focal length lens so that the focal point fell on the middle of the fused silica flow cell. The laser was tuned to 488 nm. It provided approximately 0.5 W of power at this wavelength. The 20 ul flow cell was positioned roughly with a lab-jack and then more precisely with two positioning screws on the aluminum flow cell holder (the cell holder and other metallic surfaces were painted flat black to minimize light scattering). The optimal position of the flow cell was determined visually. The fluorescence radiation emitted at 90 degrees to the laser beam was imaged with a 2 cm focal length lens through an orange glass filter (50% transmission at 510 nm) and onto the surface of a silicon PIN photodiode. The lens was positioned manually and the photodiode was positioned with the x-y translator. The signal from the photodiode was amplified with the OP121 operational amplifier (Burr Brown, Tucson, AZ) using the low-noise, high-gain circuit shown in Figure II.C.10. The circuit was critical to the success of the detection system. The amplified signal was fed into a Spectra Physics, San Jose, CA) 4100 computing integrator for recording and further data processing. Although not absolutely necessary, the apparatus was assembled on an optical table for stability.

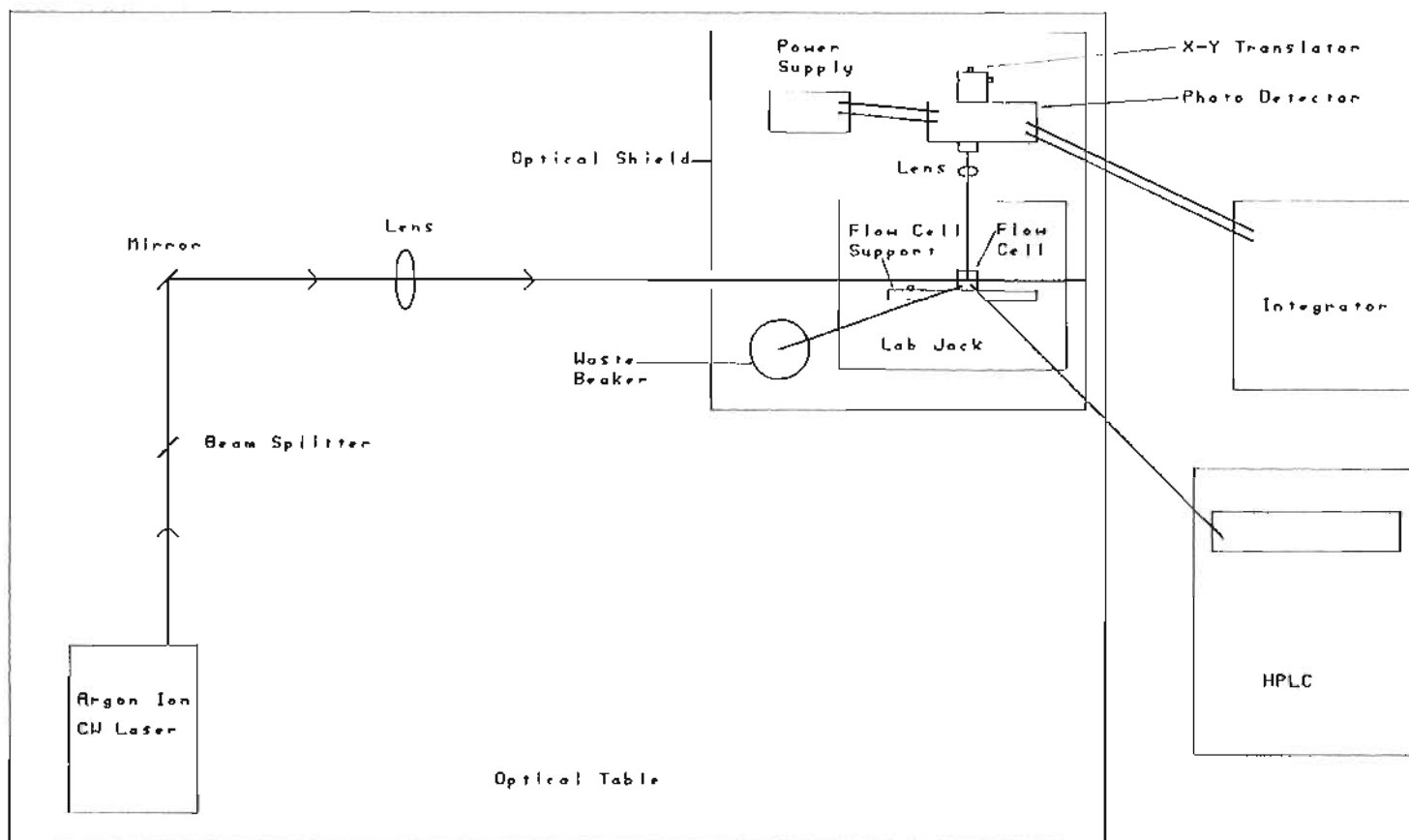


Figure II.C.9 Schematic drawing of the laser-induced fluorescence detection apparatus.

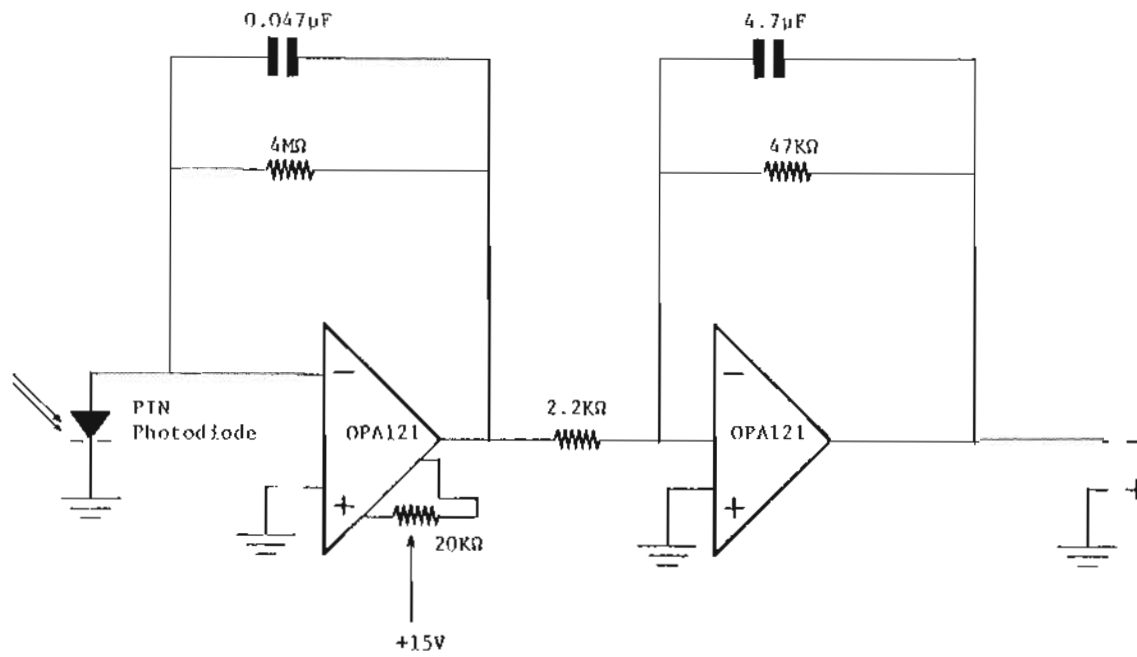


Figure II.C.10 Diagram of the low-noise, high-gain circuit used to amplify signals from the photodiode.

A principal feature of the fluorometric detector was the absence of any highly specialized hardware. The use of the commercially-available flow cell, the simple photodiode radiation detector, and the type of laser found in most Raman spectrometers, provided the opportunity for the development of laser-induced fluorescence as a routine tool for groundwater tracer analysis.

#### II.C.7.c. Standard Operating Procedure

Standard solutions were prepared in the range 0.2 ppb to 50 ppb by serial dilution of a mixture containing 10 ppm of each of the dyes. The system was calibrated daily prior to analysis. Figure II.C.11 shows calibration curves for several of the compounds. The quality assurance steps taken included analyzing a standard with a concentration in the range of that determined for the previous sample and a sample repeat after every tenth sample. The results of the replicate analyses were used to estimate the pooled coefficients of variation (CV) by assuming that the CV was independent of concentration within the specified concentration ranges. The CV results are presented in Table II.C.6 and show that analytical precision improved with increasing concentration. The relatively poor precision at low concentrations (< 1 ppb) was the main limitation in quantifying low level samples. A quantitation limit instead of a detection limit was therefore used to set the lower limit for statistically significant

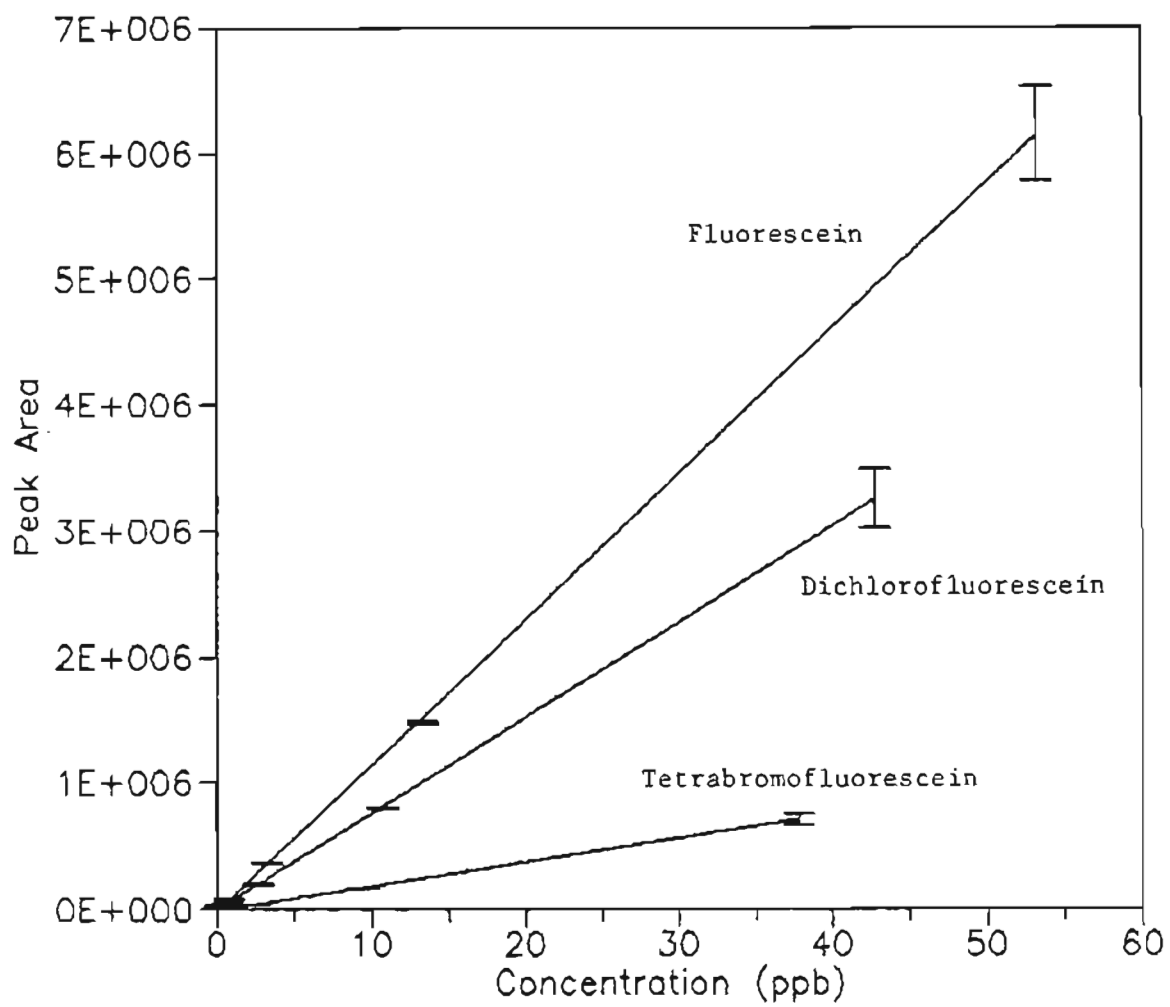


Figure II.C.11 HPLC laser-induced fluorescence calibration curves for several of the tracer dyes (injection volume = 10  $\mu$ l).



TABLE II.C.6 Estimated coefficients of variation for fluorescein and 4'-chlorofluorescein

Compound	Concentration Range (ppb)	n	Mean Conc. (ppb)	CV (%)
fluorescein	<1	19	0.5	32
fluorescein	1-10	33	3.4	24
fluorescein	>10	15	21.	10
4'-chlorofluorescein	<5	5	2.8	25
4'-chlorofluorescein	>25	7	6.7	10

concentrations. The limit of quantitation (LOQ) was calculated by first multiplying the CV for the 0 to 1 ppb range (32%) by the mean concentration of the replicate analyses in the 0 to 1 ppb range (0.54 ppb) to form an absolute standard deviation for low level samples (0.17 ppb). Next, the absolute standard deviation was multiplied by three to estimate the LOQ (0.5 ppb). Only fluorescein was quantitated in enough of the samples that underwent repeat analysis to justify this procedure. In the absence of a direct estimate for the 4'-chlorofluorescein, the fluorescein limit of quantitation was also applied to the 4'-chlorofluorescein data. This was a conservative approach since the CV in the 1 to 10 ppb range was lower for 4'-chlorofluorescein than it was for fluorescein. Quantitation limits a factor of ten below those in Table II.C.6 were easily obtainable by using a larger injection volume combined with a concentrator column. However, the larger injection volume was rejected since it would have necessitated the installation of additional ventilation equipment to reduce personal exposure to the volatile organic contaminants in the groundwater samples. In addition, the potential for rapid column degradation was a concern due to the high levels of organic compounds from the existing contaminant plume.

#### II.C.8. Tracer Dye Stabilities

An experiment was conducted to evaluate the stability of fluorescein during storage and handling. Aliquots of groundwater were

removed from the sample bottles and spiked in the field by adding them to identical bottles containing fluorescein solutions of known concentrations. The spikes represented increases in fluorescein concentrations of 10 to 150%. The spiked and unspiked samples were analyzed shortly after collection (2 days). The samples were then stored in the same manner as the rest of the samples in the study and then re-analyzed two more times during the next three months. Table II.C.7 contains the results of the concentration versus time determinations and shows that the difference between the spiked and unspiked samples remained constant. This indicates that degradation of fluorescein during storage was negligible.

A similar stability analysis was not necessary for 4'-chlorofluorescein, the tracer used in tracer test #2, because all of the samples for test #2 were analyzed within four days of sample collection.

#### II.D. Partition Coefficient Measurements

The partition coefficient ( $K_p$ ), a measure of the relative affinity of a solute A for the aqueous and solid phases, is defined as:

$$K_p = C_s/C_w = (M_a - V_w C_w) / M_s C_w \quad (\text{II.1})$$

where:

$C_s$  = concentration of solute A in soil (g of A/g dry soil)

TABLE II.C.7 Results of the fluorescein stability analysis (ppb)

Stability Pair	After 2 days in storage			After 25 days in storage			After 98 days in storage		
	Spiked	Unspiked	Delta	Spiked	Unspiked	Delta	Spiked	Unspiked	Delta
1	18	8	10+-5	14	8	6+-4	15	9	6+-4
2	23	9	14+-6	18	8	10+-5	19	9	10+-5
3	6	6	0+-2	6	7	-1+-2	6	7	-1+-2
4	3	3	0+-1	3	4	-1+-1	3	3	0+-1
5	9	7	2+-3	9	7	2+-3	10	8	2+-3
6	20	7	13+-5	20	7	13+-5	22	8	14+-6
7	17	12	5+-5	21	10	11+-6	18	11	7+-5

$C_w$  = concentration of A in water (g of A/ml water)

$M_a$  = total mass of A in the system

$V_w$  = total volume of water in the system, and

$M_s$  = total mass of dry soil in the system

Batch equilibrium experiments were conducted to determine  $K_p$  for fluorescein and 4'-chlorofluorescein. Standard solutions (10 ppb), made up with uncontaminated groundwater collected upgradient of the CDS, were used in the tests. The soil was an uncontaminated composite sample collected between 0.5 m and 3 m below the surface. One gram of dry soil was added to 10 mL of a standard solution in a 35 mL glass vial. The solutions were mixed continuously for 24 hours by end-over-end rotation at a rate of 50 rpm. The mixing took place in a cooler held at 6 C. This temperature was chosen since it is approximately the average groundwater temperature at the site. After equilibrium, the solutions were centrifuged to separate the liquid and the soil. The supernatant was then analyzed by the previously discussed HPLC procedure. Each experiment was run in triplicate. Standard solutions without soil were run as controls.

No significant adsorption was detected for either tracer. The three experiments for each of the dyes resulted in  $K_p$  values of 0 +/- 2.5. The uncertainty in  $K_p$  from equation II.D.1 assuming that only the measurement of  $C_w$  involved significant error is:

$$s_K = \sqrt{\text{CoV}_{\text{Hplc}}^2 \{ (V_w/M_s)^2 + K_p^2 \}} \quad (\text{II.2})$$

where:

$s_K$  = standard deviation in  $K_p$ , and

$\text{CoV}_{\text{Hplc}}$  = fractional coefficient of variation in aqueous concentration of A.

For weakly sorbing solutes,  $s_K$  is dominated by the analytical error and the ratio of water to soil. Lowering the water to soil ratio is impractical as a means of error reduction since at ratios less than 10 to 1 the solution becomes too thick for effective experimentation.

The weighted mean of the three measurements of  $K_p$  for a single compound was 0 +/- 1.4, where the standard deviation of the mean was calculated by propagation of the errors in the individual determinations. This result implies that an upper 95% confidence limit of  $K_p$  is 2.3.

## II.E. Characterization of the Groundwater Flow System

### II.E.1. Water Table Measurements

The existing network of surveyed piezometers (Johnson, 1984) was used to monitor the water table during the tracer tests. The network, and its relationship to the tracer test site, are shown in Figure

II.E.1. The height of the water table was obtained by measuring the distance between the top of the piezometer casing and the water table as sensed by a conductance probe. Water table values were referenced to the top of Well 2 (Figure II.E.1) which was arbitrarily set to 1000 cm. Six water table contour maps, developed from measurements made during the study, are plotted in Figures II.E.2 - II.E.6. It can be seen that throughout the study, the general direction of large scale flow was parallel to the principal axis of the tracer test sampling network. The annual water level cycles in wells S-3 and S-15 are plotted in Figure II.E.7. In agreement with Pankow et.al. (1984), the highest and lowest water table levels in the area surrounding the CDS were found to occur during the spring and fall, respectively. Near the tracer test site, the water table fluctuated over a range of 26 cm. The depth to groundwater was always less than 1 m. The hydraulic gradient was estimated between the two contour lines which are closest to the tracer site in each of Figures II.E.2 - II.E.6. The gradient is plotted as a function of time in Figure II.E.8. During this study, the gradient fluctuated within the narrow range 0.0003 to 0.0006.

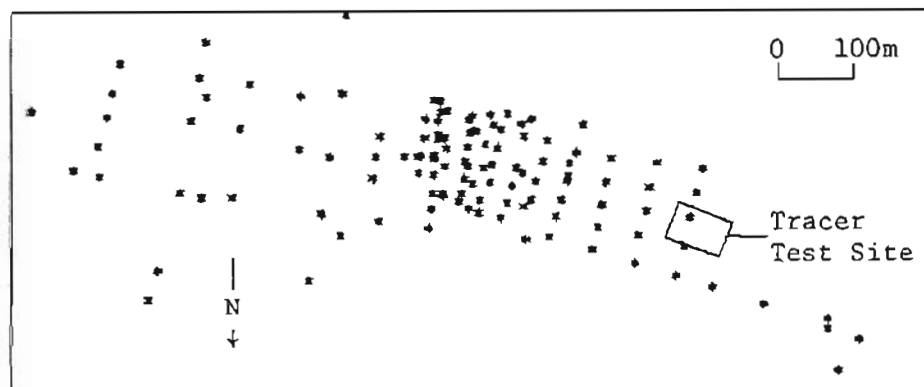


Figure II.E.1 Map showing the locations of piezometers used for water table measurements during the tracer tests (\*'s represent piezometer locations).



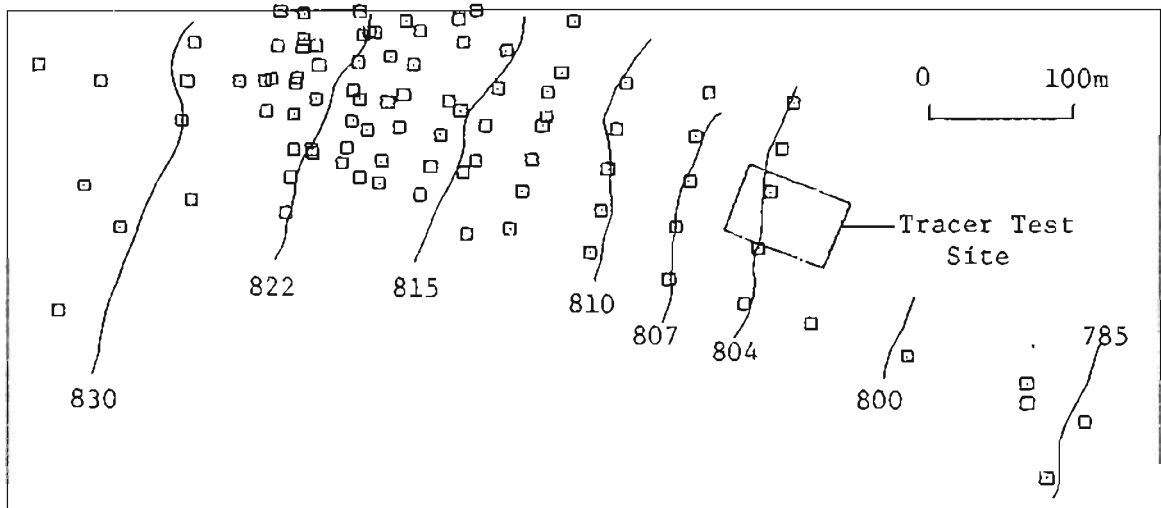


Figure II.E.2 Water table map in centimeters for 6/14/84.

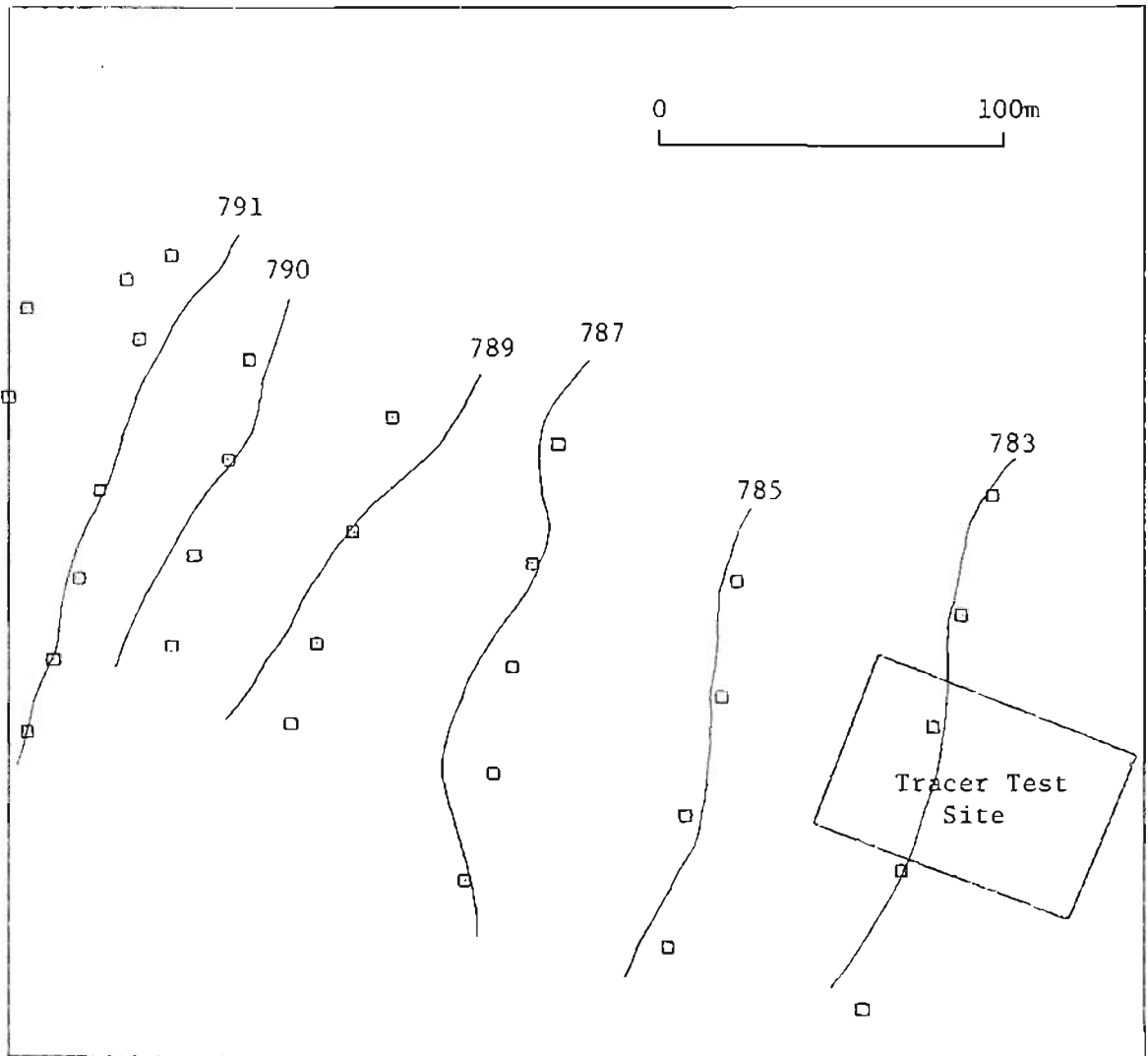


Figure II.E.3 Water table map in centimeters for 11/10/84.

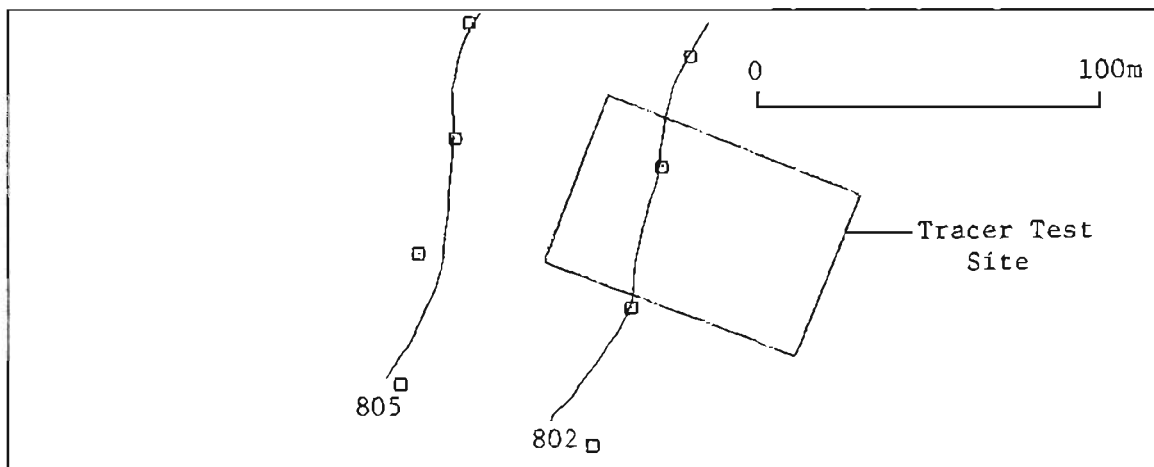


Figure II.E.4 Water table map in centimeters for 4/8/85.

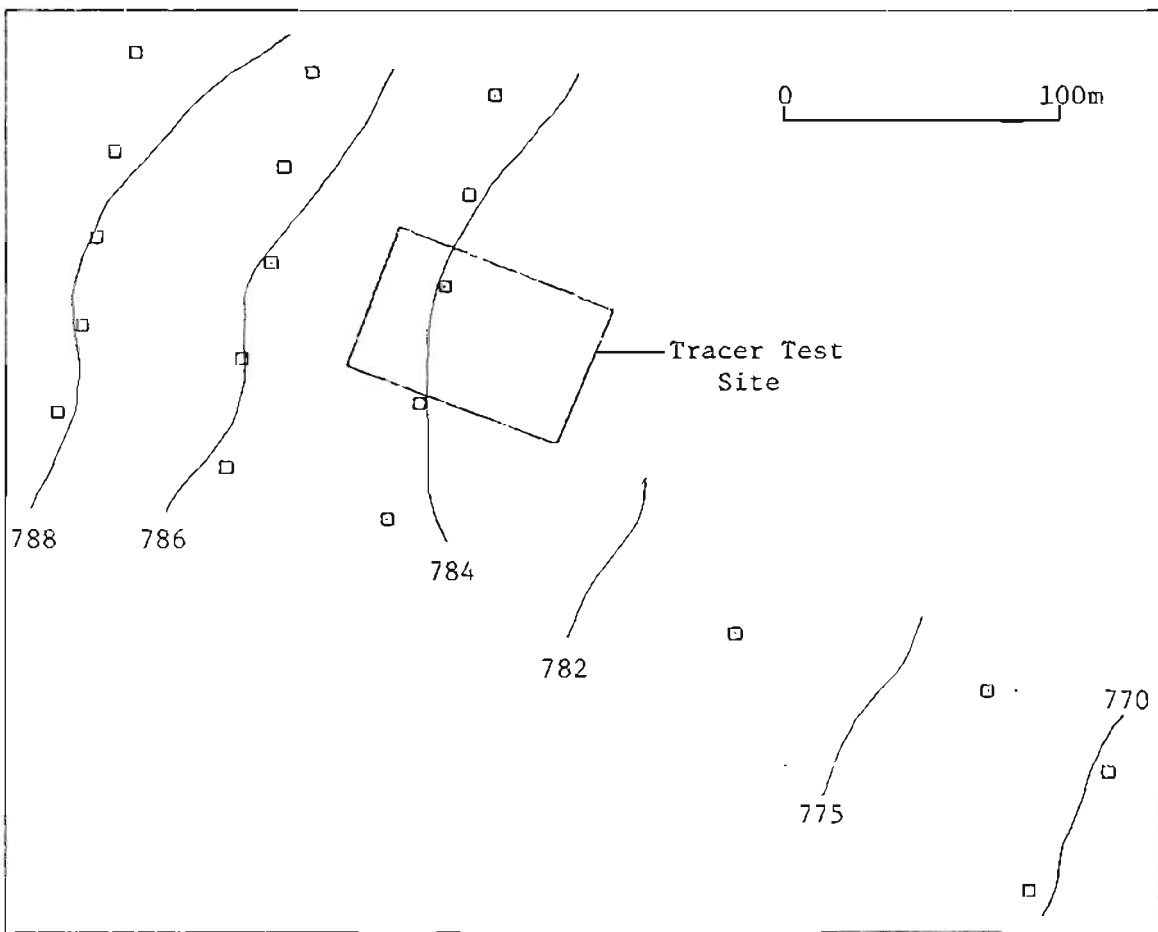


Figure II.E.5 Water table map in centimeters for 7/15/85.

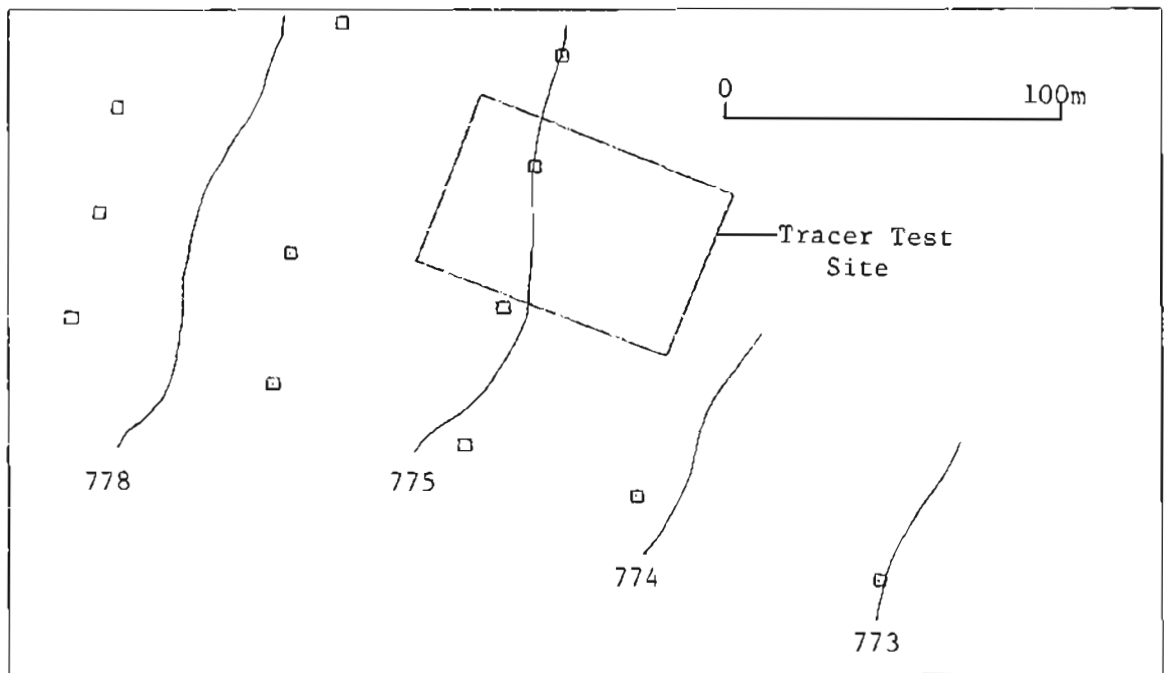


Figure II.E.6 Water table map in centimeters for 10/3/85.

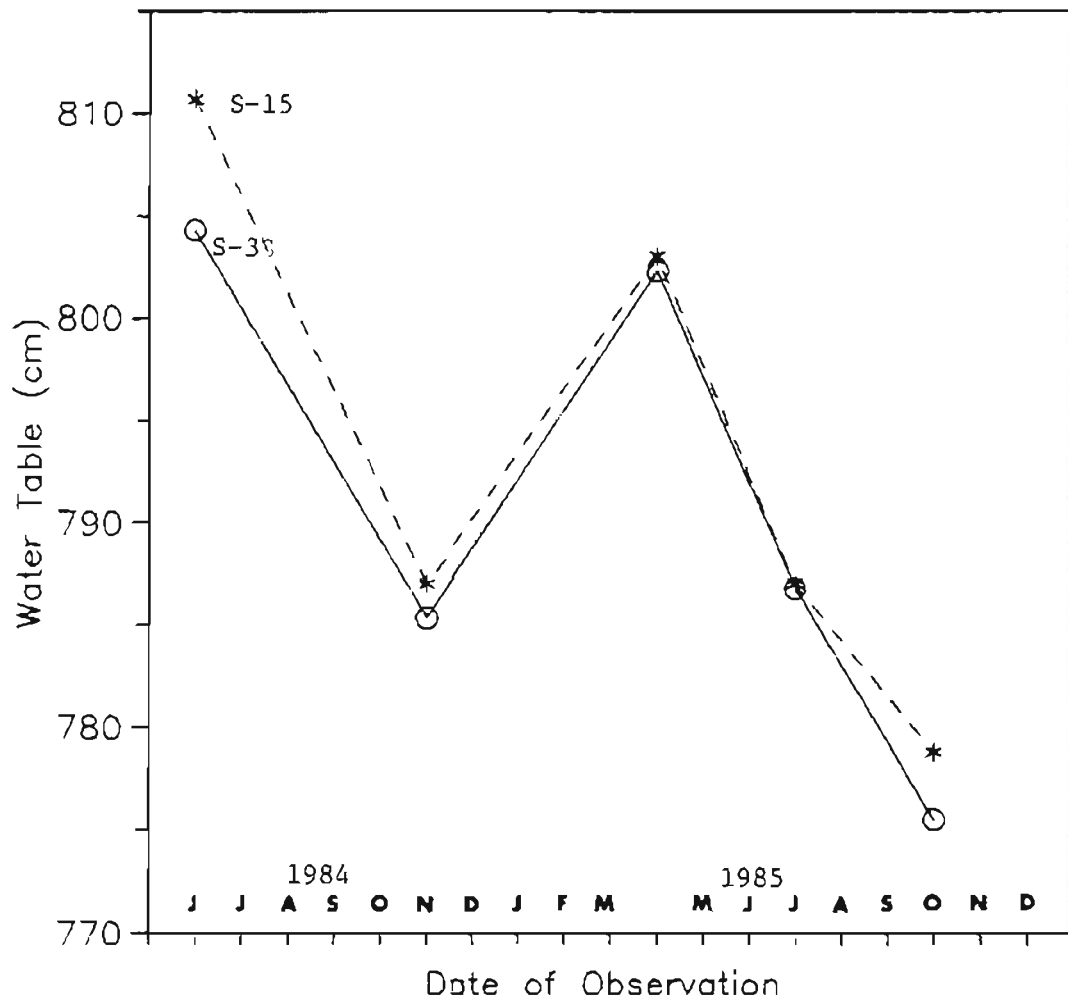


Figure II.E.7 Water table in centimeters at piezometers S-3 and S-15 as a function of time during the period 1984-1985.

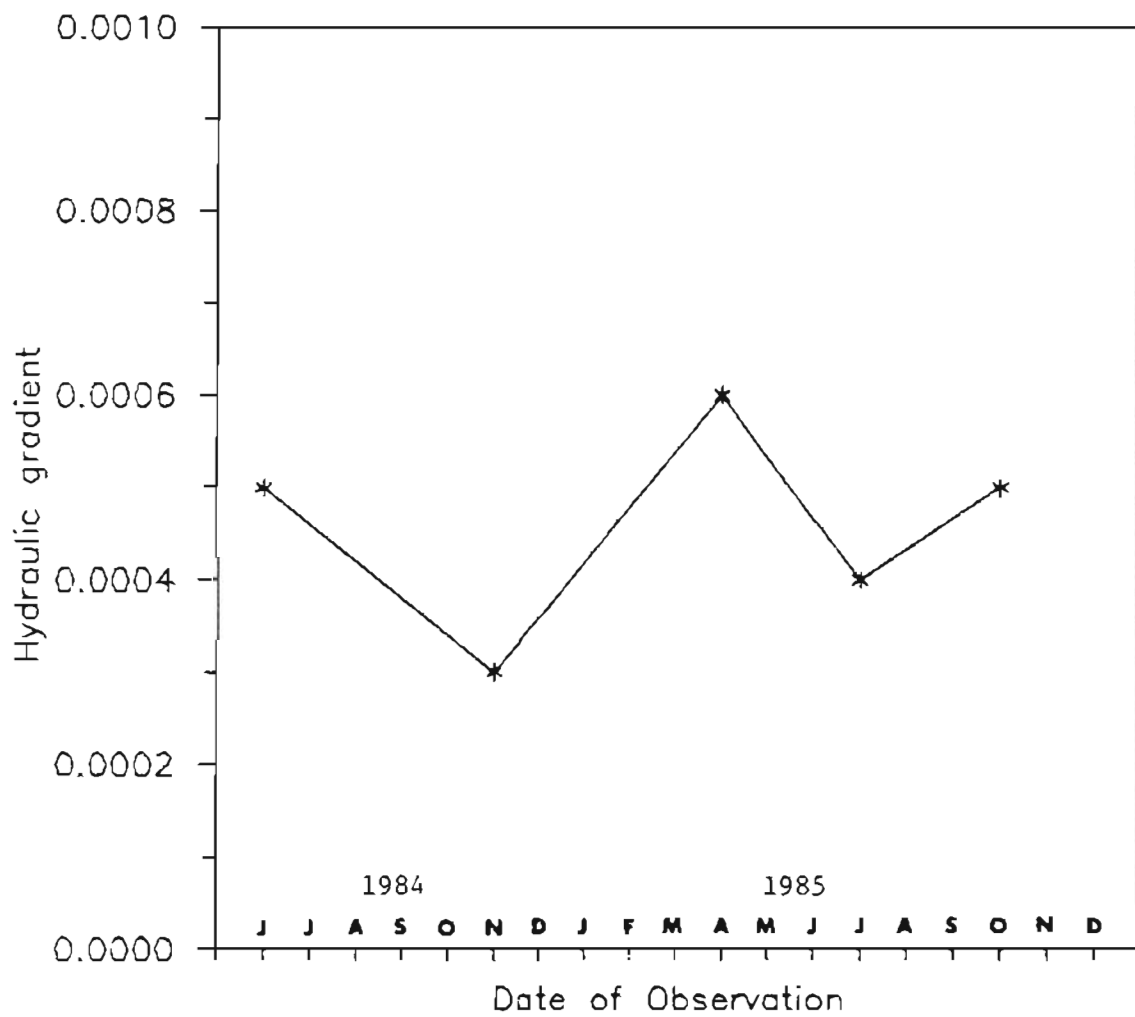


Figure II.E.8 Hydraulic gradient in the tracer test site as a function of time during the period 1984-1985.

## II.E.2. Hydraulic Conductivity Measurements

### II.E.2.a. Experimental

Figure II.E.9 shows the locations within the tracer site where slug tests to determine  $K_H$  were carried out on some of the single level piezometers described in Section II.C.2. To carry out each test, a water filled reservoir was first fitted to the top of a piezometer casing. A schematic diagram of the slug test reservoir is shown in Figure II.E.10. The valve at the bottom of the reservoir was then opened and the drop in the water level within the reservoir was monitored through a translucent nylon tube which was located on the exterior of the reservoir. The time was recorded when the water level reached several pre-selected values.

The method used to analyze the data was a variation of the procedure developed by Hvorslev (1951) and modified by Johnson (1984). Briefly, the appropriate equation to estimate  $K_H$  for an isotropic medium is:

$$K_H = r^2 \ln(L/R) / 2LT_0 \quad \text{for } L/R > 8 \quad (\text{II.3})$$

where  $L$  = length of the screened interval,

$R$  = radius of the screened interval,

$r$  = radius of the reservoir, and



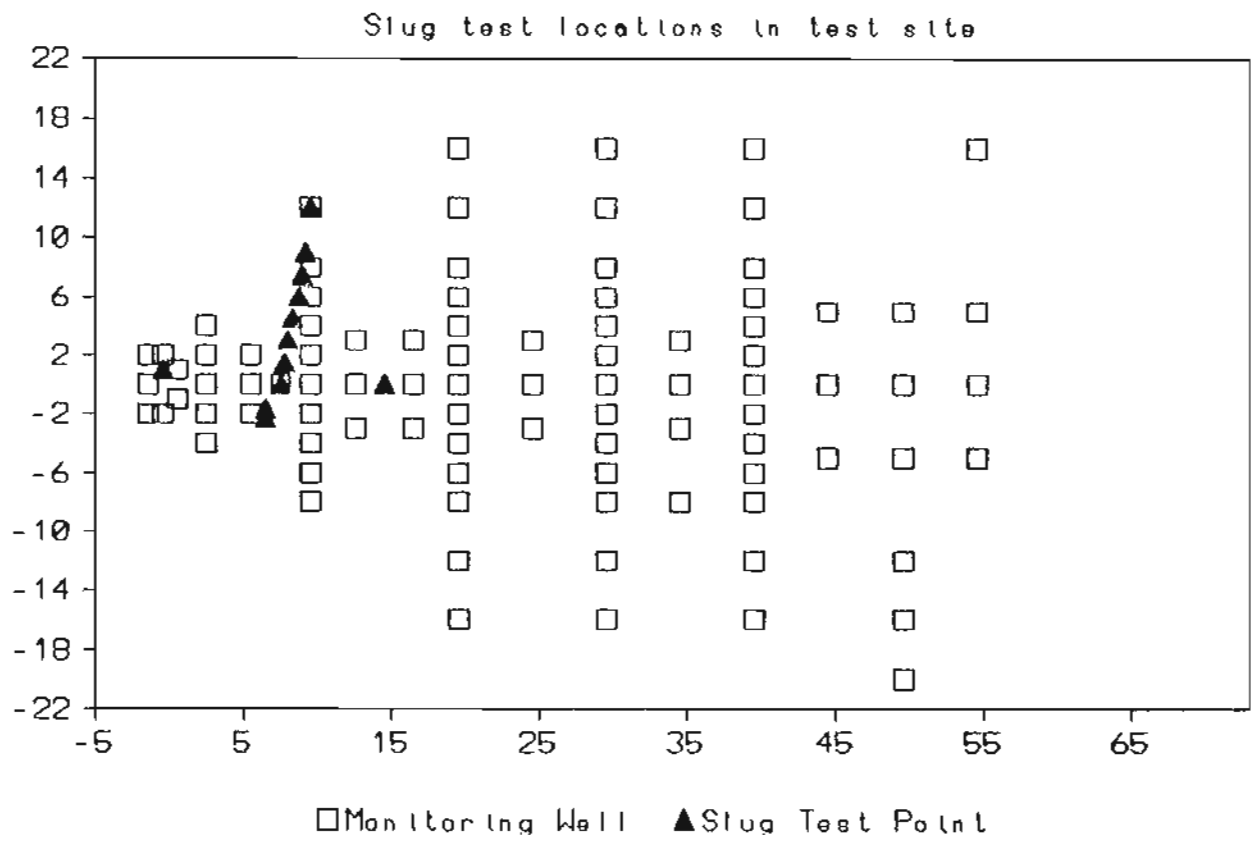


Figure II.E.9 Map showing the locations within the tracer site where slug tests were performed to determine  $K_H$ .

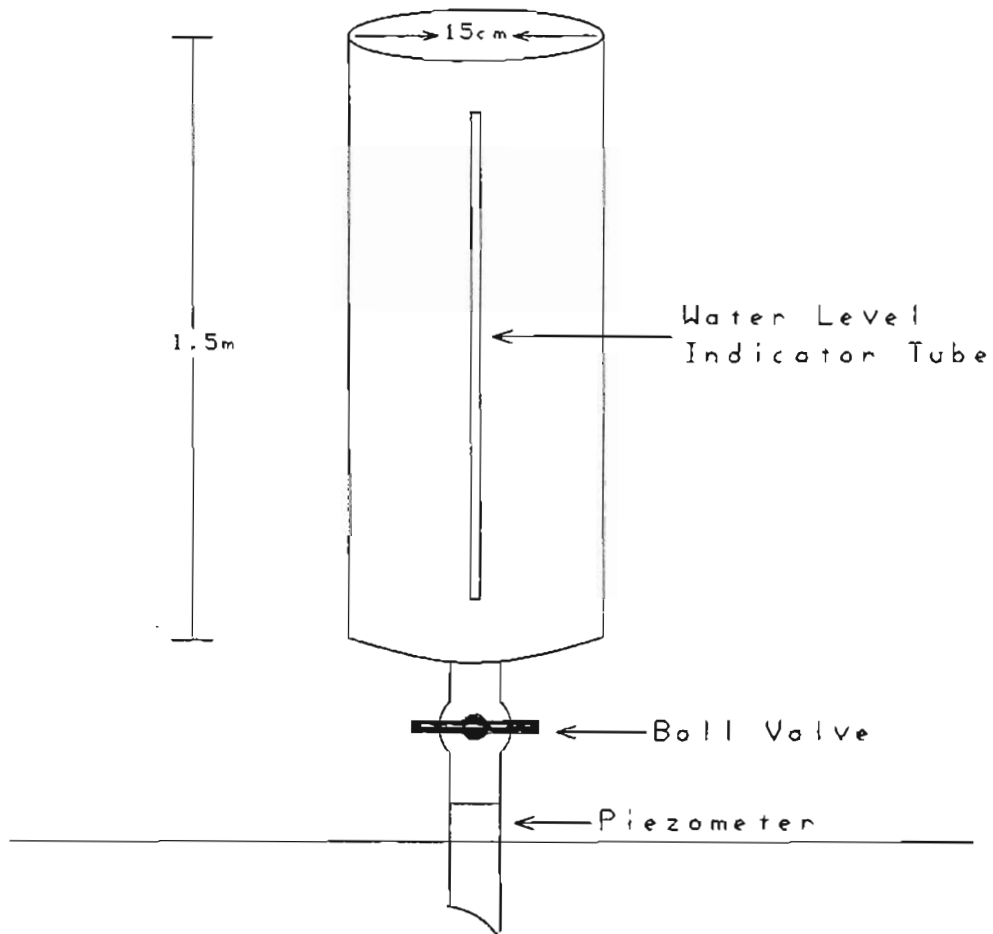


Figure II.E.10 Schematic drawing of the slug test reservoir (after Johnson, 1984).

$T_0$  = the basic time lag.

$T_0$  is defined as the time at which the water level falls to 37% ( $1/e$ ) of its initial level. To estimate  $T_0$ ,  $\ln[\text{water level at time}(t)/\text{water level at time}(0)]$  was regressed against time( $t$ ). The regression equation was then solved for  $T_0$  by setting  $[\text{water level at time}(t)/\text{water level at time}(0)] = 0.37$ . A typical regression curve is shown in Figure II.E.11.

#### II.E.2.b. RESULTS

Values of  $K_H$  at ~1 m depth are given in Table II.E.1 for the locations shown in Figure II.E.9. The relative measurement precision was 9% as estimated by the pooled coefficient of variation formed from the results of replicate tests.

The distribution of  $K_H$  is described by its mean,  $\bar{K}_H$  (0.00021 m/s), standard deviation (0.00012 m/s), and range (0.00002 to 0.00036). The large values for standard deviation and range indicate the heterogeneous nature of the site with respect to hydraulic conductivity.  $K_H$  has often been reported to follow a lognormal distribution. Frequency histograms for  $K_H$  and  $\ln[K_H]$  are shown in Figures II.E.12 and II.E.13 which indicate that  $K_H$  is neither normally nor lognormally distributed at the test site.

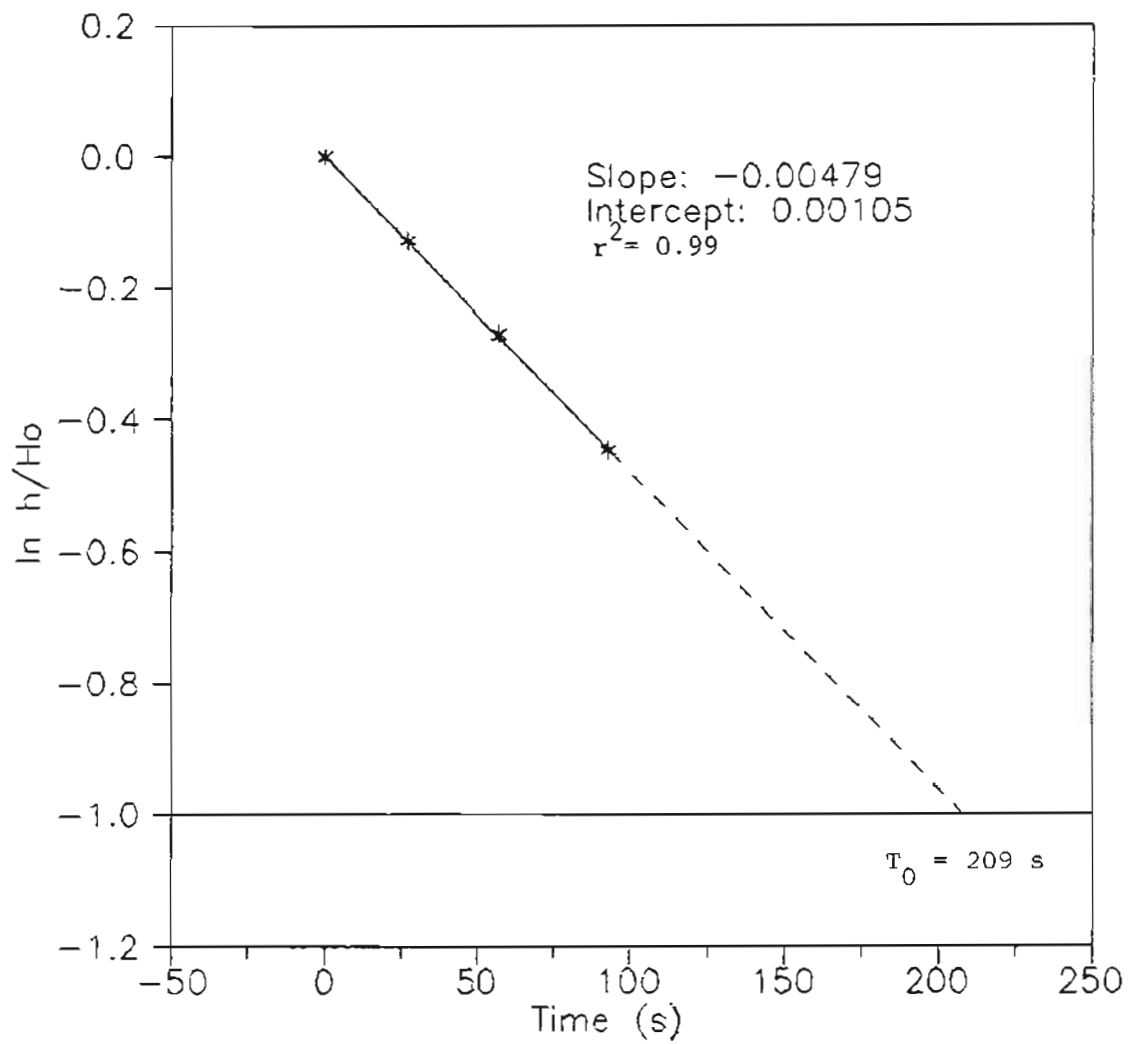


Figure II.E.11 Typical regression curve used to estimate  $K_H$  from slug test data.

TABLE II.E.1 Hydraulic conductivity ( $K_H$ ) data

Piezometer Location <sup>1</sup>	$K_H$ ( $\times 10^4$ m/s)
(8,0,6)	3.5
(8,0,6)	3.1
(8.3,1.5,6)	1.1
(8.5,3,6)	0.2
(8.8,4.5,6)	0.4
(9.2,6,6)	0.3
(9.5,7.5,6)	2.3
(9.7,9,6)	1.8
(9.7,9,6)	1.6
(10,12,6)	3.0
(7,-1.7,6)	1.4
(7,-1.7,6)	1.5
(7,-2.3,6)	0.9
(0,1,7)	3.6
(0,1,9)	3.3
(15,0,7)	3.2

<sup>1</sup>Locations given as x, y, z coordinates of screened interval; x and y are horizontal coordinates in meters; z is depth in feet.

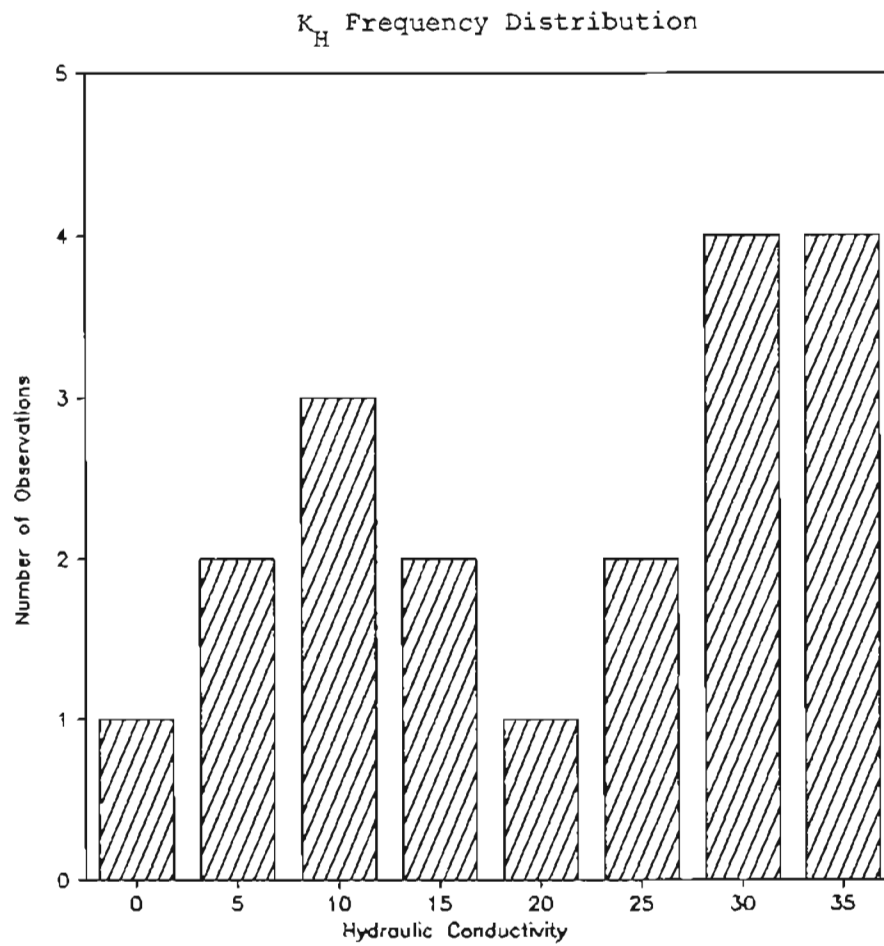


Figure II.E.12 Frequency histograms of  $K_H$  based on  $K_H$  measurements made within the tracer site.

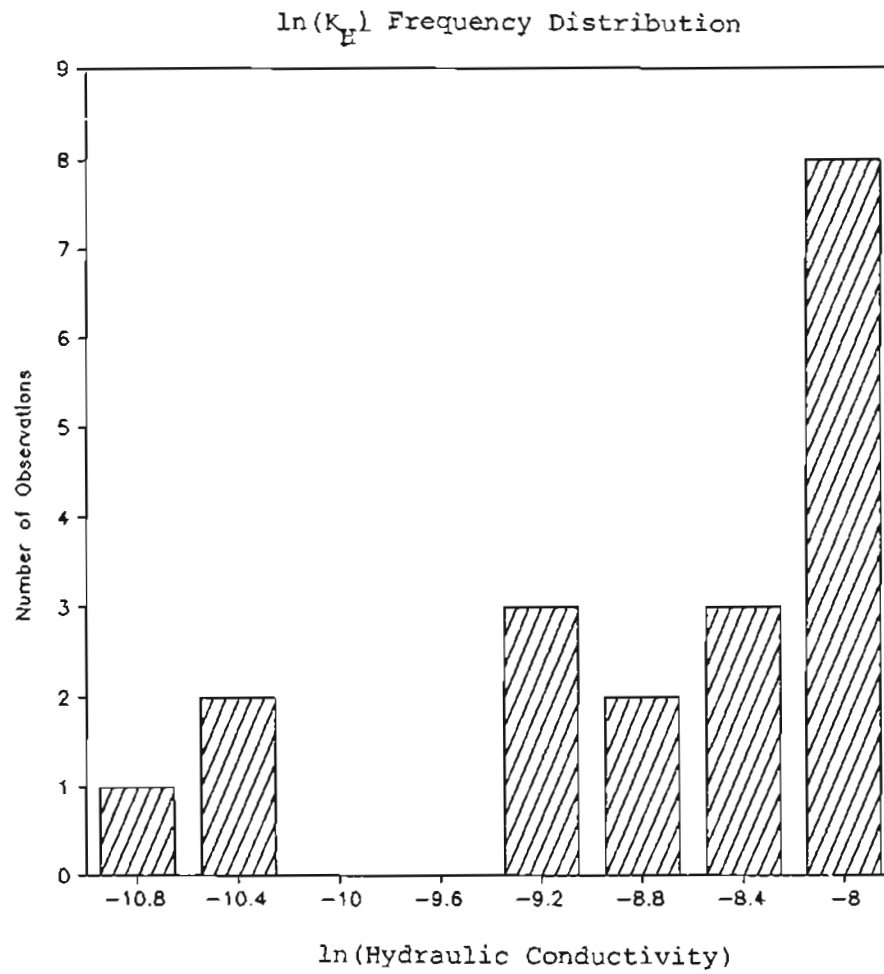


Figure II.E.13 Frequency histograms of  $\ln(K_H)$  based on  $K_H$  measurements made within the tracer site.

Ten of the slug test locations (Figure II.E.9) form an approximately 14 m long transect across the tracer site.  $K_H$  vs. distance along the transect is plotted in Figure II.E.14. The absence of a trend in the plot indicates that the spatial correlation in  $K_H$  is very weak even at the small separation distance of 1.5 m.



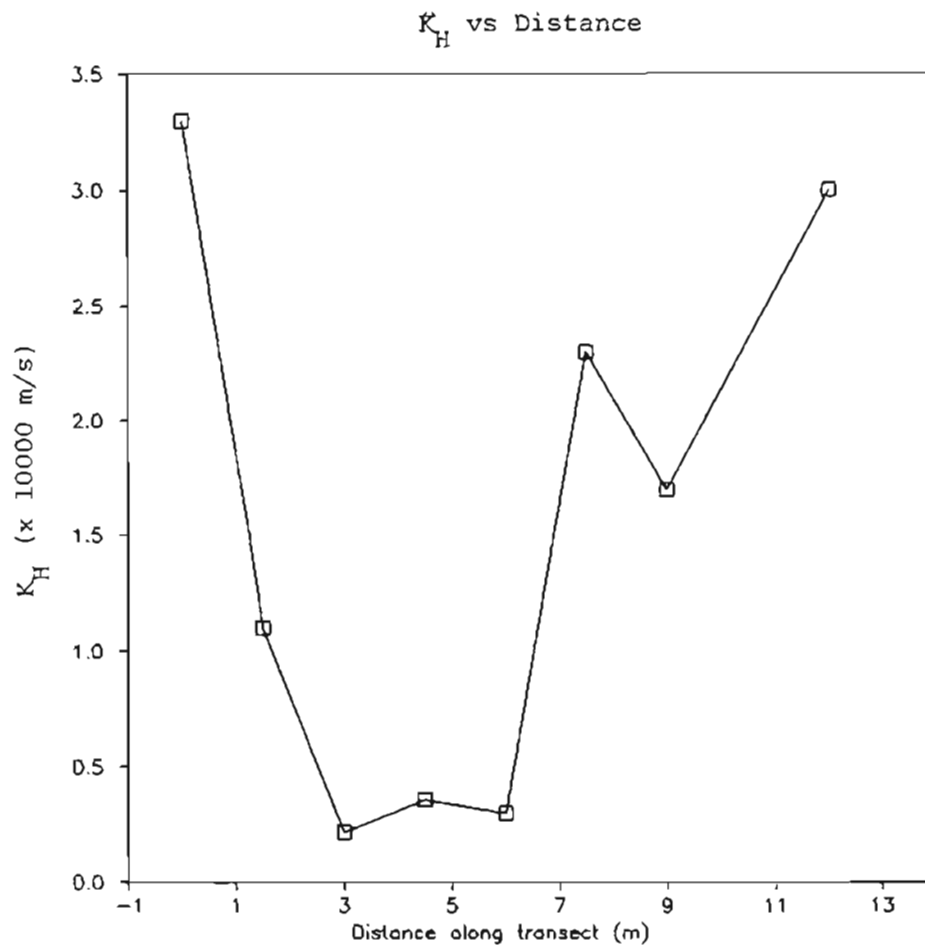


Figure II.E.14  $K_H$  as a function of distance along the 14 m transect on which  $K_H$  was measured within the tracer site.

### III. TRACER PLUME MAPPING METHODOLOGIES

Each tracer study sampling episode provided a set of concentration values from the monitoring network. To facilitate understanding the migration of the tracers, the measured values were used to 1) estimate the tracer concentrations at the nodes of a dense grid covering the study domain, and 2) produce contour maps of the tracer plume surface. The availability of concentration estimates at the grid nodes was useful for calculating plume parameters such as center of mass and mass balance. In addition, gridded data was a prerequisite to most contour drawing algorithms. Contour maps find their utility in their ability to communicate the spatial features of a plume more effectively than tables of measured values and sampler locations.

There are numerous methods available for estimating a surface on a uniform grid from a limited set of observations. Each of these methods results in a different set of gridded data and corresponding contour map. Unfortunately, since the true plume surface is unknown, it is difficult to quantitatively determine the gridding method of choice. In addition, at present there is little guidance in the environmental literature on the "best" techniques for contouring groundwater contaminant plumes. There is, however, an abundance of information on estimating the surfaces of other spatial variables (e.g. ore grades, rainfall, and hydraulic head). Even in the areas where contouring has long been considered important and has been the object of extensive research, though, there is no consensus on the preferred gridding

method. Also, there is no a priori reason to expect that the assumptions which may be appropriately applied for contouring spatial variables such as ore grades may also be applied to solute plumes.

The above discussion indicates the need for choosing an appropriate gridding method as well as a lack of obvious information upon which to base this choice. To overcome this deficiency, a typical data set was subjected to five gridding and contouring methods and the results from a series of tests were compared. Four of the methods were based on a weighted moving mean; they differed primarily in the calculation of the weights. The fifth approach was a nonparametric method employing a weighted moving median.

The major objectives of the method evaluation process were to:

- 1) determine an appropriate method of gridding and contouring the data from the tracer tests conducted in this study;
- 2) evaluate the dependence of plume parameters (e.g. center of mass) on the gridding method;
- and 3) estimate the potential influence of the gridding method on the evaluation of transport models and the determination of the processes controlling solute migration.

### III.A. Data Set Used for Contour Method Evaluation

The primary test data set was made up of the fluorescein concentrations of samples collected at a depth of 6 feet on day 342 of the first tracer test. This was the most complete data set (88 samples) and was chosen with the hope that the large number of samples would allow more definite conclusions to be reached from the comparison of the methods. Two other sets were also used in the evaluation. The first was a perturbed data set formed by adding to each member of the complete data set the product of the data value, the relative analytical error, and a random number from a normal distribution over the interval  $-1$  to  $1$ . The second was a reduced data set formed by removing 10 random values from the complete data set. The three data sets will henceforth be referred to as the complete data set, the perturbed data set, and the reduced data set.

### III.B. Evaluation Procedure

Comparisons of mapping procedures have rarely been conducted, and no set of standard tests for carrying out such comparisons have emerged. For this evaluation, a pragmatic procedure was devised in an attempt to reduce the comparisons to a reasonable number of indexes. The five gridding algorithms were compared and contrasted on the basis of five steps:

1. The precision and bias of the algorithms with respect to reproducing the measured values of the complete data set was determined by calculating the correlation coefficient, mean absolute deviation, mean squared deviation, and mean deviation between the measured values and the predicted values at the sampling points.
2. The precision and bias in the predictive ability of the methods was examined by calculating the correlation coefficient, mean absolute deviation, mean squared deviation, and mean deviation between the ten removed values and their levels as estimated using the reduced data set. This is known as "validation on an independent sample", and is a standard method for checking statistical analyses. It has been used previously by Creutin and Obled (1982) to compare rainfall mapping algorithms.
3. The influence of analytical error on plume parameters was examined by comparing the center of mass and mass balance estimates based on the gridded data provided by the complete data set and the perturbed data set.
4. The influence of a small number of data points on plume parameters was examined by comparing the center of mass and mass balance estimates based on the gridded data provided by the complete data set and the reduced data set.
5. Since some of the gridding algorithms require extensive numerical calculations, the times required to estimate the values of the regular grid were compared. The computer used to perform the gridding calculations was a "PC Clone" with a 4.77 MHz 8088 CPU and an 8087 floating-point co-processor.

### III.C. Description of the Mapping Procedure

Most of the gridding algorithms used the linear estimation model:

$$z^*(p_0) = w_1 z(p_1) + w_2 z(p_2) + \dots + w_n z(p_n) \quad (\text{III.1})$$

where  $z^*(p_0)$  = the value to be estimated,

$w_i$  = the calculated weights, and

$z(p_i)$  refers to the measured concentration at the  $i$ th sampler among  $N(i=1..N)$  with spatial coordinates  $p_i = (x_i, y_i)$ . The four weighted moving average methods differ principally in the procedure used to calculate the weights.

The nonparametric approach relies on a weighted median calculated by:

$$z^*(p_0) = \text{median} (F_w(g)) \quad (\text{III.2})$$

where  $F_w$  is a weighted distribution function in which each  $z_i$  value is assigned a relative frequency  $w_i$  and

$$w_1 + w_2 + \dots + w_n = 1 \quad (\text{III.3})$$

In the following discussion, the mapping procedures are classified as statistical or deterministic. The classification procedure follows Creutin and Obled (1982) who state:

"In statistical methods the fields are considered as realizations of a two-dimensional random process and their optimality is generally conceived in terms of minimizing the estimation variances. On the otherhand, deterministic methods rely on arbitrary choices of surface types and optimality criteria."

### III.C.1. Inverse Distance Squared (IDS) Mapping Procedure

The simplest of the evaluated weighted mean approaches employed uses the inverse distance squared between the estimated point  $p^*$ , and each measured point  $p_i$ , as the weights in equation III.1. This commonly used weighting scheme is deterministic in that it relies on an arbitrary basis for weight determination. The IDS method is known to be biased when used with a non-uniform sampling grid (Ripley, 1981). Its principal advantage is calculational simplicity.

The IDS gridding was carried out using QGRID (Golden Software 1985) with a smoothing factor of 0.8, a search radius of 25 meters, and a grid density of 1 meter. In QGRID the smoothing factor is adjustable in the interval 0 (infinite smoothing) to 1 (no smoothing). The smoothing was implemented by adding to  $p^*-p_i$ , a length  $l_s$ , where the magnitude of  $l_s$  was determined by the value of the smoothing factor. The search radius is simply the maximum distance between  $p^*$  and any point  $p_i$  to be included in Equation III.1 for estimating  $z^*$ . Contouring of the IDS grid was done with TOPO (Golden Software 1985).

### III.C.2. Kriging - Isotropic Linear Variogram (KILV) Mapping Procedure

Kriging is a geostatistical technique for calculating the best linear unbiased estimates (BLUE) of spatial variables (e.g., see Ripley, 1980; Rendu, 1978; and Clark, 1979). It looks to find the set of  $w_i$  which minimizes the estimation variance  $E [(z^*(p_i) - z(p_i))^2]$  and satisfies the nonbias constraint  $E [z^*(p_i) - z(p_i)] = 0$ . Carrying out the minimization and incorporating the nonbias constraint  $w_i = 1$ , leads to the kriging system

$$\begin{aligned} \sum_{j=1}^n w_j y(p_i, p_j) + v &= y(p_i, p^*) \quad i=1, 2, \dots, n \quad (\text{III.4}) \\ \sum_{j=1}^n w_j &= 1 \quad j = 1 \end{aligned}$$

where  $v$  is a Lagrange multiplier and  $y(p_i, p_j)$  is the variogram and is defined as

$$\gamma(p_i, p_j) = 1/2 E [(z_i - z_j)^2] \quad (\text{III.5})$$

The variogram  $\gamma$  is estimated from the measured values by invoking the 'intrinsic hypothesis' which requires a constant mean and

$$\gamma(p_i, p_j) = \gamma(p_i - p_j) \quad (\text{III.6})$$

Equation III.6 states that the variogram depends only on separation distance and is independent of location. To calculate the empirical



variogram, Equation III.5 is applied to the data points and the results plotted against separation distance. Next, a functional form of  $\gamma$  is chosen from a small number of commonly used variogram functions by inspection of the variogram plot. The parameters of the chosen variogram function are then determined by a least-squares fit with the empirical variogram. A significant advantage of kriging is that it provides error estimates for the gridded data.

The KILV gridding was carried out using QGRID (Golden Software, 1985) with no smoothing (i.e. no "nugget" effect), a search radius of 25 meters, and a grid density of 1 meter. The QGRID-KILV approach was deterministic in that it arbitrarily assumed an isotropic linear functional form for the variogram. This assumption had the advantage of providing a kriging solution that was independent of the variogram slope. However, since the variogram form was assumed and not derived from the data, calculation of error estimates was not justified. Contouring of the KILV grid was done with TOPO (Golden Software, 1985).

### III.C.3. Kriging - Anisotropic Linear Variogram (KALV) Mapping Procedure

Figure III.1 shows the two empirical variograms for the complete data set. The upper variogram was calculated parallel with the direction of travel while the lower variogram was calculated along the horizontal orthogonal direction. The anisotropic nature of the plume shape resulted in the different slopes associated with each direction. For kriging, the empirical variograms were fit to the analytical

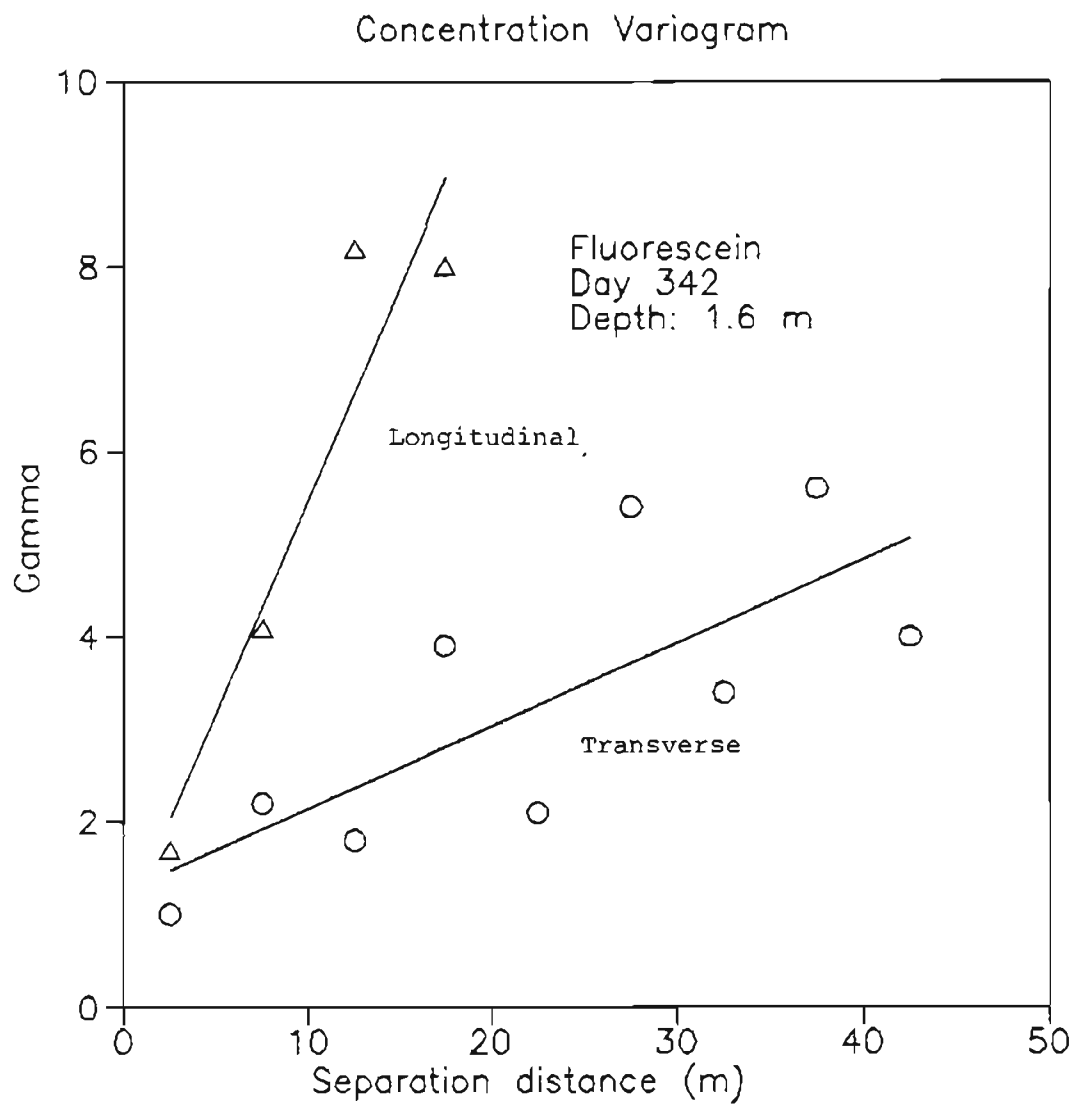


Figure III.C.1 Longitudinal and transverse linear variograms calculated on the basis of the complete data set.

anisotropic linear variogram model:

$$\gamma(h) = C_0 + m_x (x_1 - x_2)^2 + \{m_x m_y^{-1} (y_1 - y_2)\}^2 \quad (\text{III.7})$$

where  $C_0$  = is the "nugget" effect defined as the y-intercept

$m_x$  = slope of the x-direction variogram, and

$m_y$  = slope of the y-direction variogram.

Equation III.7 explicitly incorporates the directional dependency of interpoint correlation.

The KALV gridding and error estimation were carried out with a modified version of KGRID (Barnes, 1985) with  $m_x = 0.1$ ,  $m_y = 0.33$ , and  $C_0 = 1.5$ . This was the only purely statistical gridding approach evaluated. Contouring of the KALV grid was done with TOPO (Golden Software, 1985).

#### III.C.4. Nonparametric Geostatistical Gridding (NGG) Mapping Procedure

The use of nonparametric statistics as a basis for gridding has been advanced (Henley, 1981). The method used for this comparison is nonparametric in that it 1) relies on a weighted median (Equation III.2), and 2) calculates part of the weights (Equation III.3) based on the distribution-free Kolmogorov-Smirnov one sample distribution test.

The mathematical details of the approach can be found in Henley (1985). Briefly, an anti-clustering weight is estimated for each sample point using the Kolmogorov-Smirnov test. This weight is then multiplied by the IDS weight to form the weights in Equation III.3. The only assumption required by the method is the use of the IDS weights and the only adjustable parameter is the search radius. Since the weights used are partially deterministic and partially statistical, the NGG method must be classified as a statistical-deterministic approach.

The NGG gridding was carried out using NPK (Appendix A), with a search radius of 25 meters and a grid density of 1 meter. Contouring of the NGG grid was done with TOPO (Golden Software, 1985).

#### III.C.5. Triangular Mesh Weights (TMW) Mapping Procedure

The commercial contouring package TRIMAP (Contoursoft, 1985) was evaluated. This package generates a triangular mesh between the data points. Using a proprietary algorithm, the weights required by Equation III.1 are estimated based on relative areas and intercenter distances of neighboring triangles. This package directly contours the data and does not make available a regular grid of points. Because of this, many of the evaluation criteria could not be applied to maps generated with TRIMAP.

### III.D. Results and Discussion

The contour plots produced by each method for the complete data set, the perturbed data set, and the reduced data set are shown in Figures III.2 - III.7. Examination of these figures reveals some interesting comparisons. The differences in the three plots for each method were relatively small, indicating that none of the methods were unduly influenced by either the absence of a few data points or measurement error. The inter-method variability was greater, with the KILV, KALV, and TMW approaches appearing to converge on a very similar shape, while the NGG- and IDS-derived maps exhibited successively greater differences.

Before discussing the comparison criteria results, a qualifying statement is necessary. An attempt was made to apply each of the methods in an optimal manner. However, there were subjective choices required by each method and their influences on the results are not easily resolved. Therefore, the conclusions which were reached from comparing the different methods, in part, may be somewhat subjective.

The precision of the methods with respect to honoring the measured values is indicated by the correlation coefficient, mean squared deviation and mean absolute deviation between the measured, and the predicted values at the sample locations (Table III.C.1). For these calculations, the predicted value at a sample point was estimated as

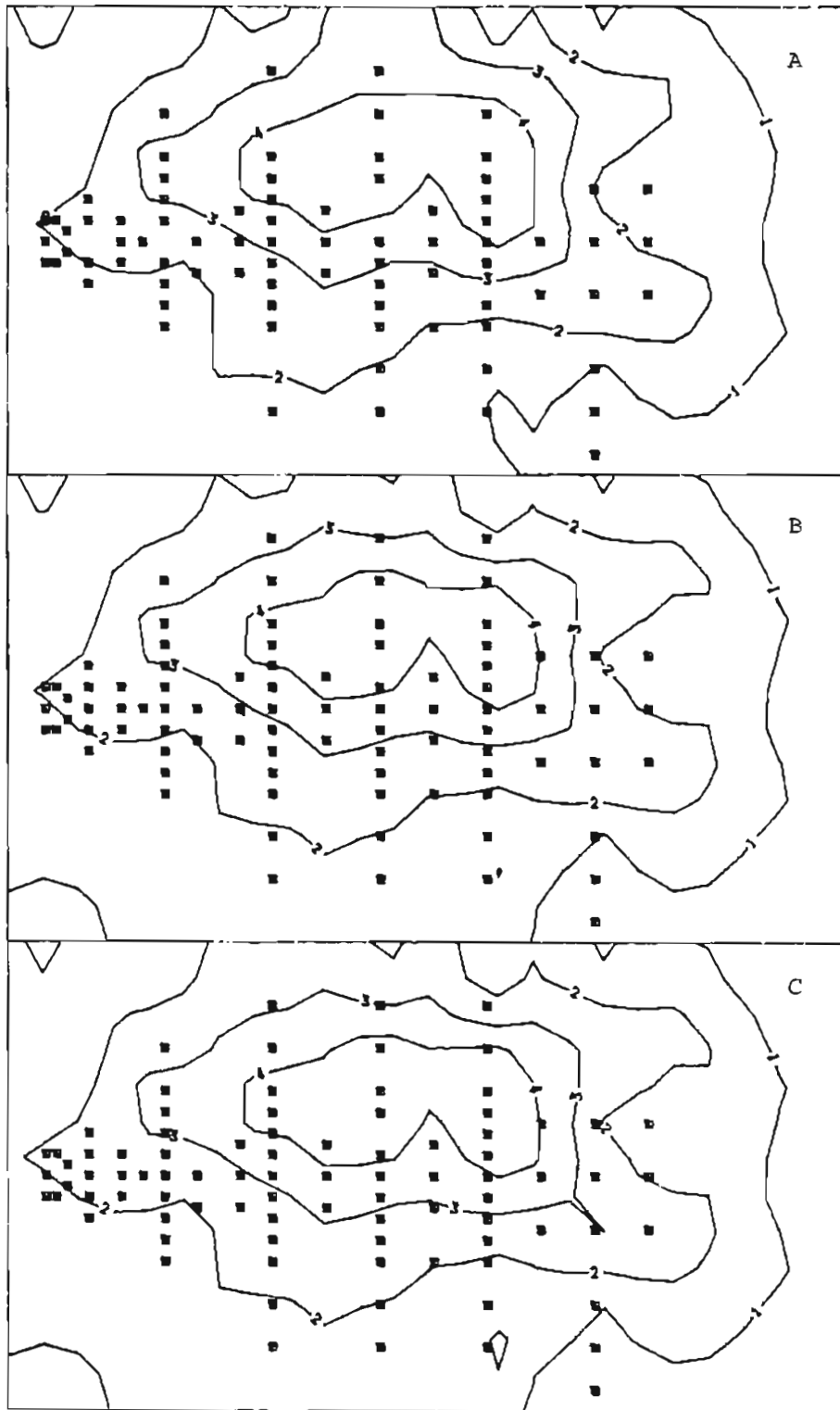


Figure III.C.2 Concentration contour maps produced by the IDS method for the A) complete data set, B) perturbed data set and C) reduced data set.

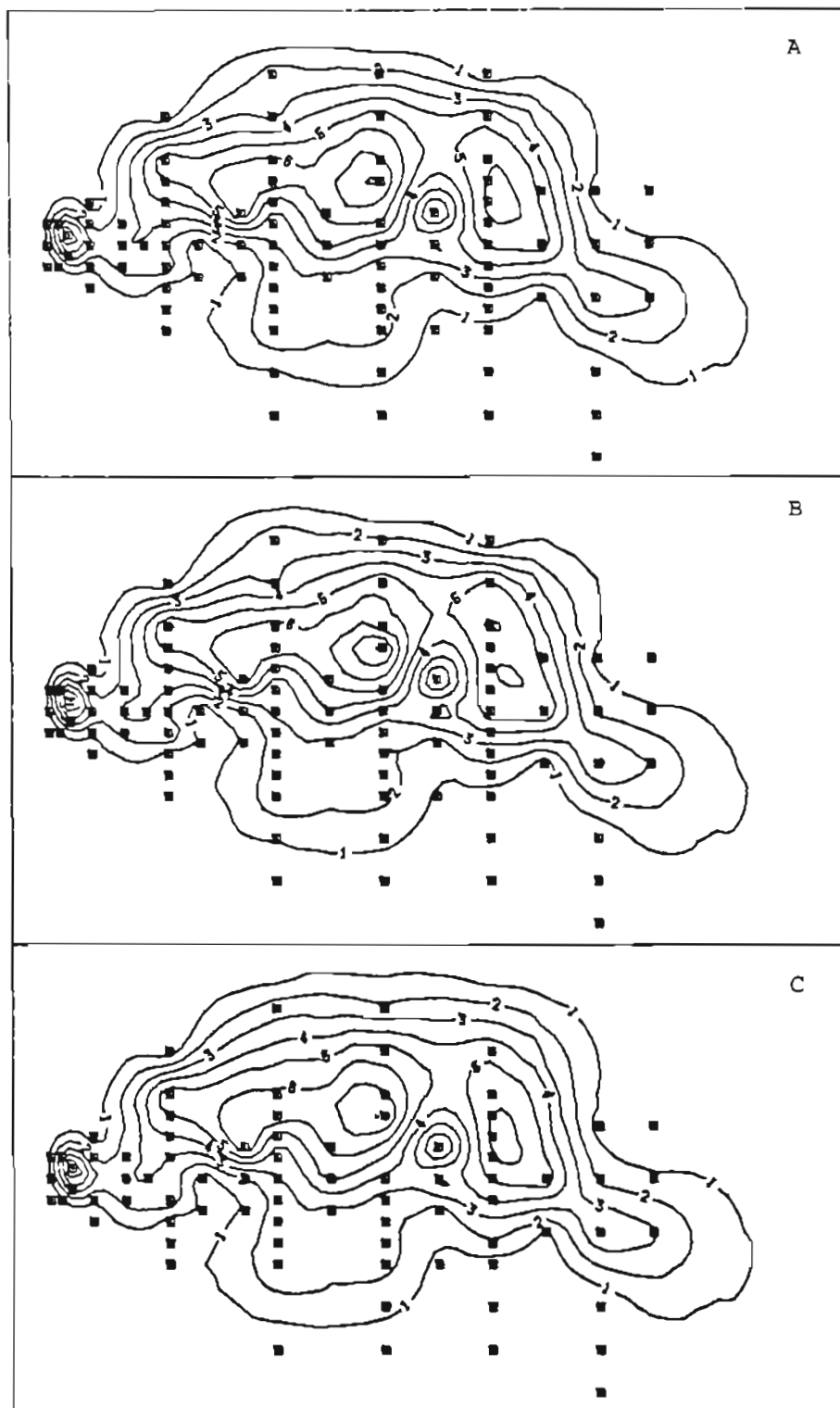


Figure III.C.3 Concentration contour maps produced by the KILV method for the A) complete data set, B) perturbed data set and C) reduced data set.

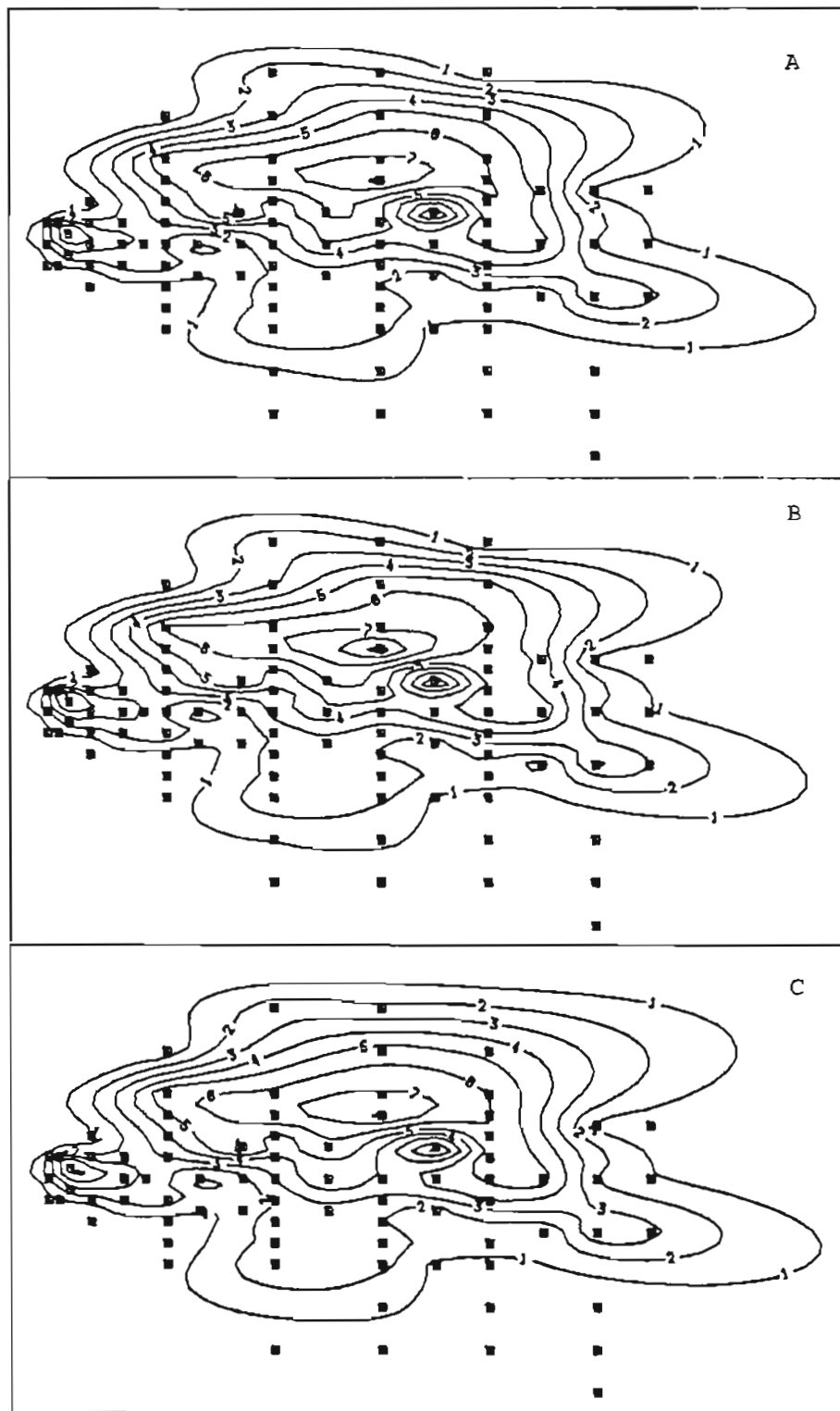


Figure III.C.4 Concentration contour maps produced by the KALV method for the A) complete data set, B) perturbed data set and C) reduced data set.



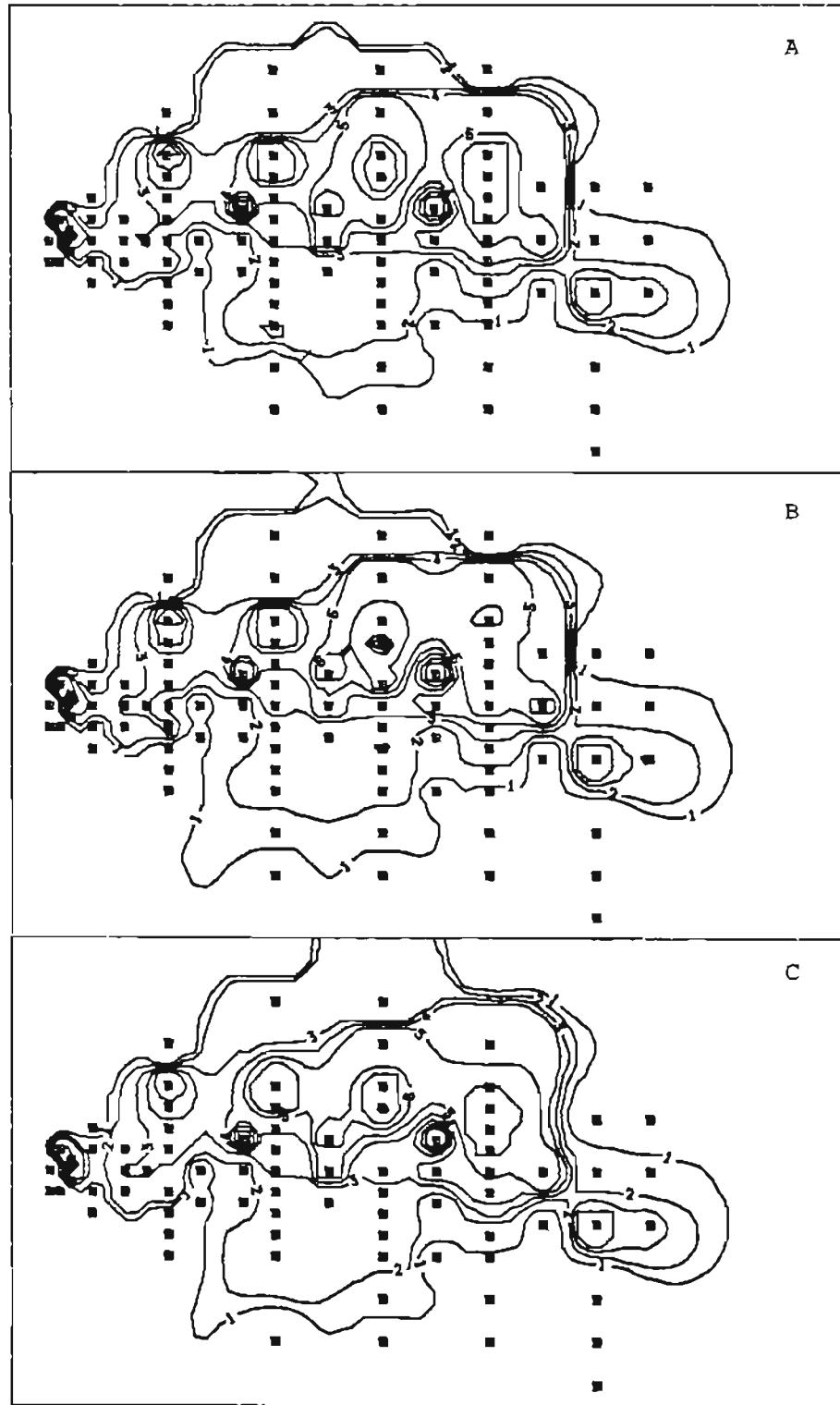


Figure III.C.5 Concentration contour maps produced by the NPK method for the A) complete data set, B) perturbed data set and C) reduced data set.

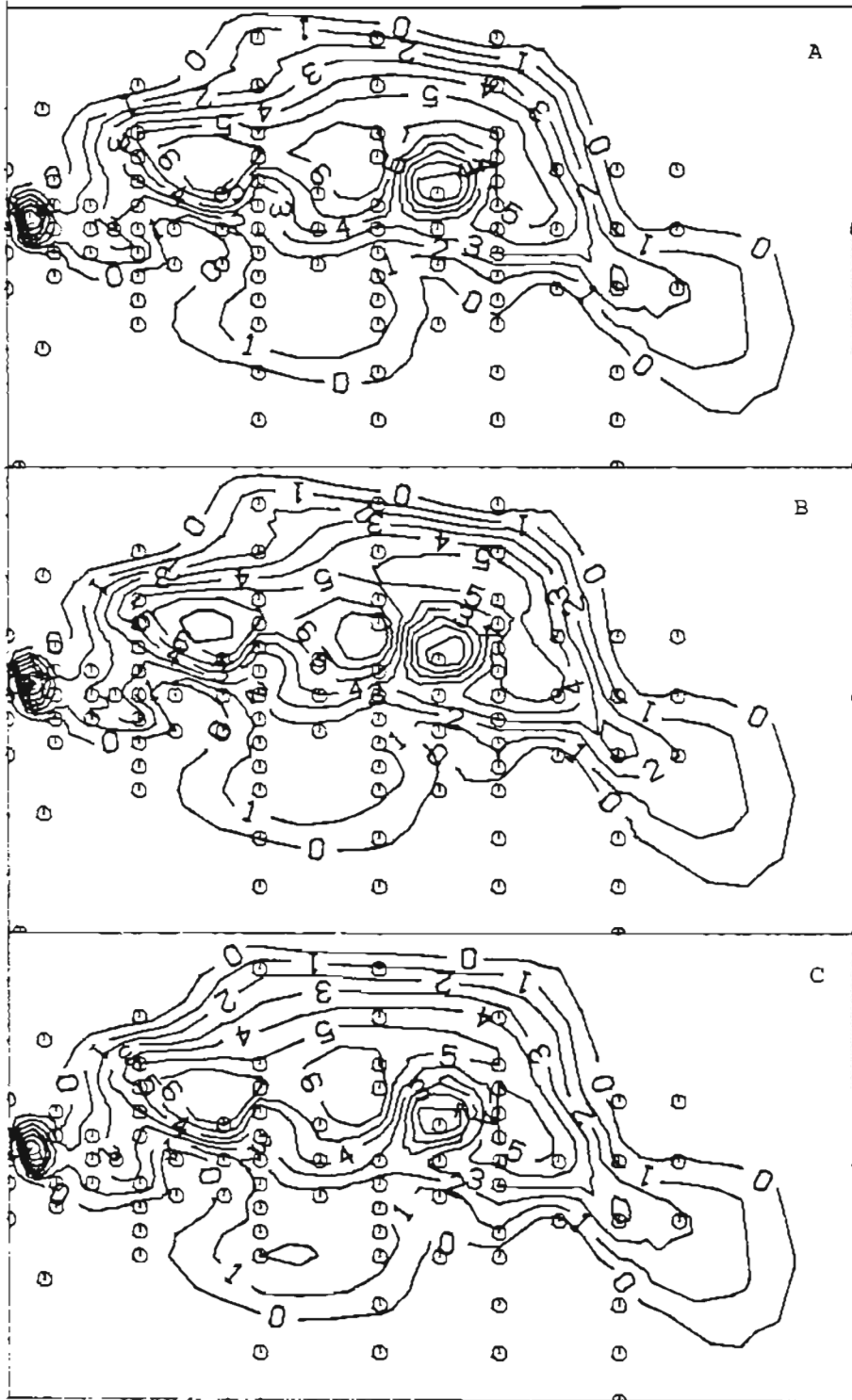


Figure III.C.6 Concentration contour maps produced by the TMW method for the A) complete data set, B) perturbed data set and C) reduced data set.

TABLE III.C.1 Inter-method comparison of the gridding methods with respect to honoring the measured values

Method	r	$E\{(z^* - z)^2\}$ (ppb <sup>2</sup> )	$E\{(z^* - z)\}$ (ppb)	$E[ABS(z^* - z)]$ (ppb)	Execution Time(hrs) <sup>a</sup>
IDS	.89	1.7	0.11	1.1	0.2
KILV	.99	0.1	-0.04	0.2	0.3
KALV	.98	0.2	0.004	0.3	7.
NPK	1.0	0.0005	-0.005	0.01	0.5
TMW	NA	NA	NA	NA	0.5

a) Tested with a PC "Clone" with a 4.77 MHz 8088 CPU and 8087 NPU

the predicted value of the grid node closest to the sample point. With the exception of IDS, the remaining methods reproduced the original points with adequate precision. In contrast, the IDS approach reproduced the measured values with considerably less precision. The bias of the mapping approaches with respect to honoring the data points is indicated by the mean deviation. The mean deviation for each method (Table III.C.1) suggests that all of the methods are reasonably unbiased in this respect.

The results of the validation criteria which test the predictive ability of the methods are contained in Table III.C.2. The numbers used for calculating the values related to the TMW method were taken from Figure III.6.c. The results in Table III.C.2 are critical because prediction of the plume concentration at an unmeasured point is the most important function of a gridding algorithm. The predictive precision, as indicated by the correlation coefficient, mean square deviation, and mean absolute deviation, showed considerable inter-method variability. The KILV, KALV, and TMW methods predicted the excluded sample values more precisely than the IDS and NGG methods. The bias in prediction of the excluded points followed a different pattern. With regard to prediction bias, the KALV and IDS methods were respectively the best and worst performers, while the KILV, NGG, and TMW approaches evidenced an intermediate level of bias.

TABLE III.C.2 Inter-method comparison of the gridding methods with respect to predicting the removed values using the reduced data set

Method	$r$	$E\{(z^* - z)^2\}$ (ppb <sup>2</sup> )	$E\{(z^* - z)\}$ (ppb)	$E\{ABS(z^* - z)\}$ (ppb)
IDS	.47	3.6	.8	1.6
KILV	.86	1.2	.4	.8
KALV	.82	1.3	.1	.8
NPK	.43	3.8	.6	1.4
TMW	.95	.8	.5	.7

The center of mass is defined as the intersection of the lines parallel to the x and y axes which bisect the plume mass. To perform the necessary calculations, the value of a grid node is taken as the estimate of the plume concentration for the square area around the node equal to the grid block size. The required integrations are then approximated by

$$\sum_{x_{\min}}^{x_c} \sum_{y_{\min}}^{y_{\max}} z^*(x,y) = 0.5 \sum_{x_{\min}}^{x_{\max}} \sum_{y_{\min}}^{y_{\max}} z^*(x,y) \quad (\text{III.8})$$

where  $x_c$  is the x coordinate of the center of mass. The y coordinate is calculated by simply reversing the summation parameters in Equation III.8 appropriately. The mass balance calculations are carried out using

$$\text{mass} = nbl^2 \sum_{x_{\min}}^{x_{\max}} \sum_{y_{\min}}^{y_{\max}} z^*(x,y) \quad (\text{III.9})$$

where  $n$  is the bulk porosity,  $b$  is the plume thickness and  $l^2$  is the area of a grid block. Although it is possible to estimate the center of mass and mass balance by methods which are independent of the gridded data, the use of Equations III.8 and III.9 provide internal consistency between the contour plots and the estimated plume parameters.

Tables III.C.3 and III.C.4 contain the center of mass and mass balance estimates for the different methods using each of the data

TABLE III.C.3 Inter-method and inter-data set comparison of center of mass calculations. Values given are x, y coordinates in meters.

Method	Complete Data Set	Perturbed Data Set	Reduced Data Set
IDS	29,3	28,2	29,3
KILV	28,3	28,3	28,3
KALV	29,4	29,4	30,4
NPK	28,3	29,3	28,4
TMW	NA	NA	NA

TABLE III.C.4 Inter-method and inter-data set comparison of mass balance calculations. Values given are percent of injected fluorescein mass.

Method	Complete Data Set	Perturbed Data Set	Reduced Data Set
IDS	120	127	123
KILV	78	80	81
KALV	84	87	88
NPK	80	83	86
TMW	NA	NA	NA



sets. The tables suggest that all the methods provide gridded data which are stable with respect to measurement error and the influence of a small number of observations. Inter-method comparisons indicate good agreement among the methods on the center of mass predictions. In contrast, the mass balance comparisons show IDS predicted mass as approximately 40% higher than the other methods. Finally, it should be noted that KALV is the only method which provided an estimate of the mass balance error. However, the utility of the error estimate is questionable since the mass balance error is dominated by uncertainty in the porosity and tracer plume thickness.

The computer times required to generate a single set of gridded data by each method are shown in Table III.C.1. The execution times are comparable with the exception of the amount of time needed to complete the KALV approach (7 hours).

### III.E. Conclusions

Six gridding algorithms were evaluated with respect to the mapping of a groundwater solute plume. Two of the methods produced unsatisfactory gridded data and were eliminated as possible methods for this study. The IDS method was eliminated because it did not adequately reproduce the measured values and exhibited poor precision and high bias in predicting values of points which were known but

excluded from the prediction process. In addition, The IDS method provided a mass balance estimate approximately 40% greater than the other approaches. This indicates the dependence of plume parameters on the selection of a gridding method and the potential for influence on subsequent tracer test interpretation. The NGG approach was eliminated as a possible gridding method for this study due to its poor performance in predicting the removed observations. The TMW method produced acceptable predictions for the removed observations, but also was eliminated since it did not provide a regular grid of data and my reluctance to base the tracer test interpretation on contours generated by an unknown algorithm.

The remaining two methods honored the observations and provided similar plume parameter estimates as well as reasonable predictions for the removed sample points. The KALV method had the lowest bias estimates and was the only method which provided error estimates. The disadvantages of this method included computational burden (7 hours per run) and considerable subjectivity in choosing an appropriate functional form for the variogram. The KILV approach performed similarly to KALV, and had the advantages of fast execution time and more objective operation. Based on these comparisons, the decision was made for this study to use the KALV method to map the tracer plume once the plume was large enough to be found at enough monitoring wells to justify the variogram fitting procedure. For times when the plume covered a smaller area, the KILV procedure was used.

The evaluation reported in this chapter suggests a procedure for objectively calibrating any of the gridding methods. The parameters required for a method (e.g. variogram slope) can be adjusted to minimize the bias and variability in predicting a subset of observations which are not used in the prediction process. The set of parameters which provide the minimization can then be used with the complete data set to estimate the values for the regular grid.

#### IV. DESCRIPTION OF TRACER MIGRATION PATTERNS

The two large scale natural-gradient tracer tests were carried out in close proximity to each other (injection points separated by approximately 10 m) and underwent 6 rounds of sampling during a 419 day period and 5 rounds of sampling during a 178 day period, respectively. The two plumes evidenced many interesting similarities and some remarkable differences. The similarities included: 1) the plumes moved initially at an angle of  $30^{\circ}$  to the large-scale hydraulic gradient; 2) at the completion of sampling, the plumes evolved into smooth shapes in all three dimensions with directions of travel approximately parallel to the large-scale gradient; 3) the centers of mass migrated at steadily decreasing velocities; 4) the plumes were strongly dispersed with a ratio of longitudinal to horizontal transverse dispersion of approximately six; 5) at the completion of sampling, the peak concentrations exhibited by the plumes were over three orders of magnitude lower than the injected concentrations; and 6) while the tracers were injected over very short time intervals ( $<0.5$  hr), instead of operating as pulse type sources, they appeared to behave as exponentially decaying source functions. The most striking differences between the plumes were: 1) the approximately  $60^{\circ}$  angle between their initial directions of travel; and 2) the 2-3 times lower migration velocity of the second plume compared to the first plume.

#### IV.A. Tracer Concentration Contour Maps

The concentration contour plots for the three discrete sampling depths and the six sampling rounds of tracer test #1 are presented in Figures IV.A.1-IV.A.18. The vertically averaged contour plots for tracer test #1 are shown in Figures IV.A.19-IV.A.24. The contour maps for the 1.8 m sampling depth used for tracer test #2 are given in Figures IV.A.25-IV.A.29. The contour plots were constructed using the measured tracer concentration values to estimate the tracer concentration at the nodes of a regular grid covering the test region and then contouring the values from the grid using the program TOPO (Golden Software, 1985). The gridding was performed using the KILV procedure (see section III.C.2) for Figures IV.A.1-IV.A.12, IV.A.19-IV.A.22, and IV.A.25-IV.A.29 and the KALV procedure (see section III.C.3) for Figures IV.A.13-IV.A.18, IV.A.23, and IV.A.24. The gridded data was stored for use in estimating the center of mass, total mass and variance of the tracer plumes.

Examination of Figures IV.A.1-IV.A.18 reveals that for the first 50 days of test #1, the fluorescein moved rapidly through a narrow strip at an angle of approximately  $30^{\circ}$  to the central axis of the monitoring network. From day 50 through day 123, the migration appears to have continued at an elevated velocity, however the direction of travel became approximately parallel with the network axis. From day 123 through day 419, the plume movement progressed at a reduced velocity but continued in line with the network axis. The contour maps

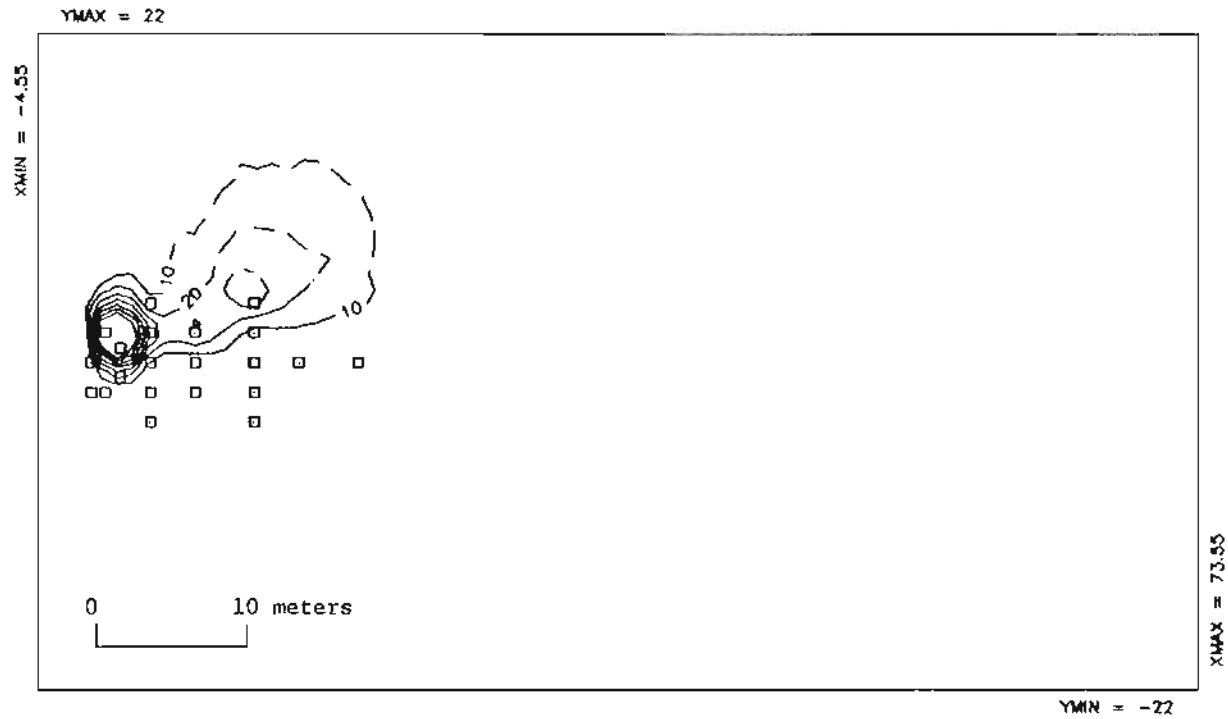


Figure IV.A.1 Contour map of fluorescein concentration measured on day 50 of tracer test #1 at the 1.8 m sampling depth.

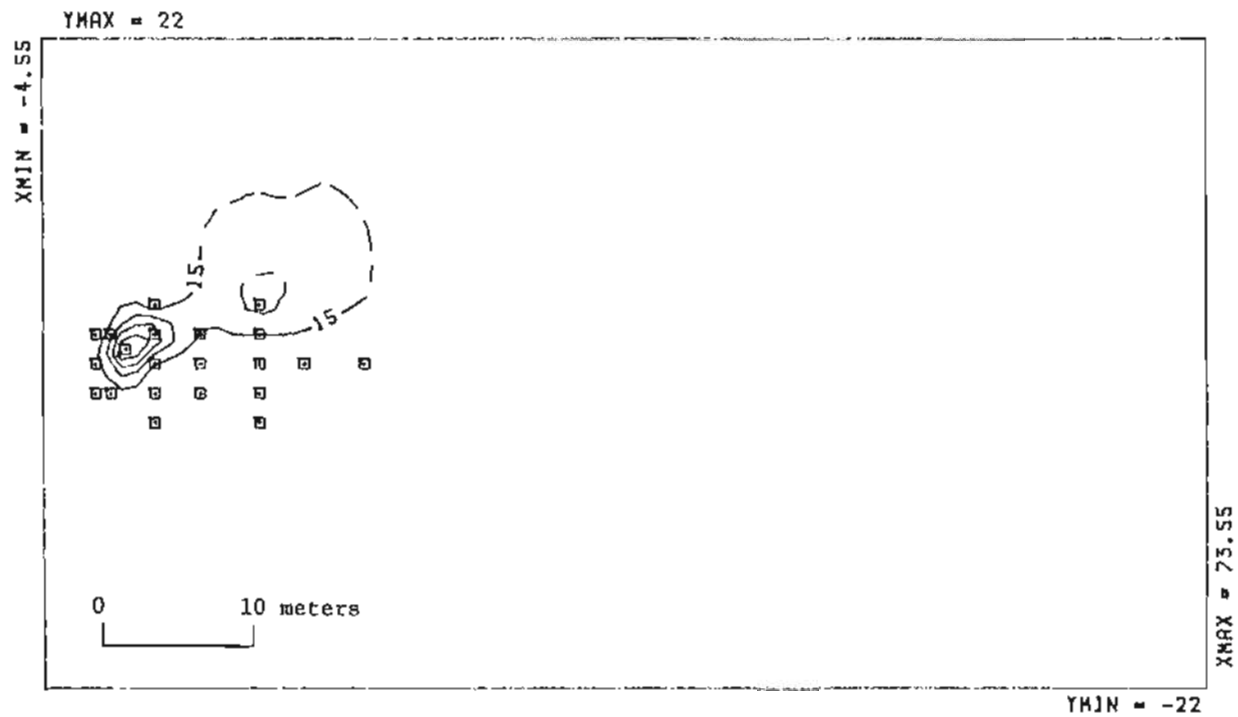


Figure IV.A.2 Contour map of fluorescein concentration measured on day 50 of tracer test #1 at the 2.4 m sampling depth.

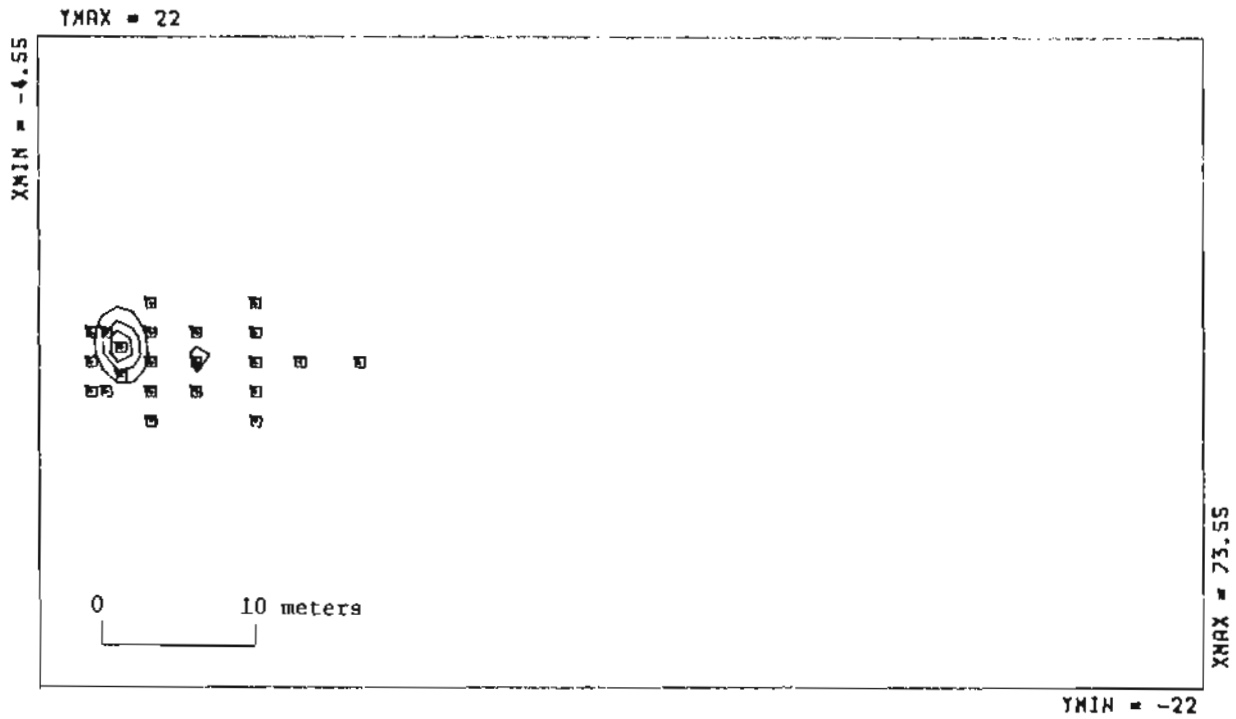


Figure IV.A.3 Contour map of fluorescein concentration measured on day 50 of tracer test #1 at the 3.0 m sampling depth.



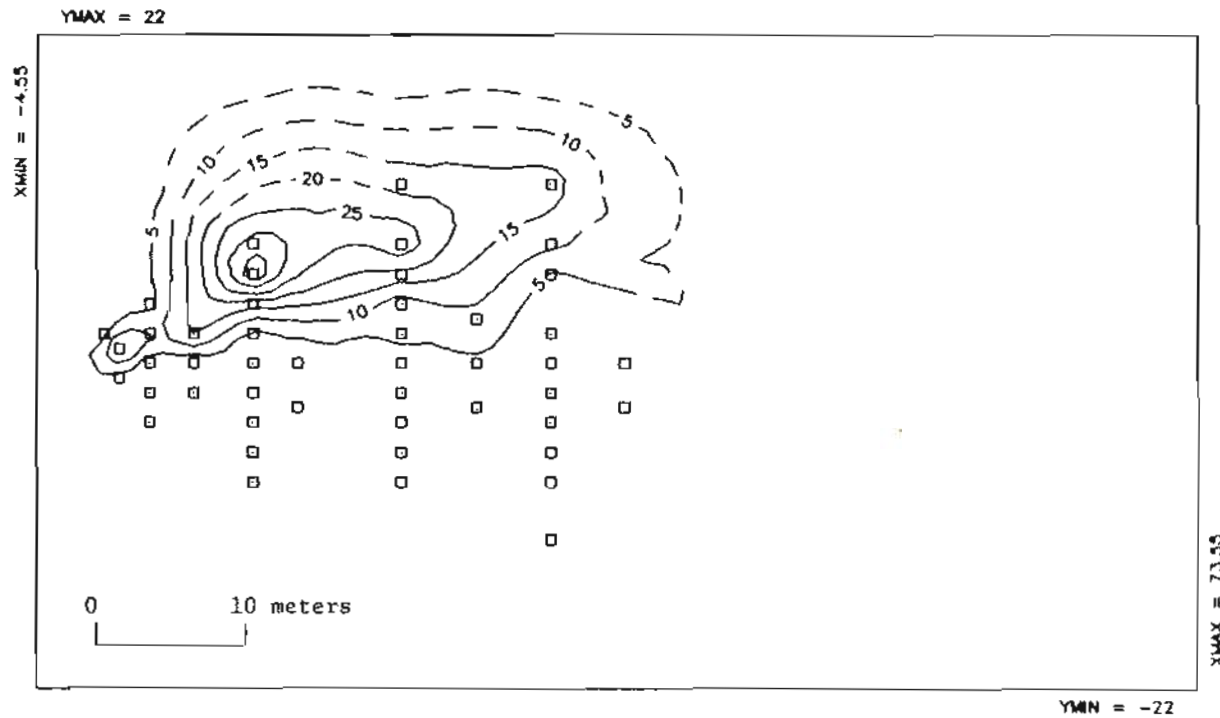


Figure IV.A.4 Contour map of fluorescein concentration measured on day 93 of tracer test #1 at the 1.8 m sampling depth.

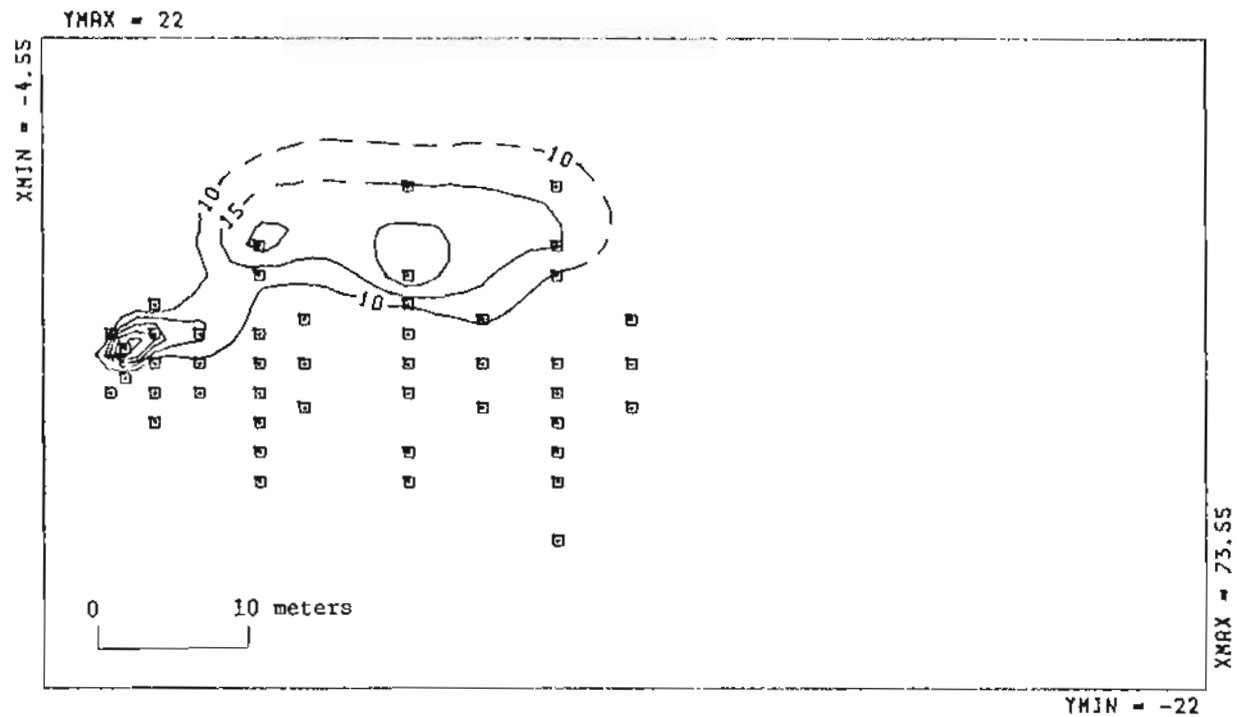


Figure IV.A.5 Contour map of fluorescein concentration measured on day 93 of tracer test #1 at the 2.4 m sampling depth.

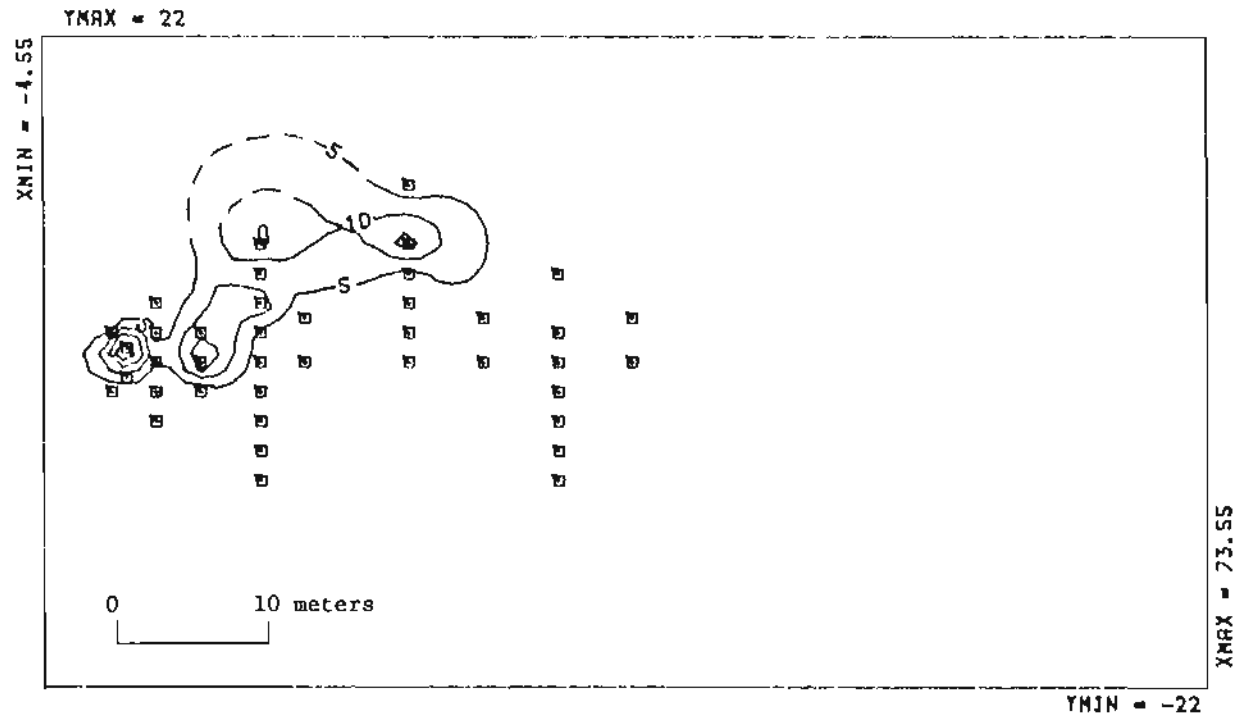


Figure IV.A.6 Contour map of fluorescein concentration measured on day 93 of tracer test #1 at the 3.0 m sampling depth.

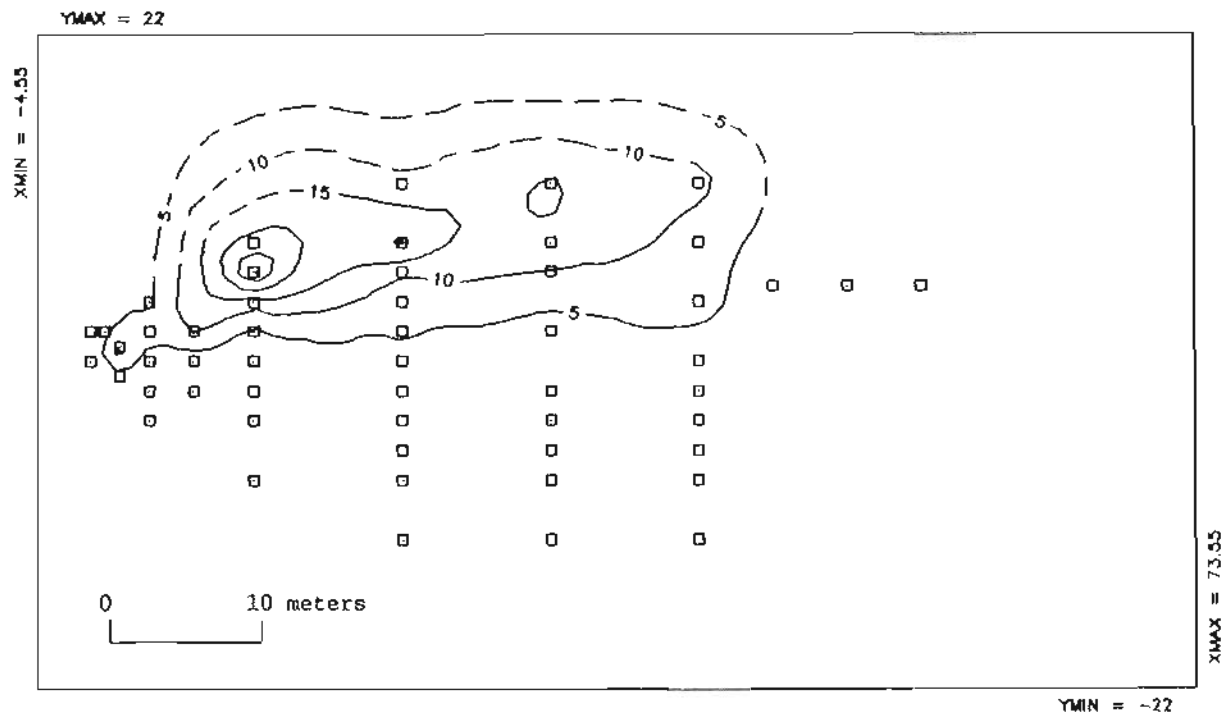


Figure IV.A.7 Contour map of fluorescein concentration measured on day 123 of tracer test #1 at the 1.8 m sampling depth.

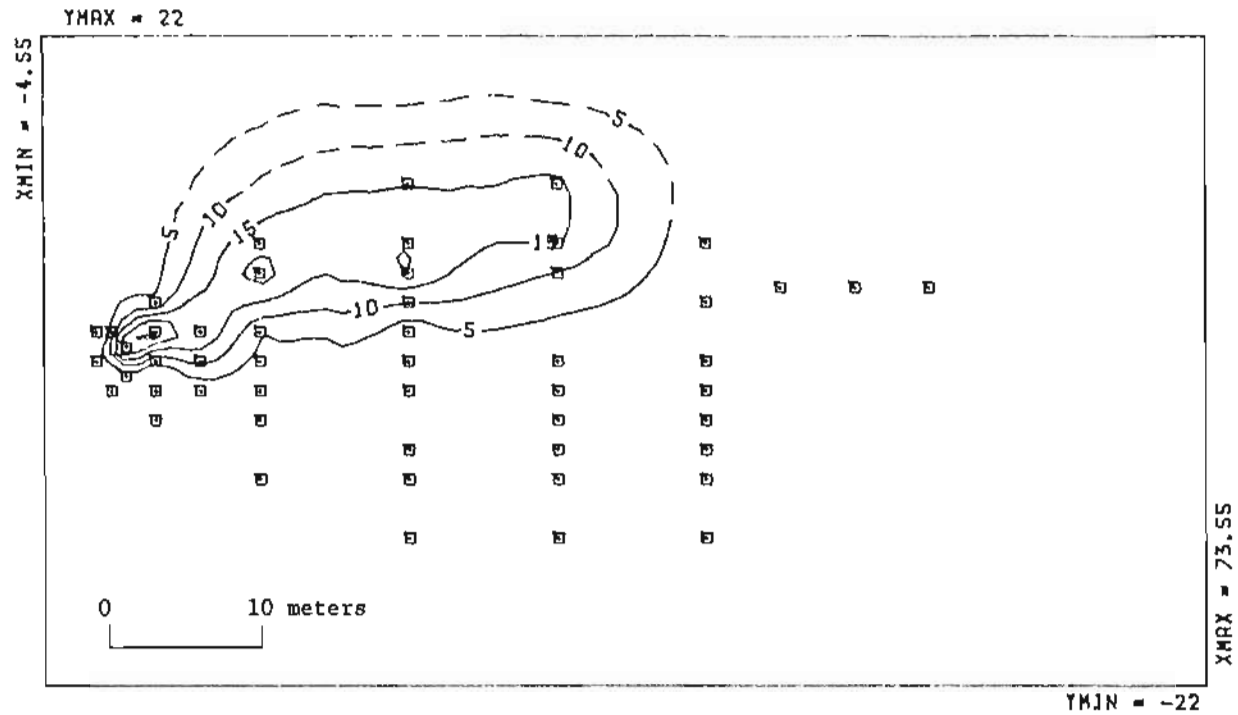


Figure IV.A.8 Contour map of fluorescein concentration measured on day 123 of tracer test #1 at the 2.4 m sampling depth.

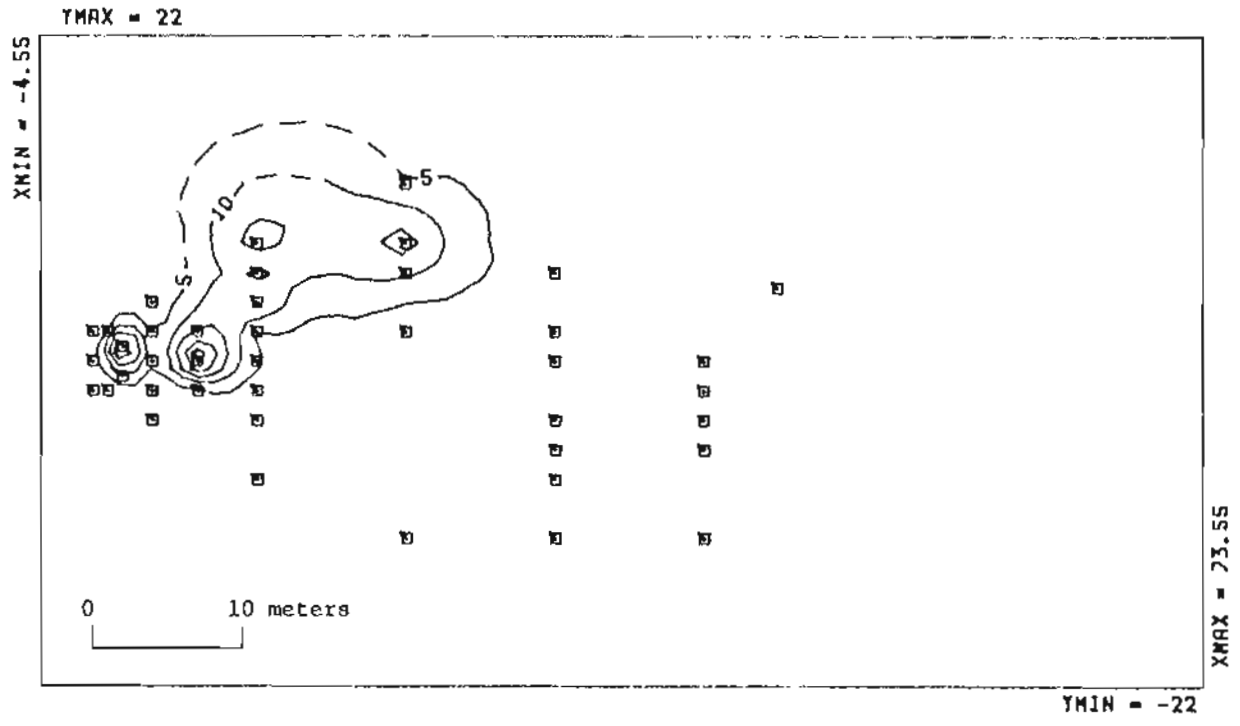


Figure IV.A.9 Contour map of fluorescein concentration measured on day 123 of tracer test #1 at the 3.0 m sampling depth.

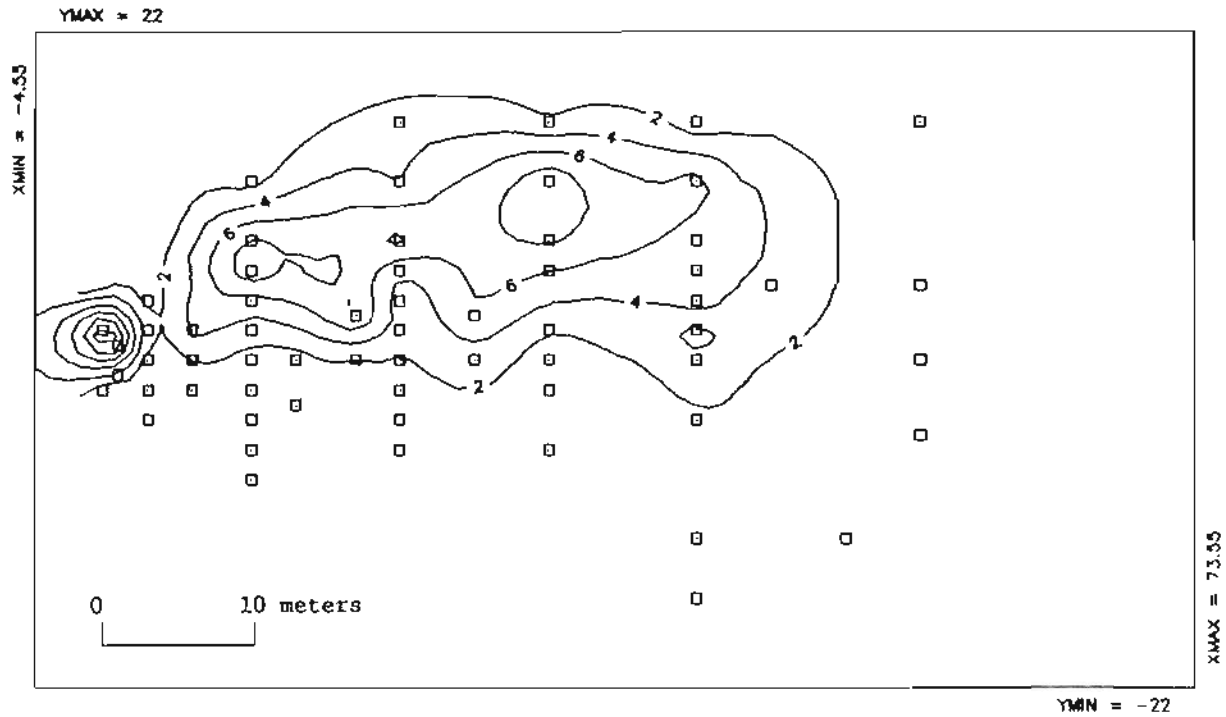


Figure IV.A.10 Contour map of fluorescein concentration measured on day 232 of tracer test #1 at the 1.8 m sampling depth.

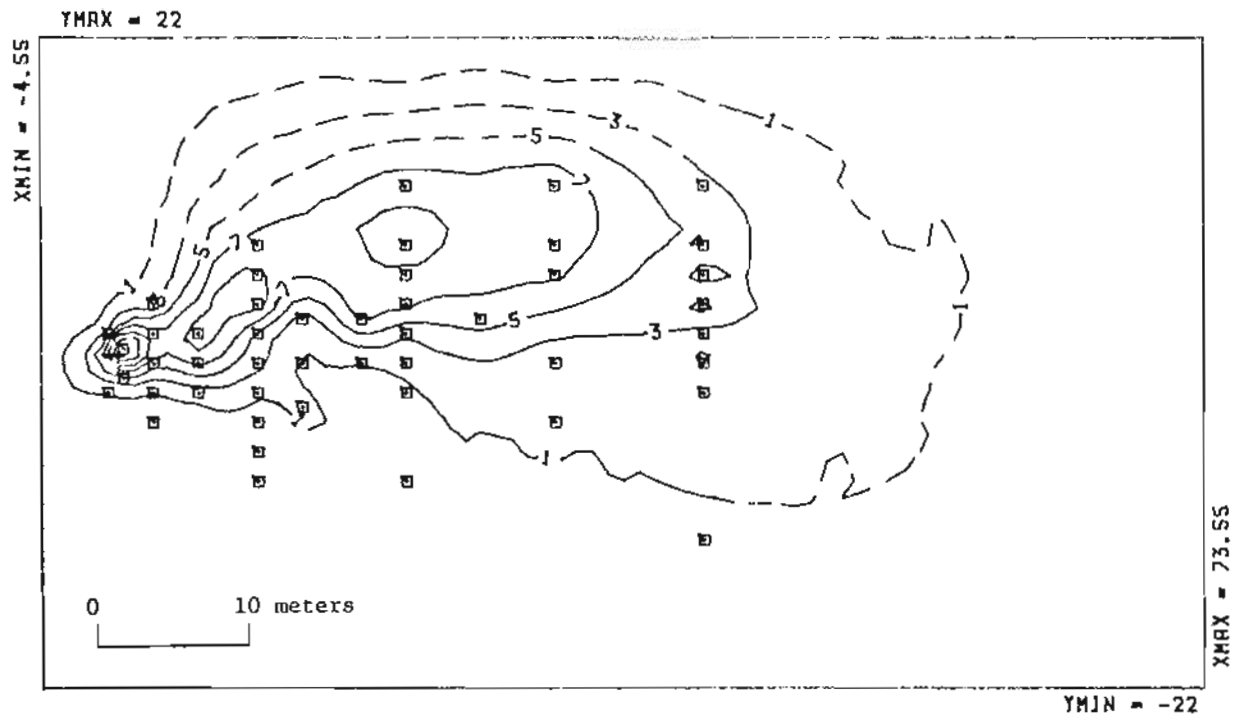


Figure IV.A.11 Contour map of fluorescein concentration measured on day 232 of tracer test #1 at the 2.4 m sampling depth.



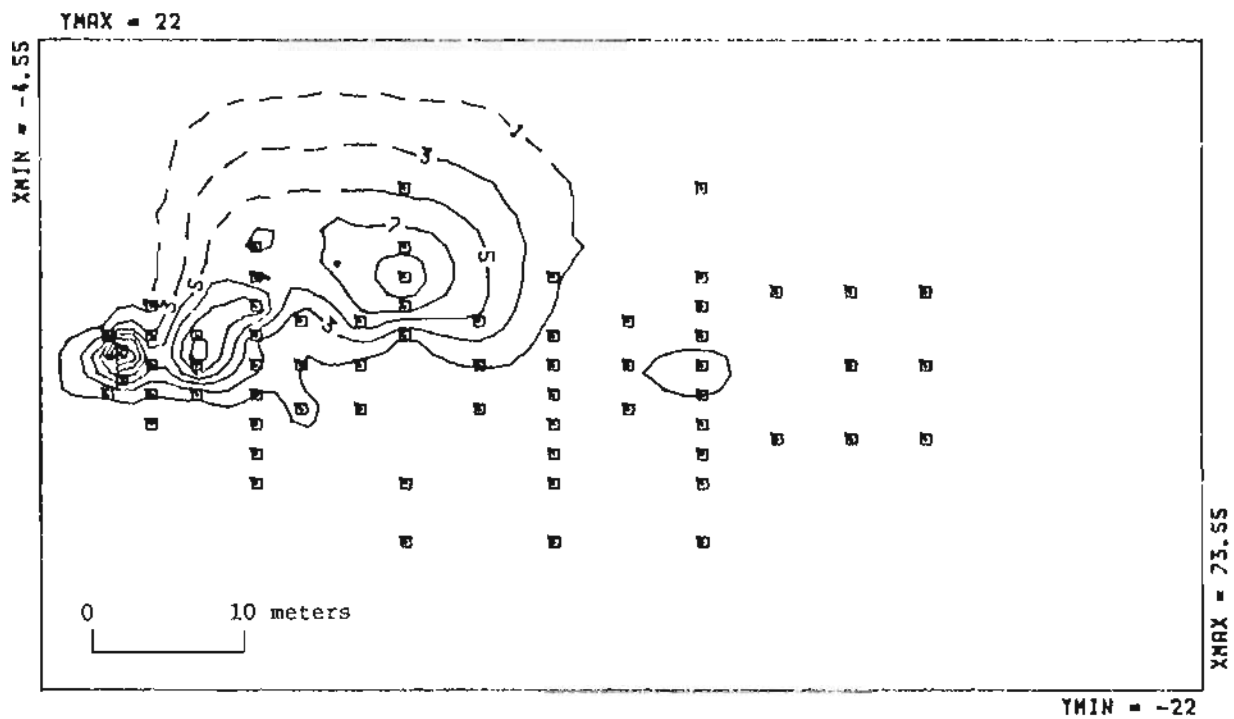


Figure IV.A.12 Contour map of fluorescein concentration measured on day 232 of tracer test #1 at the 3.0 m sampling depth.

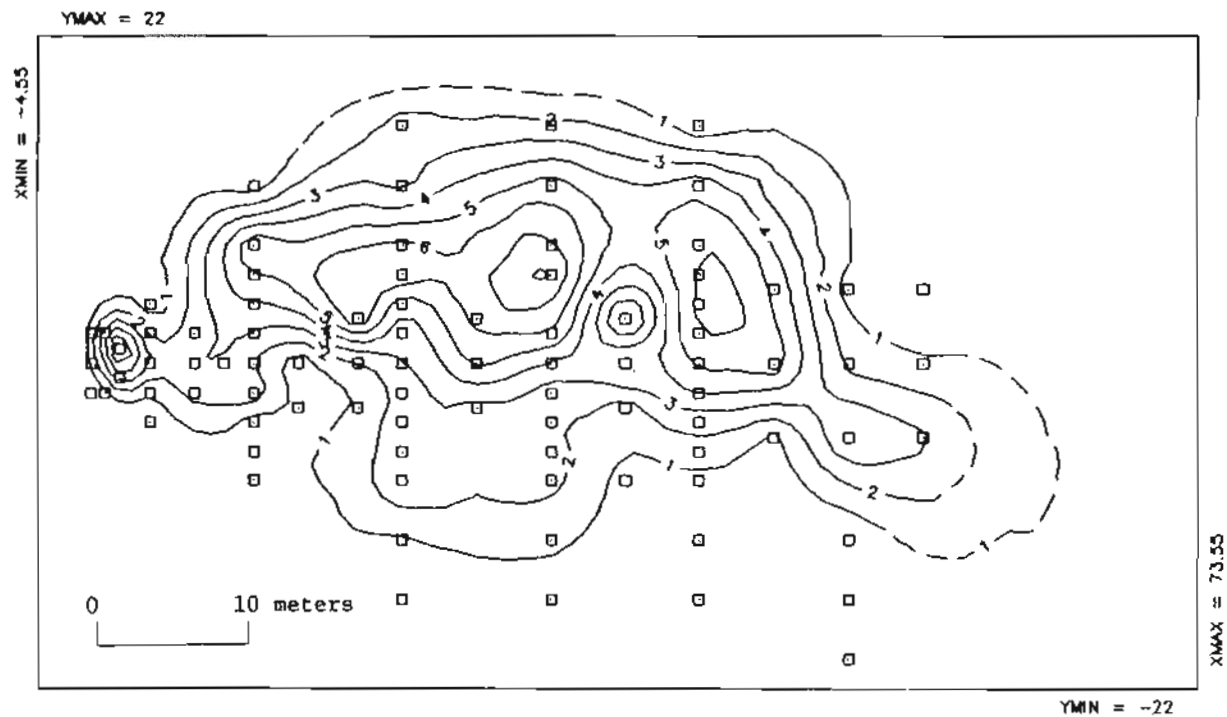


Figure IV.A.13 Contour map of fluorescein concentration measured on day 342 of tracer test #1 at the 1.8 m sampling depth.

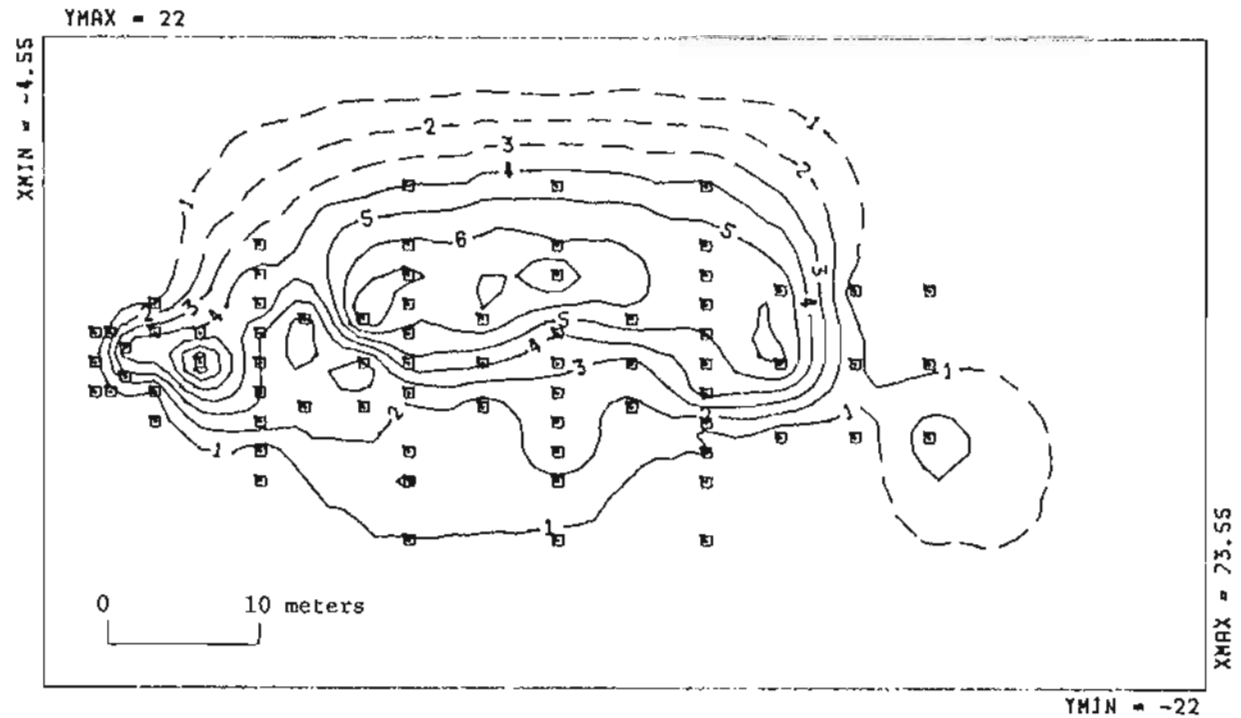


Figure IV.A.14 Contour map of fluorescein concentration measured on day 342 of tracer test #1 at the 2.4 m sampling depth.

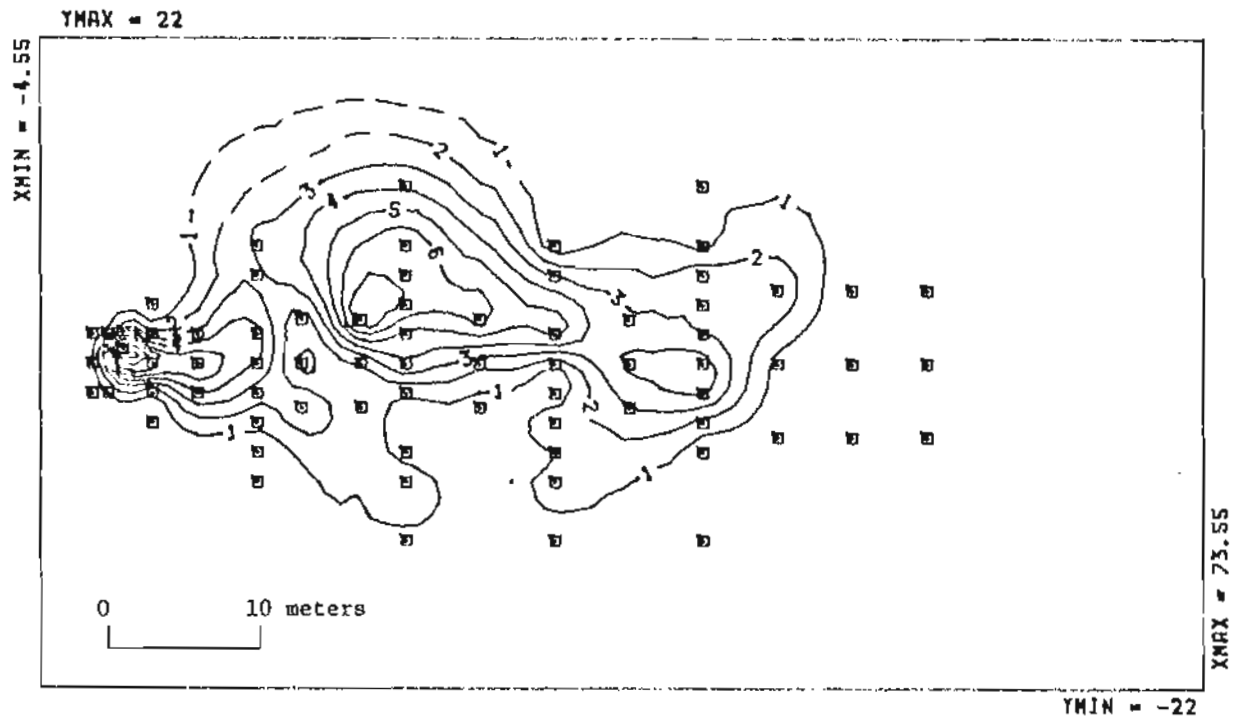


Figure IV.A.15 Contour map of fluorescein concentration measured on day 342 of tracer test #1 at the 3.0 m sampling depth.

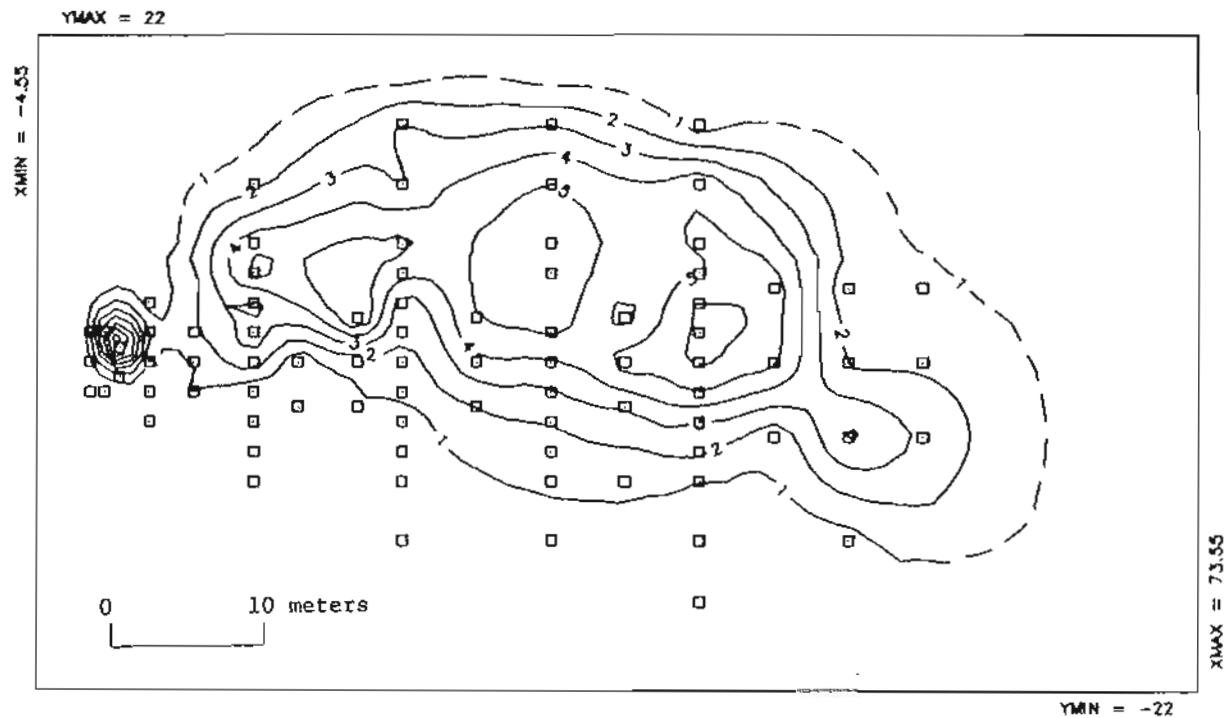


Figure IV.A.16 Contour map of fluorescein concentration measured on day 419 of tracer test #1 at the 1.8 m sampling depth.

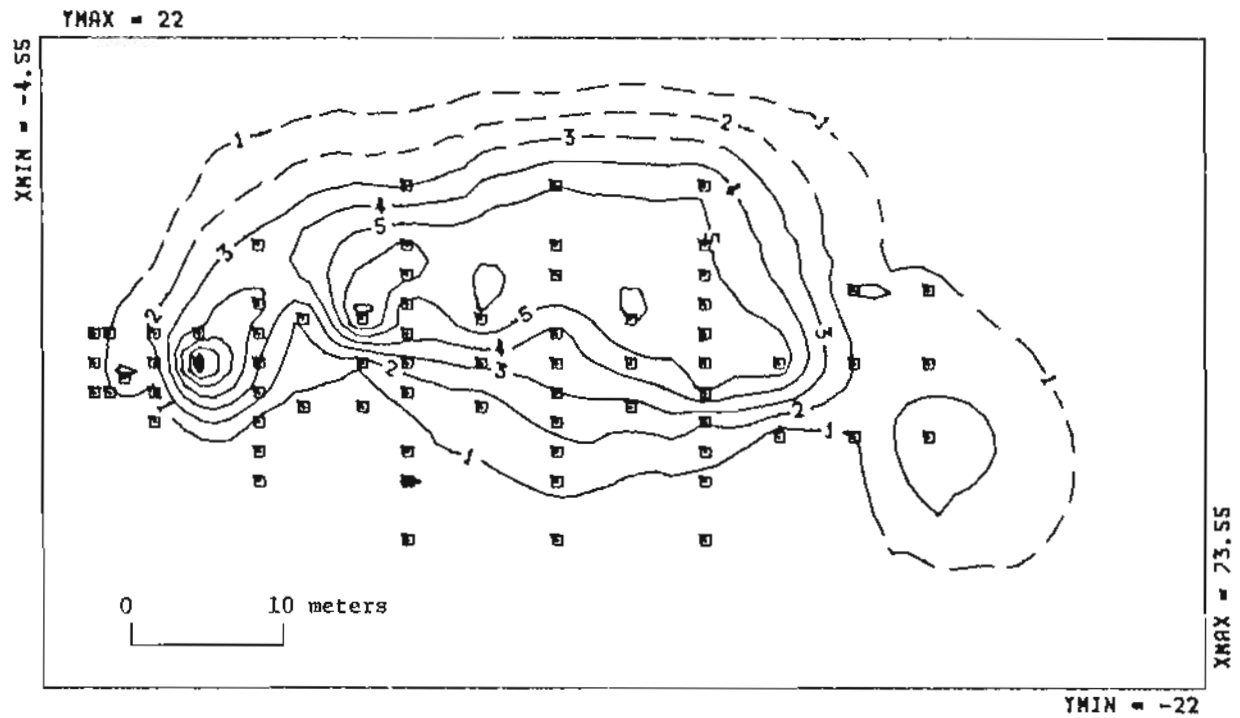


Figure IV.A.17 Contour map of fluorescein concentration measured on day 419 of tracer test #1 at the 2.4 m sampling depth.

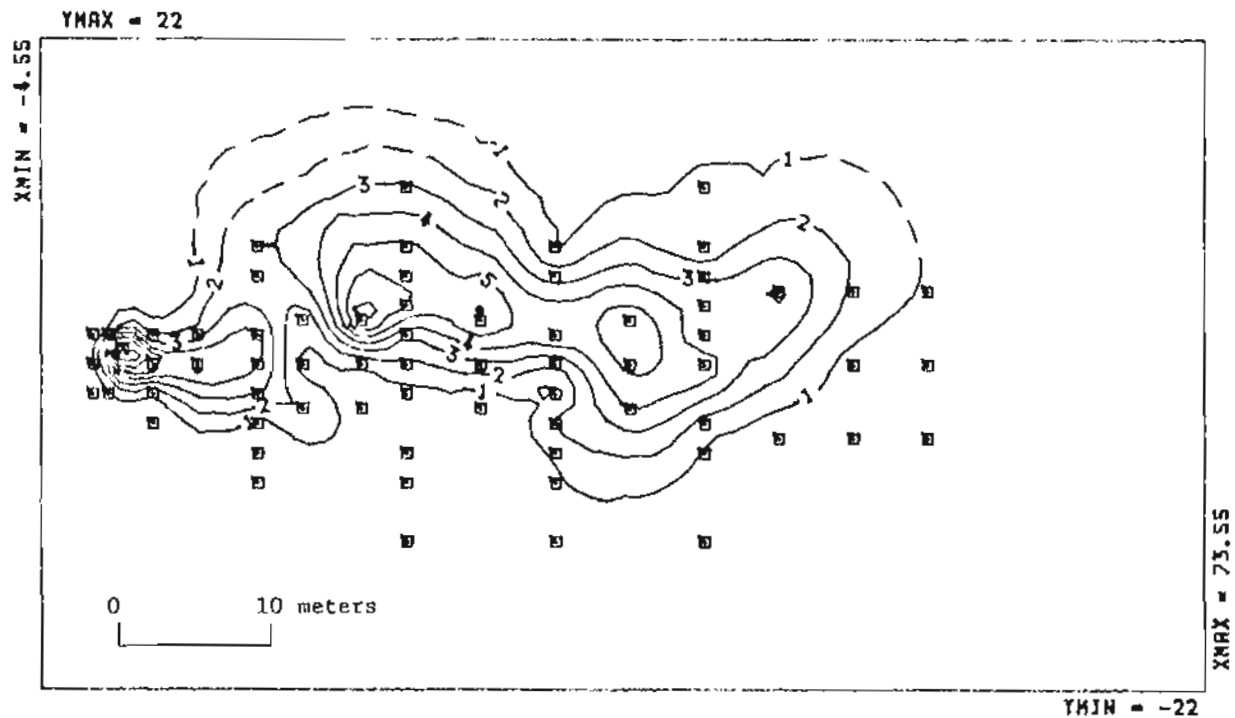


Figure IV.A.18 Contour map of fluorescein concentration measured on day 419 of tracer test #1 at the 3.0 m sampling depth.

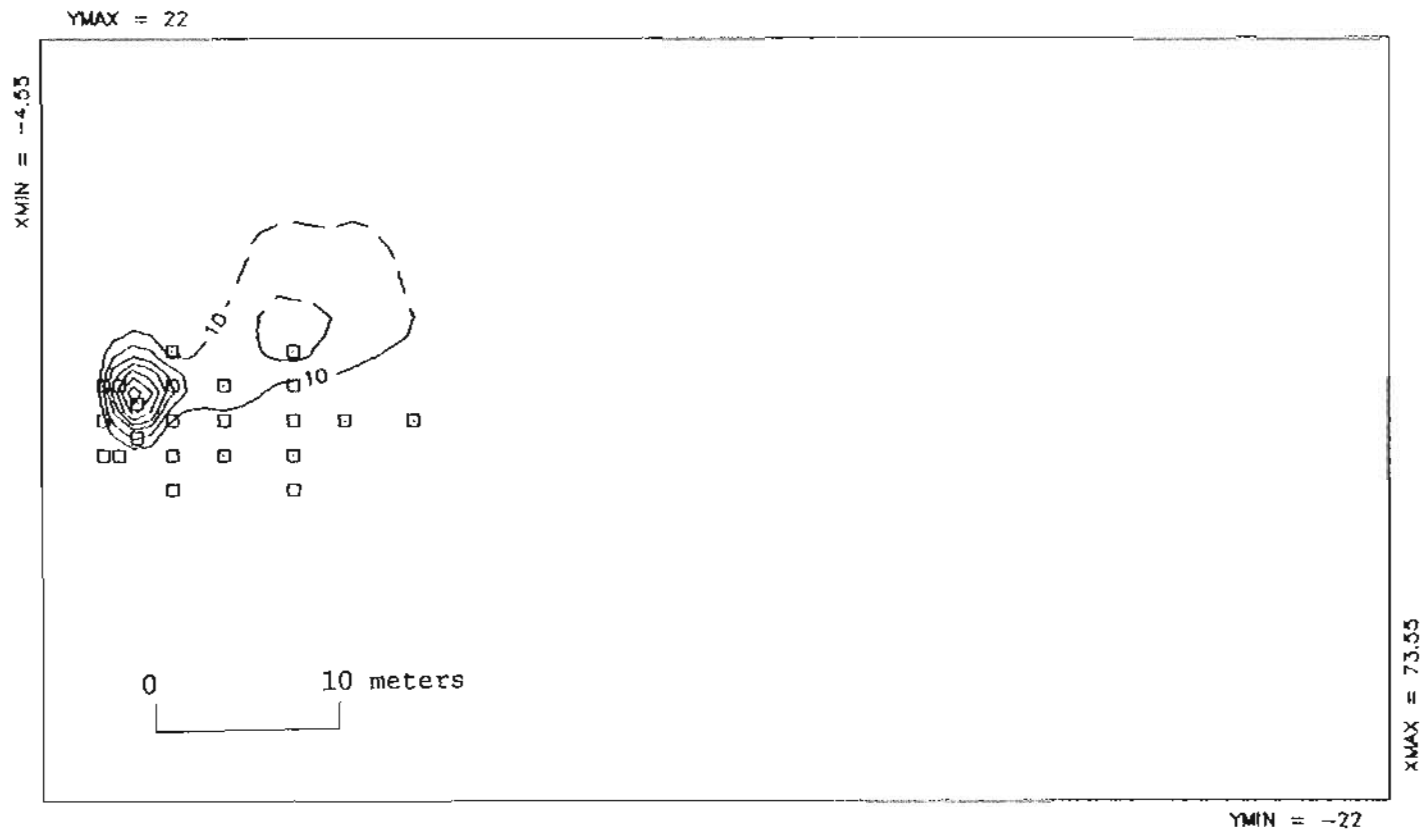


Figure IV.A.19 Vertically averaged contour map of fluorescein concentration measured on day 50 of tracer test #1.



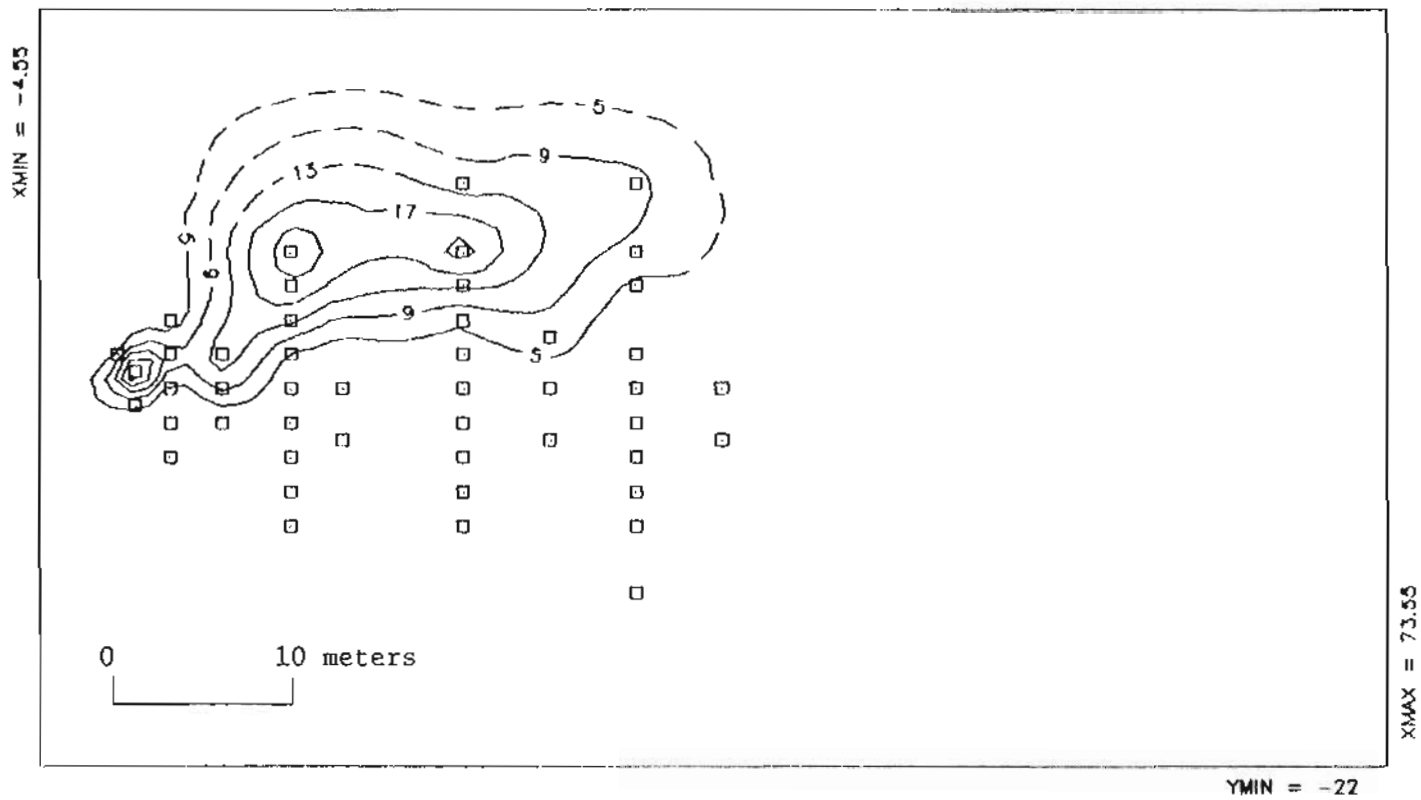


Figure IV.A.20 Vertically averaged contour map of fluorescein concentration measured on day 93 of tracer test #1.

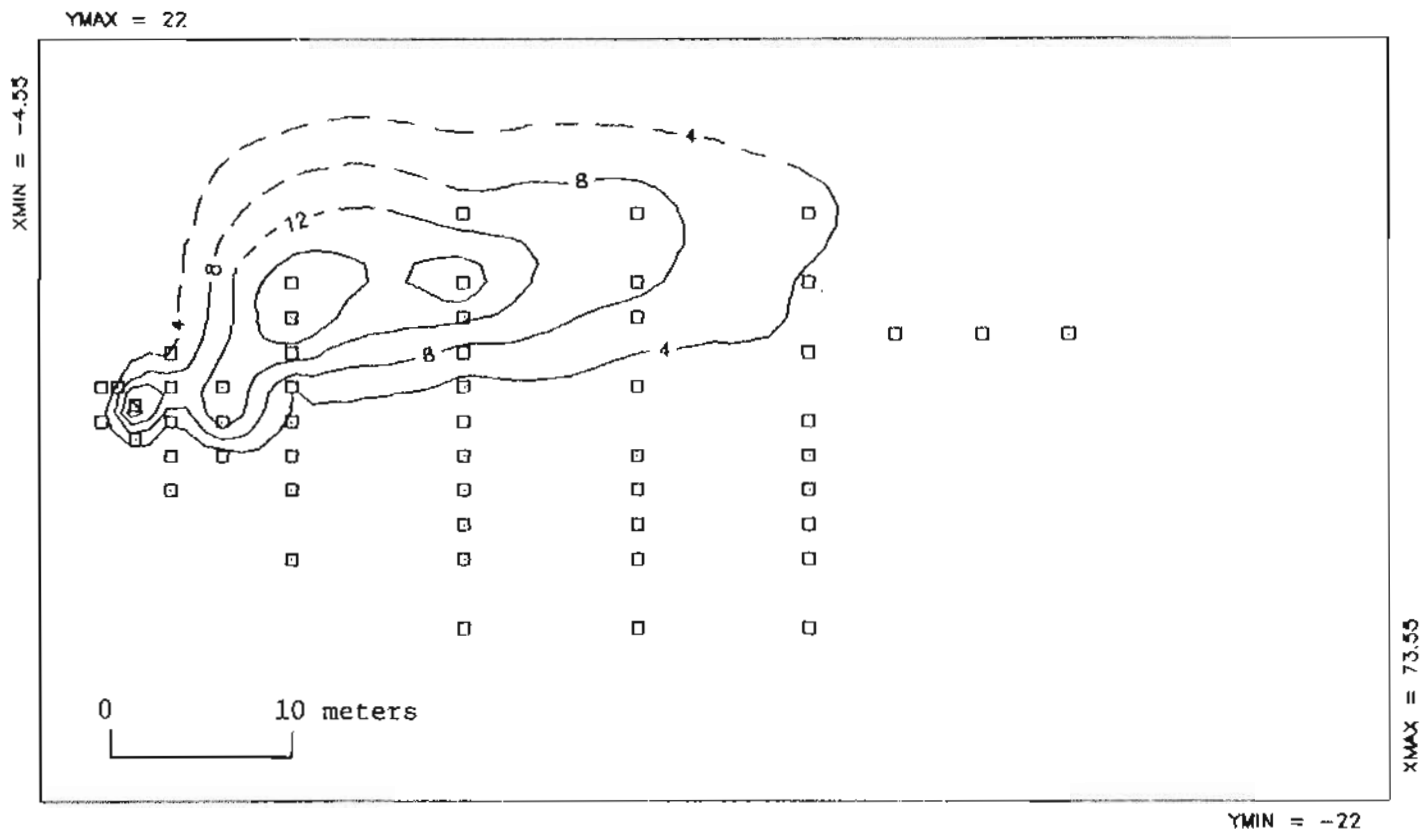


Figure IV.A.21 Vertically averaged contour map of fluorescein concentration measured on day 123 of tracer test #1.

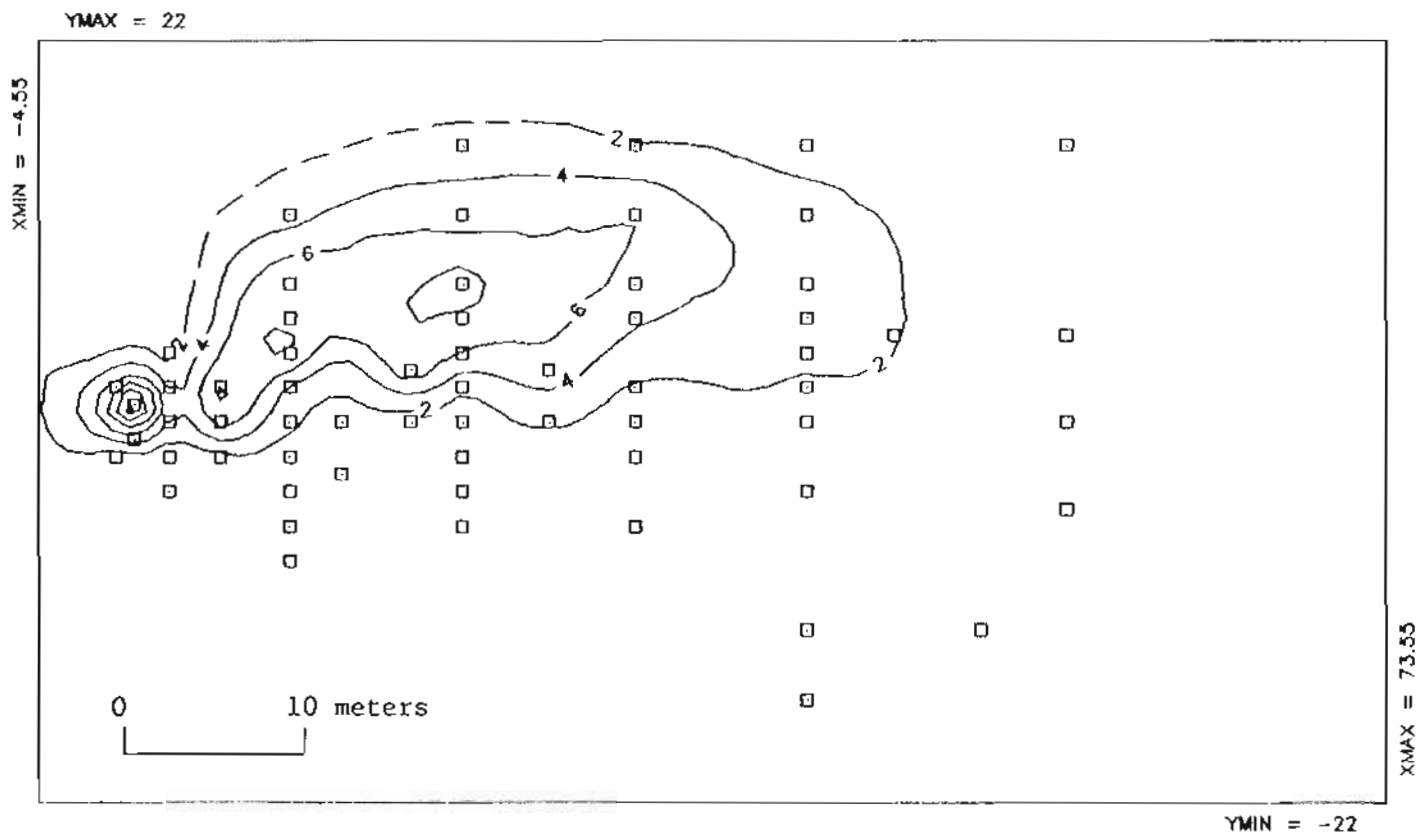


Figure IV.A.22 Vertically averaged contour map of fluorescein concentration measured on day 232 of tracer test #1.

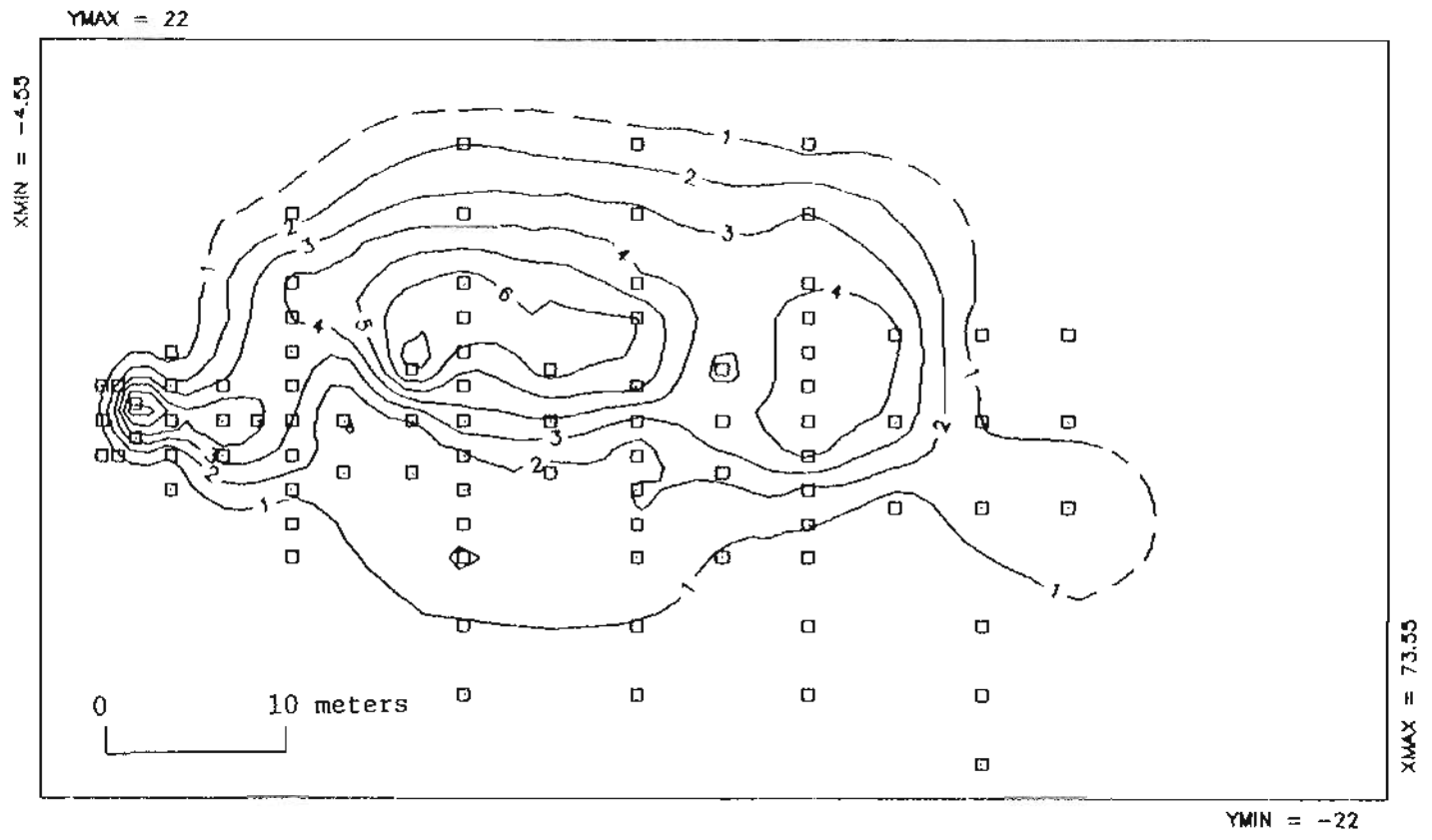


Figure IV.A.23 Vertically averaged contour map of fluorescein concentration measured on day 342 of tracer test #1.

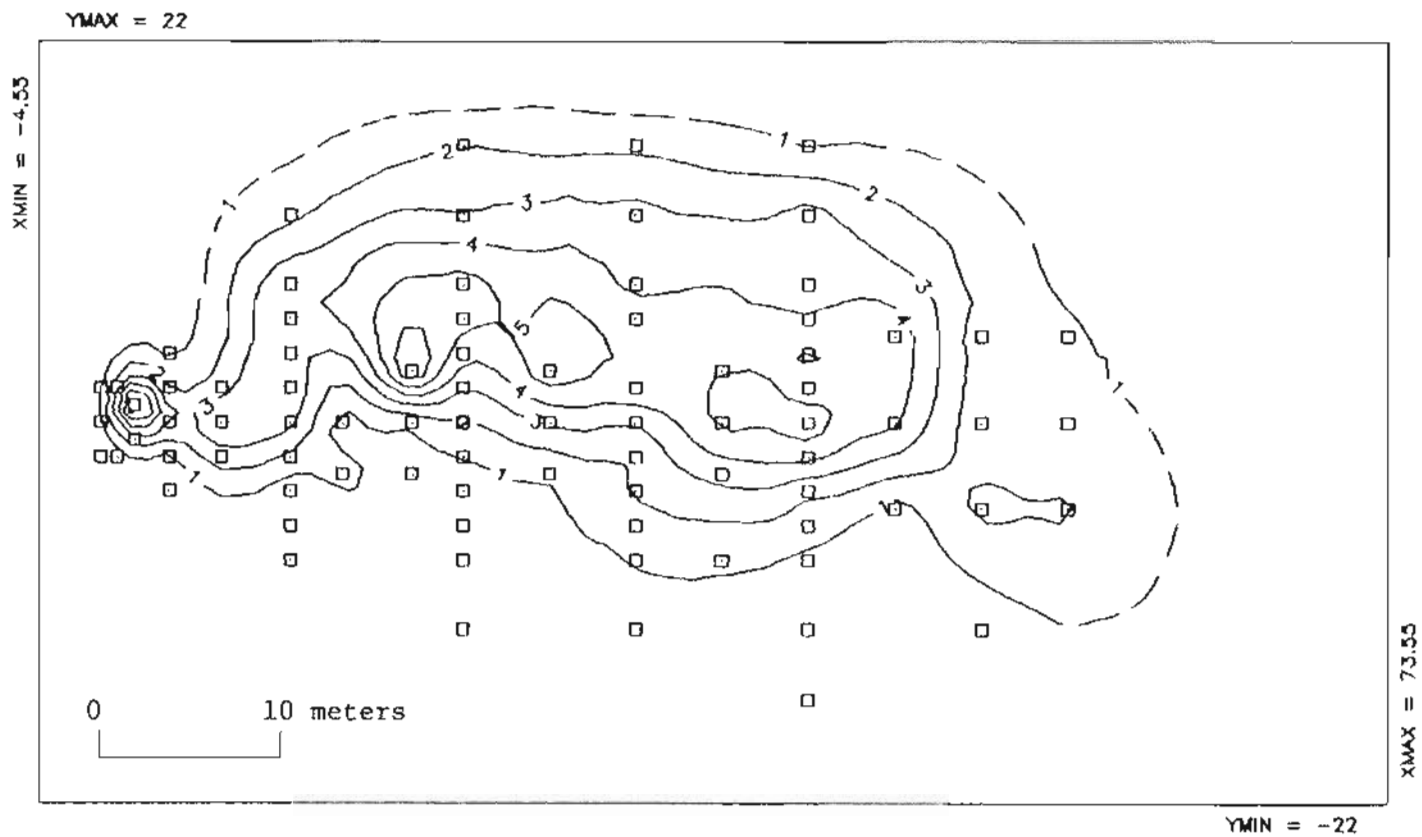


Figure IV.A.24 Vertically averaged contour map of fluorescein concentration measured on day 419 of tracer test #1.

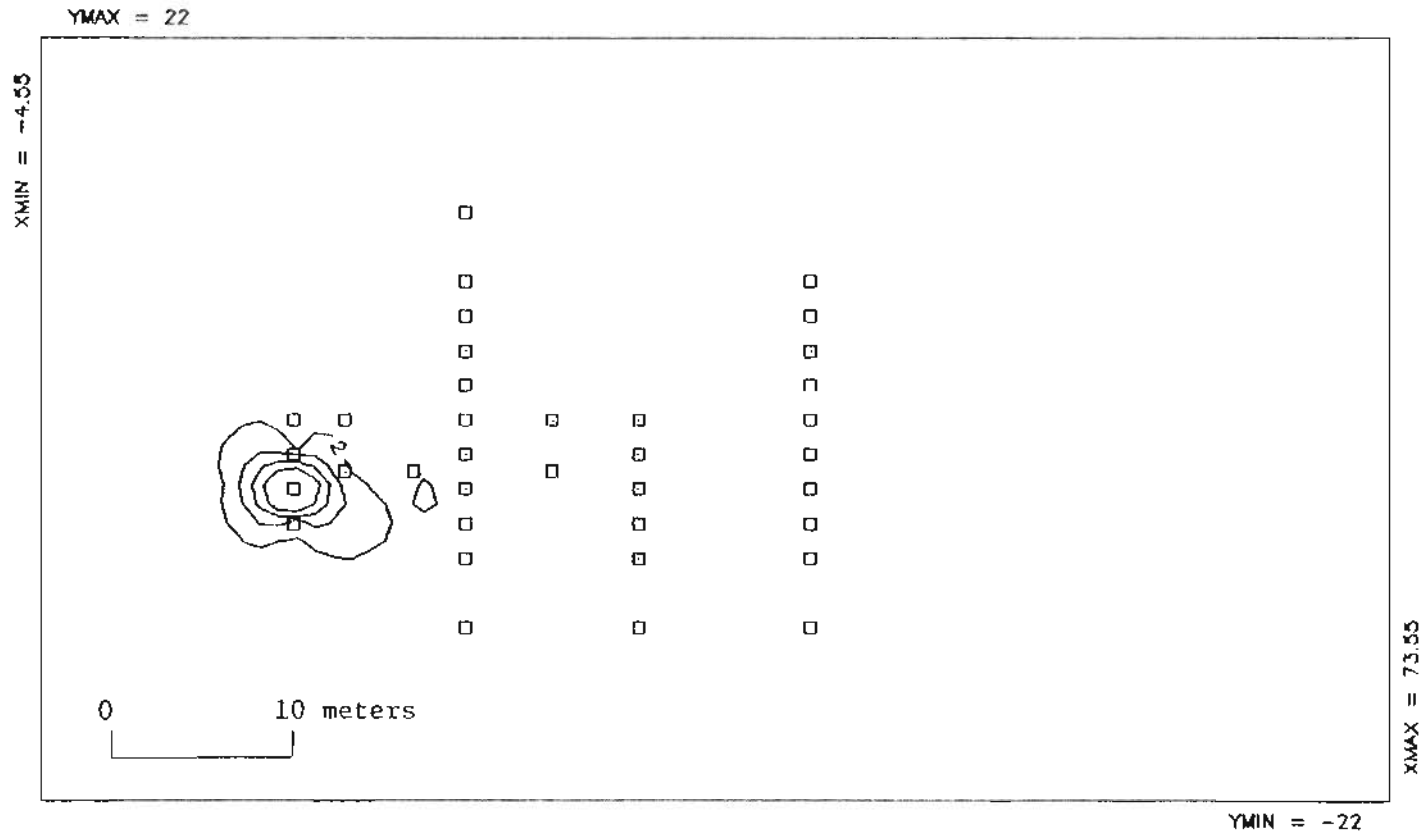


Figure IV.A.25 Contour map of 4'-chlorofluorescein concentration measured on day 10 of tracer test #2 at the 1.8 m sampling depth.

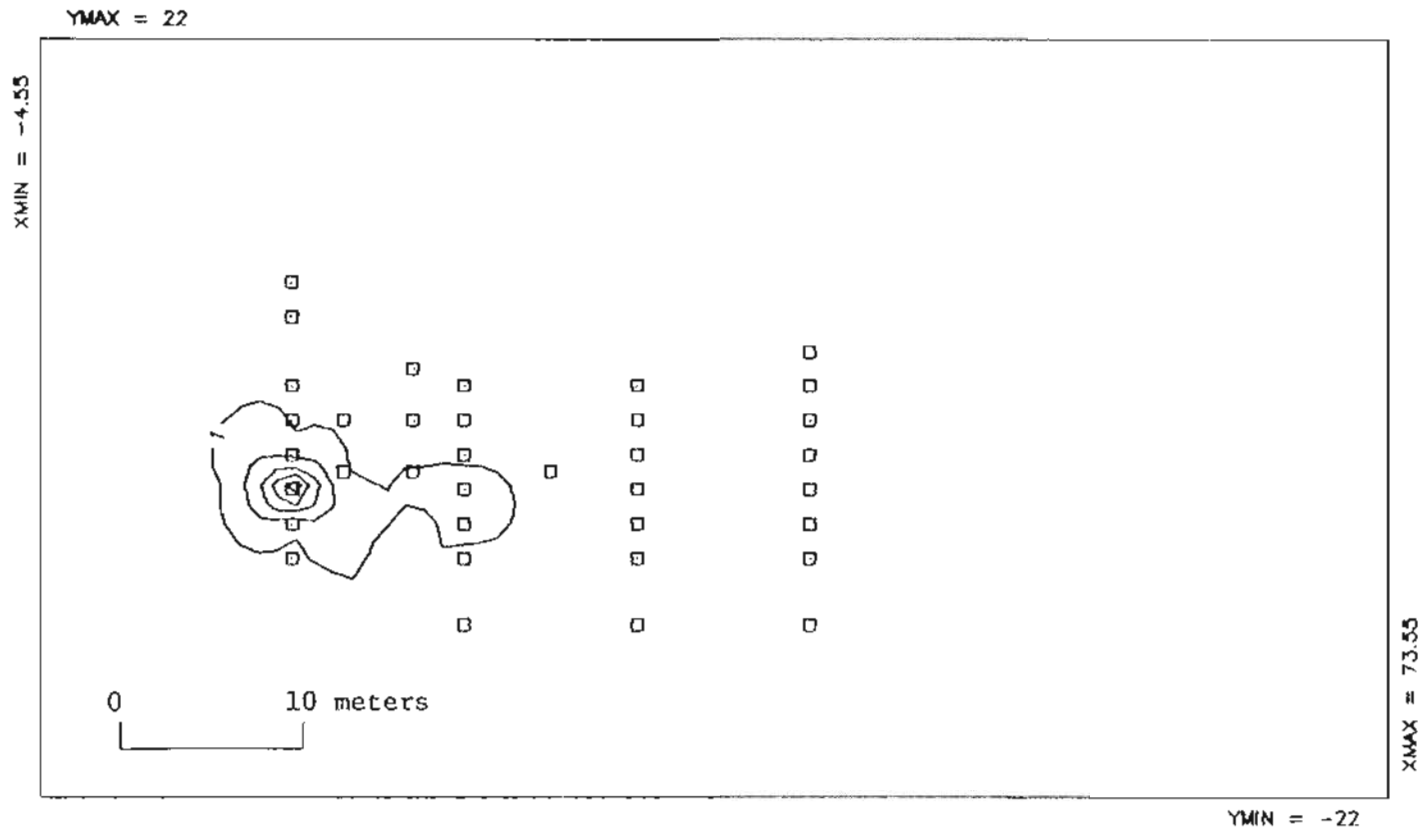


Figure IV.A.26 Contour map of 4'-chlorofluorescein concentration measured on day 20 of tracer test #2 at the 1.8 m sampling depth.

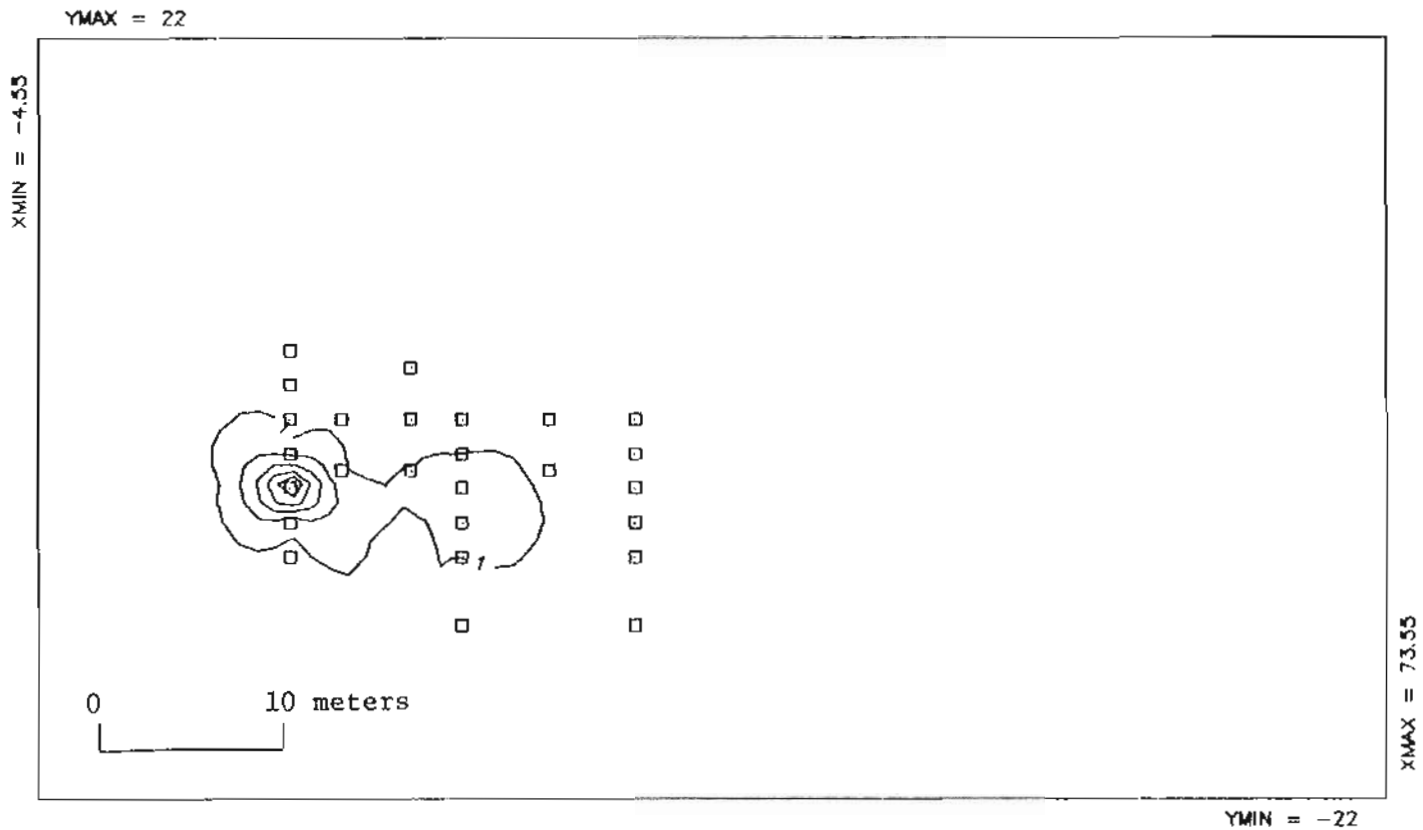


Figure IV.A.27 Contour map of 4'-chlorofluorescein concentration measured on day 45 of tracer test #2 at the 1.8 m sampling depth.



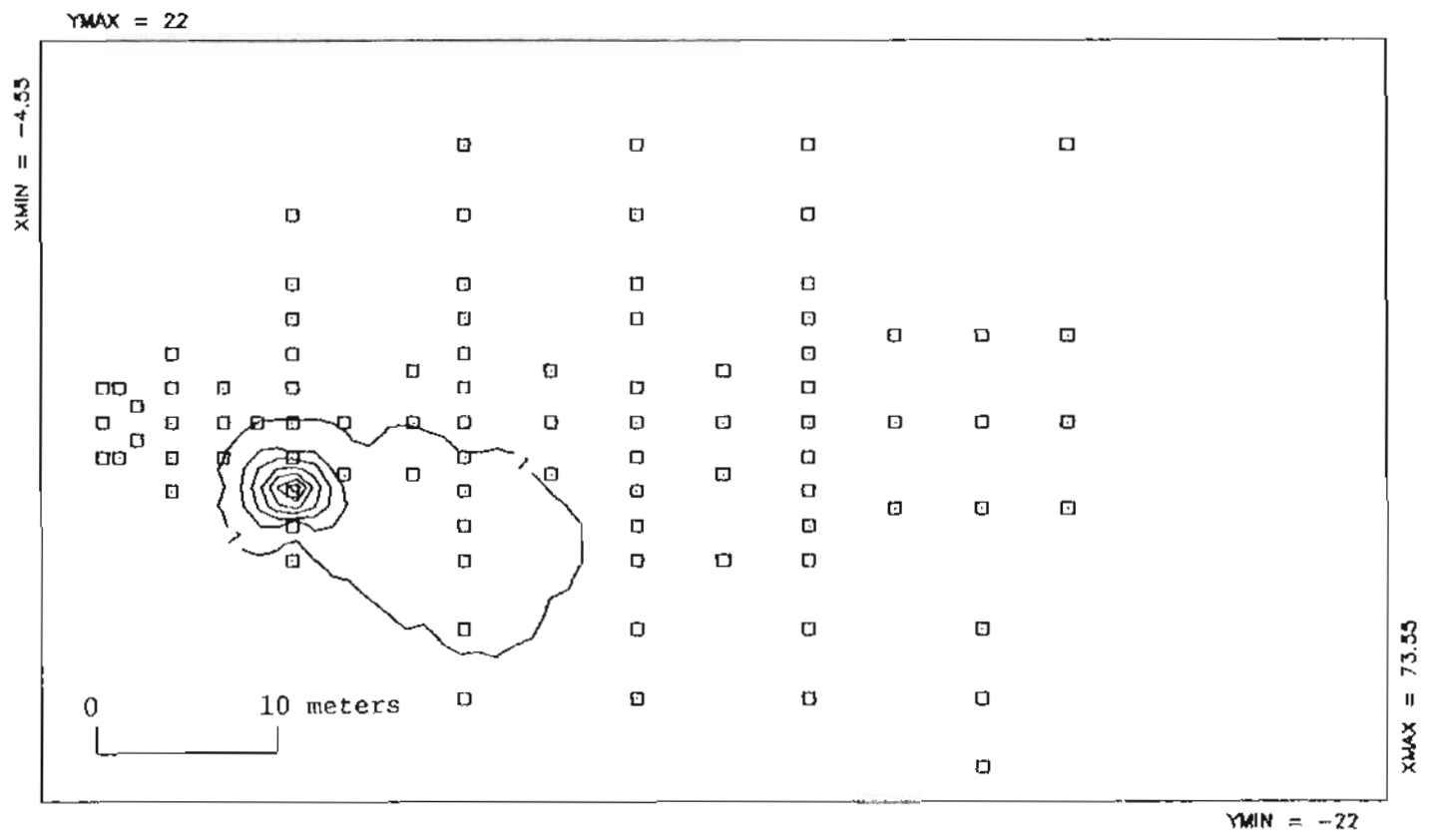


Figure IV.A.28 Contour map of 4'-chlorofluorescein concentration measured on day 101 of tracer test #2 at the 1.8 m sampling depth.

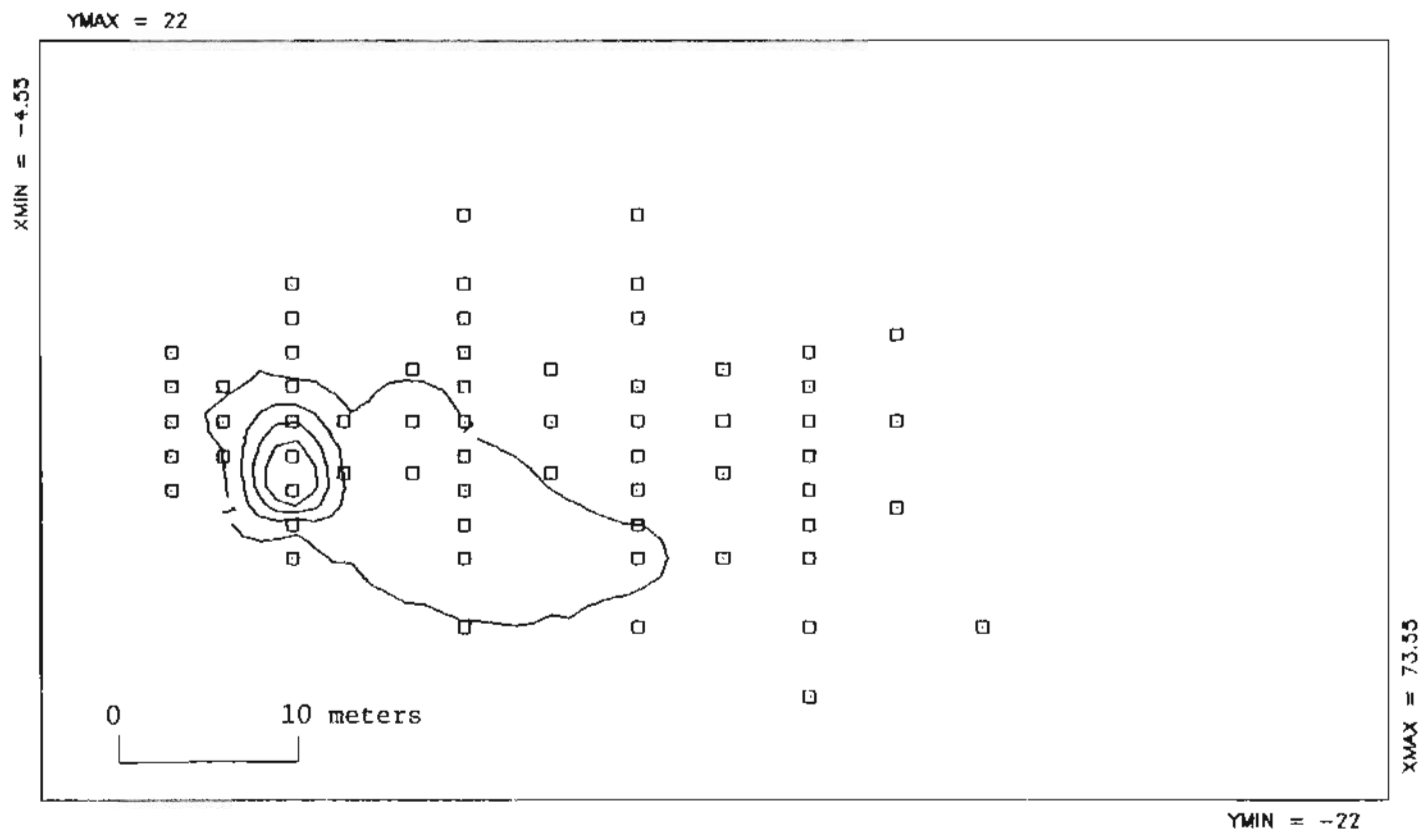


Figure IV.A.29 Contour map of 4'-chlorofluorescein concentration measured on day 178 of tracer test #2 at the 1.8 m sampling depth.

for the 1.8 and 2.4 m sampling depths were very similar while at 3.0 m the plume initially moved slower than at the upper levels. With increased travel time the differences between the 3.0 m level and the upper levels were diminished. A very noticeable characteristic of the fluorescein plume is its continual connection with the injection region. This is an indication that the rapid injection of tracer resulted in a source function different from the expected pulse type source. Also noteworthy is the fact that after only 419 days of migration, the maximum measured concentration was over 4 orders of magnitude below the injected concentration.

The movement of 4'-chlorofluorescein (MCFL) used in the second tracer test is presented in Figure IV.A.8. The purpose of the second test was to provide a better defined picture of the early stages of solute transport. In general, the migration of MCFL followed a pattern very similar to the fluorescein employed in the first test. For the first 10 days, MCFL moved rapidly and at an angle of approximately  $-30^{\circ}$  to the central axis of the monitoring network. After the initial surge, the plume slowed and appeared to travel approximately parallel with the network axis. As in the first test, the injection area was continually within the plume.

#### IV.B. Integrated Transects of the Tracer Plumes

Integrated transects are a one-dimensional representation of the tracer plumes. If a transect is calculated in the direction of flow, it will provide focus on the following aspects of solute transport: 1) advection in the direction parallel with the hydraulic gradient; 2) the longitudinal component of dispersion; and 3) the behavior of the source function. The transects derived from the vertically averaged measurements from the first and second tracer tests are given in Figures IV.B.1 through IV.B.11. In agreement with the contour maps, the transects indicate that the rate of advection is approximately 2-3 times greater for tracer test #1 than for tracer test #2. In addition, the transects indicate that dispersion in the direction of flow also is greater for tracer test #1. Perhaps the most interesting feature common to the transects associated with tracer tests #1 and #2 is their bi-modal nature. After injection the tracer appears to partition between a decaying source region and a migrating plume. The presence of the decaying source function is clearer in the test #2 transects due to more frequent sampling during the early stages of migration. The length of the source regions for tests #1 and #2 can be estimated from the transects. For test #1 in which the injection occurred at  $x$  equal to 0, the source area extends from approximately -1 to 6 m on the  $x$ -axis. For test #2, the injection occurred at  $x$  equal to 7 m and the front and back boundaries of the source region are approximately 12 and 6 m, respectively.

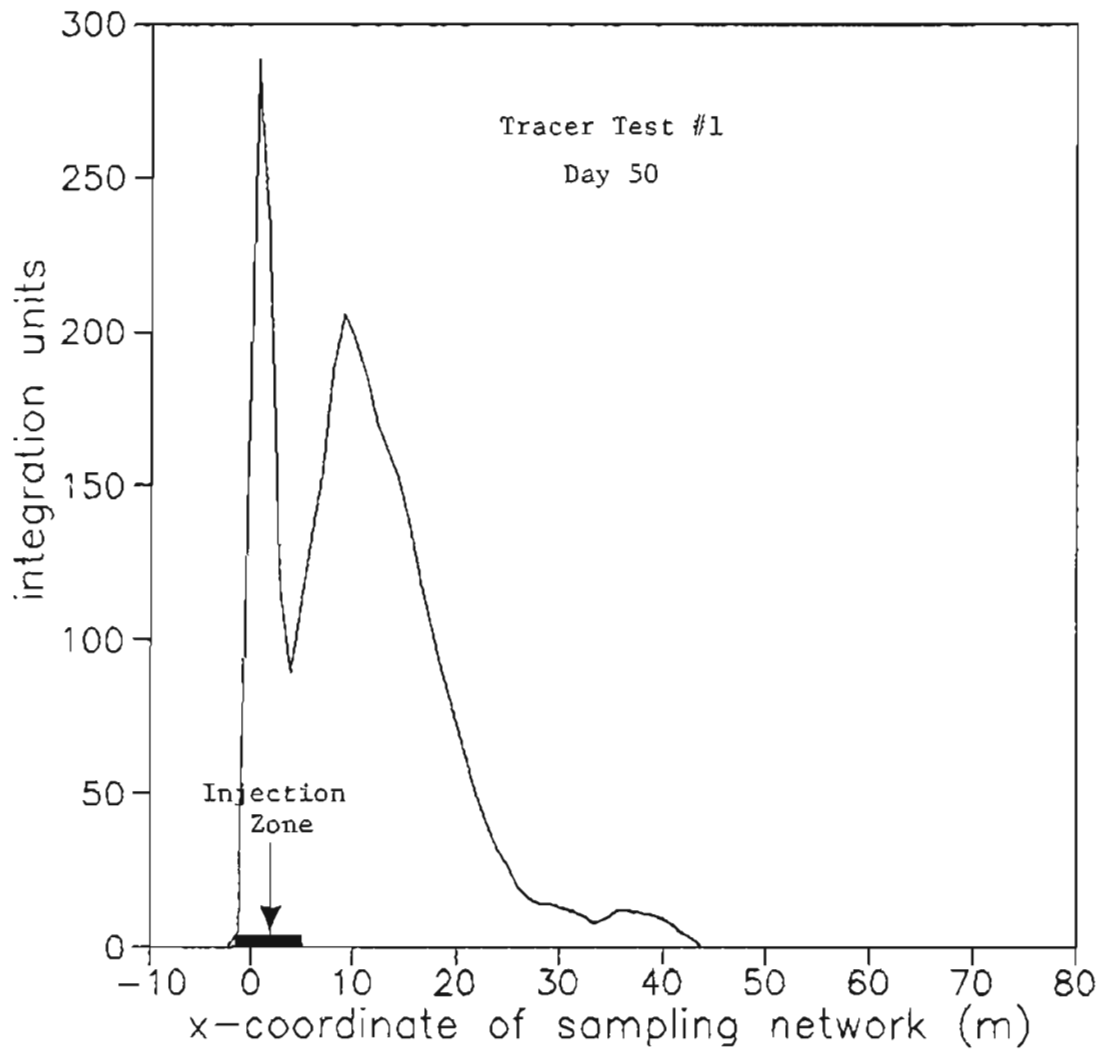


Figure IV.B.1 Integrated transects derived from the vertically averaged fluorescein concentrations for day 50 of tracer test #1.

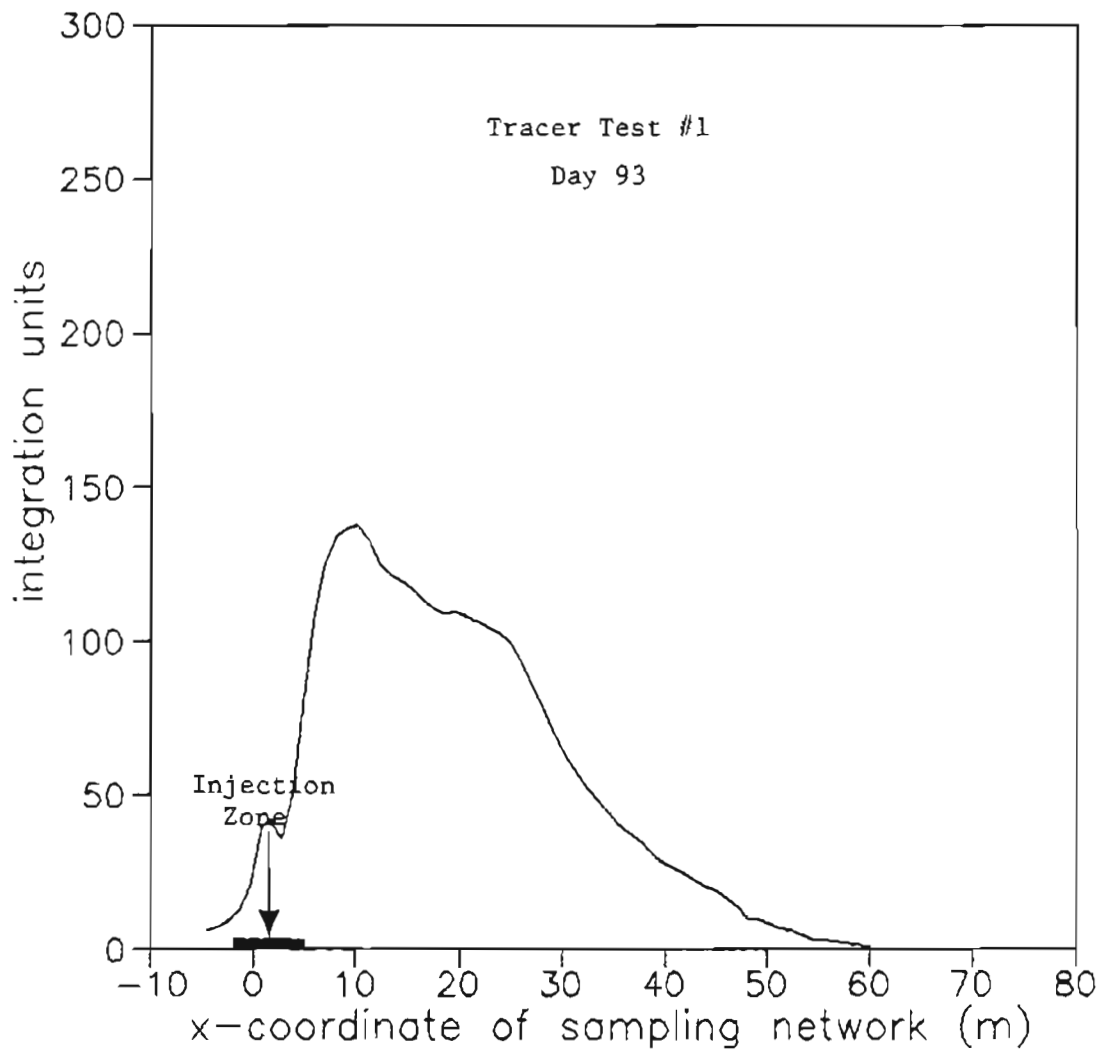


Figure IV.B.2 Integrated transects derived from the vertically averaged fluorescein concentrations for day 93 of tracer test #1.

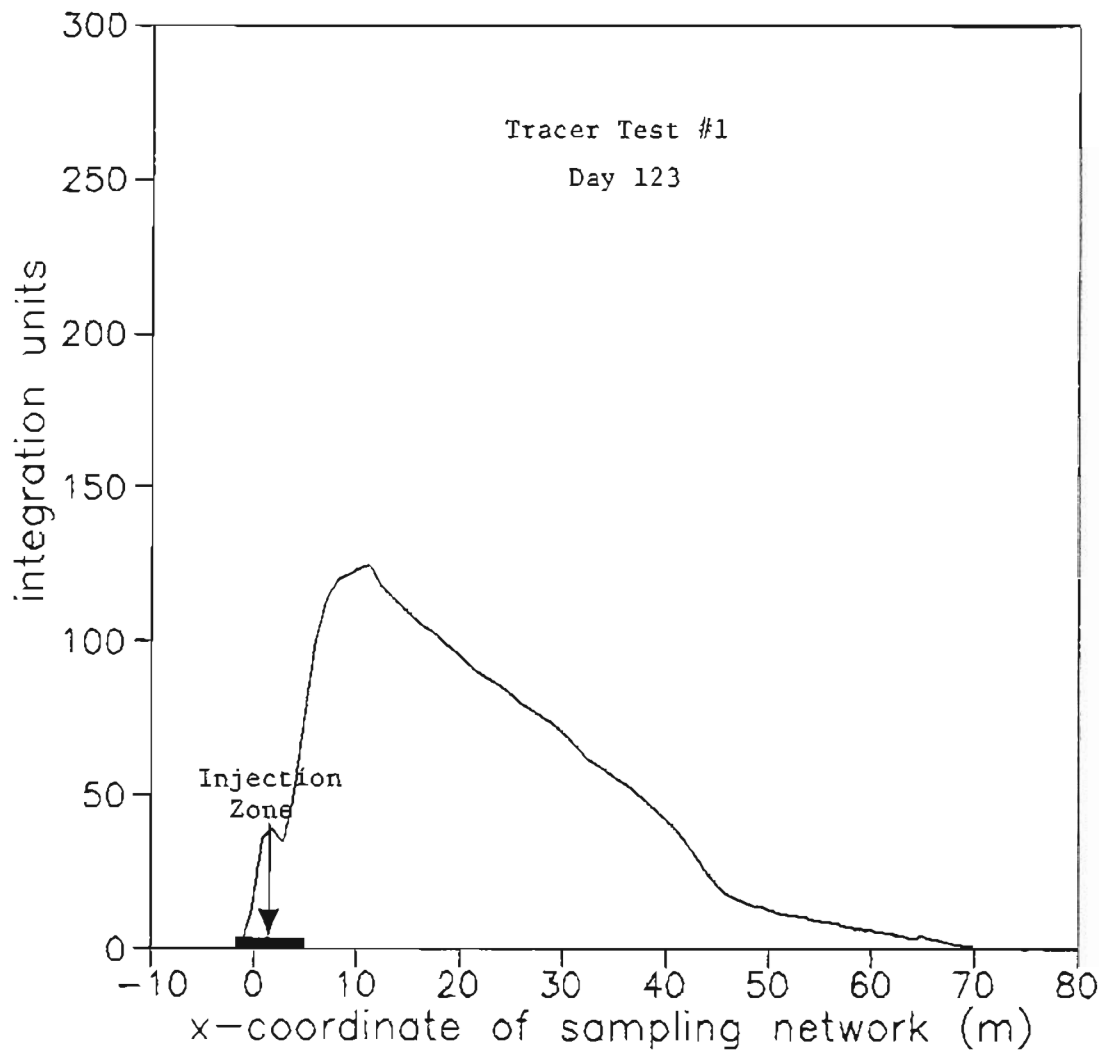


Figure IV.B.3 Integrated transects derived from the vertically averaged fluorescein concentrations for day 123 of tracer test #1.

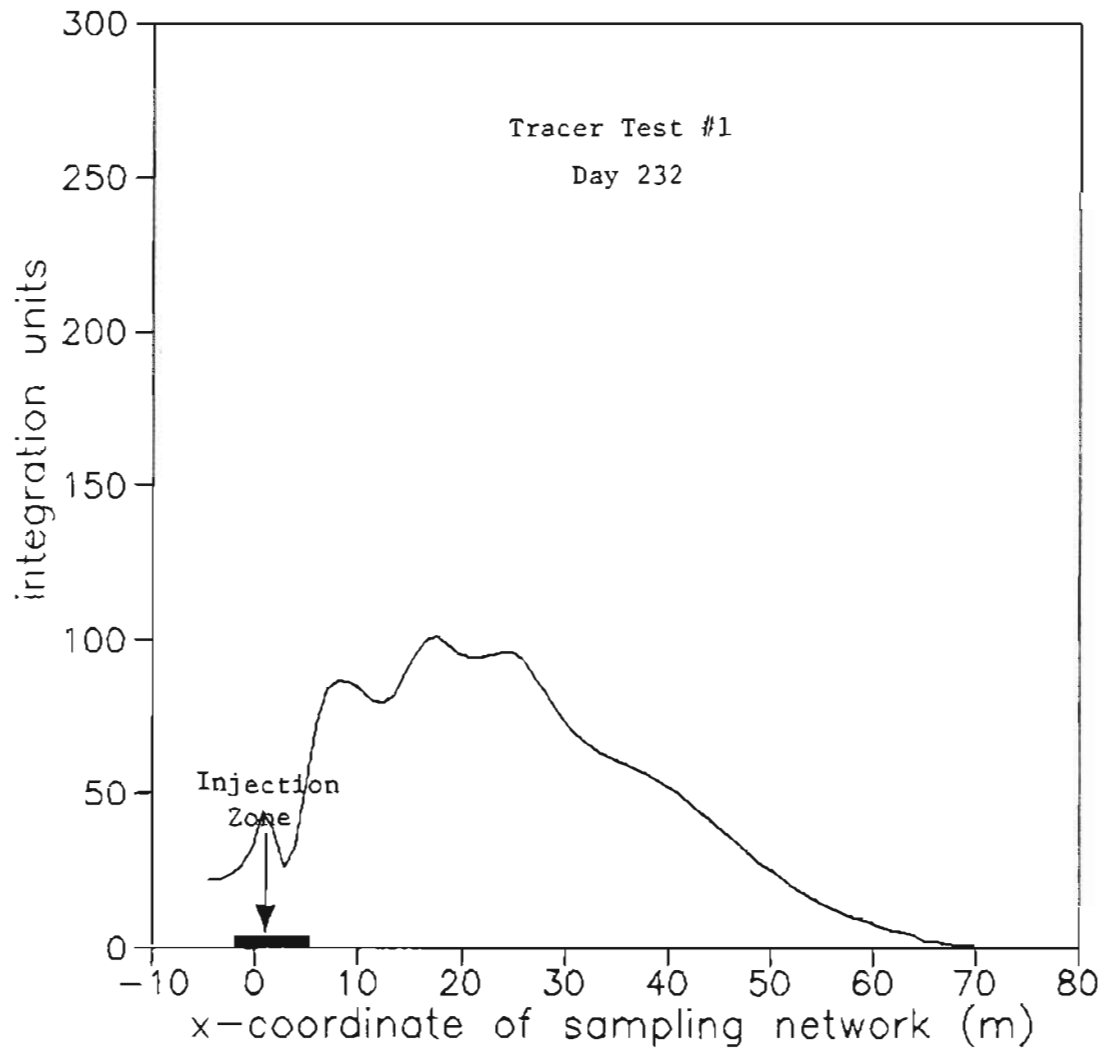


Figure IV.B.4 Integrated transects derived from the vertically averaged fluorescein concentrations for day 232 of tracer test #1.



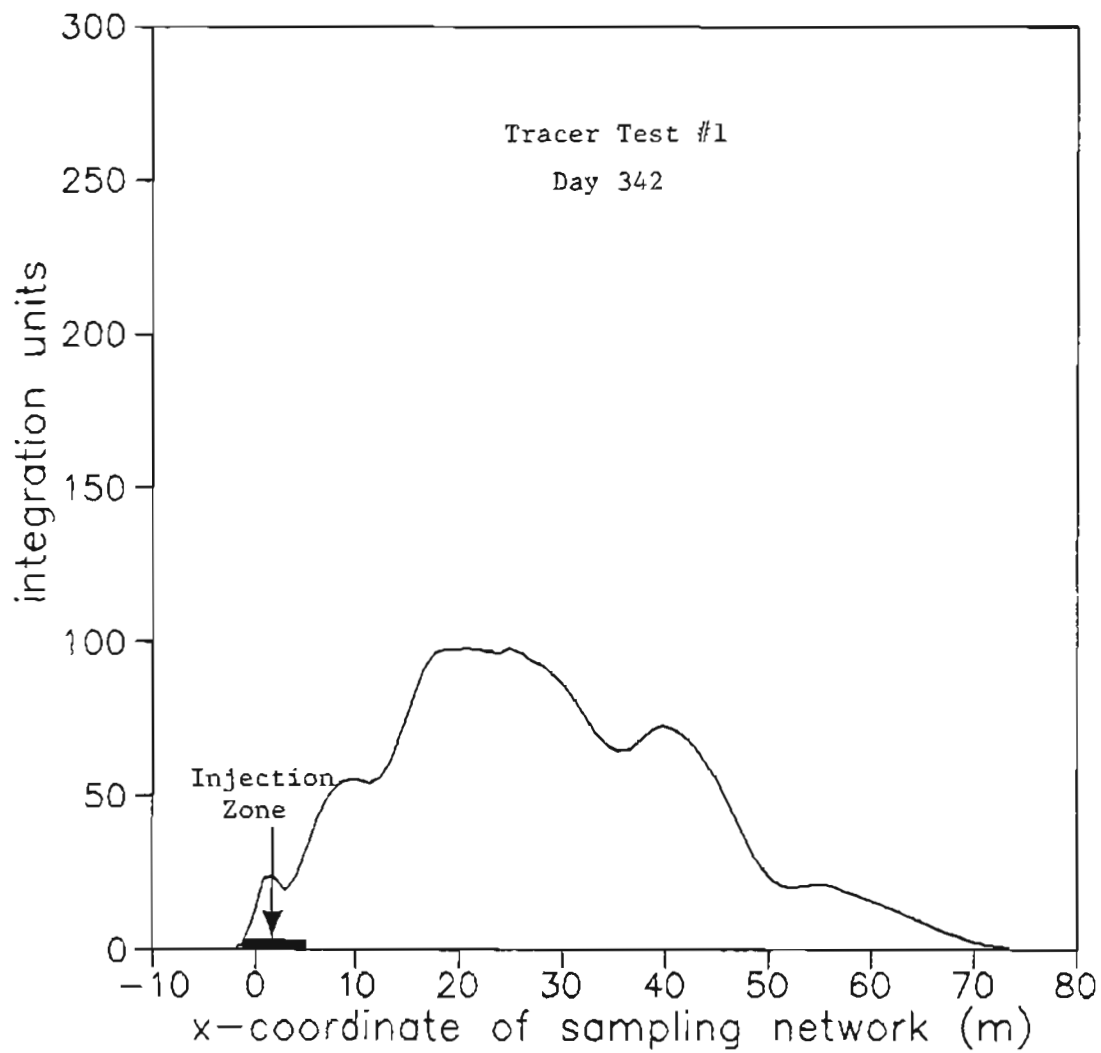


Figure IV.B.5 Integrated transects derived from the vertically averaged fluorescein concentrations for day 342 of tracer test #1.

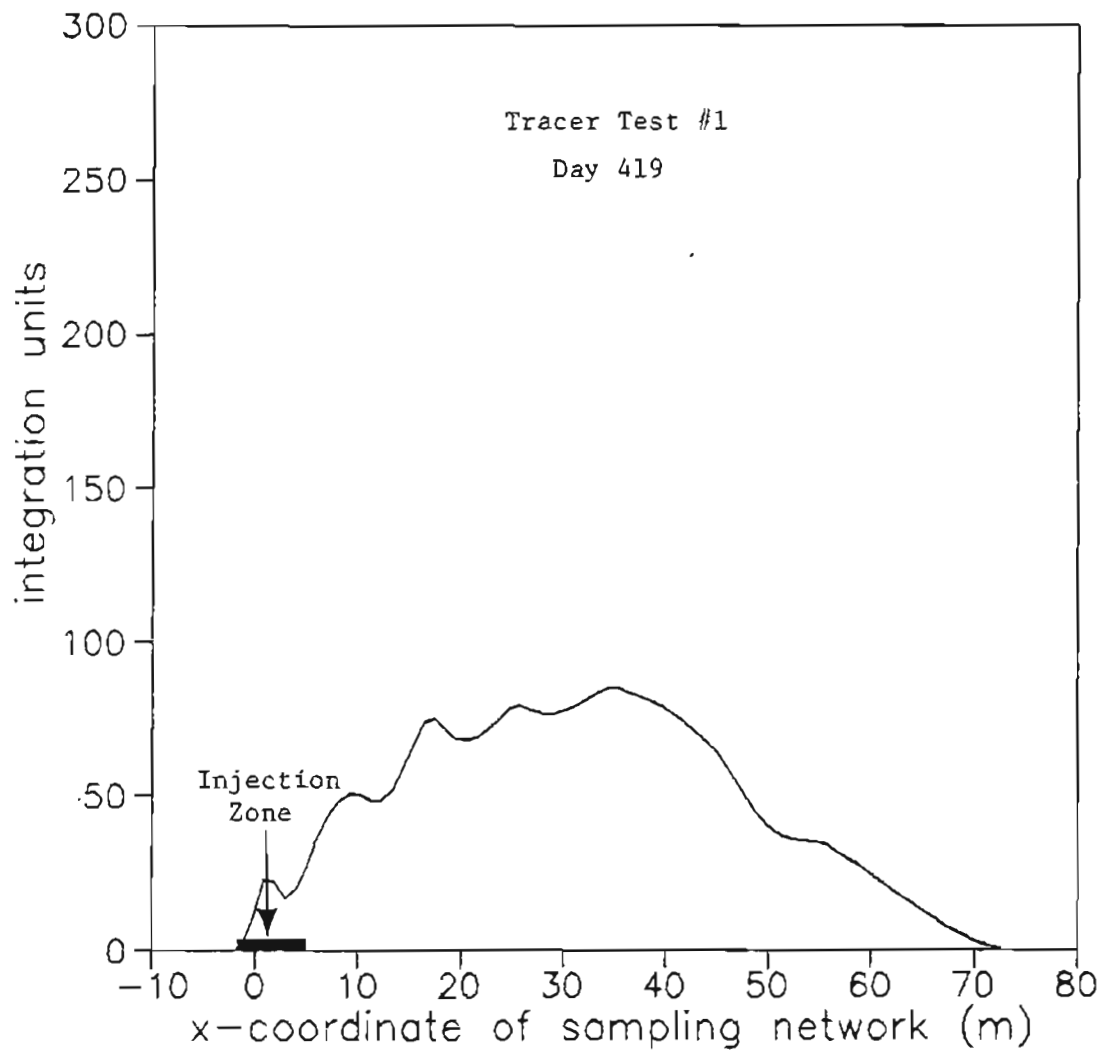


Figure IV.B.6 Integrated transects derived from the vertically averaged fluorescein concentrations for day 419 of tracer test #1.

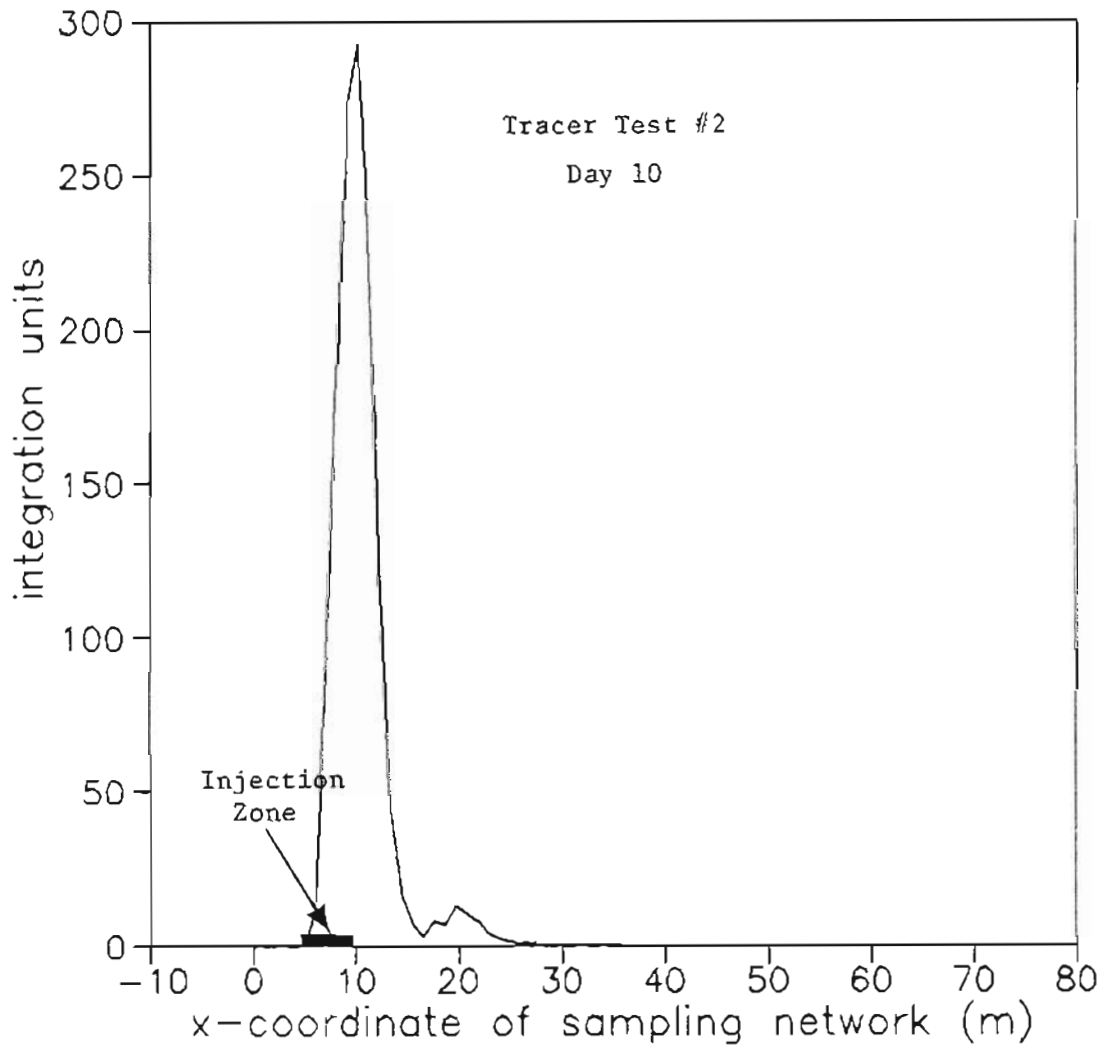


Figure IV.B.7 Integrated transects derived from the vertically averaged 4'-chlorofluorescein concentrations for day 10 of tracer test #2.

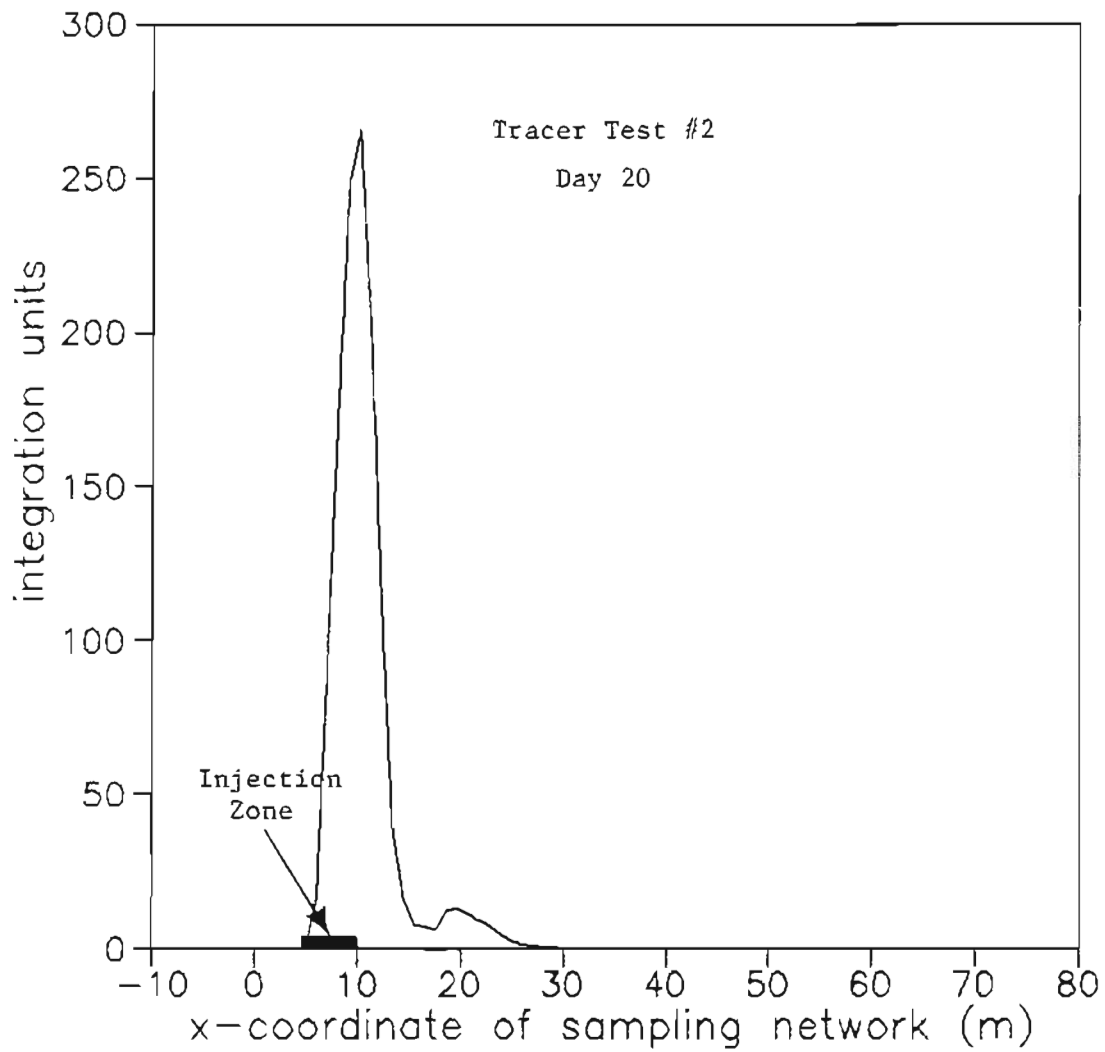


Figure IV.B.8 Integrated transects derived from the vertically averaged 4'-chlorofluorescein concentrations for day 20 of tracer test #2.

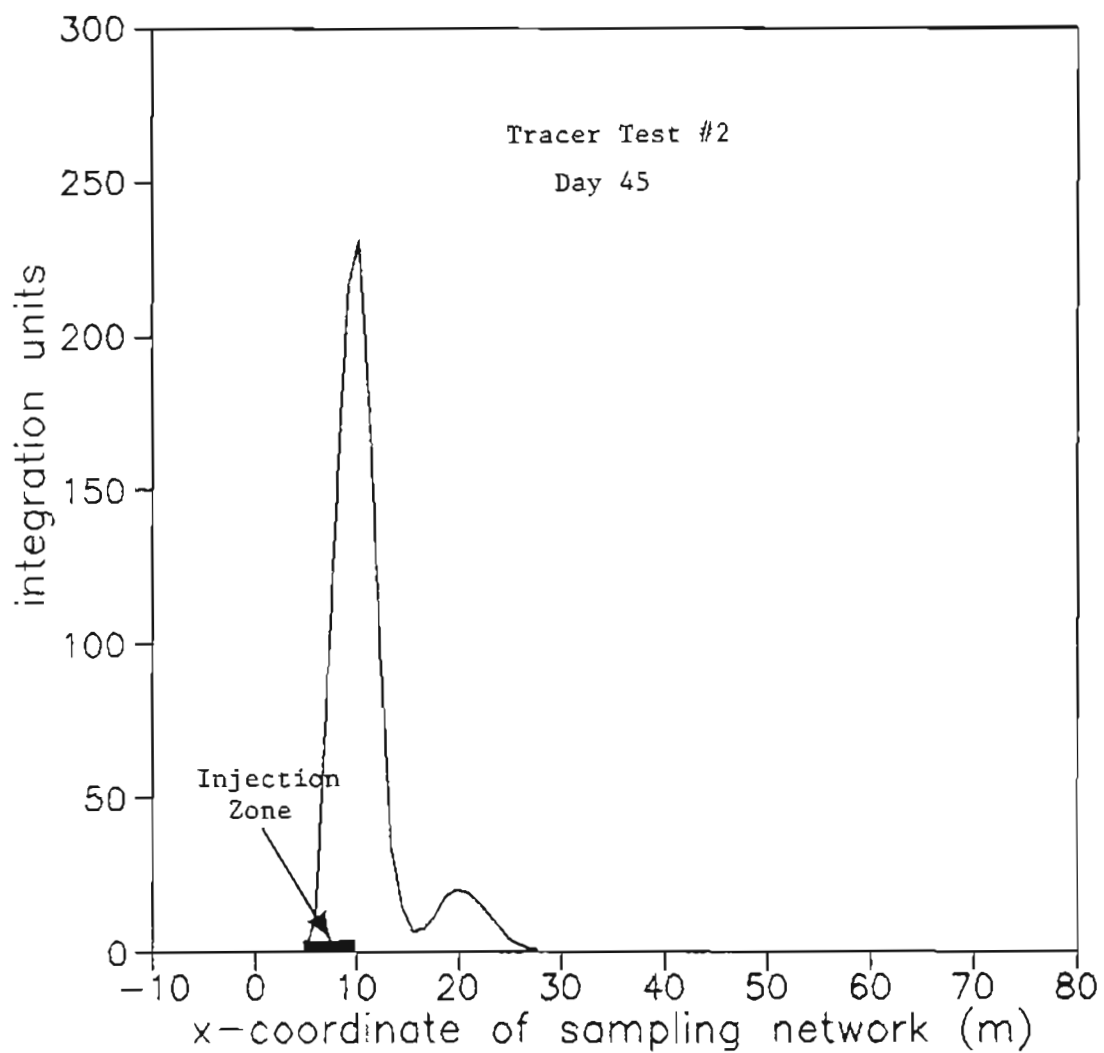


Figure IV.B.9 Integrated transects derived from the vertically averaged 4'-chlorofluorescein concentrations for day 45 of tracer test #2.

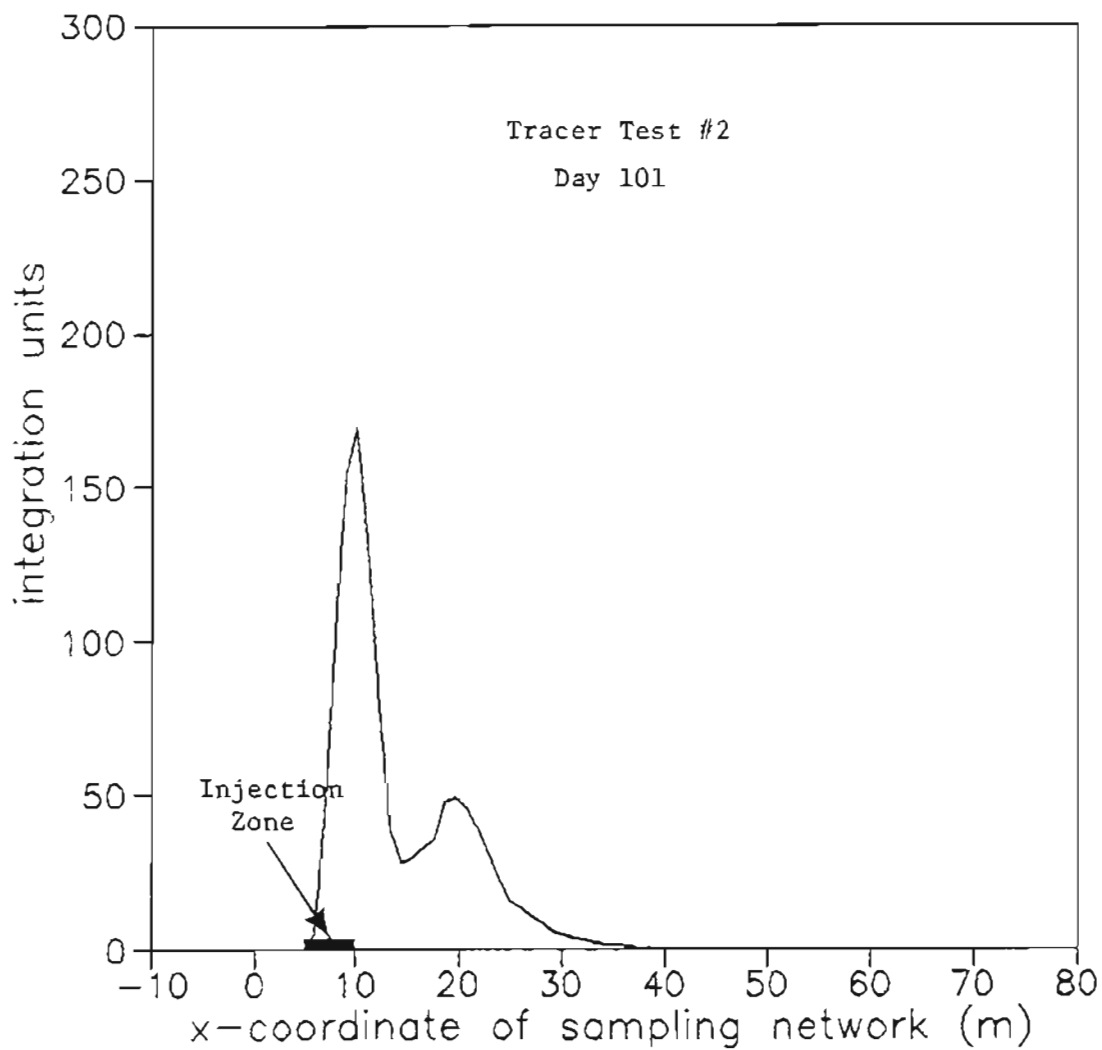


Figure IV.B.10 Integrated transects derived from the vertically averaged 4'-chlorofluorescein concentrations for day 101 of tracer test #2.

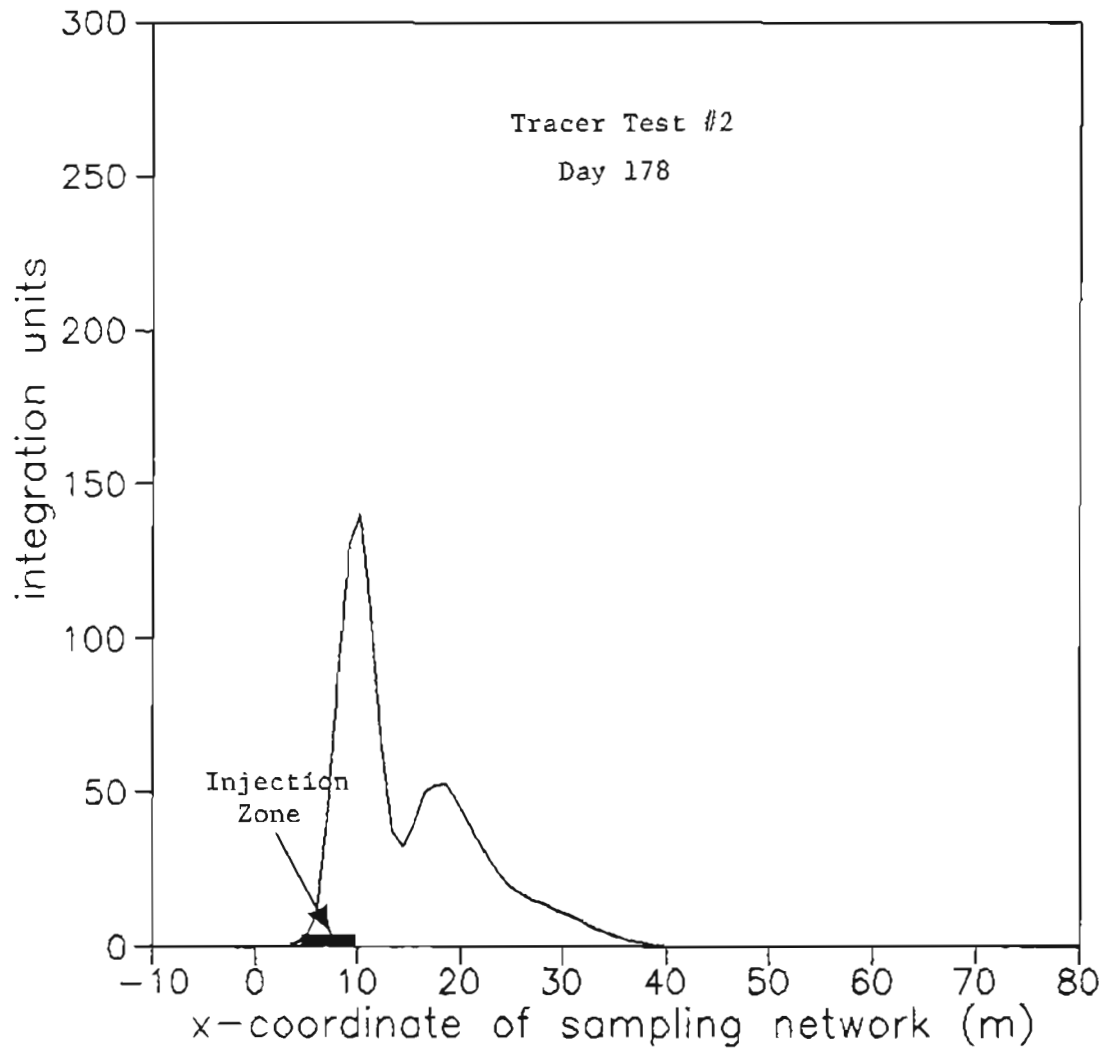


Figure IV.B.11 Integrated transects derived from the vertically averaged 4'-chlorofluorescein concentrations for day 178 of tracer test #2.

#### IV.C. Empirical Evidence for an Exponentially Decaying Source Function

The contour maps and integrated transects demonstrated that in both tracer tests, the injected tracer slugs exhibited decaying source function behavior. Consider Figure IV.C.1 which represents a cross section within a fractured porous system of the area surrounding an injection well. After injection, the tracer quickly spreads out over a length  $L$  in the fracture network under the influence of the pressure change caused by the injection process. Assuming that equilibrium between the mobile and immobile groundwater is established quickly, then shortly after injection the tracer concentration,  $C$ , must be equal in the fractures and in the matrix. As was discussed in section I.D.1, this rapid establishment of equilibrium, which has been validated at Alkali Lake using push-pull tests (Johnson, 1984), is the fundamental condition required for the valid application of the EPM approach to fractured porous media.

Tracer concentration measurements made close to the injection wells suggest an exponential decay as the appropriate form for modeling the source function and provide estimates of the function parameters. For example, Figures IV.C.2 and IV.C.3 show plots of  $\ln[\text{tracer}]$  vs. time after injection for tracer tests #1 and #2, respectively. As predicted by Equation IV.C.3, the plots exhibit a linear relationship between  $\ln[\text{tracer}]$  and time. The slopes of the regression lines are



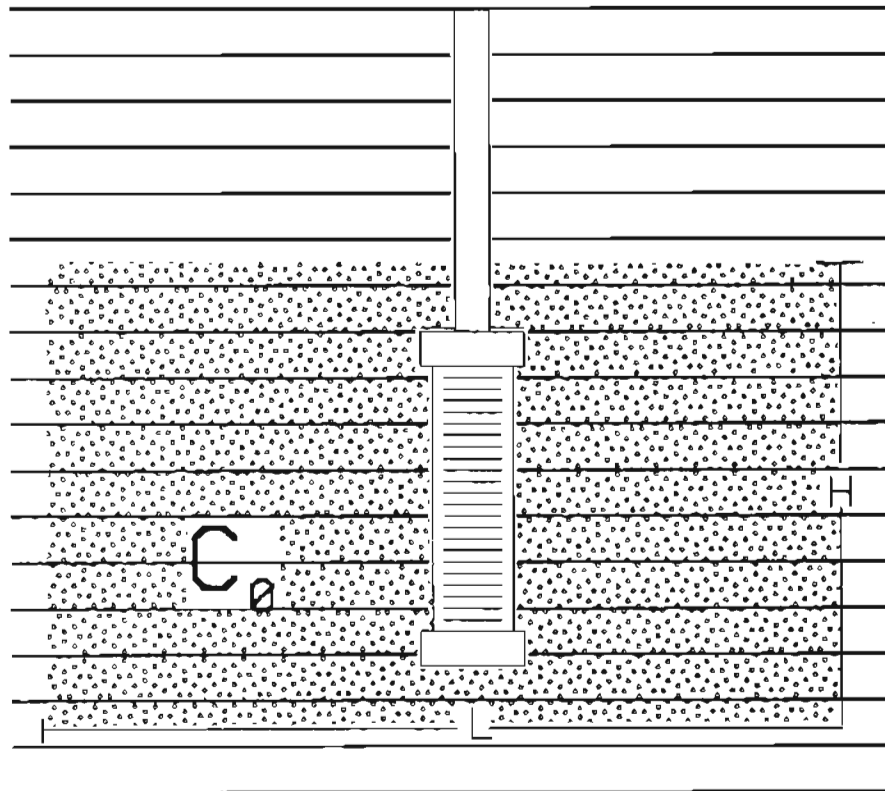


Figure IV.C.1 Schematic drawing of a vertical cross-section of an idealized fractured porous system surrounding an injection well.

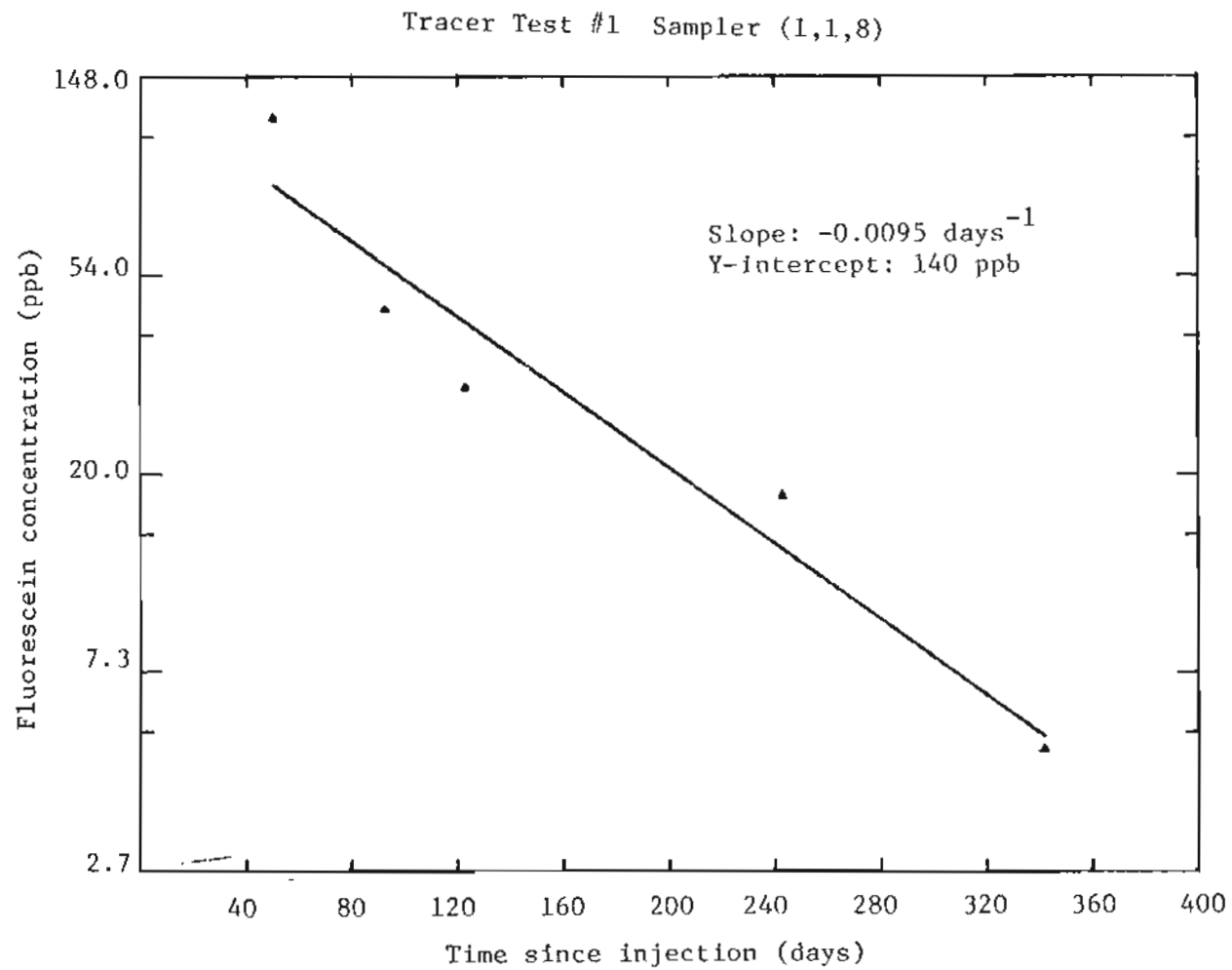
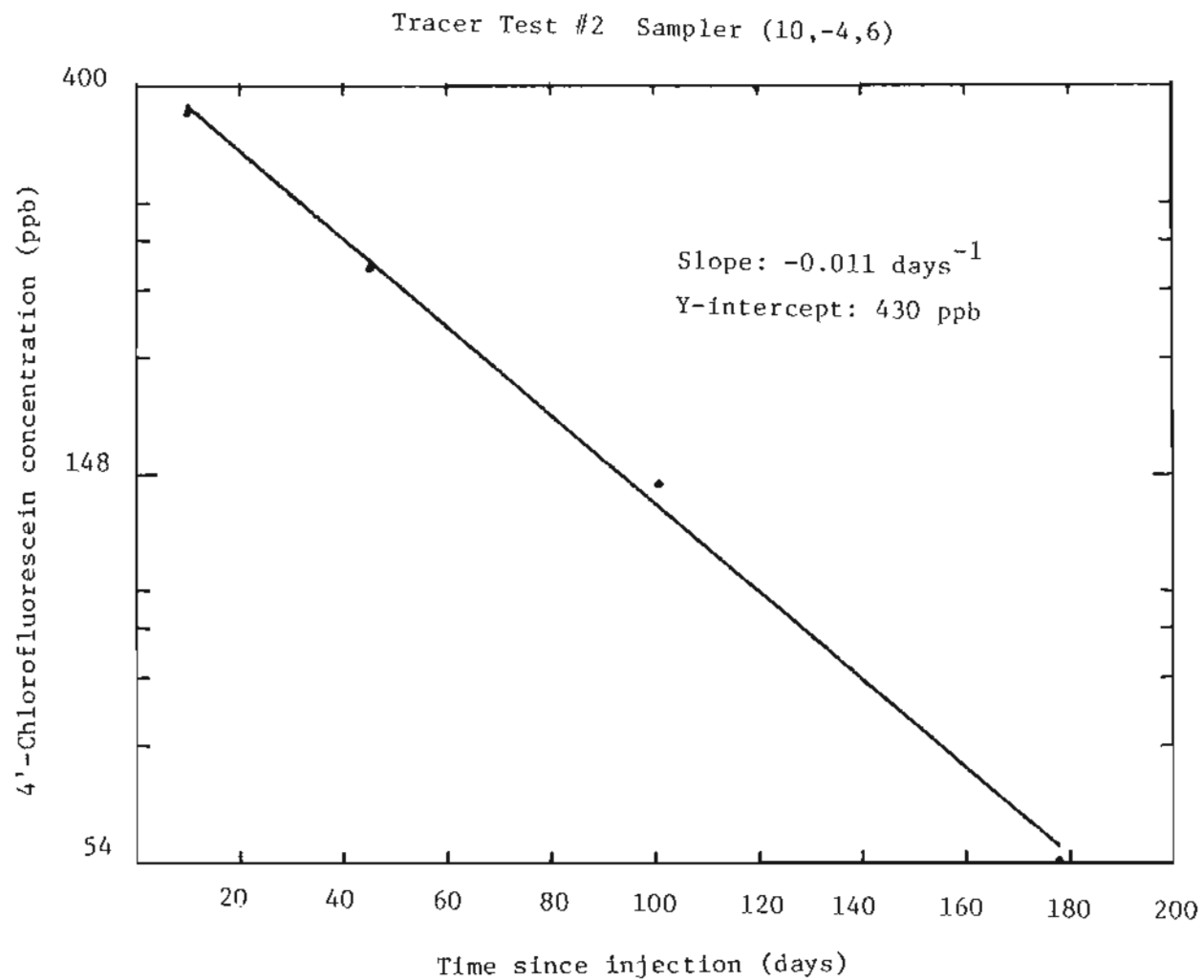


Figure IV.C.2 Ln[fluorescein] as a function of time after injection for tracer test #1 at sampler (1,1,8) which was located approximately 1 m from an injection well.



injection for tracer test #2 at sampler (10,-4,6) which was located approximately 4 m from an injection well.

estimates of the decay constant,  $\alpha$ . From Figures IV.C.2 and IV.C.3, the source half-lives were estimated as 77 and 62 days for test #1 and test #2, respectively ( $t_{1/2} = 0.69/\alpha$ ). In addition to estimating the decay constants, the regression lines provide estimates of  $C_0$  in Equation IV.C.3. Using the relationship:  $C_0 = \exp(\text{y-intercept})$ ,  $C_0$  is estimated as 140-170 ppb for test #1 and 430 ppb for test #2. For test #1 this implies that the 60 L of 150 ppm fluorescein solution which was injected to initiate the test, was diluted shortly after injection by a factor of approximately 1000 and occupied a source volume of approximately  $100 \text{ m}^3$ . From the contour maps and integrated transects presented previously, the dimensions of the  $100 \text{ m}^3$  source volume may be estimated as H equal to 3 m, W equal to 4 m and L equal to 8 m, where H, W, and L are defined as for Equation IV.C.1. The  $C_0$  estimate for test #2, which was started with a 20 L injection of 250 ppm 4'-chlorofluorescein, provides a dilution factor of approximately 600 and a source volume of  $12 \text{ m}^3$ . The dimensions of the source volume for test #2 are estimated as H equal to 1.5 m, W equal to 2 m and L equal to 4 m.

The dilution factors calculated above for the tracer tests are approximately ten times greater than anticipated prior to injection based on a fracture porosity of 0.01 (Johnson, 1984). Dilution factors of 500-1000 imply a fracture porosity closer to 0.001. However, as will be seen in Chapter V and VI, the movement of the tracer plumes

support a fracture porosity of 0.01. In an attempt to resolve this inconsistency, a series of "push-pull" tests were conducted in the single level piezometers described in section II.C.2. The "push-pull" test procedure has been described in detail by Johnson (1984). Briefly, 7 L of 10 ppm 2',7'-dichlorofluorescein solution were injected into the groundwater through a single level piezometer. The piezometer was then flushed of 2',7'-dichlorofluorescein by injecting 3 L of groundwater. After a pre-determined time, groundwater was pumped to the surface from the piezometer and collected as a series of 10 L samples. Aliquots of the 10 L samples were returned to the laboratory for analysis. Figure IV.C.4 is a plot of maximum  $C/C_0$  vs. the time after sampling that pumping was initiated for series of "push-pull" tests. This figure shows that the maximum  $C/C_0$  decreased rapidly with increasing residence time (i.e., the time between injection and removal of tracer from the immediate vicinity of an injection well by either pumping or advection) and that only four hours after injection, the maximum recoverable concentration was approximately 100 times lower than the injected concentration. Therefore, the observed dilution factors of 500-1000 appear possible since the natural-gradient tracer tests have residence times on the order of several days.

The vertical fractures which have been observed in soil cores taken near the tracer site provide a possible explanation for why a lower value of fracture porosity is estimated based on the dilution factors. In the soil cores the vertical fractures appeared to have

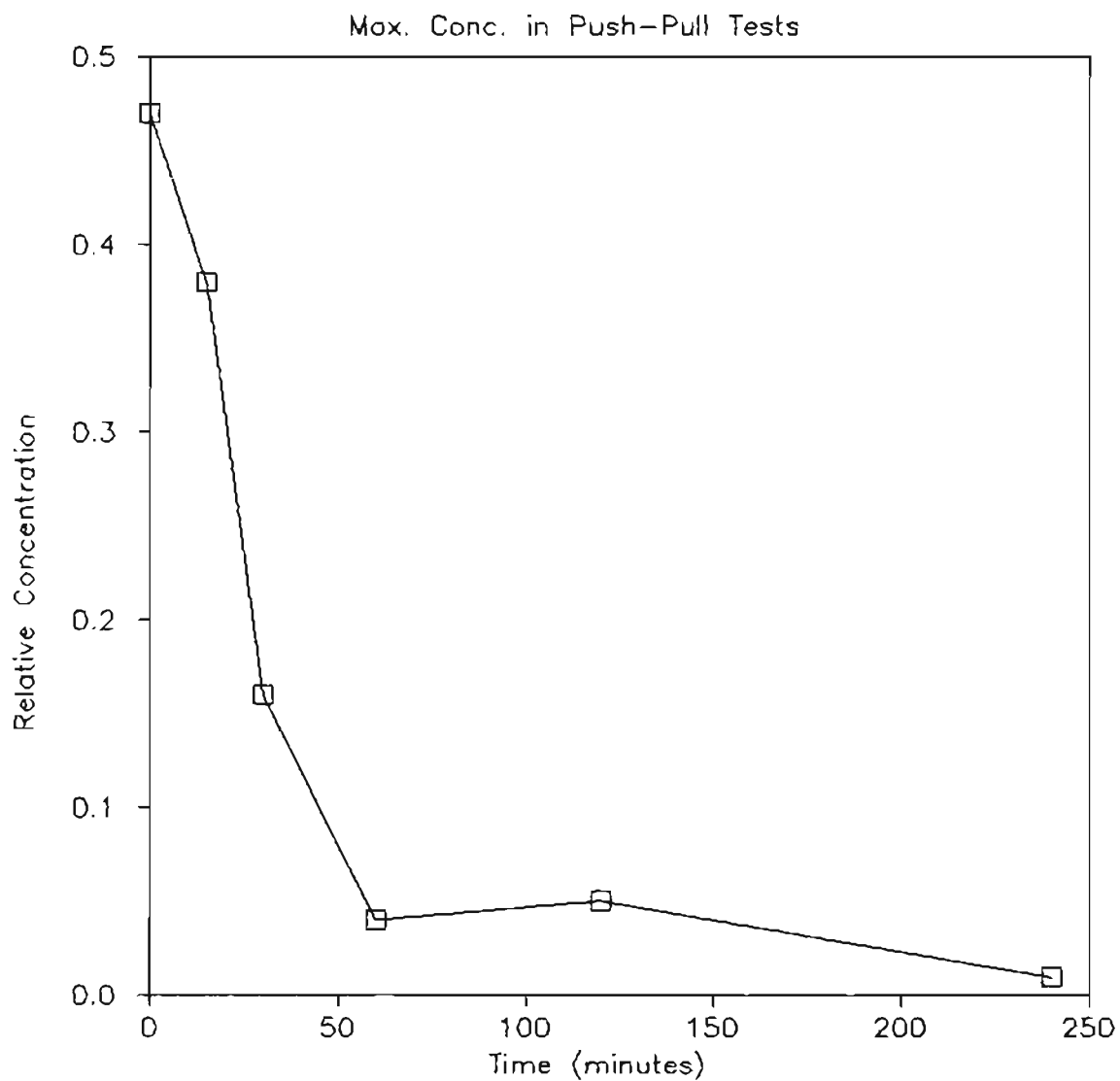


Figure IV.C.4 Maximum relative 2',7'-dichlorofluorescein concentration as a function of elapsed time between tracer injection and sampling initiation for a series of "push-pull" tests.

larger apertures and to be more widely and irregularly spaced than the horizontal fractures. The vertical fractures might then be the primary conduits for transport of the solution in the time immediately after injection. If the vertical fractures are continuous for distances on the order of 1-10 m, then the fractured soil would behave with a local-scale fracture porosity of 0.001 and a macro-scale fracture porosity of 0.01.

Additional estimates of the source decay constant may be obtained from the integrated transects (Figures IV.B.1 and IV.B.2). The total tracer mass in the source region may be estimated by integrating a transect between the lower and upper x-axis boundaries of the source regions. The  $\ln$ [tracer mass in the source region] vs. time after injection are plotted for tracer tests #1 and #2 in Figure IV.C.5. As was done above for the measurements within the source region, the slopes of the regression lines in Figure IV.C.5 may be used to estimate the source half-lives for the two tracer tests. This provides source half-life estimates of 54 days for test #1 and 109 days for test #2. These values agree well with the half-lives estimated based on measurements in individual samplers within the source region.

#### IV.D. The Moments of the Tracer Plumes

Effective assessment of the advective and dispersive nature of the tracer plumes is supplied by examination of the spatial moments of the

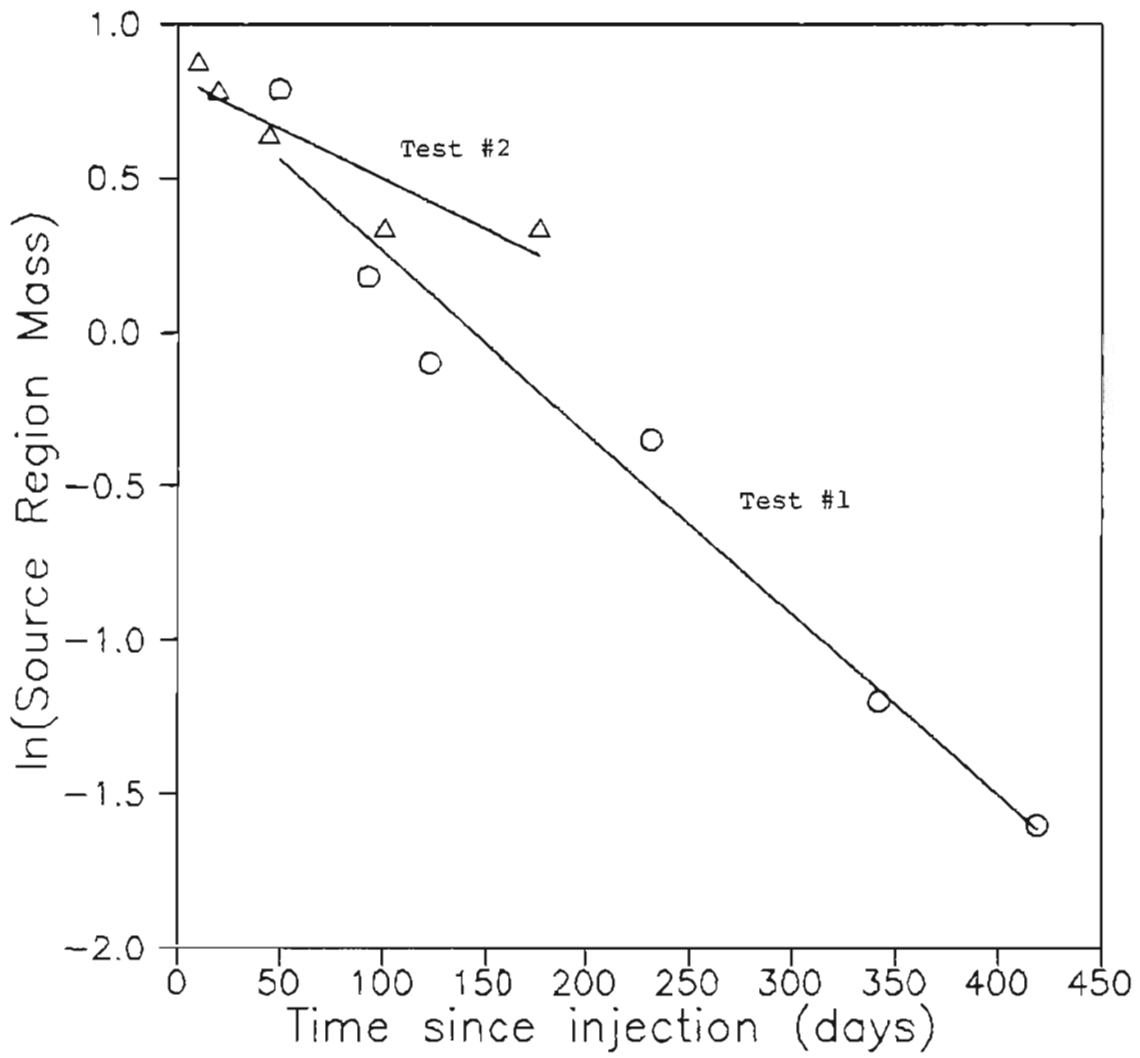


Figure IV.C.5 Ln[tracer mass in the source region] as a function of time after injection for tracer tests #1 and #2.



concentration distributions. The spatial moments are defined as

$$M_{ijk} = \iiint_{-\infty}^{\infty} x^i y^j z^k nC(x, y, z, t) dx dy dz \quad (\text{IV.D.1})$$

where  $n$  is the total porosity. The moments of greatest interest are

$$\begin{aligned} M_{000} &= \text{total mass of tracer} \\ \bar{X}_C &= M_{100}/M_{000} = \text{x-coordinate of the center of mass} \\ \bar{Y}_C &= M_{010}/M_{000} = \text{y-coordinate of the center of mass} \\ \sigma_{xx}^2 &= M_{200}/M_{000} - X_C^2 = \text{variance about } X_C \\ \sigma_{yy}^2 &= M_{020}/M_{000} - Y_C^2 = \text{variance about } Y_C \\ \sigma_{xy}^2 &= M_{110}/M_{000} - X_C Y_C = \text{covariance in the xy-plane} \end{aligned}$$

The spatial moments of the vertically averaged plumes associated with the first and second tracer tests are presented in Tables IV.D.1 and IV.D.2, respectively. The tables each contain two columns for tracer mass. The columns labeled  $M_t$  refer to the mass in the total concentration distribution which includes the source and plume regions (see section IV.B). The columns labeled  $M_p$  refer only to the plume region of the concentration distributions and were calculated from Equation IV.D.1 by setting the lower limit of integration for the  $x$ -dimension equal to the origin of the plume as indicated by the integrated transects. In the case of the first test, for example, the origin of the plume was set at  $x = 6\text{m}$ .

TABLE IV.D.1 Spatial moments of the vertically averaged fluorescein plume from tracer test #1

Time Since Injection (days)	A Total Mass (grams)	B Source Mass (grams)	A-B Plume Mass (grams)	B/A	Center of Mass		Average Velocity		Plume Variance			Prin. Values of Variance	
					$\bar{X}$ (m)	$\bar{Y}$ (m)	$\bar{V}_x$ (cm/day)	$\bar{V}_y$ (cm/day)	$\sigma_{xx}^2$ (m <sup>2</sup> )	$\sigma_{yy}^2$ (m <sup>2</sup> )	$\sigma_{xy}^2$ (m <sup>2</sup> )	$\lambda_{xx}^2$ (m <sup>2</sup> )	$\lambda_{yy}^2$ (m <sup>2</sup> )
50	7.7	2.2	5.5	0.28	14.5	6.9	17	14	51	40	-13	60	31
93	12.3	1.2	11.2	0.10	21.	8.3	16	9	119	37	-11	120	36
123	12.5	0.9	11.6	0.07	23.	7.8	14	6	164	45	-9	165	44
232	7.8	0.7	7.1	0.09	26.	6.0	9	2	179	53	-13	180	52
342	7.6	0.3	7.3	0.04	29.5	3.4	7	1	196	57	-22	199	54
419	7.5	0.2	7.3	0.03	32.5	4.1	6	1	220	53	-33	226	47

TABLE IV.D.2 Spatial moments of the vertically averaged 4'-chlorofluorescein plume from tracer test #2

Time Since Injection (days)	A Total Mass (grams)	B Source Mass (grams)	A-B Plume Mass (grams)	B/A	Center of Mass		Average Velocity		Plume Variance			Prin. Values of Variance	
					$\bar{X}$ (m)	$\bar{Y}$ (m)	$\bar{v}_x$ (cm/day)	$\bar{v}_y$ (cm/day)	$\sigma_{xx}^2$ (m <sup>2</sup> )	$\sigma_{yy}^2$ (m <sup>2</sup> )	$\sigma_{xy}^2$ (m <sup>2</sup> )	$\lambda_{xx}^2$ (m <sup>2</sup> )	$\lambda_{yy}^2$ (m <sup>2</sup> )
10	3.0	2.4	0.6	0.80	15.0	-5.7	30	-37	17	--	--	--	--
20	2.8	2.2	0.6	0.78	15.3	-4.8	16	-14	16	--	--	--	--
45	2.5	1.9	0.6	0.76	16.4	-5.1	10	-7	18	3	-2	18	3
101	2.6	1.4	1.2	0.54	19.	-7.6	6	-5	26	24	-11	36	14
178	2.5	1.4	1.1	0.56	20.	-6.2	4	-2	34	22	-13	42	14

The estimates of total tracer mass,  $M_T$ , presented in Table IV.D.1 demonstrate that the monitoring network was successful in accounting for greater than 83% of the injected fluorescein mass on each sampling trip. On two occasions (sampling trips 2 and 3) the mass balance estimates exceeded 100%. However, by examining Figures IV.A.20 and IV.A.21 it can be seen that on days 93 and 123 the mass balance estimates would be expected to have an elevated uncertainty due to the large amount of mass which was in a sparsely sampled region of the monitoring network. The overall good agreement between injected and measured fluorescein mass provides strong evidence that a significant fraction of the tracer was not missed by the monitoring network.

The mass balance estimates for test #2 are more consistent than for test #1. However, only 50%-60% of the injected 4'-chlorofluorescein was accounted for by the monitoring network. The most likely explanation for the low recoveries is that a significant fraction of the injected mass remained trapped near the injection well. An alternate explanation is provided by the fact that the center of the plume for test #2 was in a region of the monitoring network in which few piezometers were located. This low density of piezometers increased the probability of underestimating the maximum concentration and therefore lower estimated recoveries.

The centers of mass of the plumes generated by tests #1 and #2, as estimated by the first central moment, are also presented in Tables IV.D.1 and IV.D.2. The source regions of the concentration distributions were excluded from the calculations of the center of mass estimates. The first moment estimates indicate that the average direction of travel over the duration of the tests was approximately parallel with the hydraulic gradient and the x-axis of the monitoring network. This can be seen clearly in Figure IV.D.1 which shows the center of mass versus time for both tests. Figure IV.D.1 also suggests that the rate of change of central location decreased with increasing distance and time.

The rate of change of central location or average velocity was calculated from the first central moment by

$$v_{ave} = \{(x_i - x_0)^2 + (y_i - y_0)^2\}^{0.5} / (t_i - t_0) \quad (IV.D.2)$$

Average velocity versus time for test #1 and #2 is plotted in Figure IV.D.2 which clearly demonstrates that the average velocity decreased with increasing time and distance for both tests. This trend does not correlate with the observed fluctuation in hydraulic gradient. However, it will be shown in Chapter 5 that the observed decreasing rate of translation of the center of mass (excluding the source region) is consistent with a plume originating with an exponentially decaying source function and traveling under the influence of a constant groundwater velocity.

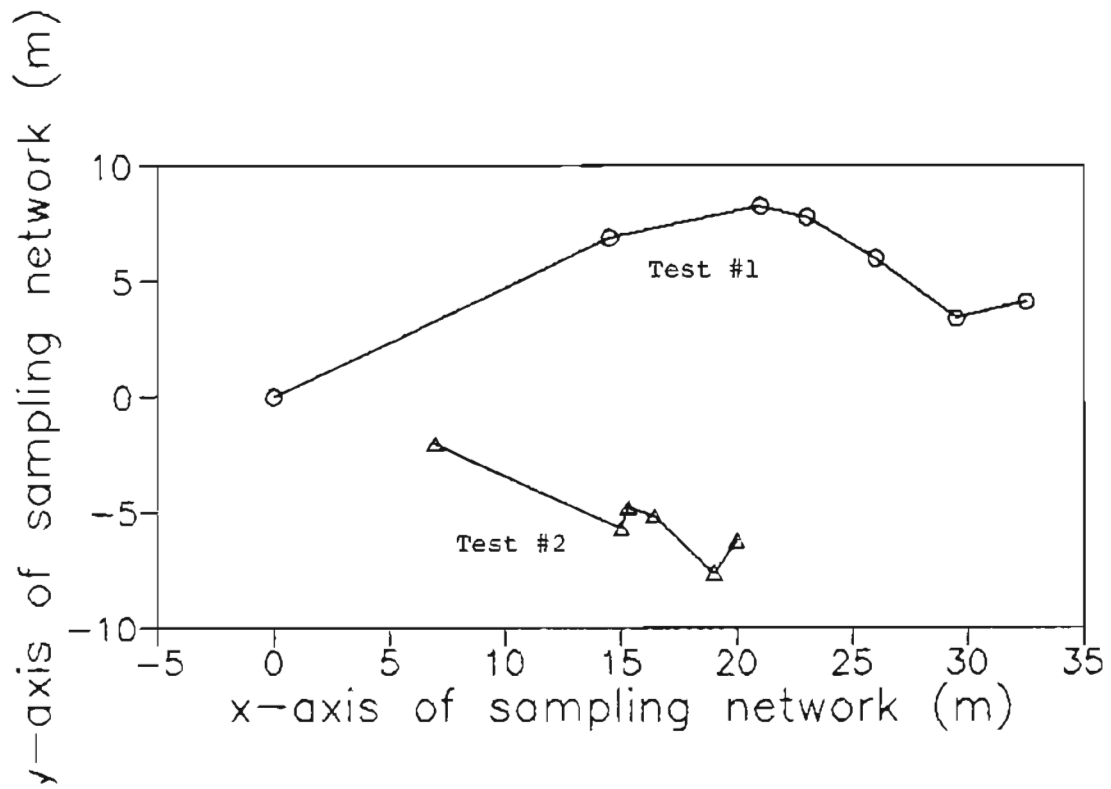


Figure IV.D.1 Plume center of mass as a function of time after injection for tracer tests #1 and #2.

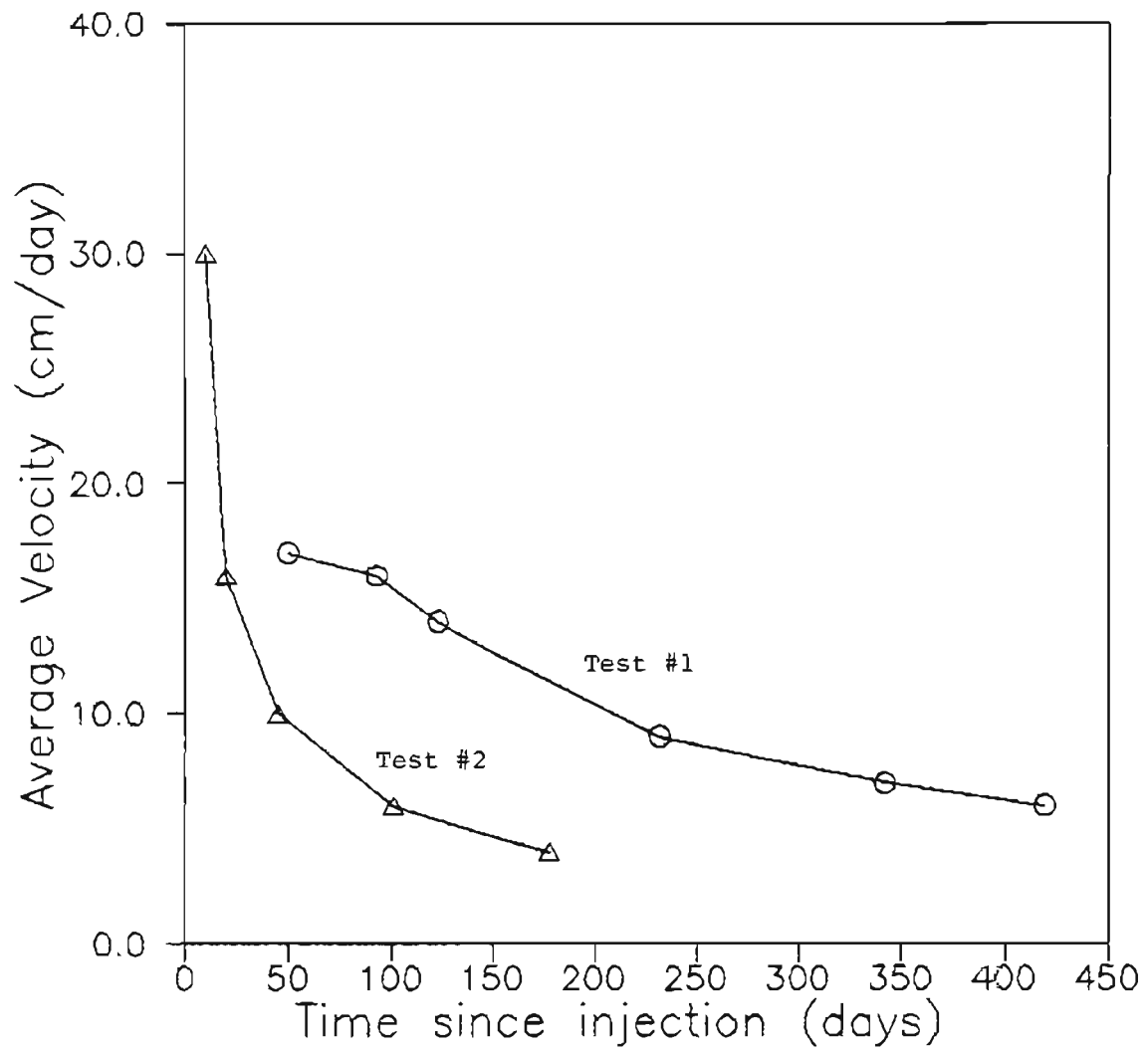


Figure IV.D.2 Average plume velocity as a function of time after injection for tracer tests #1 and #2.

The variances and covariances associated with the plume from each test are also contained in Tables IV.D.1 and IV.D.2. The variances along the x- and y-directions are seen to have increased with time and distance. The relatively small values for covariance in comparison to the variances suggests that the principal axes of the plumes correspond closely with the principal axes of the monitoring network. However, it is useful to diagonalize the variance-covariance tensor of the vertically averaged concentration distributions before proceeding with further interpretation of the 2nd central moments. This transformation, accomplished by calculating the eigenvalues of the variance-covariance tensor, provides a simpler form of the variance-covariance tensor with the values of off-diagonal members (covariances) equal to zero. The principal values of the variance-covariance tensors,  $\lambda_{11}$  (longitudinal) and  $\lambda_{22}$  (horizontal transverse), also are contained in Tables IV.D.1 and IV.D.2. Since the magnitude of the covariances in the untransformed tensors was relatively small, the transformation does not have a large impact and the principal values agree closely with the original variance estimates.

The principal values of the longitudinal and horizontal transverse variances are shown in Figures IV.D.3 and IV.D.4 for tests #1 and #2, respectively. The figures demonstrate that, as expected, both tests evidenced the greatest spreading in the direction of groundwater flow. The observed ratios of longitudinal to transverse variance (ranging from 3/1 to 5/1) are lower than the 10/1 to 20/1 ratios commonly quoted



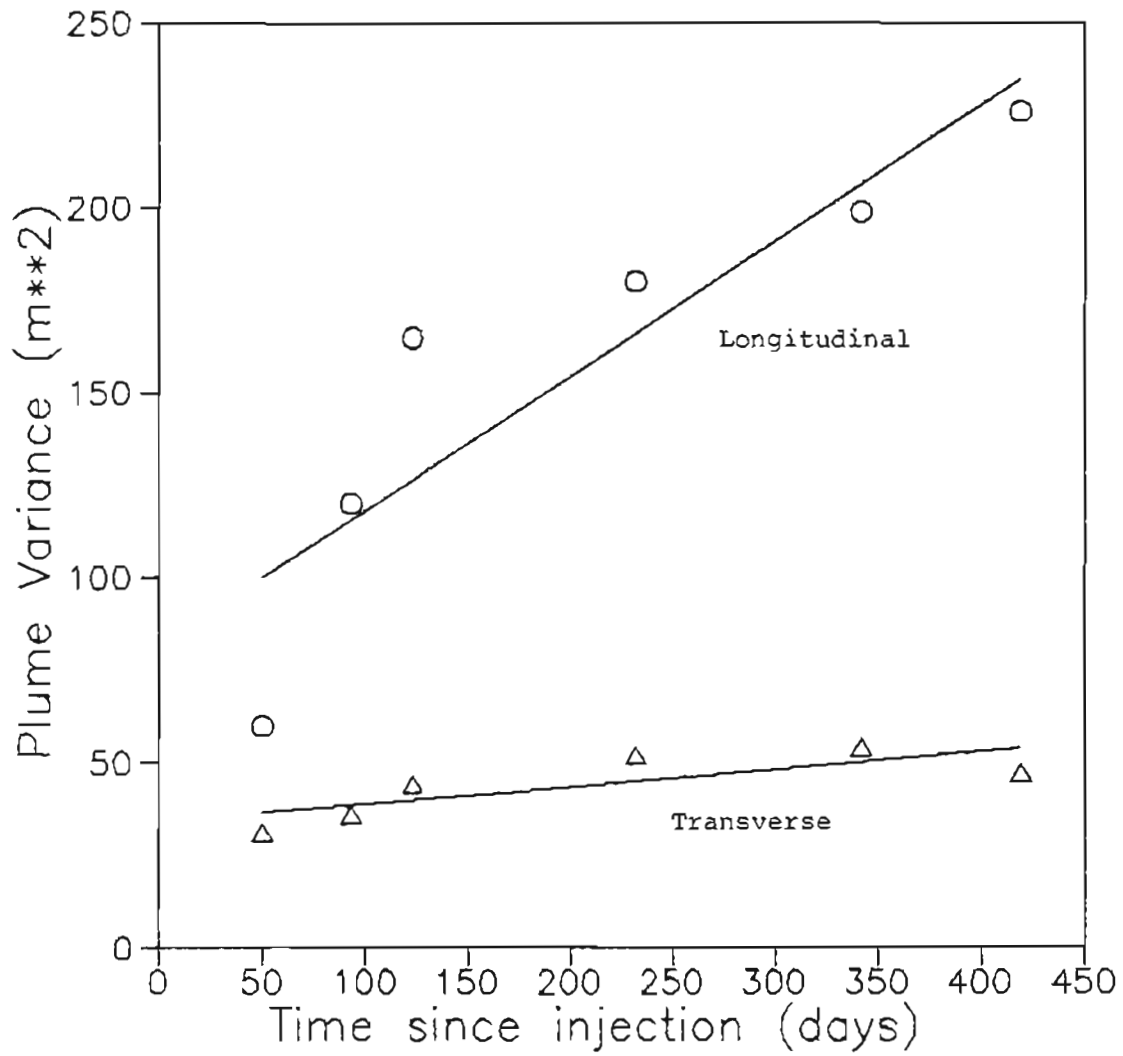


Figure IV.D.3 Principal values of the longitudinal and horizontal transverse plume variances as a function of time after injection for tracer test #1.

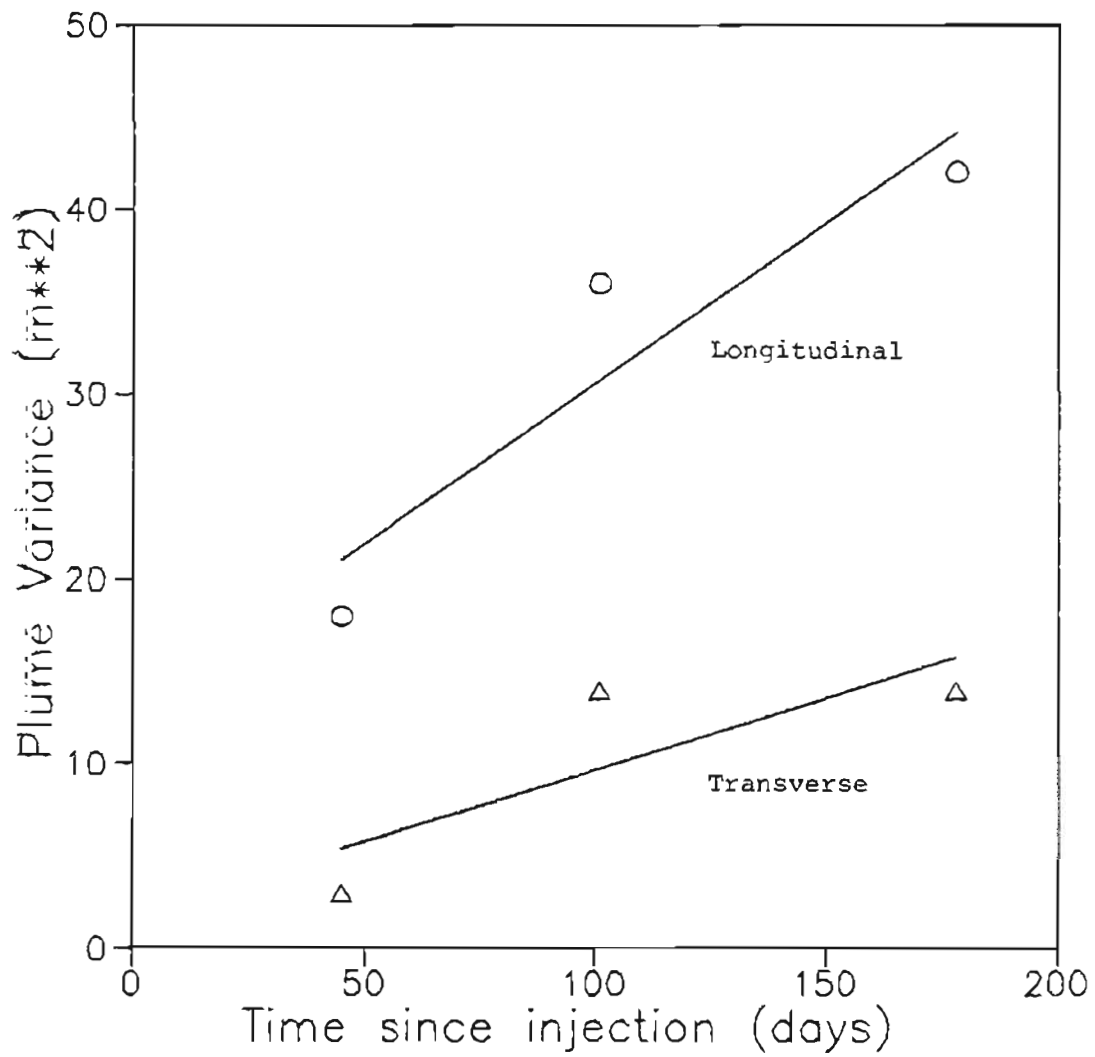


Figure IV.D.4 Principal values of the longitudinal and horizontal transverse plume variances as a function of time after injection for tracer test #2.

for large contaminant plumes (Anderson, 1979), but do agree well with ratios reported for other recently conducted natural-gradient tracer tests (4/1, Sudicky et.al., 1984; and 6/1, Freyberg, 1986). Figures IV.D.3 and IV.D.4 show that, in general, the longitudinal and transverse variances increase with time for both tests. A functional form may not be confidently assigned to the observed growth rates due to the small number of variance estimates together with the uncertainty associated with the estimates. However, as a first approximation, the figures include the least-squares regression lines for the data points. The linear fits appear to describe the observed variance growth rates reasonably well.

Classic advection-dispersion theory predicts that the variance of an injected slug will increase linearly with time. The use of linear fits in Figures IV.D.3 and IV.D.4 therefore assumes that the classic advection-dispersion description of an injected slug is appropriate for describing the tracer tests conducted for this study. Under this assumption, longitudinal and transverse dispersivities ( $A_{jj}$ ) may be estimated as

$$A_{jj} = D_{jj}/v \quad (\text{IV.D.3})$$

where  $v$  is the average plume velocity and  $D_{jj}$  is the dispersion coefficient defined by

$$D_{jj} = d\sigma_{jj}^2 / 2dt \quad (\text{IV.D.4})$$

The dispersion coefficients are therefore simply one-half the slopes of the best fit lines in Figures IV.D.3 and IV.D.4. Using Equations IV.D.3 and IV.D.4 and the slopes from Figures IV.D.3 and IV.D.4, apparent dispersivities were calculated as:

$$\begin{array}{lll} A_{xx} = 2.6m & A_{yy} = 0.4 m & \text{for test \#1} \\ A_{xx} = 2.2m & A_{yy} = 0.9m & \text{for test \#2} \end{array}$$

The above dispersivities represent average values over the duration of each test. The values for longitudinal dispersivity agree well with a series of dispersivity estimates that were judged to be highly reliable in a recent review of field-scale porous media transport processes (Gelhar et.al., 1985).

#### IV.E Summary

This chapter has presented a detailed description of the observed tracer migration patterns. The basis of this description was the large data base provided by the periodic sampling of the dense array of multi-level piezometers. This data base was summarized graphically with contour maps and integrated transects which provided a means for qualitatively assessing the direction and rate of plume movement as well as the degree of spreading. In addition, examination of the graphical representations prompted an investigation into the possibility of a decaying source function. Investigation of this possibility provided experimental evidence which has clearly

demonstrated that the functional form of the source function associated with each tracer test was best described as an exponential decay with a time constant of approximately  $0.01 \text{ days}^{-1}$ .

The data base generated by the periodic sampling of the two tracer tests was mathematically summarized by estimating the zeroeth-, first-, and second-order moments of the measured concentration distributions. The lower order moments provided a concise method of characterizing the spatial structure of the tracer distributions. The mass balance estimates provided by the zeroeth-order moments demonstrated that the monitoring network accounted for greater than 83% of the injected fluorescein mass on each sampling trip associated with tracer test #1. Estimates of the first moments indicated that the average direction of travel over the duration of the tests was approximately parallel with the observed hydraulic gradient and the x-axis of the monitoring network. In addition, the average plume velocity, as estimated by the first moments, decreased with increasing time for both tests. The second-order moments characterized the degree of spreading associated with the tracer plumes. As expected, plume spreading was strongest in the direction of groundwater flow. Furthermore, the second-order moments together with the classical advection-dispersion equation served as the basis for estimating longitudinal and transverse dispersivities characteristic of the site. The estimated dispersivities agreed well with those reported recently by other workers (Freyberg, 1986; and Gelhar et.al., 1985).

## V. MODELING THE TRANSPORT OF THE TRACER COMPOUNDS

### V.A Introduction

The preceding chapter described the observed behavior of tracer compounds migrating under the influence of the natural flow regime at the Alkali Lake CDS. The tracer migration patterns were found to exhibit features associated with porous media transport (e.g., regularity of plume shape) and fractured media transport (e.g., exponentially decaying source function). The tracers were shown to be influenced by matrix diffusion, advection and dispersion. In this chapter the relative roles will be determined for the processes which produced the concentration profiles observed in the tracer tests. Computer simulations will be the primary tool for carrying out these determinations. Two physical models will serve as the basis for the simulations; an idealized fracture network and an equivalent porous medium (EPM). The purposes for employing the two physical models are:

- 1) to evaluate the relative merits and limitations of both approaches in terms of their abilities to explain solute transport at the CDS; and
- 2) to provide the perspective which comes from performing an examination from more than a single point of view.

## V.B. Application of an Idealized Fracture Network Model

### V.B.1. Determining the Appropriate Fracture Network Model

There are innumerable fracture network idealizations which can serve as the physical model for simulating transport in the fractured soil at the Alkali Lake CDS. Selection of a specific idealization is a compromise between remaining faithful to the observed properties of the CDS and retaining tractability with respect to computational and data input requirements. The idealization should incorporate the most important features of the observed system. Therefore, it is useful at this point to review the physical properties of the fractured soil in which the tracer tests were conducted.

The soil in the area of the tracer tests is imbedded with a dense network of apparently highly interconnected fractures. There are two sets of fractures; a horizontal set and a vertical set. The work of Johnson (1984) and this study have resulted in the characterization of the fracture system. The properties of the horizontal fractures include very regular interfracture spacing of  $\sim 3\text{mm}$  and average aperture of  $\sim 100\mu\text{m}$ . There is also evidence which indicates the horizontal fractures have considerable spatial continuity. The vertical fractures are less regularly spaced at intervals of 5 - 10cm with apertures averaging approximately 1mm. The continuity of the vertical fractures appears limited in comparison to the horizontal fractures. In addition, there is considerable variability in the orientation of the

vertical fractures with respect to the centerline of the tracer site. The soil matrix which separates the fractures consists of a highly porous material possessing significantly lower permeability.

As stated above, there are many possible conceptual idealizations of fracture networks. Potentially the most realistic idealization would be a 3-dimensional network such as the one illustrated schematically in Figure V.B.1. Recently, 3-dimensional networks have provided the basis for simulations reported by Smith et.al. (1985). Those simulations required very detailed specification of the fracture networks including the spatial structure of each fracture and the location of all fracture intersections. The fracture parameters were described probabilistically because available field data did not justify deterministic specification.

Theoretically, 3-dimensional network models should provide the greatest physical accuracy due to the ability to consider features such as more than one set of fractures. However, there are several severe problems with implementing the simulation of transport at the Alkali Lake CDS on the basis of a 3-dimensional network model. One problem is that mixing at fracture intersections is a poorly understood phenomenon. Therefore, any specific mathematical description of the mixing process is difficult to justify. The second problem is that, at their current stage of development, computer programs available for simulating 3-dimensional networks exclude matrix diffusion, a process which must be considered at the Alkali Lake site. The third problem is



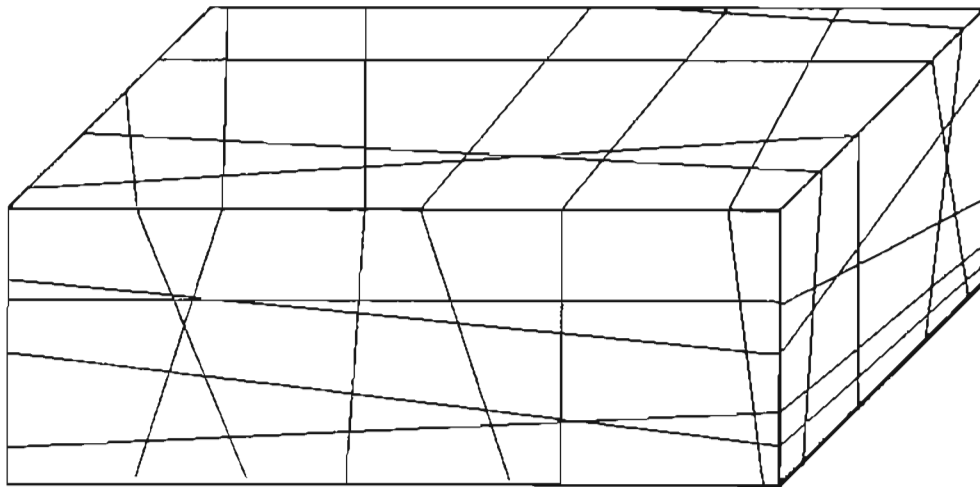
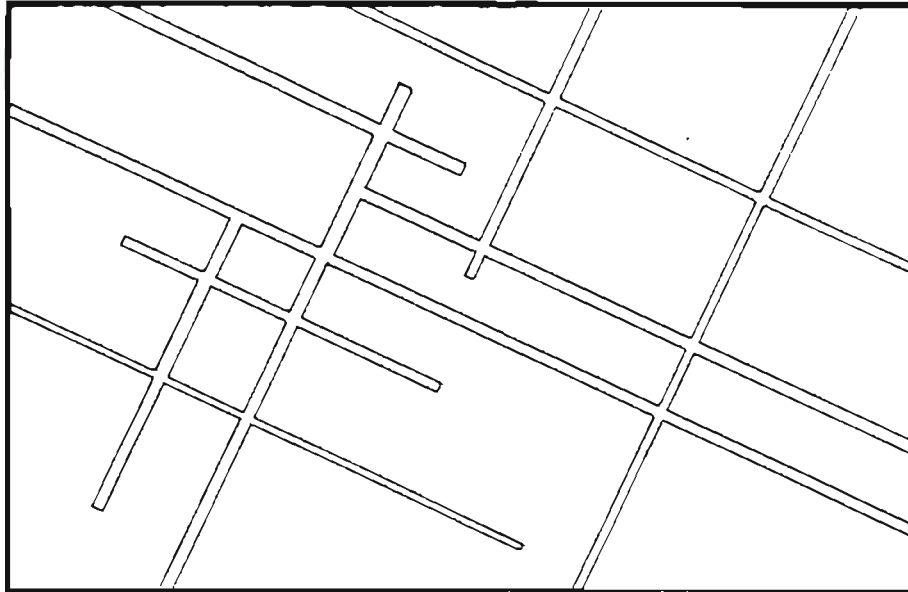


Figure V.B.1 Schematic drawing of an idealized three-dimensional fracture network.

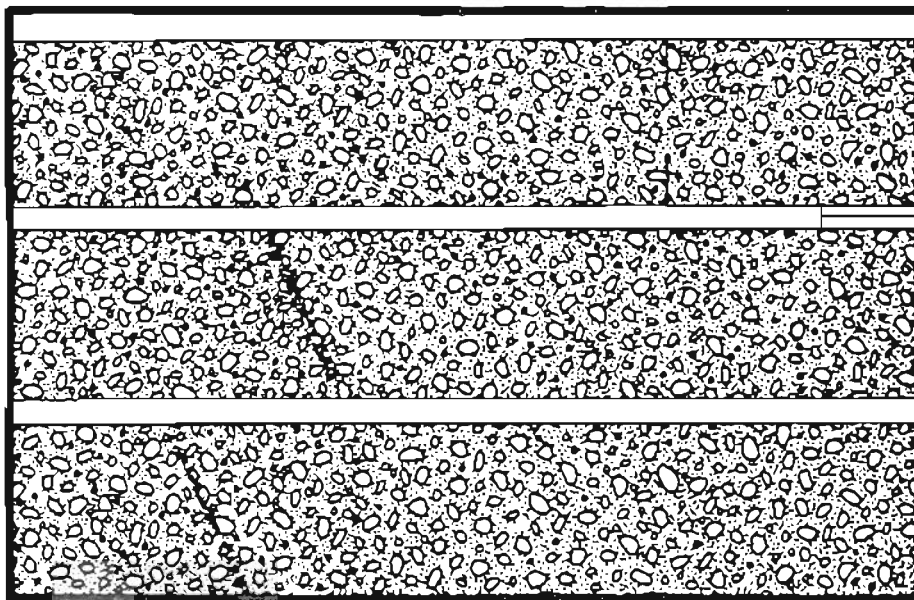
that because of the dense fracture network and the scale at which transport is of interest (10 - 100m), the computational and data storage requirements would mandate the use of a super-computer, even if matrix diffusion was not considered. Therefore, a 3-dimensional conceptual model was not selected as the appropriate fracture network idealization for this study.

The obvious next step down the ladder of idealizations is to employ a 2-dimensional conceptual model. As shown in Figure V.B.2, the possibilities are a plan view and a vertical cross-section. Each of the possibilities has advantages and disadvantages. The primary advantage offered by the plan view idealization is the possibility for examining horizontal transverse dispersion. This advantage is more than offset by the fact that the plan view concept neglects the horizontal set of fractures which the field evidence indicated was important. In addition, the currently available computer programs for a plan view network suffer the same practical problems as the 3-dimensional programs including: 1) the lack of a consensus for the functional form of mixing at fracture intersection; 2) the inability to consider matrix diffusion; and 3) the need for a super-computer because of computational and data storage requirements. Therefore, the plan view idealization was not investigated further in this study.

The 2-dimensional vertical cross-section idealization offers several advantages with respect to the Alkali Lake site. Firstly, it



A)



B)

Figure V.B.2 Schematic drawings of an idealized two-dimensional fracture networks: A) Plan view and B) Vertical cross-section.

focuses on the set of horizontal fractures, an important feature of the tracer site. Secondly, because of the observed regularity in interfracture spacings, the concept of symmetry may be invoked to enable the derivation of solutions which consider matrix diffusion. Thirdly, the cross-sectional model served as the basis for Johnson's (1984) successful simulations of push-pull tests conducted at the site. The main disadvantage of the cross-sectional model is the lack of a method for examining horizontal transverse dispersion. In view of the alternatives, this was not considered to be a major drawback and the vertical cross-section concept was selected as the idealization on which to base discrete fracture modeling of transport at the CDS.

The description of the vertical cross-section idealization has been very general to this point. This description must be further refined, by stating the specific characteristics of the fractures and soil matrix, in order to define a unique fracture system idealization amenable to mathematical description. The following characteristics uniquely define the cross-sectional idealization employed in this study: 1) the fractures are represented by a series of evenly spaced, identical, constant aperture, parallel plates of infinite extent in the horizontal plane; 2) the fracture apertures are much less than the interfracture spacings; 3) the groundwater velocity in the fractures is constant and much greater than in the soil matrix; 4) plug flow occurs within the fractures (i.e. the velocity profile is flat); 5) mechanical dispersion within the fractures is negligible; 6) sorption on the

fractures walls and in the soil matrix is negligible; 7) the soil matrix has constant, uniform porosity of non-negligible magnitude; 8) diffusion within the matrix occurs only perpendicularly to the direction of groundwater flow.

Because of the symmetry in the system described above, only one-half of one fracture and one-half of one matrix block need to be simulated. The governing equations for transport in the defined idealized fracture network may be written as:

$$\text{fracture } \frac{dC}{dt} + \frac{v dC}{R dz} - \frac{n D dC'}{b R dx} \Big|_{x=b} = 0 \quad 0 < z < \infty \quad (V.1)$$

$$C(z, 0) = 0 \quad \text{initial condition}$$

$$C(0, t) = g(t) \quad \text{boundary condition}$$

$$C(\infty, t) = 0 \quad \text{boundary condition}$$

$$\text{matrix } \frac{dC'}{dt} - \frac{D d^2 C'}{R' dx^2} = 0 \quad b < x < B \quad (V.2)$$

$$C'(x, z, 0) = 0 \quad \text{initial condition}$$

$$C'(b, z, t) = c(z, t) \quad \text{boundary condition}$$

$$\frac{dC'}{dx} (B, z, t) = 0 \quad \text{boundary condition}$$

where

$C$  = solute concentration in the fracture.

$C'$  = solute concentration in the matrix block.

$n$  = matrix porosity

$b$  = one-half of the fracture aperture

$B$  = one-half of the interfracture spacing

$D$  = molecular diffusion coefficient in the matrix

$z$  = coordinate axis in the direction of flow

$x$  = coordinate axis perpendicular to the flow

$v$  = groundwater velocity in the fracture.

### V.B.2 Application of the Selected Fracture Idealization

A number of numerical and semi-numerical solutions have been reported for the coupled set of equations defined by Equations V.1 and V.2. Examples of numerical solutions include the finite-element based approach of Huyakorn et.al. (1983), and the finite-difference based methods of Grisak and Pickens (1980) and Johnson (1984). The numerical solutions share the advantages of providing potential for removing the requirement of evenly spaced and identical fractures and the ability to readily incorporate a variety of source functions. However, the numerical approaches are limited by unmanageable computational and data storage requirements due to the difference between the scale at which matrix diffusion must be modeled (hundreds of microns) and the scale of interest for the tracer transport (several tens of meters).

The semi-numerical (semi-analytical) solutions available include those of Barker (1982) and Skopp and Warick (1974). The approach of Barker was not employed for this study because it relies on the numerical inversion of a complicated Laplace transform, an inherently

unstable and highly specialized operation. On the other hand, the only numerical procedure required by the solution of Skopp and Warick is the evaluation of a single integral, an operation for which many standard techniques exist. Therefore, the solution of Skopp and Warick (1974) was selected for implementation in this study. From Skopp and Warick (1974), the concentration in a fracture is given by:

$$\frac{C}{C_0} = \frac{2}{\pi} \int_0^{\infty} \exp(-wh^-) \left\{ \sin \left[ \frac{\varepsilon^2 T^0}{2} - wh^+ \right] + \sin(wh^+) \right\} \frac{d\varepsilon}{\varepsilon} \quad (V.3)$$

where  $T^0 = t - \frac{z}{v}$

$$h_{\pm} = \frac{\varepsilon}{2} \left[ \frac{\sinh(\sigma\varepsilon) \pm \sin(\sigma\varepsilon)}{\cosh(\sigma\varepsilon) + \cos(\sigma\varepsilon)} \right]$$

$$\sigma = \frac{B - b}{\sqrt{D}}$$

$$w = \frac{\theta z \sqrt{D}}{bv}$$

and  $\theta$  = fracture porosity

Equation V.3 provides the following advantages: 1) relatively straightforward evaluation; 2) requires evaluation only for times and locations of interest; 3) computer program to implement Equation V.3 will run quickly and require only a small amount of memory.

Two computer programs were developed to calculate the solute concentration in the fracture according to Equation V.3 for specified

times and distances along the fracture. The distinguishing feature between the two programs was the use of different numerical integration algorithms. The first program used a weighted Gaussian quadrature algorithm with 64 Gauss points based on the Gauss-Laguerre formula. This algorithm has been applied successfully to Equation V.3 by Sudicky et.al. (1982). The second program employed an adaptive quadrature routine based on the algorithm presented by Forsythe et.al. (1977). The adaptive routine was designed to determine the location and number of nodes at which a function should be evaluated in order to estimate an integral with some prescribed degree of accuracy. Both programs were verified by running them for the parameters given in the Case 3 example of Sudicky et.al. (1982). Figure V.B.3 presents the results of running the example case and indicates that the program which used weighted Gaussian quadrature integration calculated concentrations which agreed very closely with those obtained by Sudicky et.al. (1982) while the program which relied on the adaptive integration algorithm did not perform acceptably.

The tracer tests conducted in this study were initiated with injections of short duration. However, Equation V.3 and the programs discussed above are based on a constant source function. Therefore, the programs required modification in order to simulate a pulse type source function. The modification was implemented by applying the principle of superposition which states that partial problem solutions can be added to form a composite solution. This principle applies to



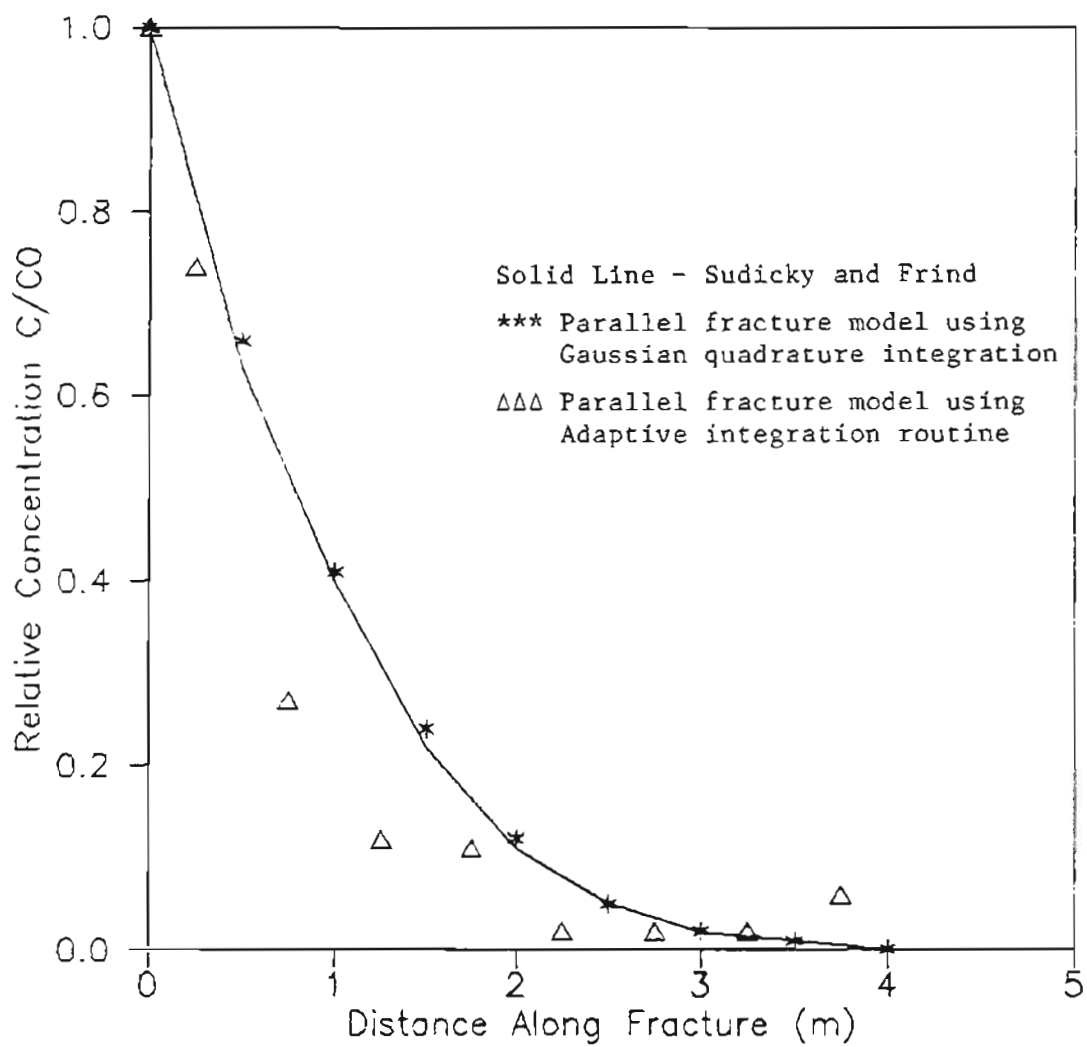


Figure V.B.3 Modeled concentrations provided by the two numerical integration algorithms as a function of distance along a fracture compared with the results of Sudicky and Frind (1982).

systems which are governed by linear partial differential equations (Reilly et.al., 1984). Examination of Equations V.1 and V.2 shows that the equations are linear and therefore forming linear combinations of their partial solutions is valid. The method of applying superpositioning to Equation V.3 to simulate a pulse type source was as follows: 1) evaluate Equation V.3 for a continuous positive source starting at  $t=0$ ; 2) evaluate Equation V.3 for a continuous negative source starting at  $t=p$  where  $p > 0$  and is equal to the duration of the injection pulse; and 3) add the concentrations from 1 and 2 to obtain the concentration for a given time and location. This three step procedure is illustrated in Figure V.B.4 which indicates a potential source of error in the method. Figure V.B.4 shows that superpositioning requires obtaining the difference between two large numbers, an inherently uncertain operation. This imposes a requirement that the integration in Equation V.3 be evaluated very accurately. To simulate the tracer tests, accuracy to five or more significant figures was needed because the maximum measured concentration after one year was over three orders of magnitude lower than the injected concentration.

The principle of superpositioning provided for the straightforward modification of the programs in order to simulate an injection slug. The programs were then applied to simulate the tracer tests by setting the parameters in Equation V.3 to the following values.

$$v = 1.0\text{m/day}$$

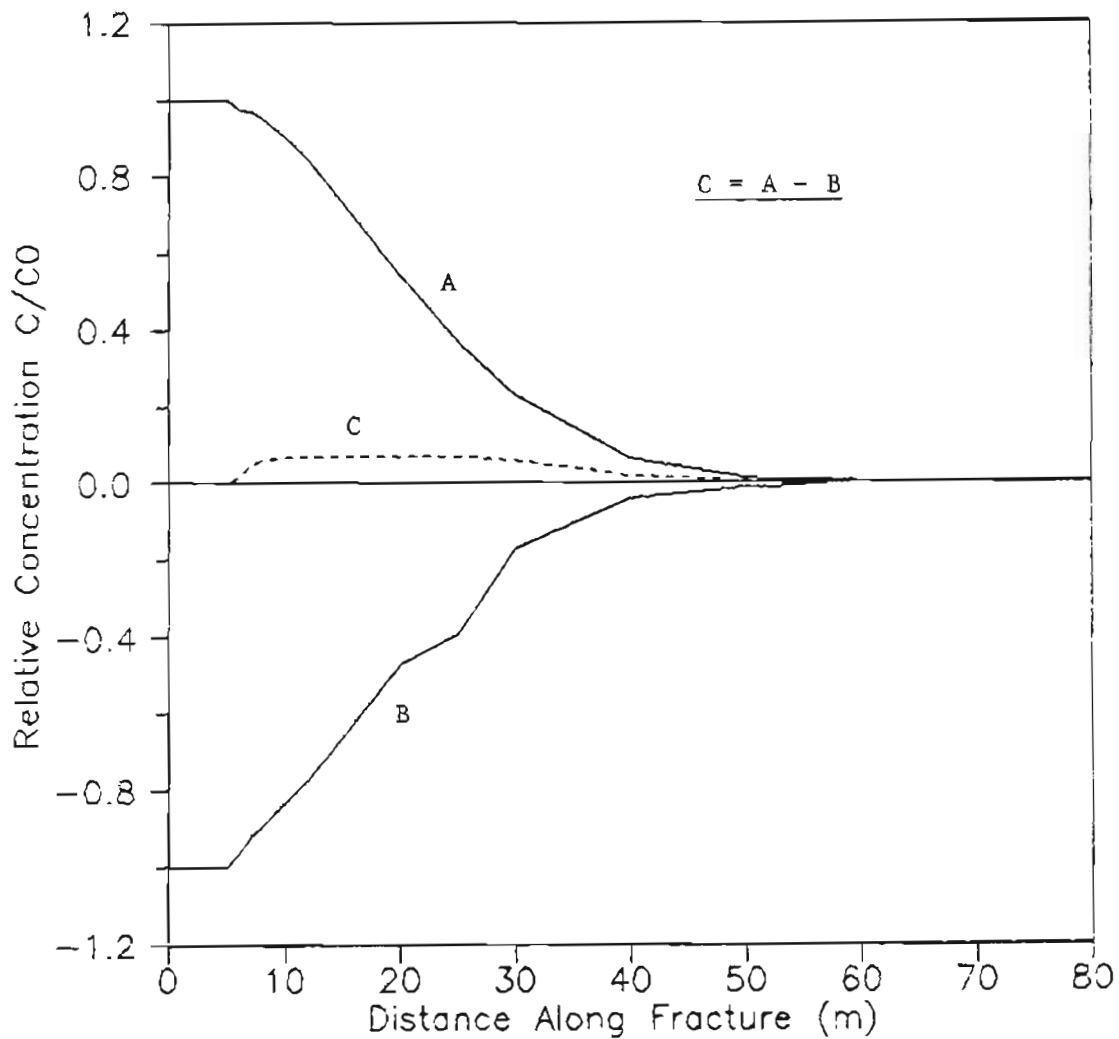


Figure V.B.4 Schematic diagram of the procedure used to apply the principle of superposition to simulate a pulse type source with a constant source function. Curve A is the relative concentration for a continuous positive source starting at  $t = 0$ ; Curve B is the relative concentration of a continuous negative source starting at  $t = p$  where  $p$  is the duration of the injection pulse; and Curve C is the sum of A and B and represents the relative concentration resulting from a pulse type source.

$$\theta = 0.6$$

$$B = 1.5\text{mm}$$

$$b = 50\mu\text{m}$$

$$D = \text{m/day}^2.$$

Neither integration routine proved capable of delivering the degree of accuracy necessary to precisely evaluate the subtraction operation mandated by the pulse type source function. Even with extensive operator intervention in an effort to optimize the integration parameters, both integration algorithms produced physically inconsistent concentration profiles (e.g., negative concentrations of non-negligible magnitudes).

Examination of Figure V.B.5 which is a graph of  $f(x)$  versus  $x$  where  $f(x)$  is the integrand in Equation V.3, provides some clues related to the difficulties encountered in accurately evaluating the integral. The apparent sources of error are 1) the wide range over which the function is of roughly equal magnitude; and 2) its highly oscillatory nature. These qualities are inherent in the function and are not readily mitigated by standard techniques such as variable transformation or re-scaling. Therefore, it is concluded that the cross-sectional fracture network idealization outlined in this section is not easily useful for quantitatively simulating the migration of a tracer pulse through a densely fractured porous aquifer for distances which are of interest in field situations. This in turn implies that

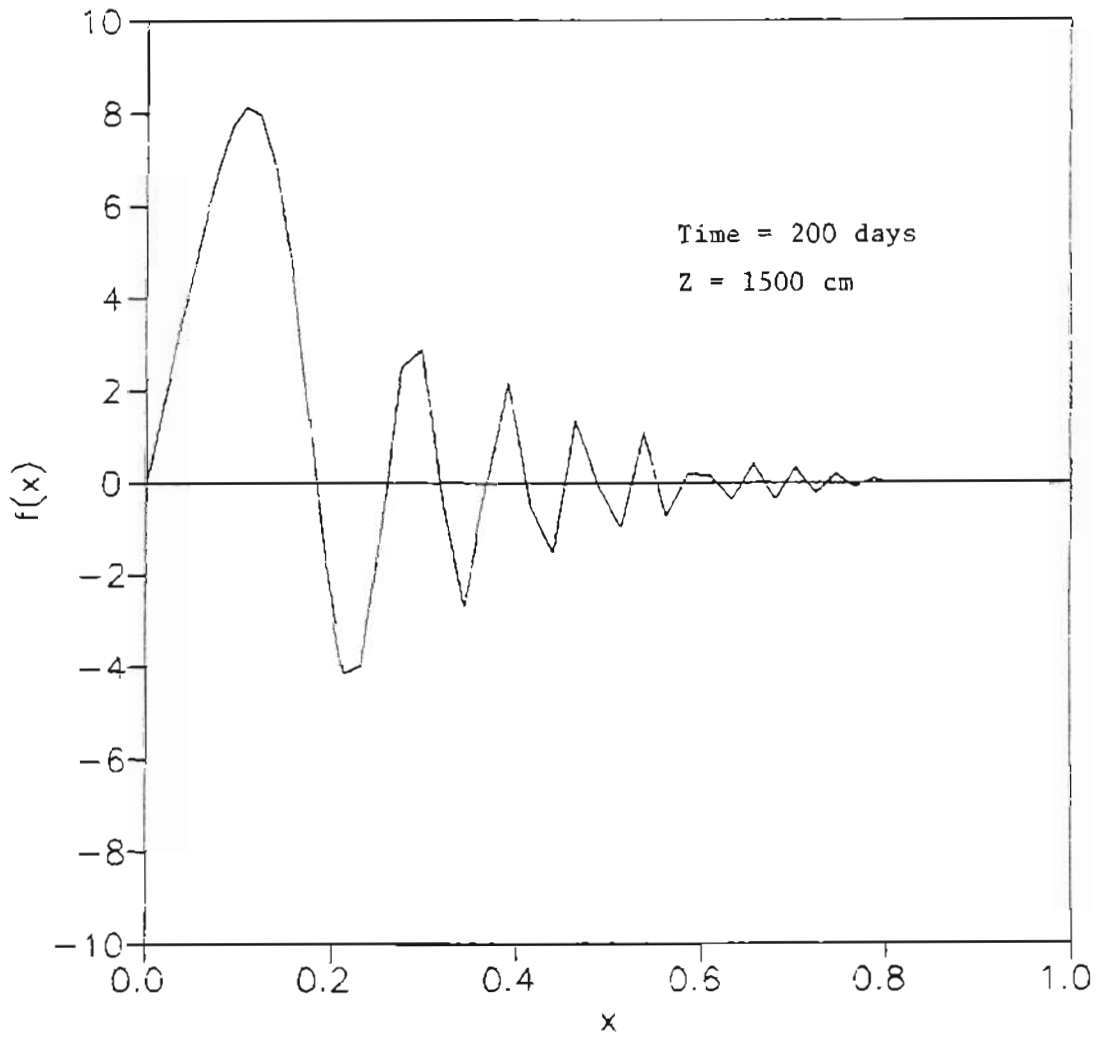


Figure V.B.5  $f(x)$  as a function of  $x$  where  $f(x)$  is the integrand in Equation V.3 illustrating the highly oscillatory nature of the function.

discrete fracture modeling of densely fractured porous systems at field scales is not readily accomplished because the fracture idealization employed in this section is the simplest justifiable conceptual model of the real system.

#### V.C. Application of the EPM Model

The EPM approach to simulating solute transport in fractured porous systems was outlined in Section I.A.2.b. The major requirement for valid application of the EPM approach is that the flux of solute between the mobile water in the fractures and the immobile water in the porous matrix rapidly approaches zero. The EPM approach provides for consideration of all the processes which are expected to have significant influence on migration of non-reactive, non-sorbing solutes, including: advection, longitudinal and transverse dispersion, and matrix diffusion. Three EPM based idealizations of the tracer site will be applied in this section, a one-dimensional homogeneous porous medium, a two-dimensional homogeneous porous medium and a two-dimensional heterogeneous porous medium.

##### V.C.1. One-dimensional Homogeneous Porous Medium Simulations

One-dimensional homogeneous porous medium simulations of the tracer tests were carried out with the following objectives: 1) evaluate the simplest form of the EPM approach in terms of its ability

to simulate the tracer test results; 2) estimate the longitudinal dispersion coefficient; 3) estimate an apparent retardation factor due to matrix diffusion; 4) estimate the decay constant in the exponentially decaying source function; 5) attempt to resolve the dilemma posed by observing a decreasing rate of translation in the center of mass of the tracer plume under measured steady-state flow conditions; and 6) compare the parameters required to simulate the tracer tests with those developed by Johnson (1984) for the CDS contaminant plumes.

The equation governing one-dimensional transport of a non-reactive solute in a porous medium is:

$$D_1 \frac{d^2 C}{dx^2} - v \frac{dC}{dx} = R \frac{dC}{dt} \quad (V.4)$$

where  $D_1$  = longitudinal dispersion coefficient ( $m^2/day$ ),

$C$  = solute concentration,

$R$  = retardation factor,

and  $v$  = average linear velocity ( $m/day$ ).

The presence of an exponentially decaying source function requires imposition of the following initial and boundary conditions:

$$C(x,t) = 0, \quad t=0 \quad (V.5.a)$$

$$\frac{dC(x,t)}{dx} = 0, \quad x = \infty \quad (V.5.b)$$

$$C(0,t) = C_0 e^{-at}, \quad t > 0 \quad (\text{V.5.c})$$

where  $a$  is the decay constant of the source function. The analytical solution to the above set of equations is (Van Genuchten, 1982):

$$C(x,t) = C_0 A(x,t) e^{-at} \quad (\text{V.6})$$

$$\text{where } A(x,t) = \frac{v}{v+U} \exp\left\{\frac{x(v-U)}{2D}\right\} \operatorname{erfc}\left\{\frac{Rx-Ut}{2(DRt)}\right\} \quad (\text{V.6.a})$$

$$+ \frac{v}{v+U} \exp\left\{\frac{x(v+U)}{2D}\right\} \operatorname{erfc}\left\{\frac{Rx+Ut}{2(DRt)}\right\}$$

$$- \frac{v^2}{2DRa} \exp\left\{\frac{vx+at}{D}\right\} \operatorname{erfc}\left\{\frac{Rx+vt}{2(DRt)}\right\}$$

$$\text{and } U = \sqrt{v^2 - 4DRa} \quad (\text{V.6.b})$$

A modified version of the program ODAST (Javendal et al., 1984) was implemented to evaluate Equation V.6. Figure V.C.1 demonstrates that the program performed as expected when applied to the example data sets given in Javendal et al. (1984). However, when parameters characteristic of the tracer site were supplied to the program, run-time errors were consistently returned. The source of this error can be found by evaluating Equation V.6.b using values for the parameters which are appropriate to Alkali Lake. Rough estimates of these parameters are: 1)  $v = 1$  m/day; 2)  $D = 5$  m<sup>2</sup>/day; 3)  $R = 10$ ; and 4)  $a = 0.01$ /day. This results in:

$$U = \sqrt{1^2 - 4(5)(10)(0.01)} = \sqrt{-1}$$



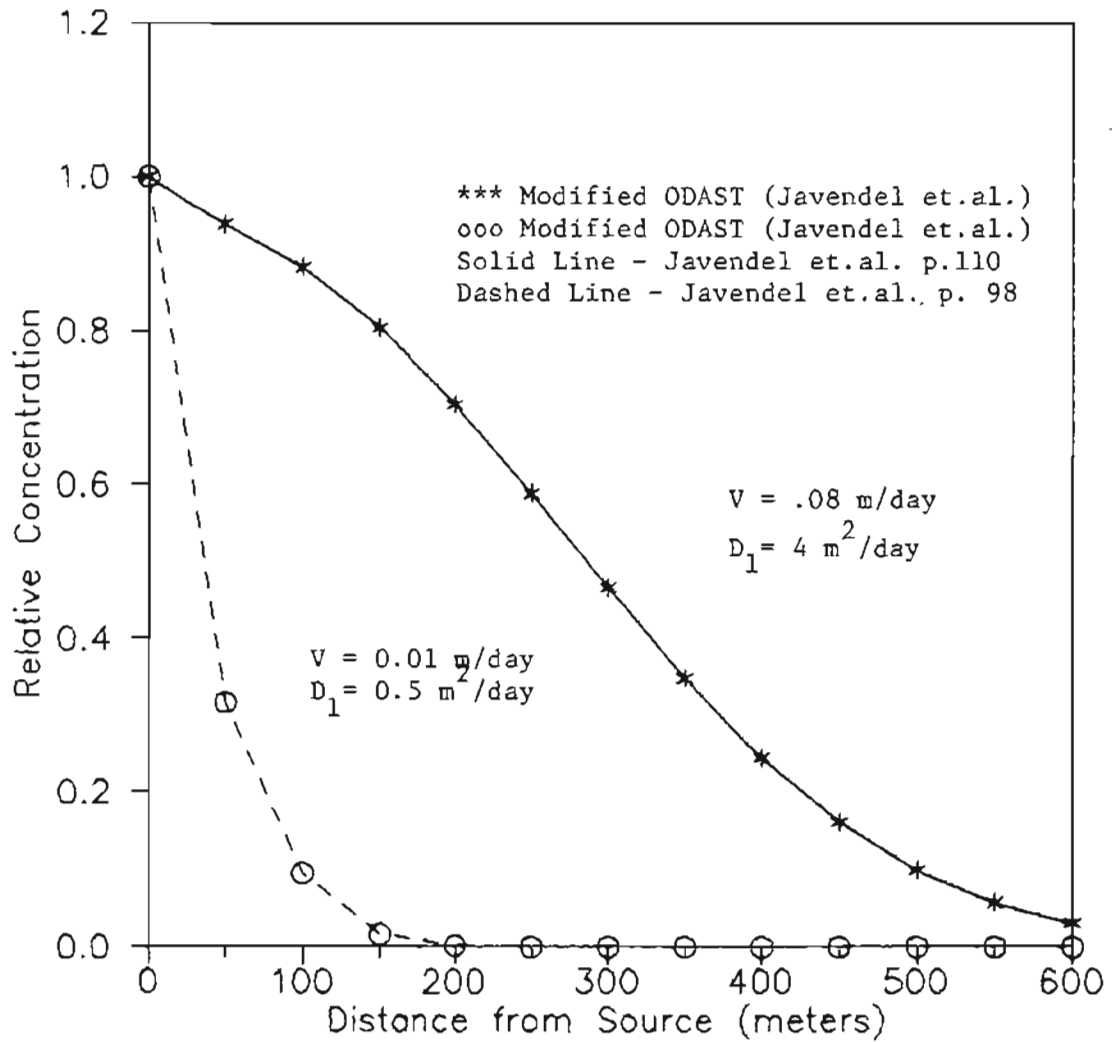


Figure V.C.1 Relative concentration produced by the analytical one-dimensional solution as a function of distance from the source for two test cases.

an obviously non-real solution.

An alternate method was developed to overcome the deficiency in the one-dimensional analytical solution. The approach was to simulate mass transport processes using a Discrete-Parcel-Random-Walk (DPRW) algorithm (Ahlstrom et.al., 1977). Over the past decade the DPRW technique has become an increasingly popular method for simulating mass transport in systems governed by the classic advection-dispersion equation (Ahlstrom et.al., 1977; Smith and Schwartz, 1981; and Prickett et.al., 1981). The mathematical and conceptual details of the DPRW algorithm are described in Ahlstrom et.al. (1977). Briefly, the DPRW method is based on the assumption that the migration of a continuum defined by the spatial distribution of a dissolved compound can be adequately represented by tracking an ensemble of a finite number of discrete particles. Carried to the molecular level, the discrete particle concept is obviously physically justifiable. However, computational restrictions do not permit the representation of each molecule of a dissolved material by its own discrete particle. In practice, this is not a limitation since experience has shown that rarely are more than 5000 particles necessary to adequately represent solute migration (Prickett et.al., 1981).

In implementing the DPRW approach, each particle is assigned an initial location and mass. With respect to transport, the particles are assumed to be independent of one another. Advective and dispersive

components of transport are treated separately. The advective motion of the particle is governed by the groundwater flow. All particles move at the velocity of the surrounding groundwater. Each particle moves at the location-dependent groundwater velocity. For example, in a steady-state, uniform flow field during a time step,  $\Delta(t)$ , all particles are advected the same distance,  $\Delta(x)$ , defined by  $v \Delta(t)$ .

The DPRW method treats the dispersive component of motion by assuming that the Fickian process described by the first term on the left hand side of Equation V.4 can be approximated by displacing each particle a statistically random distance during each time step. As more steps are taken, the dispersive movement of each particle has the properties of the well-studied random walk process. Although there are many interesting features associated with the random walk process, the most important in terms of solute transport simulations is that the root-mean-square (rms) displacement during  $\Delta(t)$ , of an ensemble of particles undergoing a random walk can be expressed for the one-dimensional case as (Alhstrom et.al., 1977)

$$x_{rms} = \sqrt{2D\Delta t} \quad (V.7)$$

The random walk step length for a particle  $p$  during  $\Delta(t)$  is generated by making a random selection from a distribution of step lengths having the proper rms value and a zero arithmetic mean. This can be accomplished by selecting a random number from a uniform distribution covering the range  $-a$  to  $+a$  chosen to satisfy the

constraint implied by Equation V.7. Alhstrom et.al. (1977) show that  $\sigma$  equals  $\sqrt{6D\Delta t}$  and that adapting this result for commonly available random number generators gives

$$x_p = \sqrt{24D\Delta t} \cdot (0.5 - \{R\}_0^1) \quad (\text{V.8})$$

where  $x_p$  = the dispersive displacement of a particle during  $t$ , and  $\{R\}_0^1$  = a random number uniformly distributed in the range  $[0,1]$ .

The DPRW approach was chosen for this study because it offers a number of advantages over more traditional numerical approaches (i.e. finite difference and finite element):

- 1) The DPRW technique is inherently simple with respect to understanding the underlying concepts, implementing the algorithm, and interpreting the results.
- 2) There is no cumulative dispersion (Alhstrom et.al., 1977; and Prickett et.al., 1981).
- 3) The source release rate and geometry are easily modified.
- 4) The technique is easily implemented within the constraints imposed by a microcomputer.
- 5) The solutions are additive. Since the particles move independently of each other, additional runs can be made and the results accumulated or averaged.
- 6) The moments of the particle distributions are very stable from run to run.

The primary disadvantage is that a graph or table of concentrations obtained with the DPRW technique will usually have a "choppy" character in contrast to the smooth curves generally

associated with analytical and numerical solutions. This choppiness is a reflection of the inability of the DPRW method to produce a completely accurate solution at every point within the system. Accuracy can be improved by increasing the number of particles. Since the number of particles located within an averaging volume has been shown to follow the Poisson distribution (Prickett et.al., 1981), the accuracy of a DPRW solution will increase with the square root of the number of particles. Fortunately, the need for high accuracy (within 5% of the true value) solutions were rarely justified for this study and acceptable results were obtained with a few hundred to a few thousand particles. In addition, the moments of a concentration distribution were very accurately defined with a much smaller number of particles than was needed to define the concentration at a large number of points.

To simulate one-dimensional solute transport using the DPRW algorithm, a computer program, RAND1D, was written. To verify that RAND1D was working properly, several example problems were run and the results compared with solutions given in Javandel et.al. (1984). Figure V.C.2 demonstrates the excellent agreement between RAND1D and Javandel et.al. (1984) for two examples and indicates that RAND1D satisfactorily simulates one-dimensional advective-dispersive solute transport.

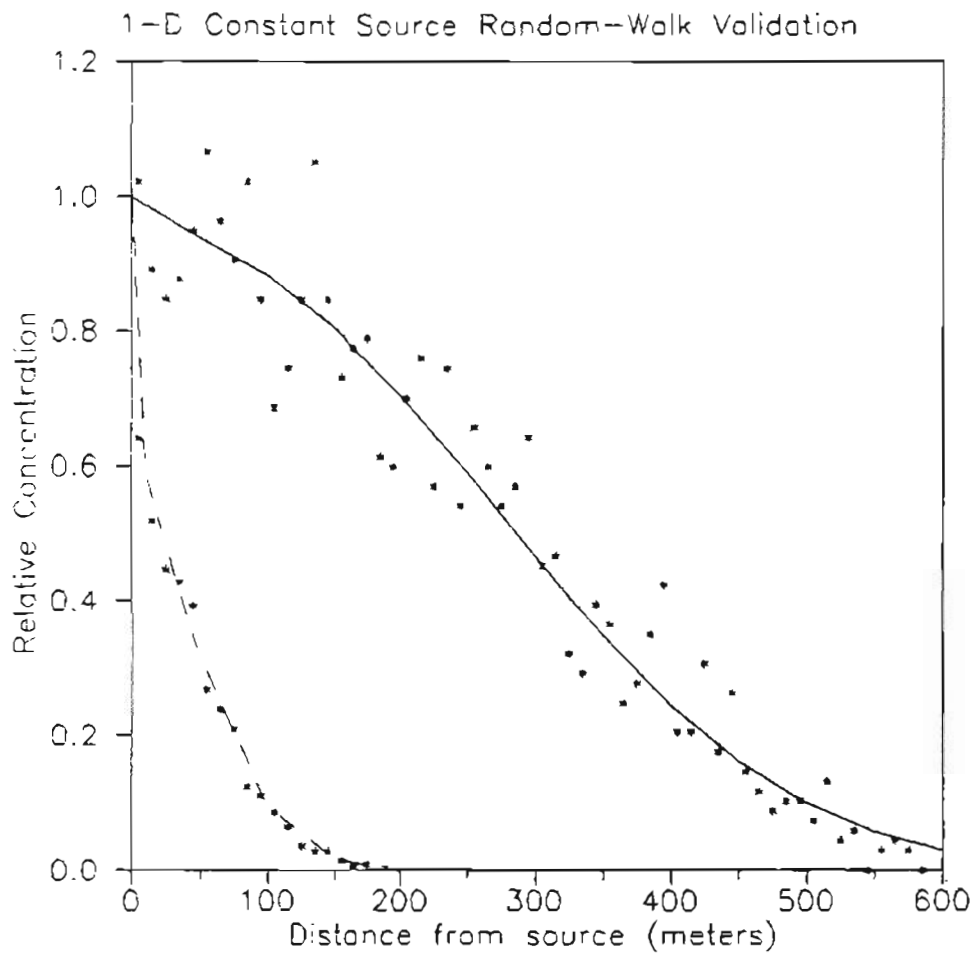


Figure V.C.2 Relative concentration produced by RAND1D as a function of distance from the source for two test cases.

To simulate the tracer tests, RAND1D was modified to include an exponentially decaying source function. This was easily implemented by releasing particles according to

# of particles released at time step  $t =$

$$\#_t = e^{-\alpha t} (1 - e^{-\alpha \Delta t}) \cdot \text{total \# of particles}$$

The RAND1D model was then used to simulate the results of tracer test #1. An iterative trial and error procedure was used to obtain a set of parameters providing the most consistent overall fit between the measured and modeled integrated transects. The set of parameters providing the best fit included:

$$v = 1 \text{ m/day}$$

$$R = 12.5$$

$$d_L = 6 \text{ m}$$

$$\text{source decay constant} = 0.01 \text{ day}^{-1}$$

The "best" set of parameters was determined by comparing the moments of the modeled and measured integrated transects. Figures V.C.3-V.C.5 present the comparisons for the six sampling rounds of tracer test #1 and demonstrates that the above set of parameters satisfactorily simulates the migration of fluorescein throughout the duration of the test.

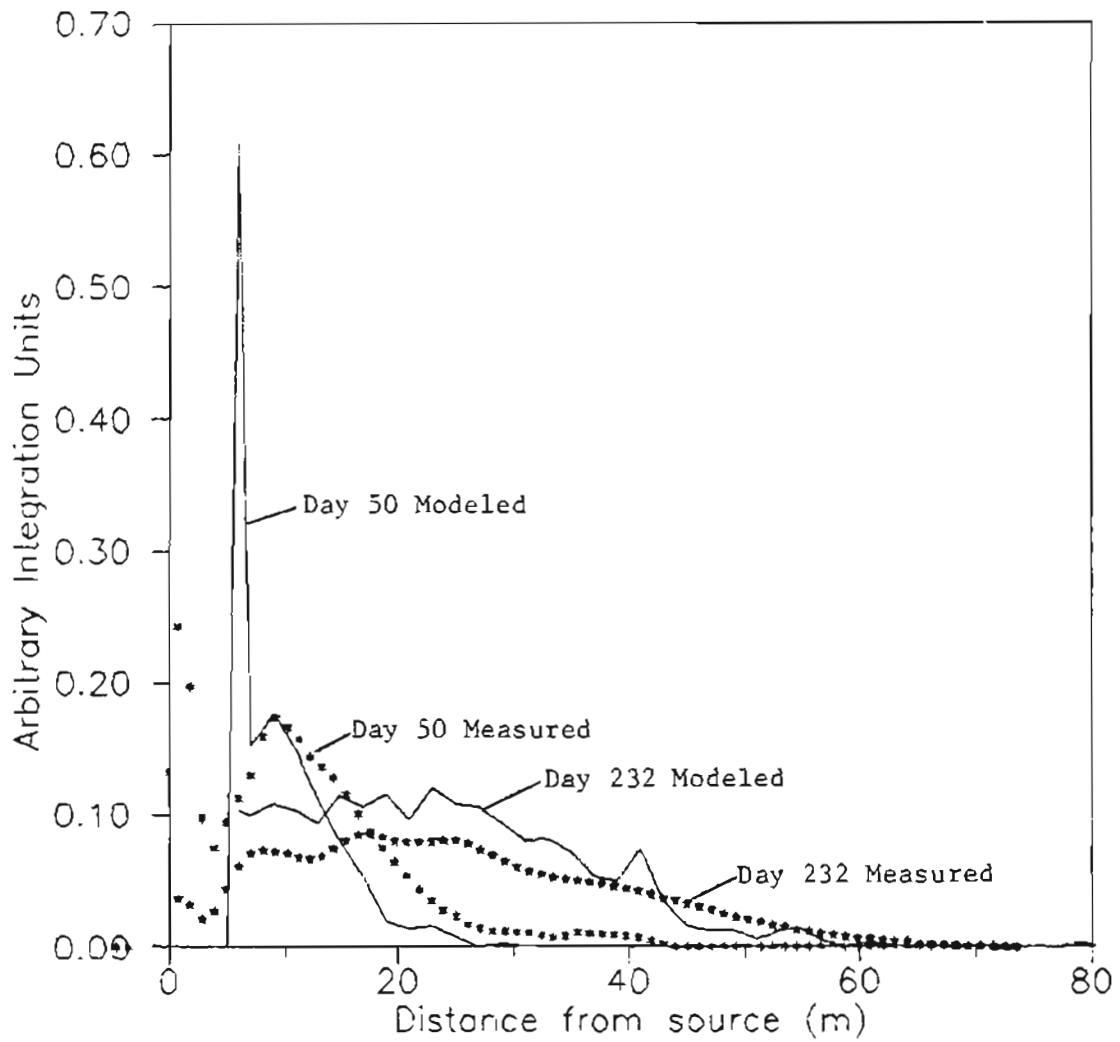


Figure V.C.3 Comparisons between the measured and modeled integrated fluoresein transects for days 50 and 232 of tracer test #1



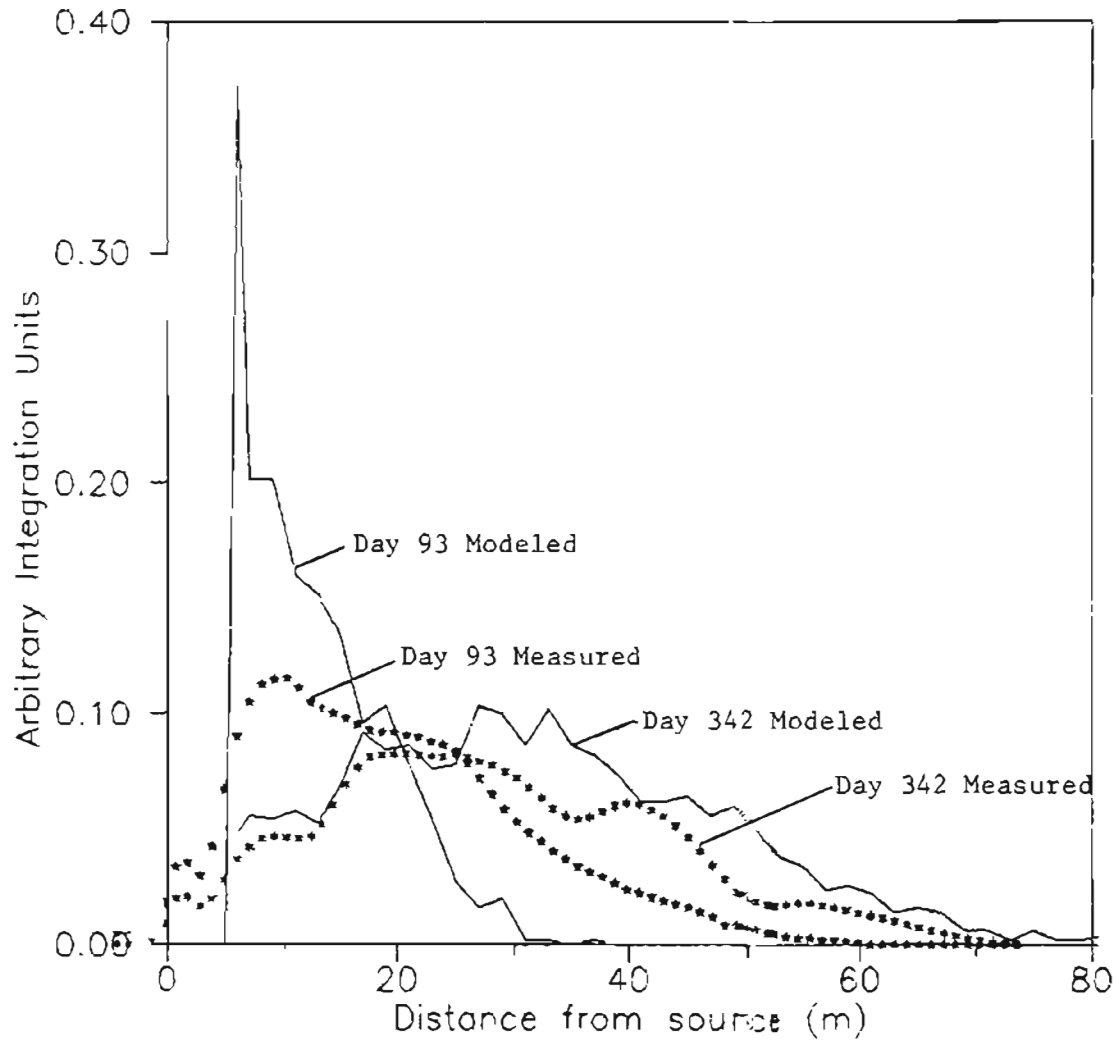


Figure V.C.4 Comparisons between the measured and modeled integrated fluoresein transects for days 93 and 342 of tracer test #1

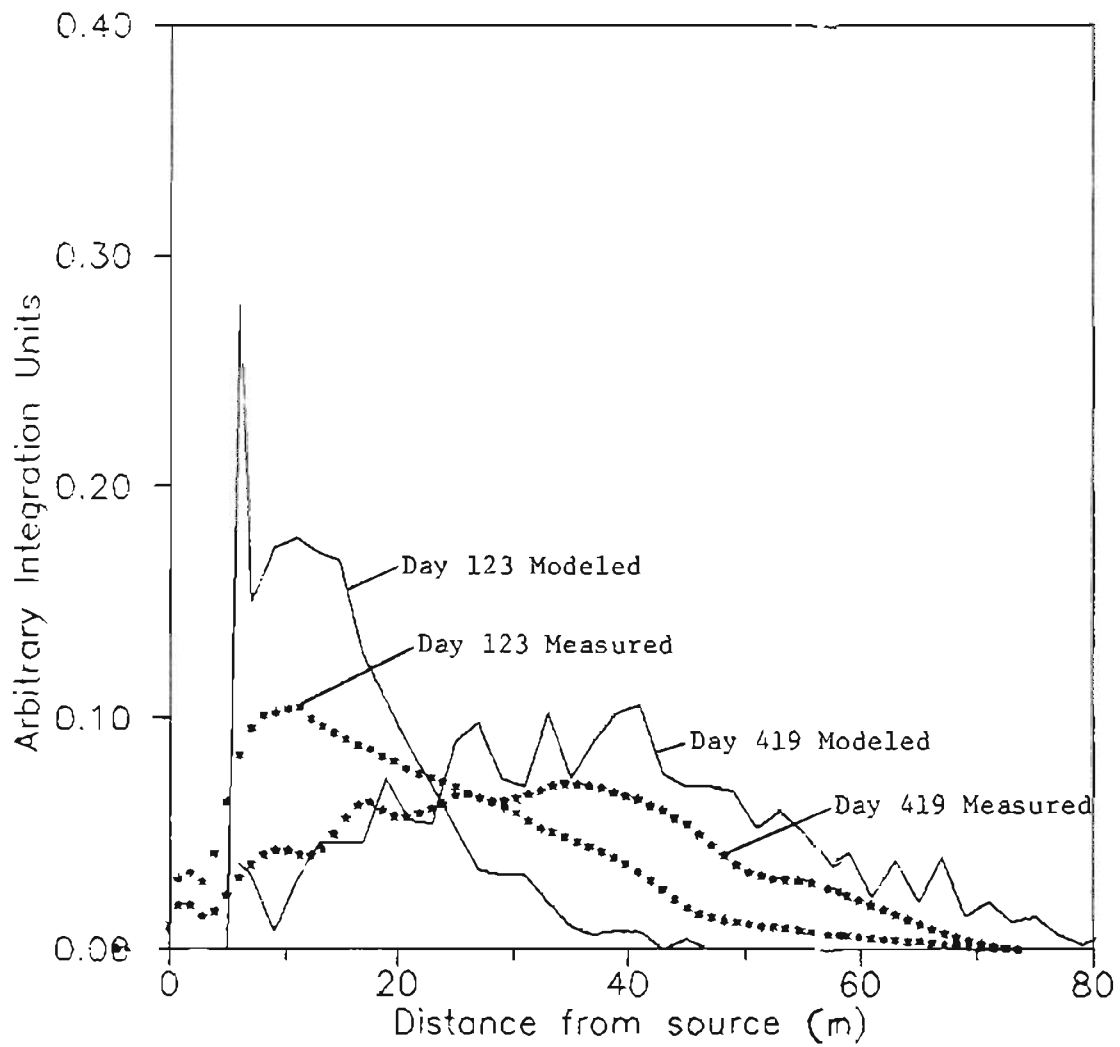


Figure V.C.5 Comparisons between the measured and modeled integrated fluoresein transects for days 123 and 419 of tracer test #1

As with most solute transport models, RAND1D did not provide a mechanism for a formal error analysis. However, a sensitivity analysis was performed in an effort to assign a qualitative level of confidence to the best fit set of parameters. The sensitivity analysis consisted of varying each of the parameters, in turn, over a predetermined range while holding the other parameters constant. Since average linear velocity,  $v$ , and retardation factor,  $R$ , are always employed as the ratio  $v/R$  within RAND1D,  $v$  was held constant and  $R$  was varied. The results of the sensitivity analysis demonstrated that the concentration distributions predicted by RAND1D were very sensitive to the values used for the retardation factor and longitudinal dispersivity. Figures V.C.6-V.C.8 use simulations of the day 342 snapshot of tracer test #1 to illustrate the large impact on the simulated transects produced by varying  $R$  and  $d_L$  by factors of two. The strong dependence of the simulation results on the values of retardation factor and longitudinal dispersivity indicates that the best estimates of  $R$  and  $d_L$  should be considered reliable within a factor of two, a degree of reliability generally considered acceptable for estimating environmental parameters. The sensitivity analysis indicated that the RAND1D results were less dependent on the source function decay constant. However, the experimental evidence presented in Section IV.C pointing to a value of  $0.01 \text{ day}^{-1}$  together with the fact that  $0.01 \text{ day}^{-1}$  performed well in the simulations of tracer test #1 suggest that the best estimate of the source function decay constant should also be considered reliable within a factor of two.

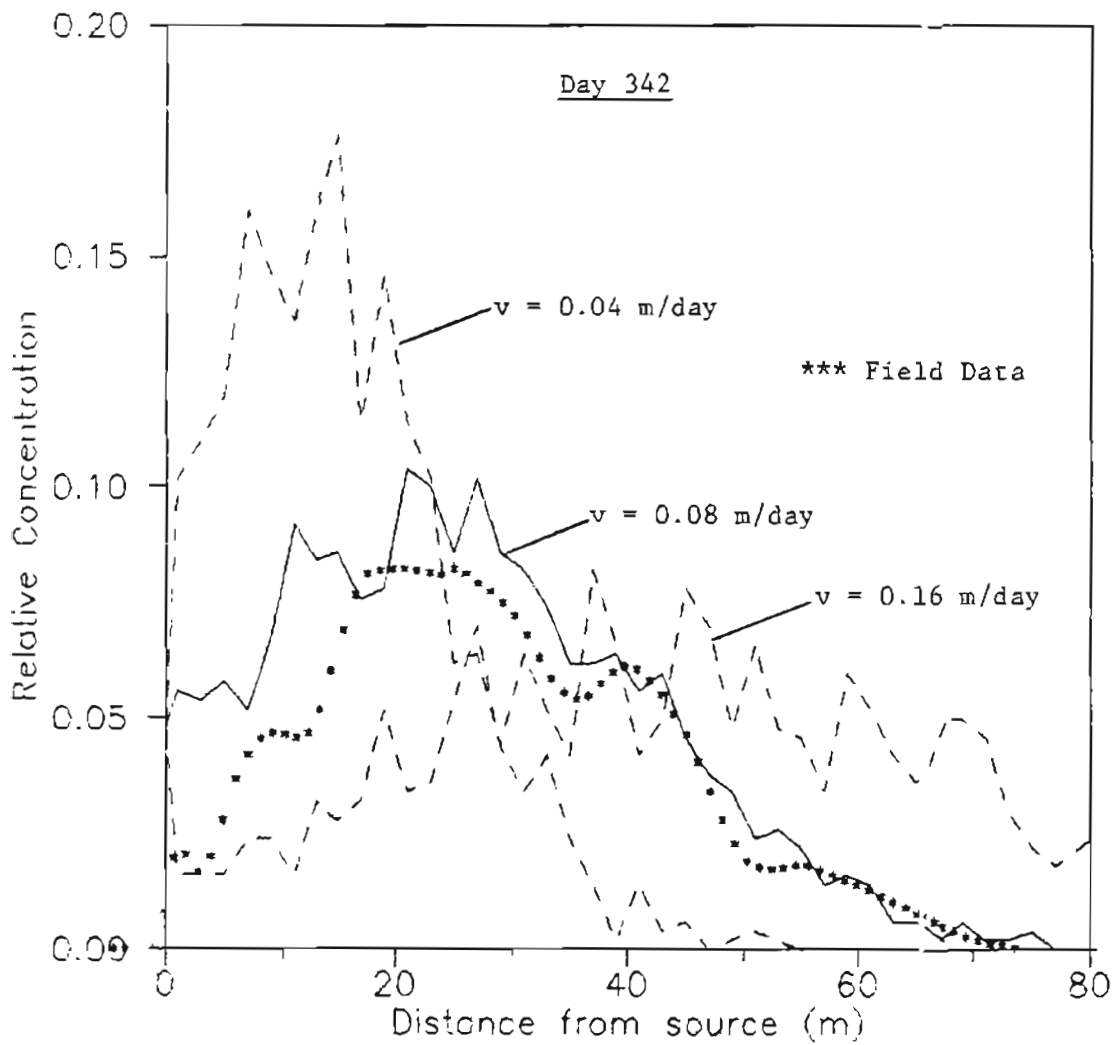


Figure V.C.6 Sensitivity of the one-dimensional EPM simulations to retardation factor for the day 342 snapshot of tracer test #1.

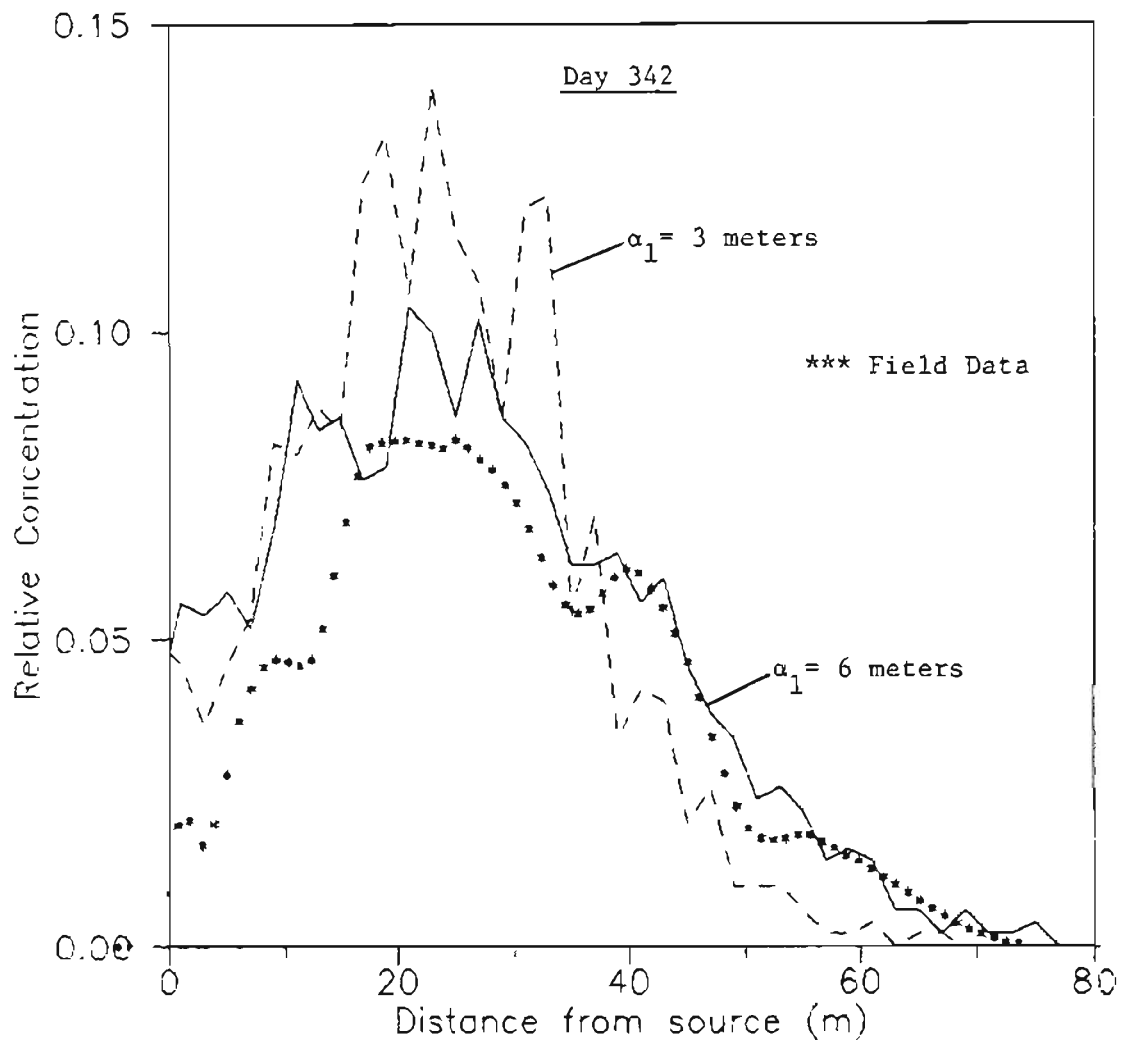


Figure V.C.7 Sensitivity of the one-dimensional EPM simulations to longitudinal dispersivities of 3 and 6 m for the day 342 snapshot of tracer test #1.

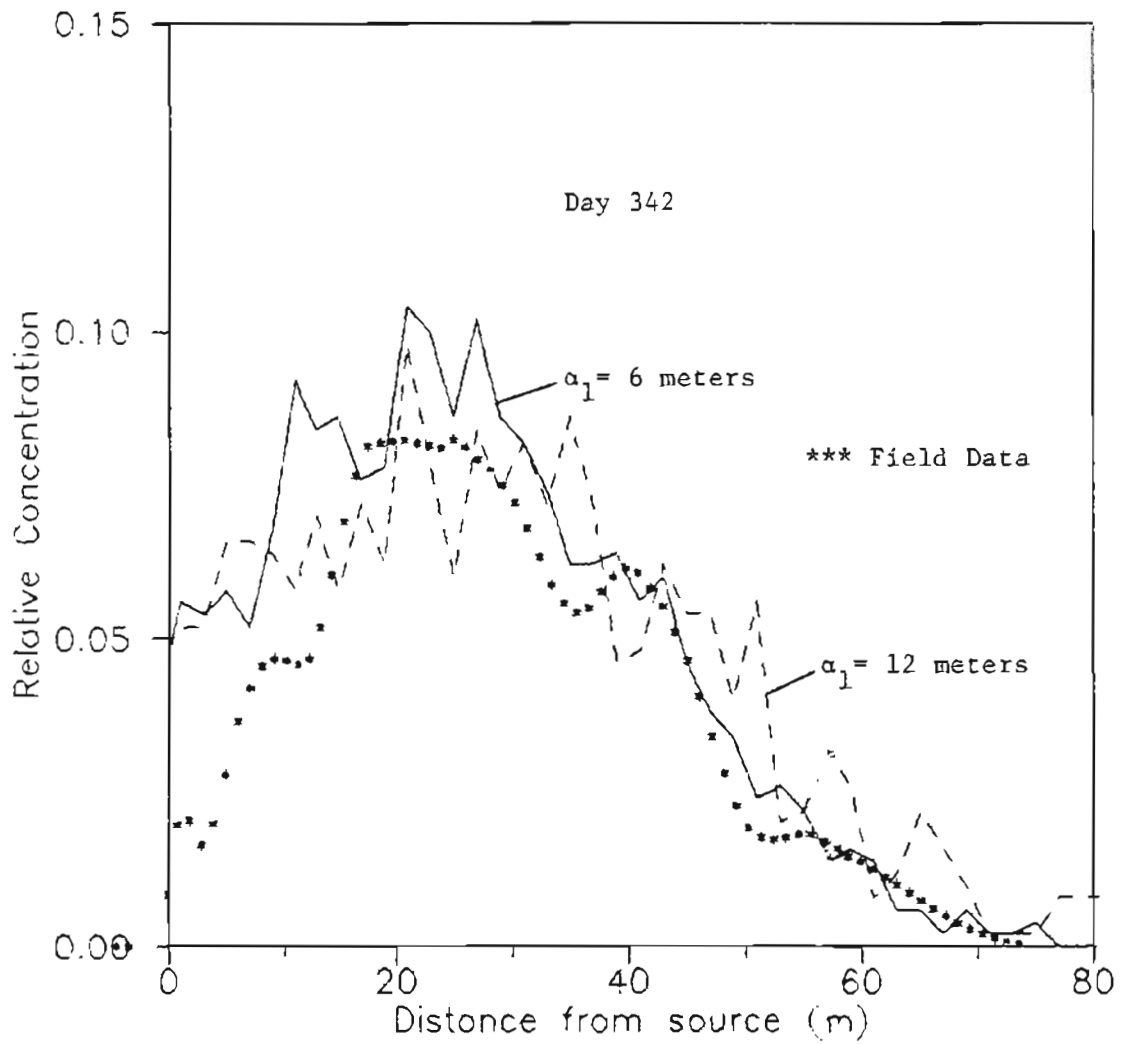


Figure V.C.8 Sensitivity of the one-dimensional EPM simulations to longitudinal dispersivities of 6 and 12 m for the day 342 snapshot of tracer test #1.

In addition to the sensitivity analysis, the reliability of the best estimate of  $R$  obtained from the RAND1D modeling (12.5) is supported by the good agreement with the value of 14 estimated for  $R$  by Johnson (1984). As was discussed in Section I.A.2.b, for a non-sorbing solute in a fractured porous system,  $R$  is a measure of retardation due to matrix diffusion. The large value estimated for  $R$  indicates that matrix diffusion strongly effects transport at the Alkali Lake site.

The decaying source function had numerous effects on solute transport at the CDS including: 1) tailing of the plume; 2) reduced plume dispersion; and 3) elevated plume velocities immediately following tracer injection. The first effect, plume tailing, is illustrated in Figure V.C.9 which shows RAND1D results for several combinations of source function decay constant and longitudinal dispersivity. A large decay constant ( $0.5 \text{ day}^{-1}$ , effectively an instantaneous source) together with  $d_L = 0 \text{ m}$  produces a very narrow, spike-shaped plume. Comparing this narrow plume with the RAND1D result shown for a decay constant =  $0.01 \text{ day}^{-1}$  and  $d_L = 0 \text{ m}$  illustrates the tailing caused by the decaying source function. Thus tailing, a non-symmetrical form of spreading or dispersion, is the result of the decaying solute release rate.

The second effect of the decaying source function, reduced plume dispersion, is in opposition to the first effect. The RAND1D results shown in Figure V.C.10 therefore illustrates how the

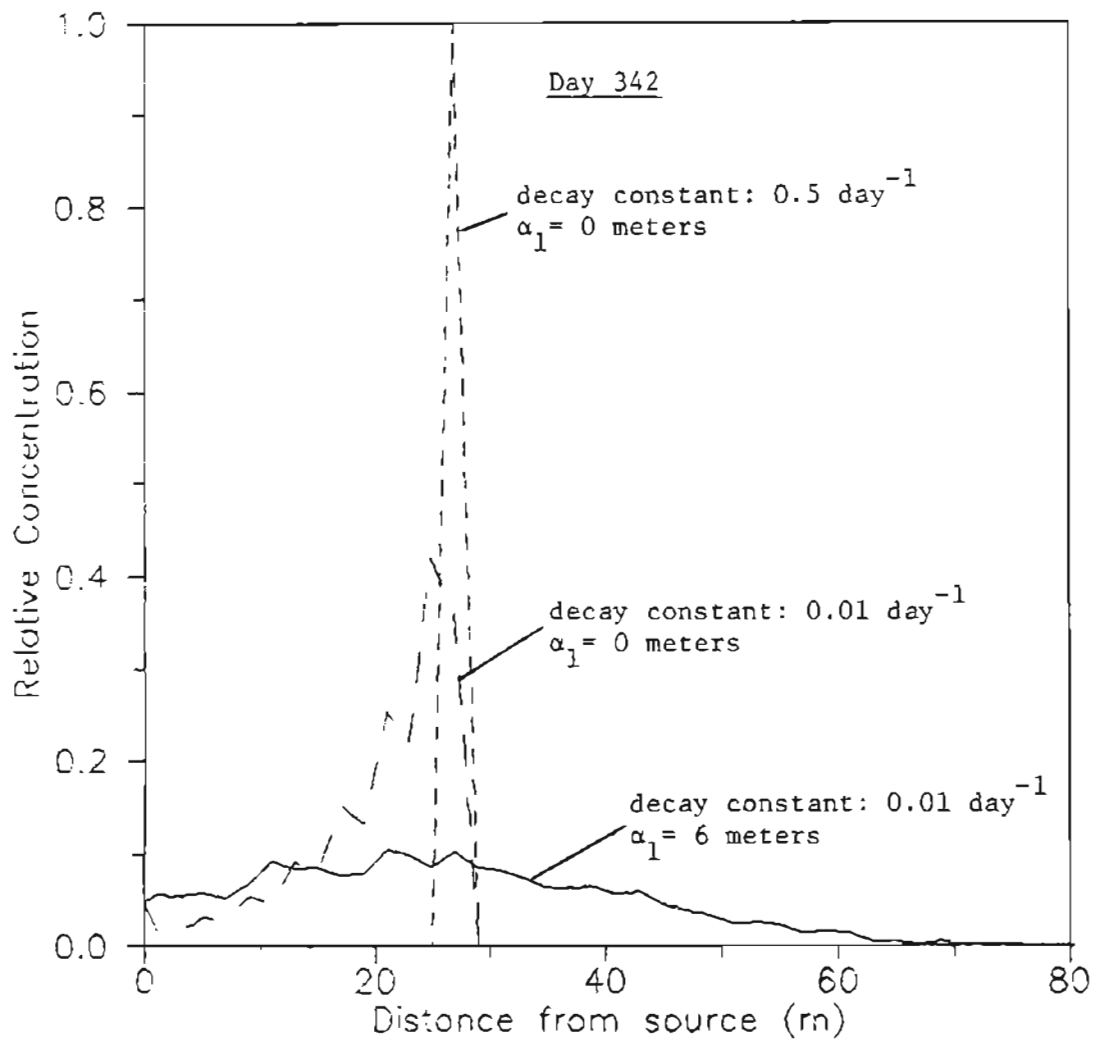


Figure V.C.9 One-dimensional EPM simulations based on the day 342 snapshot of tracer test #1 illustrating the dispersion promoting aspect of an exponentially decaying source function.



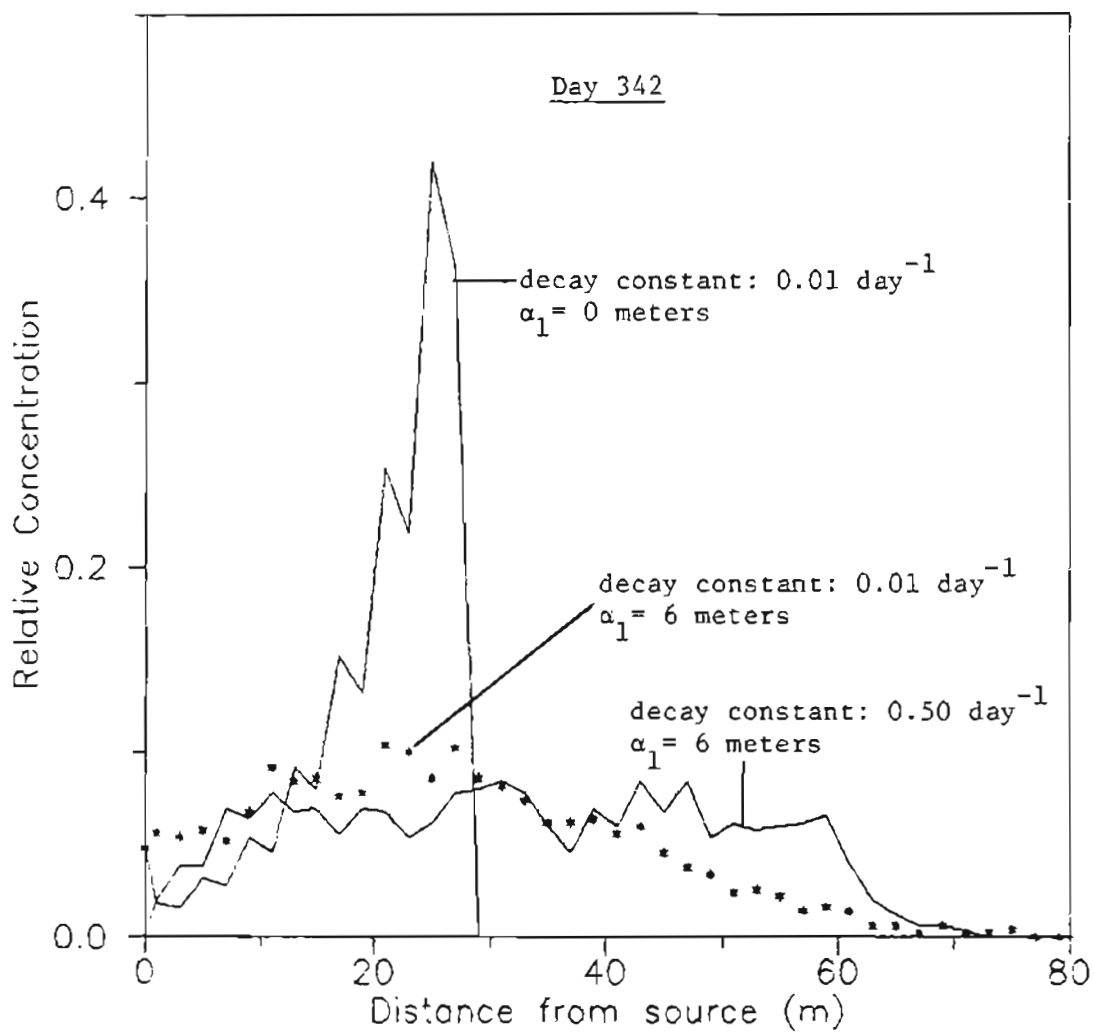


Figure V.C.10 One-dimensional EPM simulations based on the day 342 snapshot of tracer test #1 illustrating the dispersion inhibiting aspect of an exponentially decaying source function.

decaying source function can both cause and inhibit plume spreading. When hydrodynamic dispersion is negligible ( $d_L = 0$  m), the decaying source function is the principal cause of spreading. However, in the presence of significant hydrodynamic dispersion, overall plume spreading is seen to be less for a decaying source function compared to an instantaneous source. Therefore, a decaying source function can both cause and inhibit spreading depending on the relative magnitude of hydrodynamic dispersion.

The third effect of the decaying source function, an apparent velocity elevation during the early period after injection, is perhaps the most interesting. This effect is illustrated in Figure V.C.11 which shows the center of mass velocity as a function of time after injection as estimated for the results of sampling tracer tests #1 and #2 as well as modeling test #1. In all three curves, elevated velocities are apparent during the period close to injection. This is in spite of the relatively constant hydraulic gradient measured for the field tests and the constant velocity used in the modeling. The elevated velocities shown in Figure V.C.11 are artifacts of using the first central moment to estimate the center of mass of skewed concentration distributions. Consider the day 50 modeled and measured transects shown in Figure V.C.3. Both distributions are highly skewed to the right due to the exponentially decaying release rate. This skewness causes a bias in the central moment estimates of the centers of mass. This phenomenon is the well known bias which results from

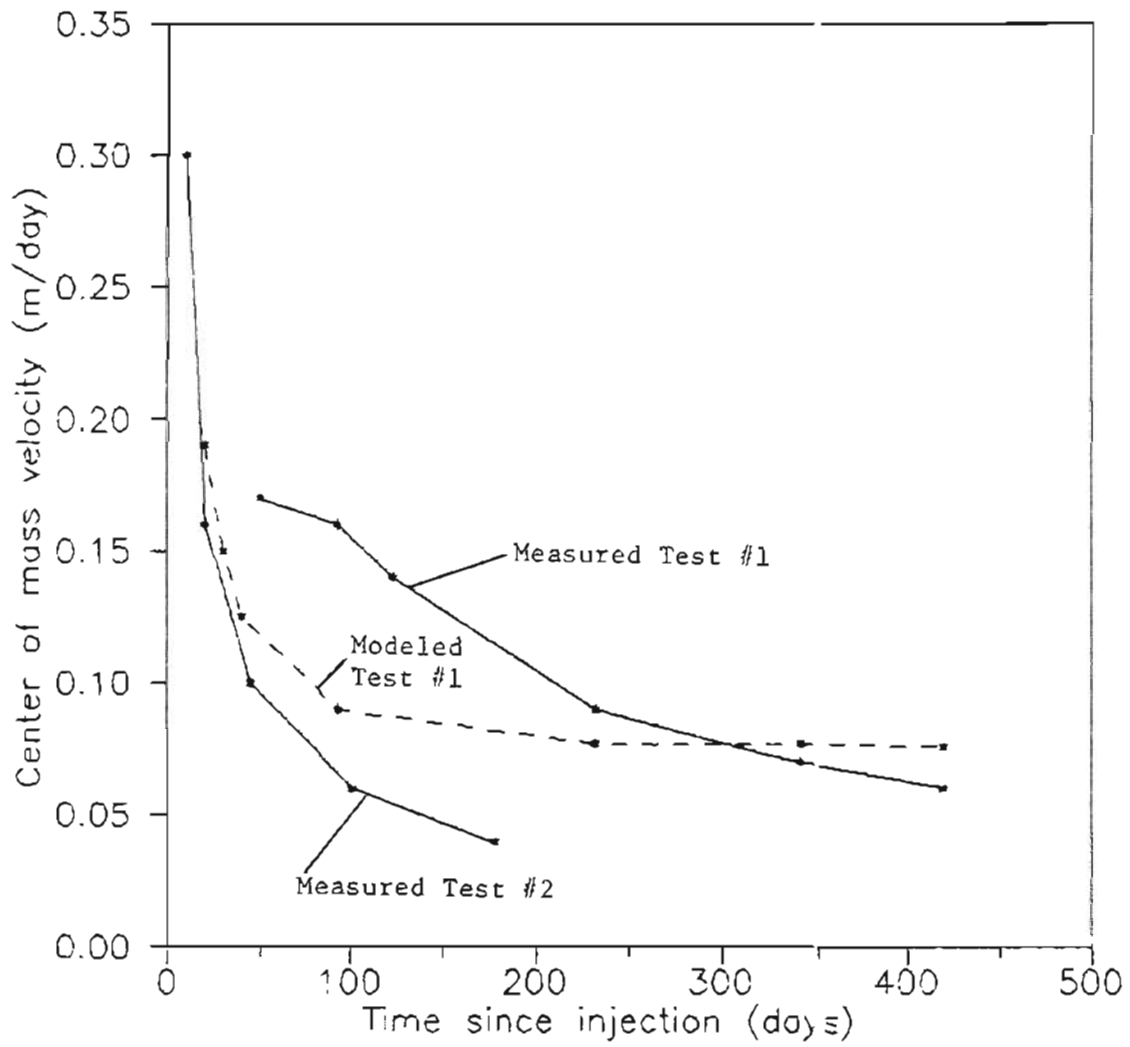


Figure V.C.11 Center of mass velocity measured for tracer tests #1 and #2 and modeled for test #1 as a function of time after injection.

using an arithmetic mean as a measure of central tendency of a skewed distribution. The positive bias in center of mass location propagates to a positive bias in velocity. This bias is largest shortly after injection because that is the period during which the concentration distribution is most strongly skewed.

The longitudinal dispersivity estimate,  $d_L=6$  m, obtained from the RAND1D modeling is twice as large as the estimates provided by the moment analysis in Section IV.D and the one-dimensional modeling conducted by Johnson (1984). A possible explanation for this difference is that the moment analysis and one-dimensional modeling by Johnson (1984) assumed a pulse-type source while RAND1D employed the more realistic decaying source function. As was described above, a decaying source function inhibits dispersion relative to an instantaneous source function. This dispersion inhibiting property of a decaying source requires a larger dispersivity to produce an equivalent degree of plume spreading.

Figure V.C.10 illustrates the two important effects on solute transport at the Alkali Lake site due to longitudinal dispersion: 1) after 342 days the peak concentration is decreased by approximately a factor of four; and 2) after 342 days the front of the plume has advanced over twice as far as would have been expected in the absence of dispersion.

The one-dimensional EPM simulations conducted with RAND1D provided considerable insight into the solute transport process at the Alkali Lake site. The relative roles of matrix diffusion, longitudinal dispersion and the decaying source function were determined. In addition, the observed inverse relationship between distance traveled and velocity was explained as an artifact of using the first central moment to estimate the centers of mass of skewed distributions. Overall, the one-dimensional EPM approach to modeling solute transport through the fractured porous system at the Alkali Lake site was very successful.

#### V.C.2 Two-dimensional Homogeneous EPM Simulations

Two-dimensional homogeneous EPM simulations of tracer test #1 were carried out to build on the understanding of solute transport in fractured porous systems which was gained from the one-dimensional EPM modeling. The principal objectives of the two-dimensional EPM modeling were to estimate 1) the width of the source region; and 2) the horizontal transverse dispersivity.

The DPRW approach was applied to the two-dimensional simulations by modifying RAND1D to incorporate transverse dispersion and a line source of finite width. This new model was named RAND2D. To verify RAND2D, several example problems were run and compared with the analytical solution for an instantaneous source. Figure V.C.12 shows the results of a typical example and demonstrates that RAND2D correctly

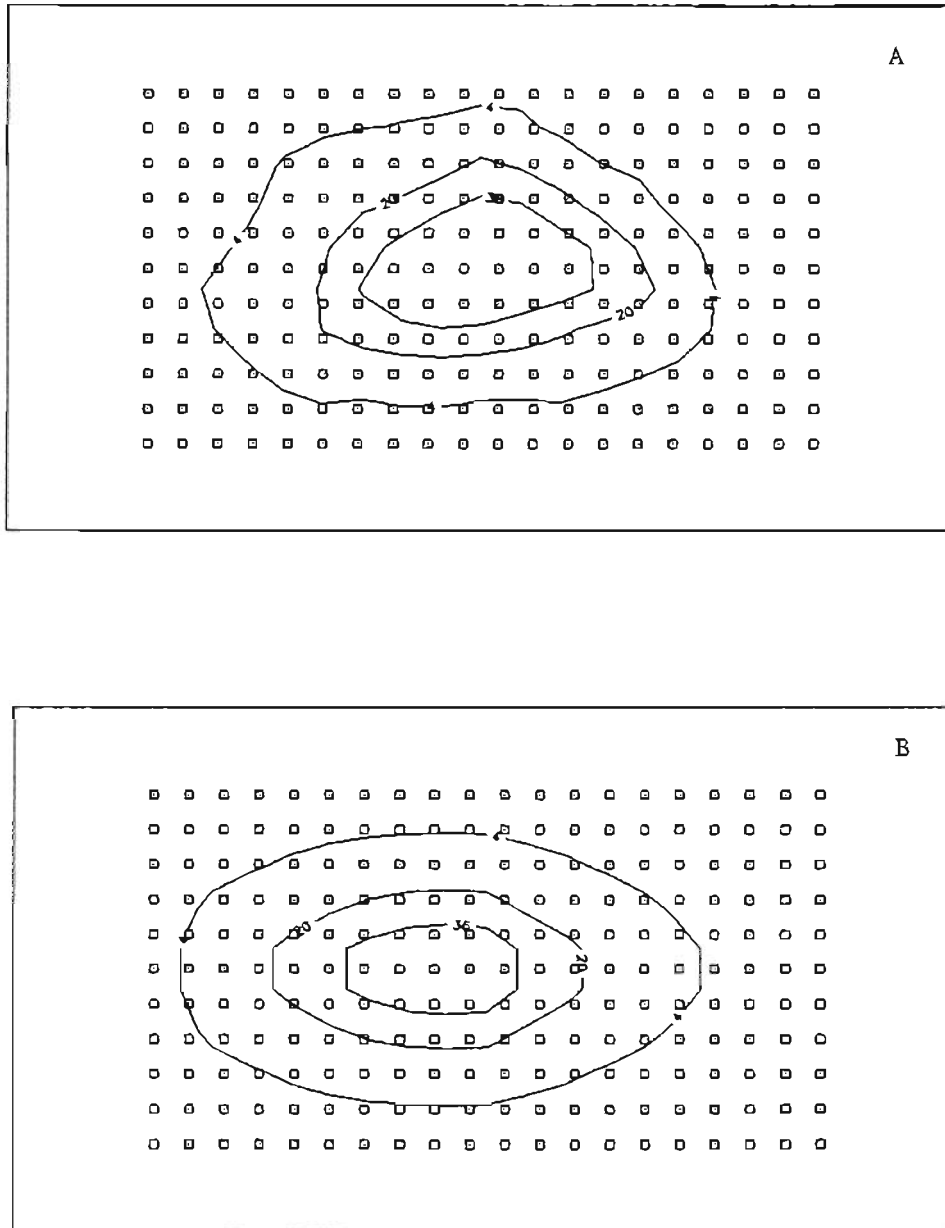


Figure V.C.12 Concentration distribution produced by RAND2D compared with the analytical solution for a pulse type source.

simulates two-dimensional advective-dispersive solute transport.

After verification, RAND2D was used to simulate the results of tracer test #1. The estimates obtained from the RAND2D modeling for  $v$ ,  $R$ ,  $d_L$ , and source decay constant were used for the RAND2D modeling. Source width and transverse dispersivity were systematically varied until a best fit was obtained between the modeled and measured concentration distributions. The best fit estimates for source width and transverse dispersivity were 6 m and 1 m, respectively. The best fit determinations were based on comparing the modeled and measured concentration distributions. Figures V.C.13-V.C.18 shows the modeled distributions for the six sampling rounds of tracer test #1 and when compared with Figures IV.A.19-IV.A.24, demonstrate the consistently good fits afforded by the best fit set of parameters. The uncertainty in the source width and transverse dispersivity were estimated by conducting a sensitivity analysis. Figures V.C.19 and V.C.20 present the results of the sensitivity analysis for day 342 which demonstrates the strong dependence of the concentration distribution on source width and transverse dispersion indicating that the best fit estimates of source width and transverse dispersivity should be accepted as reliable within a factor of two.

The ratio of longitudinal to transverse dispersivity estimated with RAND2D (6) agrees well with the value estimated by the second moment analysis (6.5, see Section IV.D). These estimates, in turn, are

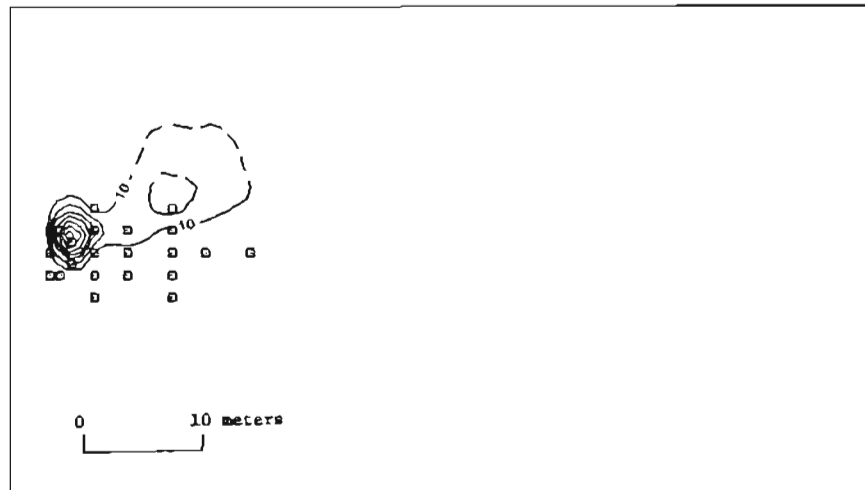
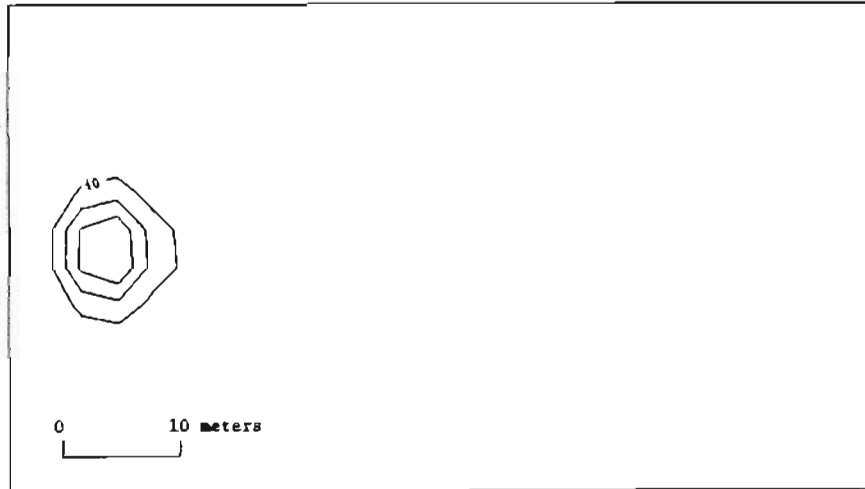


Figure V.C.13 Modeled and measured two-dimensional fluorescein concentration distributions for day 50 of tracer test #1.



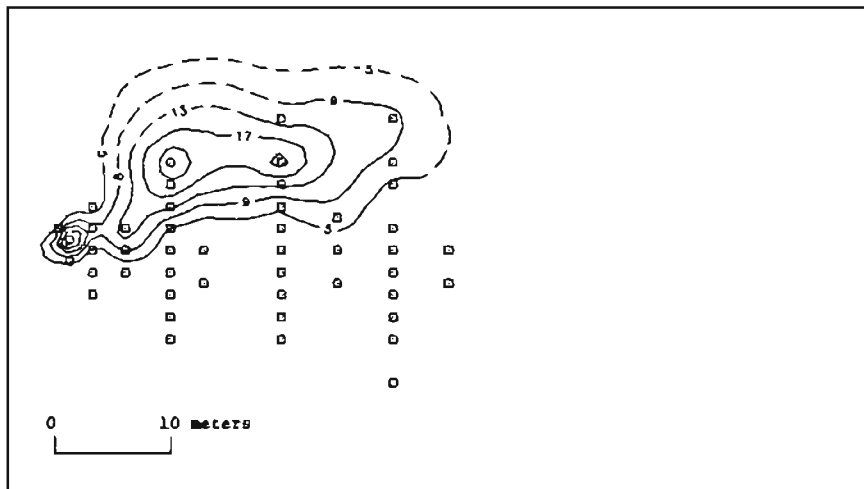
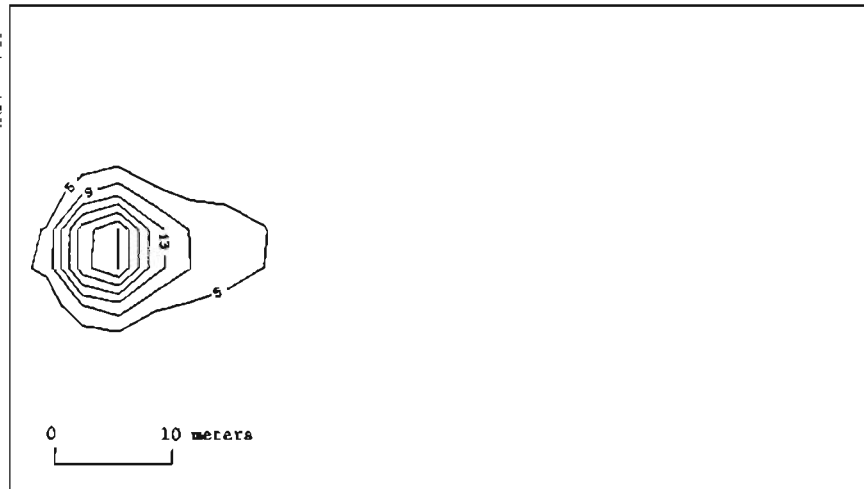


Figure V.C.14 Modeled and measured two-dimensional fluorescein concentration distributions for day 93 of tracer test #1.

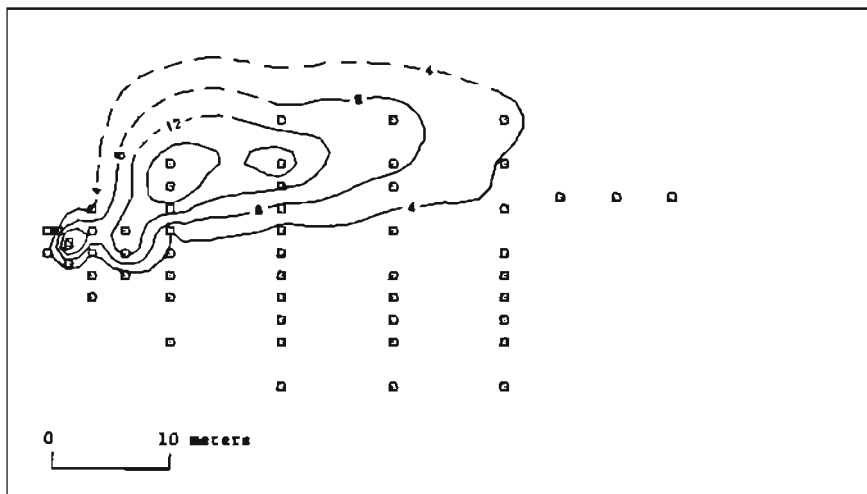
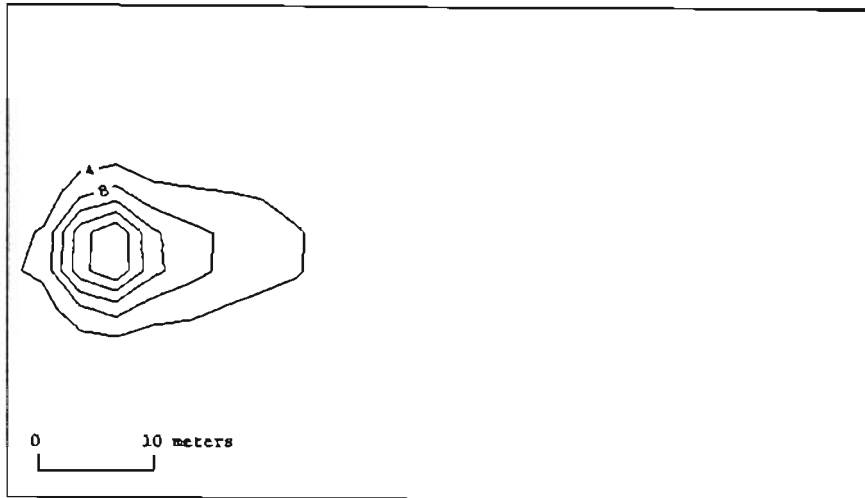


Figure V.C.15 Modeled and measured two-dimensional fluorescein concentration distributions for day 123 of tracer test #1.

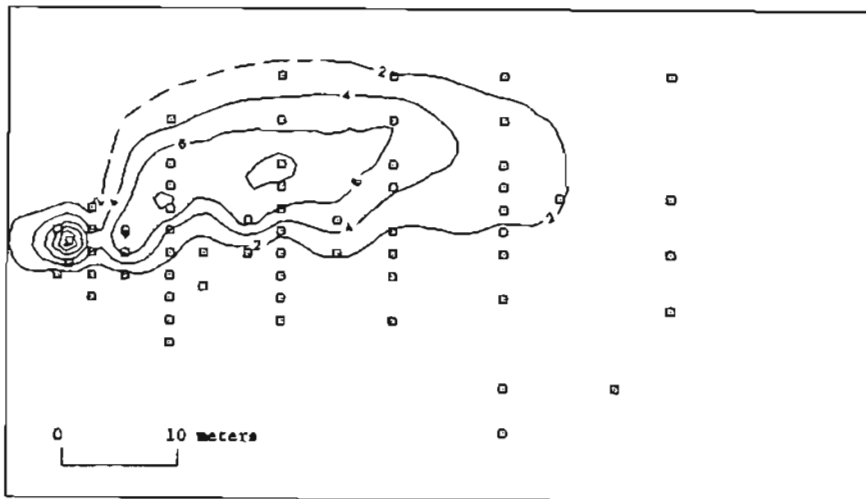
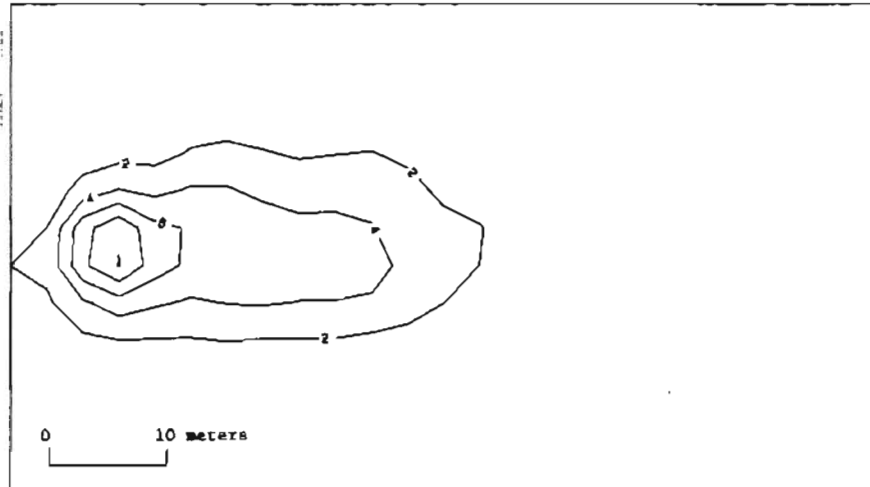


Figure V.C.16 Modeled and measured two-dimensional fluorescein concentration distributions for day 232 of tracer test #1.

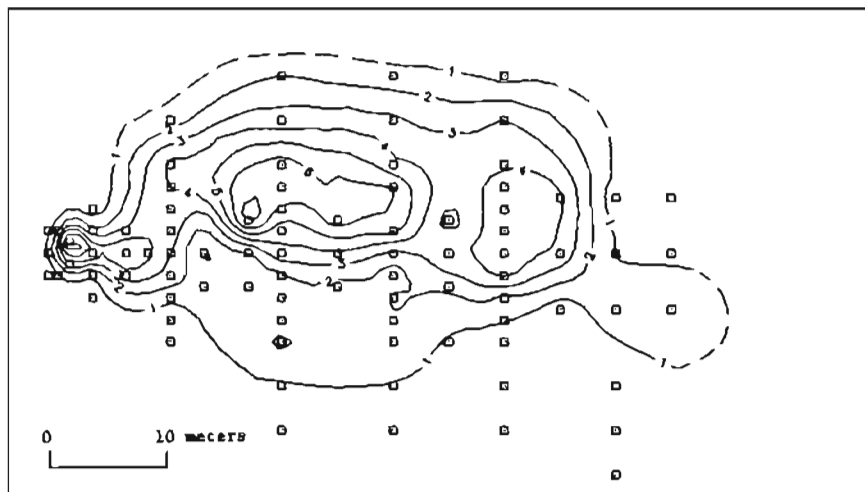
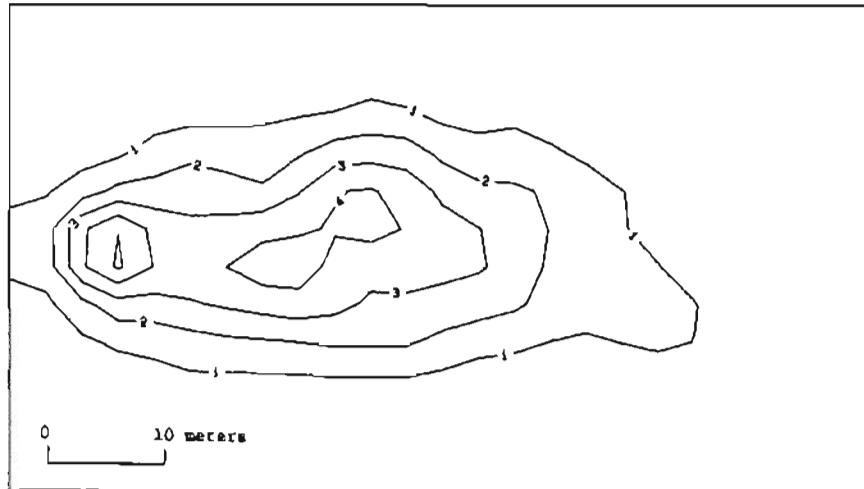


Figure V.C.17 Modeled and measured two-dimensional fluorescein concentration distributions for day 342 of tracer test #1.

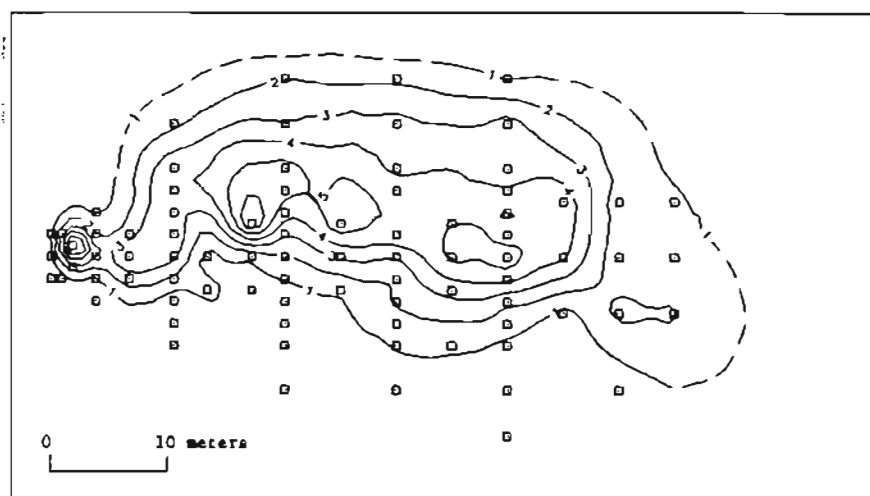
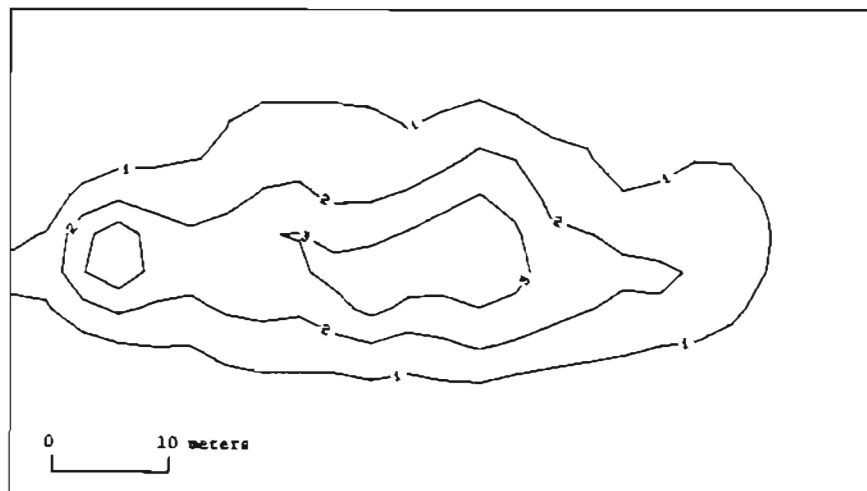


Figure V.C.18 Modeled and measured two-dimensional fluorescein concentration distributions for day 419 of tracer test #1.

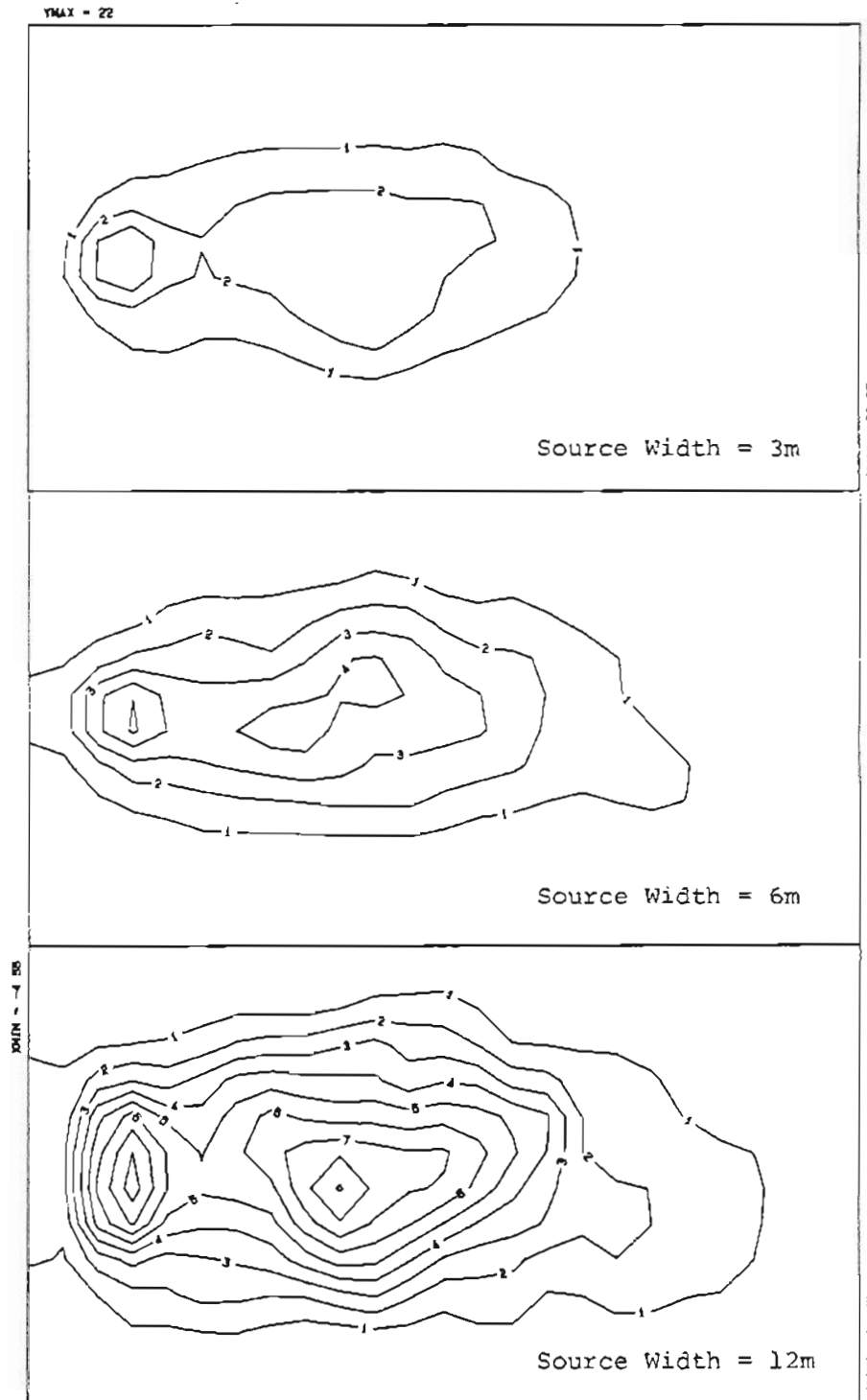


Figure V.C.19 Sensitivity of the two-dimensional EPM simulations to source width for the day 342 snapshot of tracer test #1.

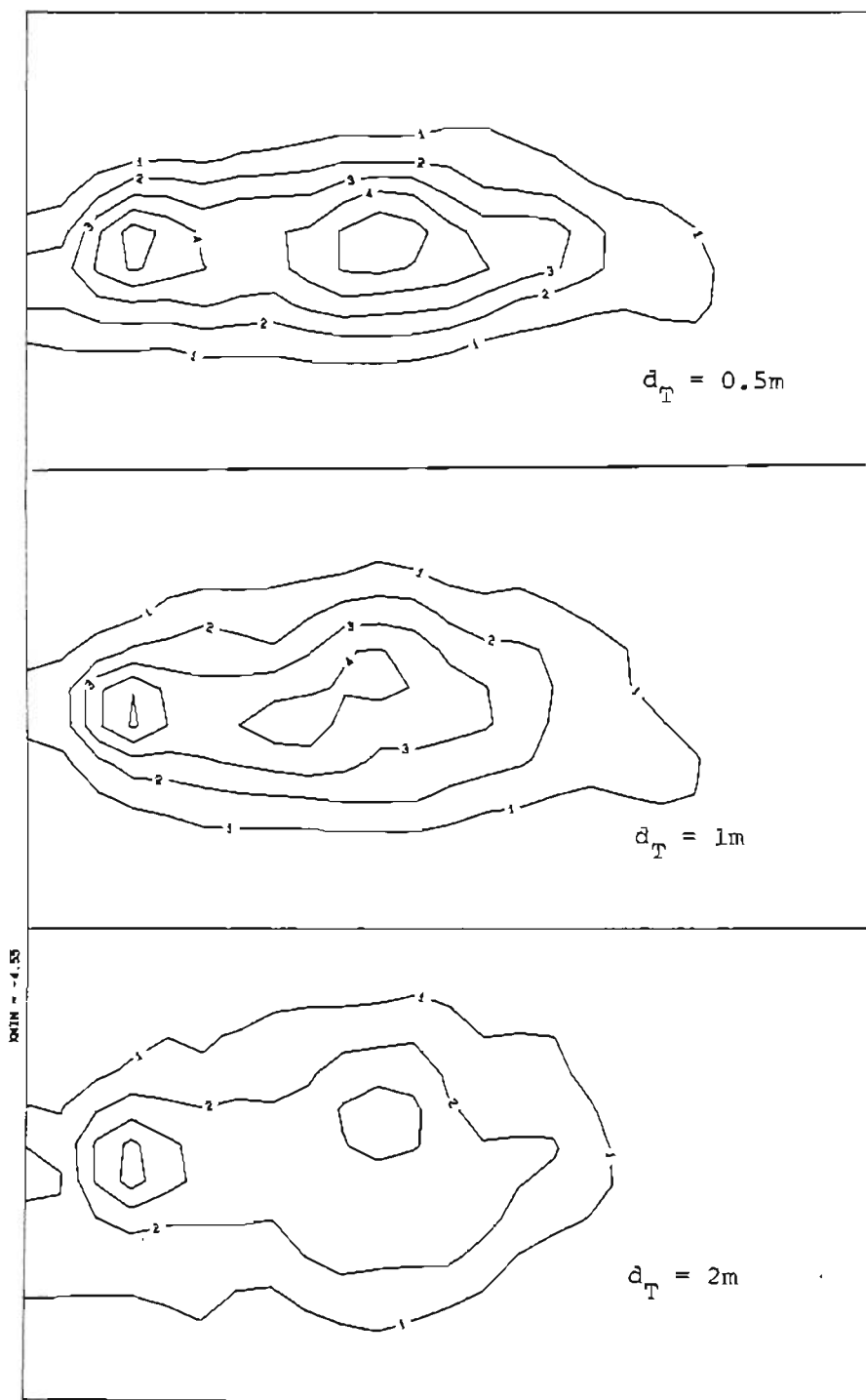


Figure V.C.20 Sensitivity of the two-dimensional EPM simulations to transverse dispersivity for the day 342 snapshot of tracer test #1.

in good agreement with the values of  $d_L/d_T$  that have been estimated for the Borden landfill (Sudicky et.al., 1984; and Sudicky, 1985), one of the few other sites for which reliable determinations have been made of both  $d_L$  and  $d_T$  (Gelhar et.al., 1985).

To gain further perspective on the relative influence of longitudinal and transverse dispersion on solute transport at the Alkali Lake site, RAND2D was used to predict the plumes which would have evolved in tracer test #1 if either longitudinal or transverse dispersion would have been negligible. Figure V.C.21 presents contour maps resulting from these simulations. Two characteristics of the contour maps in Figure V.C.21 should be considered: 1) plume shape; and 2) peak concentration. Figure V.C.21 provides striking visual evidence of the overwhelming dominance of longitudinal dispersion over transverse dispersion in terms of influencing these two plume characteristics.

The two-dimensional EPM simulations conducted with RAND2D significantly extended the understanding of solute transport at the Alkali Lake site which was gained from one-dimensional EPM modeling. Together, the one- and two-dimensional homogeneous EPM modeling successfully determined the relative roles played by the principal processes controlling solute migration. Furthermore, many of the characteristics of the tracer test plumes were demonstrated to be due to specific physical features of the fractured porous soil surrounding the Alkali Lake site. For example, the apparent inverse relationship



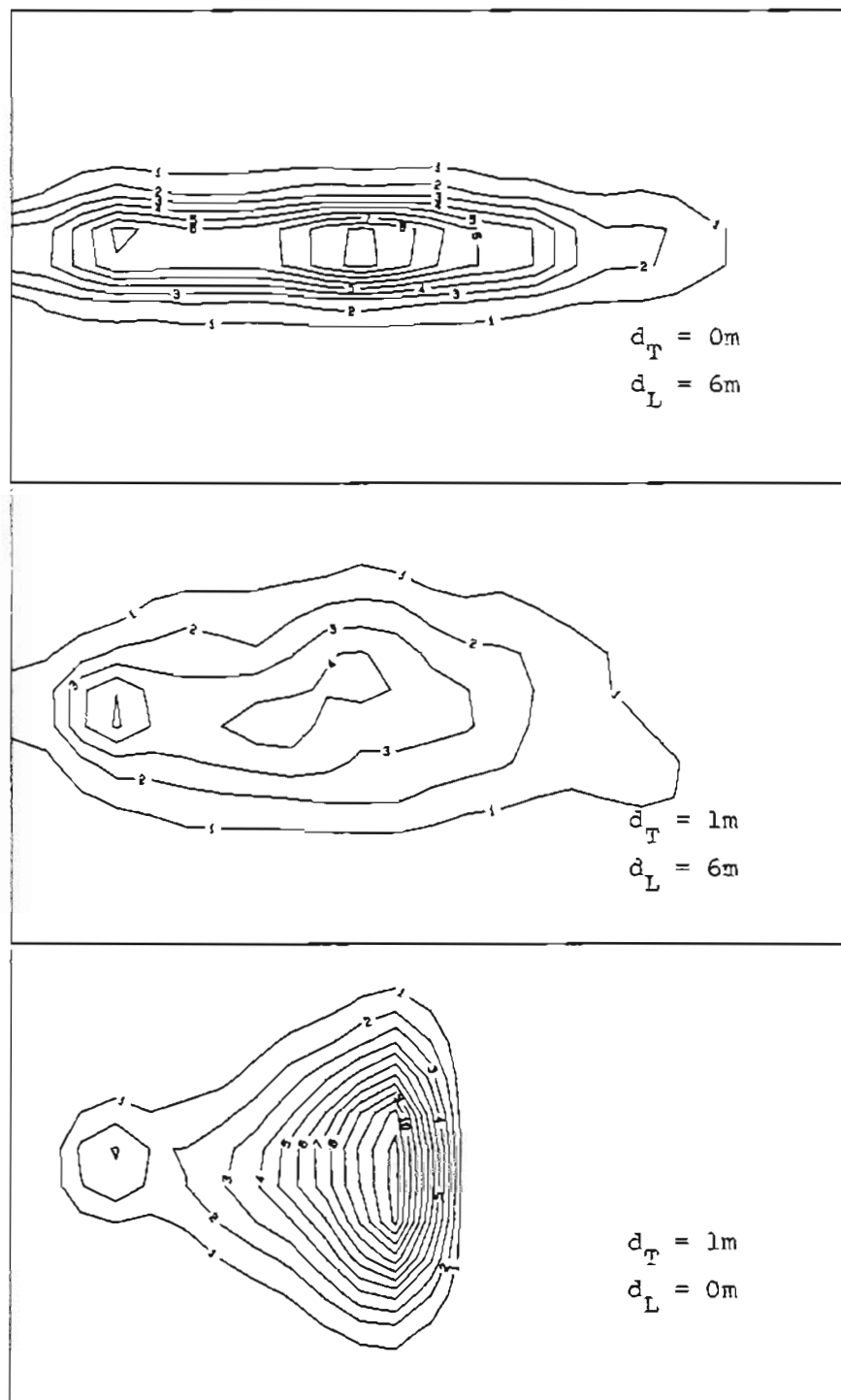


Figure V.C.21 Two-dimensional EPM simulations based on the day 342 snapshot of tracer test #1 illustrating the relative influence of longitudinal and transverse dispersion.

between velocity and travel distance was shown to be due to the decaying source function which was in turn caused by matrix diffusion within the injection area. However, the analyses described to this point have not attributed longitudinal and transverse dispersion to any particular features of the CDS deposit. The longitudinal and transverse dispersivities determined from the homogeneous EPM modeling have been strictly fitting parameters. The next section will attempt to rectify this deficiency by evaluating the possibility that the dispersion observed in the tracer tests was caused by spatial heterogeneity in hydraulic conductivity.

### V.C.3. Heterogeneous Porous Media Simulations - Introduction

For the past five years, the relationship between macroscopic dispersion and spatial distribution of hydraulic conductivity has been the object of numerous investigations (Gelhar and Axness, 1983, Smith and Schwartz, 1980 and Sposito, 1986). The three principal factors motivating these investigations have been: 1) field study observations indicating an increase in dispersivity with increasing contaminant displacement, an apparent violation of the concept of dispersivity as an aquifer property that is invariant with space or time; 2) field study based estimates of dispersion coefficients are several orders of magnitude greater than those based on laboratory column tests; and 3) a lack of consensus on the validity of scaling up the results of laboratory studies to simulate field-scale transport. A common theme

to these investigations has been the hypothesis that the classical advection-dispersion equation remains valid at some "local-scale" but the macro-scale advective and dispersive properties of an aquifer are controlled by the spatial structure of hydraulic conductivity.

Most of the previous studies of transport in heterogeneous porous media have been strictly theoretical in nature and have focused on modeling  $K_h$  variability by assuming that the spatial structure of  $K_h$  can be sufficiently characterized by a small number of statistical parameters (i.e. the mean ( $\mu$ ), variance ( $\sigma^2$ ), and correlation length scale ( $\lambda_{ijk}$ )). Because of this statistical parameterization of  $K_h$ , stochastic forms of the classical advection-dispersion equation have been used to simulate solute transport. Numerical and analytical methods have been used to solve the stochastic advective-dispersion equation. The use of numerical methods is exemplified by a series of papers by Smith and Schwartz (1981, 1982, 1983). Their procedure can be described as a four step process:

- 1) Generate a specific realization of an aquifer based on estimates of  $K_h$  statistics.
- 2) Use numerical techniques to solve the flow problem.
- 3) Use particle-tracking to simulate solute transport. The particles are moved under the influence of the solved flow field as well as a random walk.
- 4) Repeat steps 1-3 for many different realizations (i.e. Monte Carlo simulation).

The procedure outlined above is conceptually very appealing because of its strong similarity to column-scale tracer tests. The use of the

numerical simulation technique has led to several important conclusions including: (Smith and Schwartz, 1981, 1982, 1983)

- 1) Macroscopic dispersion, due to  $K_h$  variability, is the dominant process controlling spreading during mass transport. Microscopic dispersion is only of secondary importance.
- 2) Dispersion coefficients estimated in this manner are much larger than those measured in laboratory column studies.
- 3) Contaminant transport in some geological systems can be estimated with more certainty than others.
- 4) The sample grid on which field data are collected will influence the degree of precision in transport predictions.

The most frequently employed analytical approach to solving the stochastic advection-dispersion equation has been to use perturbation approximations together with spectral methods. This approach assumes that  $K_h$  is statistically homogeneous and that the spatial covariance ( $R_{ff}$ ) of  $K_h$  can be assigned a simple functional form. The analytical approach is limited to determining ensemble average properties and can not develop predictions concerning individual realizations.

Nevertheless, previous applications of analytical techniques to simulate solute transport through heterogeneous porous media have resulted in many interesting conclusions including: (Gelhar and Axness, 1983)

- 1) For a statistically isotropic  $K_h$  field, longitudinal dispersion is convectively controlled, but transverse dispersion is determined by local dispersion.
- 2) Transverse dispersion is convectively controlled only if the transverse mean hydraulic gradient is non-zero.
- 3) The variance of the mean concentration estimated at a point is

large and therefore has a high degree of uncertainty.

### V.C.3. Heterogeneous Porous Media Simulations - Applications

For this portion of the study, analytical and numerical solutions of the stochastic advection-dispersion equation were used to explore the dispersive mixing expected to result from the measured variability in hydraulic conductivity at the CDS and compare this mixing to that observed in the tracer tests. As discussed above, solutions of the stochastic advection-dispersion equation rely on a statistical description of the spatial structure of the hydraulic conductivity field. Because hydraulic conductivity has commonly been found to follow a lognormal distribution, a logarithmic transformation is generally applied to  $K_H$  measurements prior to calculating the required statistics. That is, the variable transformation

$$f(x) = \ln(K_H(x)) \quad (V.8)$$

is made and parameters describing  $f(x)$  are estimated. The statistics used to describe  $f(x)$  include: 1) mean,  $\bar{f}$ ; 2) variance,  $\sigma_f^2$ ; and 3) correlation scales,  $\lambda_1$  and  $\lambda_2$ . The correlation scales are defined as the distances to  $e^{-1}$  (.37) correlation with  $\lambda_1$  associated with the direction of flow and  $\lambda_2$  corresponding to the direction making a  $90^\circ$  angle with the flow.

From the slug test results described in Section II.E.2.b, it was possible to estimate the statistical parameters required to characterize  $f(x)$ . Sufficient observations were made of  $K_H$  to reliably estimate  $\bar{f}$  and  $\sigma_f^2$  as 2.5 and 0.9 respectively. Examination of the data shown in Figure II.E.14 for the slug tests conducted along a transect of the tracer site suggested an appropriate range for  $\lambda_2$  was 0.5 to 1.0 m. Only a very limited amount of data were available for estimating  $\lambda_1$ . Figure II.E.9 shows that three of the piezometers used for slug tests lie along a line 15 m long and approximately parallel with the direction of flow. The  $K_H$  values measured for these locations were all in very good agreement with each other suggesting that the correlation in  $K_H$  may extend much further in the direction of flow than was estimated for the orthogonal direction. However, the sparsity of data precluded development of a precise estimate of  $\lambda_1$  and therefore the broad range of 0.5 to 20 m was selected as appropriate.

Using the above statistical parameters characterizing  $f(x)$ ,  $d_L$  was estimated for the Alkali Lake site with (Gelhar and Axness, 1983)

$$d_L = \frac{\sigma_f^2 \lambda_1}{\exp 2\sigma_f^2 0.5 - \frac{\lambda_2}{\lambda_2 + \lambda_1}} \quad (V.9)$$

The values calculated with Equation V.9 are presented in Table V.C.1 which shows that  $d_L$  was predicted to fall in the range 0.4 to 8 m. This range clearly overlaps with  $d_L = 6$  m determined from the homogeneous EPM modeling and  $d_L = 3$  m estimated from the moment

TABLE V.C.1 Longitudinal dispersivities calculated with Equation V.9  
(meters)

Longitudinal Correlation Scale (m)	<u>Transverse Correlation Scale (m)</u>			
	0.25	0.5	1.0	2.0
0.25	0.2	0.3	0.4	0.4
0.5	0.3	0.4	0.5	0.8
1.0	0.5	0.7	0.9	1.
5.0	2.	2.	2.	3.
10.0	4.	4.	4.	5.
20.0	6.	6.	8.	9.
50.0	20.	20.	20.	20.

analysis. This very good agreement between the range calculated for  $d_L$  with Equation V.9 and the previous estimates strongly suggests that the observed longitudinal dispersion at the Alkali Lake site is governed by the large scale variations in  $K_H$ . In addition the fact that the magnitude of  $d_L$  for the Alkali Lake site was predictable on the basis of measurable aquifer properties supports the appropriateness of treating the fractured porous deposit at the Alkali Lake site as an EPM.

With the above success in attributing the observed longitudinal spreading to large scale  $K_H$  variability, the possibility was explored that stochastic advection-dispersion theory also could explain the observed transverse dispersion. The analytical methods developed by Gelhar and Axness (1983) were applied and provided an estimate of  $d_T = 0$ . This is obviously inconsistent with  $d_T = 1$  m as estimated by the homogeneous EPM modeling and suggested two possible conclusions; 1) there was a weakness in the solutions of Gelhar and Axness with respect to transverse dispersion; or 2) the observed transverse spreading was due to some property of the CDS other than large scale  $K_H$  variability.

Several factors supported the possibility of a weakness in the theory of Gelhar and Axness. Firstly, the only previous application of this type (Sudicky, 1985) encountered the same problem. That is, longitudinal dispersion was accurately estimated by the theory but transverse dispersion was severely underestimated. Furthermore, the field experiments for that study were conducted in a sandy aquifer,



thereby eliminating the possibility of fractures influencing transport. Secondly, the theory of Gelhar and Axness (1983) predicts negligible transverse dispersion for any aquifer experiencing essentially two-dimensional horizontal flow (e.g. the flow system at the Alkali Lake site). Intuitively, this was not a satisfying result and led to increased suspicion of the analytical solutions to the stochastic advection-dispersion equation.

The validity of the estimate of  $d_T$  provided by the technique of Gelhar and Axness was investigated by applying the numerical solution to the stochastic advection-dispersion equation developed by Smith and Schwartz (1980). The numerical modeling was conducted using a modified version of DISPER (Smith, 1982) which employed a combination of finite-element and random walk techniques. This model was used as an exploratory tool by simulating a wide variety of  $K_H$  fields and estimating the dispersivity associated with each simulated pattern of  $K_H$ . Approximately 50 patterns of the spatial structure of  $K_H$  were investigated, ranging from random to highly ordered. The patterns all produced negligible transverse dispersion. This confirmed the theory of Gelhar and Axness (1983) and suggested that large scale  $K_H$  variability was not responsible for the transverse spreading observed in the tracer tests.

One possible cause for transverse dispersion at the Alkali Lake site are the vertical fractures. The field evidence suggests that the

vertical fractures are larger, more widely spaced and more randomly oriented than the horizontal set of fractures. The sharp angles at which both plumes moved immediately after injection suggest that, over short distances, the vertical fractures served as important conduits for transport. In addition, the fact that both tests experienced an initial deflection suggests that the vertical fractures are relatively common. Furthermore, the initial trajectory of each of the two tests formed widely different angles with the direction of groundwater flow ( $+30^{\circ}$  for test #1 and  $-30^{\circ}$  for test #2; these widely varying angles are consistent with the highly irregular orientation observed in the field for the vertical fractures;). Considered together, the above facts suggest a possible mechanism for transverse dispersion. As a plume moves through the soil in the tracer site, portions of the plume encounter vertical fractures making positive angles with the overall flow while other parts of the plume are advected through fractures negatively oriented with respect to the average flow. As a plume evolves and this pattern of deflections is repeated, the resultant effect is the observed transverse dispersion.

The above discussion suggests that the transverse dispersion observed in the tracer tests was due to the vertical fractures. Unfortunately, currently available models do not provide a method for evaluating the validity of the proposed dispersion mechanism. Hopefully, future theoretical investigations of dispersion will develop better tools for understanding transverse horizontal spreading.

#### V.D. Applying the Tracer Test Modeling Results to Understanding Contaminant Migration from the CDS

The preceding sections of this chapter have presented the results of a series of modeling analyses designed to provide a better understanding of the solute migration process in the fractured soil at the Alkali Lake site and in fractured soil, in general. In this section, the usefulness of these results will be demonstrated by applying them to understanding the contaminant plumes migrating from the CDS. The usefulness will be discussed with respect to confirming the current understanding of, as well as developing new insights with regard to, migration from the CDS.

Much of the current understanding of solute migration at the Alkali Lake site was developed in an earlier study (Johnson, 1984; Pankow et.al., 1984; and Johnson et.al., 1985) which investigated the transport behavior of chlorophenolic compounds released from the CDS. Some of the conclusions reached in that study included (Johnson, 1984): 1) the EPM approach is appropriate for modeling groundwater flow and mass transport through the fractured porous soil at the site; 2) the most important factors controlling migration of non-sorbing contaminants were found to be matrix diffusion and areal variations in groundwater flow within the study area; and 3) the average velocity of a non-sorbing solute was estimated as approximately 10 cm/day.

The results presented in this chapter confirm many of the conclusions made in the earlier study including: 1) solute transport at the Alkali Lake site is reliably simulated with the EPM approach; 2) average velocity of plume travel for a non-sorbing solute is approximately 10 cm/day; 3) the effective EPM longitudinal dispersivity is approximately 6 m; and 4) the effective EPM retardation factor due to matrix diffusion is approximately 12.

Several features of the existing contaminant plumes which were investigated in the previous study (Johnson, 1984) were not examined in this study because they were very specific to the CDS and not readily transferable to fractured porous soil as a general subsurface media category. One of these features is the release rate from the CDS. This is a very site specific problem because the bottoms of the burial trenches are above the water table. In addition, groundwater flow appears to be somewhat directed around the disposal site. A second feature is that groundwater flow downgradient of the CDS appears to be non-uniform and channeled.

Although the above site specific features were not examined, other results of this study provide improved insight into transport from the CDS and within other fractured porous systems. Firstly, modeling transport at the CDS with even the simplest physically justifiable idealized fracture model was shown to be a numerically intractable problem due to the large contrast in scale between the distances which are important in diffusion and those which are of concern in advection.

Secondly, the relationship of longitudinal dispersion to field scale variations in hydraulic conductivity provides an improved understanding of a cause of spreading in the direction of flow which was noted for the contaminant plumes (Johnson, 1984). In addition, the relationship between longitudinal dispersion and hydraulic conductivity variability demonstrates that for a very densely fractured system, application of the EPM approach can be pushed to the current state of the art in porous media mass transport theory.

## VI. CONCLUSIONS

Natural-gradient tracer tests proved to be very effective for investigating solute transport in the fractured porous soil at the study site. Interpretation of the tracer test results provided for the determination of the roles played by the processes governing solute migration. Transport was strongly influenced by the fractured and porous media properties of the soil. The most important processes controlling tracer movement were advection, matrix diffusion, longitudinal dispersion and horizontal transverse dispersion.

Advection was responsible for the net movement of tracer mass. The velocities measured for the tracer plumes confirmed that the primary pathway for advective transport was the dense network of horizontal fractures observed at the site.

The process of matrix diffusion was responsible for 1) retarding the plume velocity with respect to the rate of groundwater flow and 2) the functional form assumed by the release rate of tracer mass from the injection zones. An effective retardation factor of 12 was assigned to matrix diffusion, demonstrating the importance of this process in fractured porous systems. Matrix diffusion had two important effects on the source function. First  $C_0$ , the initial tracer concentration in the fractures was much less than the injected concentration due to the immediate transfer of solute from the fractures to the matrix. Second,

the release of tracer from the injection region behaved as an exponentially decaying source function. Source lifetimes (i.e. 1/decay constant) of approximately 100 days were observed in the data from samplers close to the injection wells.

The influence of longitudinal dispersion on transport at the Alkali Lake site, as measured by the estimated longitudinal dispersivity, was at a level comparable to that commonly reported for non-fractured systems. By applying stochastic transport theory, the observed longitudinal spreading was shown to be directly attributable to the measured spatial variability in hydraulic conductivity.

Horizontal transverse dispersion had a much weaker influence on transport than did longitudinal dispersion (i.e.  $d_L/d_T=6$ ). This result was consistent with ratios reported by other studies which have developed high reliability estimates of both longitudinal and transverse dispersivity. Although the overall influence on tracer transport was relatively small, the estimated transverse dispersivity was much greater than was predicted on the basis of observed heterogeneity in hydraulic conductivity. Intermittent movement through the irregular set of vertical fractures, oriented at oblique angles to the flow, was hypothesized to be the most likely mechanism for transverse dispersion. This hypothesis was based on the observed properties of the vertical fractures together with the sharp

deflections in initial trajectory measured for the two tracer tests.

In addition to examining the transport controlling processes, the contributions of this work include: 1) development of an HPLC-laser induced fluorescence technique capable of rapid and accurate quantification of a series of fluorescein dyes in groundwater samples; 2) demonstration that the natural-gradient tracer test technique was useful in a fractured porous system; 3) evaluation of the ability of idealized fracture models to simulate field-scale transport at the Alkali Lake site; 4) evaluation of the ability of EPM models to simulate field-scale transport at the Alkali Lake site; 5) field verification of stochastic transport theory; and 6) evaluation of five gridding algorithms with respect to their abilities to accurately and precisely map a groundwater solute plume.

The HPLC-laser induced fluorescence analytical procedure developed for this study required no sample preparation and had a linear dynamic range of over four orders of magnitude providing straightforward analysis for groundwater containing between 1 and 10,000 ppb of a series of fluorescein dyes. A principal feature of the fluorometric detector was the absence of any highly specialized hardware. Specifically, the use of the commercially available flow cell, the simple photodiode radiation detector, and the type of laser found in most Raman spectrometers provides the opportunity for development of laser induced fluorescence as a routine tool for groundwater tracer



analysis.

The experiments carried out for this study are the first large-scale three dimensional natural gradient tracer tests conducted in fractured porous soil. Previously, the natural-gradient tracer test method had been used to investigate transport in 2-D or through only relatively simple systems such as shallow sand and gravel aquifers. Thus this work supports the use of the natural-gradient method in a broad range of geologic settings.

The application of a cross-sectional fracture network model was not useful for quantitatively simulating the migration of a tracer pulse through densely fractured soil for distances applicable to field situations. Application of the model required the very precise numerical integration of a highly oscillatory function. However, standard integration algorithms were incapable of the necessary level of precision. The failure of the symmetrical cross-sectional model implies that discrete fracture modeling of densely fractured porous systems at field scales is impractical because the fracture idealization evaluated in this study was the simplest justifiable conceptual model of the real system.

The EPM approach was very effective for simulating tracer migration through the fractured porous soil at the study site. the high density of fractures at the site was responsible for the success

of the EPM approach. The influence of the fractures was included in the EPM modeling through the use of the decaying source function and retardation factor. The need to represent the release rate of an injected pulse as an exponential decay was an important finding of this study which should prove useful in future applications of EPM modeling for fractured porous systems.

The applicability of the EPM approach to the tracer site was highlighted by the good agreement between the longitudinal dispersivity estimated by the moment analysis and the value predicted by stochastic transport theory on the basis of the observed heterogeneity in hydraulic conductivity. This result represents the second reported field confirmation of stochastic transport theory and significantly increases the evidence supporting that theory because: 1) the subsurface setting at the tracer site was more complex than the sandy aquifer employed for the previous confirmation; and 2) the measured variance in hydraulic conductivity at the Alkali Lake site was twice as large as that measured for the test site used in the previous confirmation.

Of the five gridding algorithms evaluated, kriging, using either an isotropic or anisotropic linear variogram, was preferable due to its ability to honor the observations as well as provide reasonable predictions for the removed data points. In addition, a procedure was

suggested for objectively calibrating any of the gridding methods. The parameters required for a method can be adjusted to minimize the bias and variability in predicting a random subset of observations which are excluded from the prediction process. The set of parameters providing the minimization can then be used with the complete data set to estimate the values for a regular grid.

## REFERENCES

- Ahlstrom, S.W., H.P. Foote, R.C. Arnett, C.R. Cole, and R.J. Serne. 1977. Multicomponent mass transport model: theory and numerical implementation (discrete-parcel-random-walk version), Battelle Pacific Northwest Lab., Richland, WA, Rep. BNWL-2127.
- Barker, J.A. 1982. Laplace transform solutions for solute transport in fissured aquifers, *Adv. Water Resources*, v.5, 98-104.
- Barker, J.A. and J.H. Black. 1983. Slug tests in fissured aquifers, *Water Resour. Res.*, v.19, 1558-1564.
- Barnes, R.A. 1985. Personal Communication.
- Bear, J. 1972. Dynamics of Fluids in Porous Media, American Elsevier, New York, NY.
- Cherry, J.A., R.W. Gillham, E.G. Anderson, and P.E. Johnson. 1983. Migration of contaminants at a landfill: A case study, 2. Groundwater monitoring devices, *J. Hydrology*, v.63, 31-49.
- Clark, I. 1979. Practical Geostatistics, Applied Science Publishers, Ltd., London, England.
- Creutin, J.D. and C. Obled. 1982. Objective analyses and mapping techniques for rainfall fields: An objective comparison, *Water Resour. Res.*, v.18, 413-431.
- Diebold, G.J. and R.N. Zare. 1977. Laser fluorimetry: Subpicogram detection of aflatoxins using high-pressure liquid chromatography, *Science*, v.196, 1439-1441.
- Environmental Protection Agency, U.S., Water Planning Division, Office of Solid Waste, Washington, D.C. 1980. Groundwater Protection, Report No. SW-886.
- Environmental Protection Agency, U.S., Region X, Seattle, WA. 1976. Report of the Alkali Lake Task Force.
- Environmental Protection Agency, U.S., EMSL, Las Vegas, NV. 1983. Topographical Map of Alkali Lake, Oregon. Project No. AMD-83060-J044.10.

- Folestad, S., L. Johnson, B. Josefsson, and B. Galle. 1982. Laser induced fluorescence detection for conventional and microcolumn liquid chromatography, *Anal. Chem.*, v.54, 925-929.
- Freeze, R.A. and J.A. Cherry. 1979. Groundwater, Prentice-Hall, Englewood Cliffs, NJ.
- Fried, J.J. 1975. Groundwater Pollution, Elsevier, Amsterdam, Netherlands.
- Gelhar, L.W. and C.L. Axness. 1983. Three-dimensional stochastic analysis of macrodispersion in aquifers, *Water Resour. Res.*, v.19, 161-180.
- Gelhar, L.W., A. Mantoglou, C. Welty, K.R. Rehfeldt. 1985. A review of field-scale physical solute transport processes in saturated and unsaturated porous media, Electric Power Research Institute, Report No. EA-4190.
- Grisak, G.E. and J.F. Picketts. 1980 Solute transport through fractured media: 1. The effect of matrix diffusion, *Water Resour. Res.*, v.16, 719-730.
- Grisak, G.E., J.F. Picketts, and J.A. Cherry. 1980. Solute transport through fractured media: 2. Column study of fractured till, *Water Resour. Res.*, v.16, 731-739.
- Henley, S. 1981. Nonparametric Geostatistics, Applied Science Publishers, Ltd., London, England.
- Hershberger, L.W., J.B. Callis, and G.D. Christian. 1979. Sub-microliter flow-through cuvette for fluorescence monitoring of high performance liquid chromatographic effluents. *Anal. Chem.*, v.51, 1444-1446.
- Hull, L.C. 1985. Physical model studies of dispersion in fracture systems, prepared by EG&G Idaho, Inc. for the Department of Energy, U.S., Idaho Operations Office, DOE Contract No. DE-AC07-76ID01570.
- Hurst, J.K., J.M. Albrich, T.R. Green, H. Rosen, and S. Klebanoff. 1984. Myeloperoxidase-dependent fluorescein chlorination by stimulated neutrophils, *J. of Biol. Chem.*, v.259, 4812-4821.

- Huyakorn, P.S., B.H. Lester, and J.W. Mercer. 1983. An efficient finite element technique for modeling transport in fractured porous media 1. Single species transport, *Water Resour. Res.*, v.19, 841-854.
- Hvorslev, M.J. 1951. Time lag and soil permeability in groundwater observations, U.S. Army Corps of Engrs. Waterway Exp. Sta. Bull. 36, Vicksburg, MS.
- Javandel, L., C. Doughty, and C.F. Tsang. 1984. Groundwater Transport: Handbook of Mathematical Models, American Geophysical Union, Washington, D.C.
- Johnson, R.L. 1984. The groundwater transport of chlorophenolics in a highly fractured soil at Alkali Lake, OR, Ph.D. Thesis, Oregon Graduate Center, Beaverton, Oregon, 97006.
- Johnson, R.L., S.M. Brillante, L.M. Issabelle, J.E. Houck, and J.F. Pankow. 1985. Migration of chlorophenolic compounds at the chemical waste disposal site at Alkali Lake, Oregon - 2. Contaminant distributions, transport, and retardation, *Groundwater*, v.23, 652-666.
- LeBlanc, D. 1987. Fate and transport of contaminants in sewage-contaminated ground water on Cape Cod, Massachusetts, Chapter B. Introduction in U.S. Geological Survey Open-File Report 87-109.
- Lumley, J.L. 1970. Stochastic Tools in Turbulence, Academic Press, New York, NY.
- Naymick, T.G. and M.e. Sievers. 1985. Characterization of dye tracer plumes: In situ field experiments, *Groundwater*, v.23, 746-752.
- Neretnieks, I. 1980. Diffusion in the rock matrix: An important factor in radionuclide retardation, *J. of Geophysical Res.*, v.85, 4379-4397.
- Neretnieks, I., T. Ericksen, and P. Tahtinen. 1982. Tracer movement in a single fissure in granitic rock: Some experimental results and their interpretation, *Water Resour. Res.*, v.18, 849-858.
- Newton, V.C. and D. Baggs. 1971. Geological evaluation of the Alkali Lake disposal site, State of Oregon Department of Geology and Mineral Industries, Open File Report. July 1.

- National Oceanic and Atmospheric Administration. 1984. Climatological Data, Oregon, 1961-1984. Environmental Data Service, Ashville, MD.
- Novakowski, K., S. Kentner, G.V. Evans, D.A. Lever, and K.G. Raven. 1985. A field example of measuring hydrodynamic dispersion in a single fracture, *Water Resour. Res.*, v.21, 1165-1174.
- Oregon Department of Environmental Quality. 1977. Alkali Lake disposal project monitoring report No. 1. June 14, 1977.
- Pankow, J.F., R.L. Johnson, J.E. Houck, S.M. Brillante, and W.J. Bryan. 1984. Migration of chlorophenolic compounds at the chemical disposal site at Alkali Lake, Oregon - 1. Site description and ground water flow, *Groundwater*, v.22, 593-601.
- Pankow, J.F., R.L. Johnson, J.P. Hewetson, and J.A. Cherry. 1986. An evaluation of contaminant migration patterns at two waste disposal sites on fractured porous media in terms of the equivalent porous media (EPM) model, *J. of Contam. Hydrol.*, v.1, 65-76.
- Patrick, G.C., C.J. Ptacek, R.W. Gillham, J.F. Barker, J.A. Cherry, D. Major, C.I. Mayfield, and R.D. Dickhout. 1985. The behavior of soluble petroleum-product derived hydrocarbons in groundwater: Phase I report, submitted to Environmental Quality Division, Petroleum Association for Conservation of the Canadian Environment (PACE).
- Prickett, T.A., T.G. Natmick, and C.G. Lonquist. 1981. A random-walk solute transport model for selected groundwater quality evaluations, *Illinois State Water Survey, Champaign, Bull.* 65.
- Reilly, T.E., O.L. Franke, and G.D. Bennett. 1984. The principle of superposition and its application in groundwater hydraulics, *U.S. Geological Survey Open File Report* 84-459.
- Rendu, J.M. 1978. An Introduction to Geostatistical Methods of Mineral Evaluation, South African Institute of Mining and Metallurgy, Johannesburg, South Africa.
- Ripley, B. 1981. Spatial Statistics, Wiley Interscience, New York, NY.
- Schwartz, F.W., L. Smith, and A.S. Crowe. 1983. A stochastic analysis of macroscopic dispersion in fractured media, *Water Resour. Res.*, v.19, 1253-1265.
- Sepaniak, M.J. and E.S. Yeung. 1980. Determination of Aldriamycin and Daunorubicin in urine by high-performance liquid chromatography

- with laser fluorometric detection, *J. of Chromatography*, v.190, 377-383.
- Skopp, J. and A.W. Warrick. 1974. A two-phase model for the miscible displacement of reactive solutes in soils, *Soil Sci. Soc. Am. Proc.*, v.38, 545-550.
- Smith, L. and F.W. Schwartz. 1980. Mass transport 1. A stochastic analysis of macroscopic dispersion, *Water Resour. Res.*, v.16, 303-313.
- Smith, L. and F.W. Schwartz. 1981a. Mass transport 2. Analysis of uncertainty in prediction, *Water Resour. Res.*, v.17, 351-369.
- Smith, L. and F.W. Schwartz. 1981b. Mass transport 3. Role of hydraulic conductivity data in prediction, *Water Resour. Res.*, v.17, 1463-1479.
- Smith, L., C.W. Mase, and F.W. Schwartz. 1985. A stochastic model for transport in networks of planar fractures, in proceedings of the Symposium on the Stochastic Approach to Subsurface Flow, ed. G. de Marsily.
- Sposito, G., W.A. Jury, V.K. Gupta. 1986. Fundamental problems in the stochastic convection-dispersion model of solute transport in aquifers and field soils, *Water Resour. Res.*, v.22, 77-88.
- Sudicky, E.A. and E.O. Frind. 1982. Contaminant transport in fractured porous media: Analytical solutions for a system of parallel fractures, *Water Resour. Res.*, v.18, 1634-1642.
- Sudicky, E.A., J.A. Cherry, and E.O. Frind. 1983. Migration of contaminants in groundwater at a landfill: A case study, 4. A natural gradient dispersion test, *J. of Hydrology*, v.63, 81-107.
- Sudicky, E.A. 1985. Spatial variability of hydraulic conductivity at the Borden tracer test site, in proceedings of the Symposium on the Stochastic Approach to Subsurface Flow, ed. G. de Marsily.
- Sutton, P.A. and J.F. Barker. 1985. Migration and attenuation of selected organics in a sandy aquifer - A natural gradient experiment, *Groundwater*, v.23, 10-16.



- Tang, D.H., E.O. Frind, and E.A. Sudicky. 1981. Contaminant transport in fractured porous media: Analytical solution for a single fracture, *Water Resour. Res.*, v.17, 555-564.
- van Genuchten, M.Th. and W.J. Alves. 1982. Analytical solutions of the one-dimensional convective-dispersive solute transport equation, U.S. Dept. of Agric. Tech. Bull. 1661.
- van Genuchten, M.Th., D.H. Tang, and R. Gunnelon. 1984. Some exact solutions for solute transport through soils containing large cylindrical macropores, *Water Resour. Res.*, v.20, 335-346.

## CURRICULUM VITAE

Richard T. DeCesar  
Keystone Environmental Resources  
440 College Park Drive  
Monroeville, PA 15146  
(412) 733-9528

Education

- 1978 Shippensburg State College, B.S., Chemistry  
1984 Oregon Graduate Center, M.S., Environmental Science  
1987 Oregon Graduate Center, Ph.D., Environmental Science

Employment History

- 1987- Keystone Environmental Resources, 440 College Park Drive, Monroeville, PA 15146. Senior Scientist in Risk Management.  
1987 University of Connecticut, Dept. of Civil Engineering, Instructor.  
1986-1987 TRC Environmental Consultants, East Hartford, CT. Senior Consulting Scientist.  
1982-1986 Oregon Graduate Center, Beaverton, OR. Graduate Student Research Assistant.  
1979-1982 Oregon Graduate Center, Beaverton, OR. Research Associate.  
1979-1982 NEA, Inc., Beaverton, OR. Supervisor for Data Management and Modeling.

Research Interests

The transport and fate of pollutants in aqueous and atmospheric systems; quantitative risk management; in situ remediation of sub-surface contaminants; development of field, laboratory and modeling techniques appropriate for contaminant transport through porous and fractured deposits; urban aerosol source apportionment; application of statistical methods for experimental design and data interpretation.